UAB
Universitat Autònoma de Barcelona

TOWARDS ORGANIC MULTI-JUNCTION RAINBOW SOLAR CELLS

Miquel Casademont Viñas

ADVERTIMENT. L'accés als continguts d'aquesta tesi queda condicionat a l'acceptació de les condicions d'ús establertes per la següent llicència Creative Commons:  https://creativecommons.org/licenses/?lang=ca

ADVERTENCIA. El acceso a los contenidos de esta tesis queda condicionado a la aceptación de las condiciones de uso establecidas por la siguiente licencia Creative Commons:  https://creativecommons.org/licenses/?lang=es

WARNING. The access to the contents of this doctoral thesis it is limited to the acceptance of the use conditions set by the following Creative Commons license:  https://creativecommons.org/licenses/?lang=en

TOWARDS ORGANIC MULTI-JUNCTION RAINBOW SOLAR CELLS

MIQUEL CASADEMONT VIÑAS

Supervisors:
Prof. Mariano Campoy-Quiles
Prof. Alejandro R. Goñi

Tutor:
Prof. Alejandro R. Goñi

Institut de Ciència de Materials de Barcelona (ICMAB)
Nanostructured Materials for Optoelectronics and Energy Harvesting (NANOPTO)

Facultat de Ciències i Biociències
Universitat Autònoma de Barcelona (UAB)

PhD in Materials Science, October 2024

QR code to acces the dedicated GitHub page of the PhD thesis containing its digital version, additional information, and extra resources.

Miquel Casademont Viñas: *Towards organic multi-junction RAINBOW solar cells.* © October 2024

PhD Thesis

October 2024

Towards organic multi-junction RAINBOW solar cells

Miquel Casademont Viñas

Institut de Ciència de Materials de Barcelona (ICMAB-CSIC)
Universitat Autònoma de Barcelona (UAB)

The real innovators did their innovating just by being themselves.

Count Basie

Life is a lot like jazz. It's best when you improvise.

George Gershwin

Dedicat als meus pares i als meus avis,
a qui els hi dec la vida.

ABSTRACT

Organic photovoltaics (OPV) is a promising green energy technology due to its lightweight, optical tunability, flexibility, and compatibility with industrial roll-to-roll fabrication. However, improvements are necessary for stability and efficiency, particularly for multi-junction OPVs based on tandem geometries. In this PhD thesis, we explore a novel multi-junction approach called RAINBOW. This geometry involves stacking sub-cells laterally instead of vertically to address processing challenges and eliminate the need for current matching. The research aimed to develop a toolkit for optimizing parameters to increase the maximum efficiency of RAINBOW and validate the RAINBOW concept. To characterize and study RAINBOW solar cells, we have developed a spectrum on demand light source (SOLS) setup and a simulation model. Proof of concept devices were fabricated to demonstrate the effectiveness of the RAINBOW concept. Additionally, through a screening of wide band-gap materials, the PTQ10:O-IDFBR blend was identified as having the potential to enhance multi-junction performance and indoor light harvesting. This finding underscores the practical implications of our research and its potential to contribute to the broader field of renewable energy.

RESUM

La fotovoltaica orgànica (OPV) és una tecnologia que gràcies a la seva lleugeresa, adaptabilitat òptica, flexibilitat i compatibilitat amb la fabricació industrial *roll-to-roll* promet ser una de les fonts d'energia verda del futur. No obstant, millores de l'estabilitat i l'eficiència són necessàries, especialment, per als dispositius OPV multiunió basats en geometries en tàndem. En aquesta tesi doctoral, explorem un nou enfocament multiunió anomenat RAINBOW. Aquesta geometria consisteix a apilar subcel·les lateralment en comptes de verticalment per abordar els reptes de processament i eliminar la necessitat d'igualar el corrent. L'objectiu de la investigació ha estat desenvolupar un conjunt d'eines per optimitzar paràmetres per tal d'augmentar la màxima eficiència RAINBOW i validar el concepte. Per caracteritzar i estudiar les cèl·lules solars RAINBOW, hem desenvolupat una instrument de mesura de font de llum a demanda (SOLS) i un model de simulació. A més a més, s'han fabricat dispositius de prova de concepte per demostrar el concepte de la geometria RAINBOW. A més, mitjançant

una selecció de materials de banda ampla, es va identificar que la mescla PTQ10:O-IDFBR té un gran potencial per millorar el rendiment de les geometries multiunió i la conversió de llum d'interiors en energia elèctrica. Aquesta troballa subratlla les implicacions pràctiques de la nostra investigació i el seu potencial per contribuir al camp més ampli de les energies renovables.

RESUMEN

La energía fotovoltaica orgánica (OPV) es una tecnología que debido a su peso ligero, capacidad de ajuste óptico, flexibilidad y compatibilidad con la fabricación industrial *roll-to-roll* promete ser una de las fuentes de energía verde del futuro. Sin embargo, son necesarias mejoras de la estabilidad y la eficiencia, en particular para las OPV de unión múltiple basadas en geometrías en tándem. En esta tesis doctoral, exploramos un nuevo enfoque de unión múltiple llamado RAINBOW. Esta geometría implica apilar subceldas lateralmente en lugar de verticalmente para abordar los desafíos de procesamiento y eliminar la necesidad de igualar la corriente. La investigación tuvo como objetivo desarrollar un conjunto de herramientas para optimizar los parámetros para aumentar la máxima eficiencia de la geometría RAINBOW y validar el concepto. Para caracterizar y estudiar estas las células solares, hemos desarrollado una configuración de fuente de luz de espectro a demanda (SOLS) y un modelo de simulación. Se fabricaron dispositivos de prueba de concepto para demostrar la eficacia del concepto RAINBOW. Además, mediante una selección de materiales de banda ancha, se identificó que la combinación PTQ10:O-IDFBR tiene el potencial de mejorar el rendimiento de las uniones múltiples y la conversión a electricidad de la luz en interiores. Este hallazgo subraya las implicaciones prácticas de nuestra investigación y su potencial para contribuir al campo más amplio de las energías renovables.

SCIENTIFIC CONTRIBUTIONS

ORCID: 0000-0002-2848-9069 **Google Scholar**: Miquel Casademont-Viñas

PUBLICATIONS

1. M. Casademont-Viñas, D. Capolat, A. Quesada-Ramírez, M. Reinfelds, G. Trimmel, M. Sanviti, J. Martín, A. R. Goñi, T. Kirchartz and M. Campoy-Quiles. Combinatorial screening of wide band-gap organic solar cell materials with open-circuit voltage between 1.1 and 1.4 V. *Journal of Materials Chemistry A* (2024). DOI: 10.1039/D4TA01944J.
2. M. Casademont-Viñas, M. Gibert-Roca, M. Campoy-Quiles and A. R. Goñi. Spectrum on demand light source (SOLS) for advanced photovoltaic characterization. *Review of Scientific Instruments* **94,** 103907 (2023). DOI: 10.1063/5.0156236.
3. M. Gibert-Roca, M. Casademont-Viñas, Q. Liu, K. Vandewal, A. R. Goñi and M. Campoy-Quiles. RAINBOW Organic Solar Cells: Implementing Spectral Splitting in Lateral Multi-Junction Architectures. *Advanced Materials,* 2212226 (2023). DOI: 10.1002/adma.202212226.
4. V. Belova, A. Perevedentsev, J. Gorenflot, C. S. P. D. Castro, M. Casademont-Viñas, S. H. K. Paleti, S. Karuthedath, D. Baran, F. Laquai and M. Campoy-Quiles. Effect of Quencher, Geometry, and Light Outcoupling on the Determination of Exciton Diffusion Length in Nonfullerene Acceptors. *Solar RRL* **6,** 2100822 (2022). DOI: 10.1002/solr.202100822.

PATENTS

1. M. Gibert-Roca, M. Casademont-Viñas, A. R. Goñi and M. Campoy-Quiles. Dispositivo de iluminación y modulador espectral. *Oficina española de patentes y marcas,* ES2956835 B2 (2023).

PRIZES

- M. Casademont-Viñas, E. Pujades-Otero, M. Campoy-Quiles and A. R. Goñi. Spectrum on Demand Light Source (SOLS) for

Advanced Photovoltaic Characterization. EmErgEnt Award from the Efficient Energy Cluster of Catalonia. (2023)

PRESENATIONS AND POSTERS

- M. Casademont-Viñas, M. Gibert-Roca, Q. Liu, K. Vandewal, A. R. Goñi and M. Campoy-Quiles. Spectral Splitting Geometries for High Efficiency Multijunction Organic Solar Cells. *International Conference on Hybrid and Organic Photovoltaics 2022 (HOPV22).* València (Spain). May 2022. Presentation.
- M. Casademont-Viñas, M. Gibert-Roca, Q. Liu, K. Vandewal, A. R. Goñi and M. Campoy-Quiles. Spectral Splitting Geometries for High Efficiency Multijunction Organic Solar Cells. *EMRS Fall Meeting 2022.* Warsaw (Poland). September 2022. Presentation.
- M. Casademont-Viñas, M. Gibert-Roca, M. Campoy-Quiles and A. R. Goñi. Spectrum on Demand Light Source (SOLS) for Advanced Photovoltaic Characterization. *Materials for Sustainable Development Conference (MATSUS23).* Valencia (Spain). March 2023. Presentation.
- M. Casademont-Viñas, M. Gibert-Roca, M. Campoy-Quiles and A. R. Goñi. Spectrum on Demand Light Source (SOLS) for Advanced Photovoltaic Characterization. *EMRS Spring Meeting 2023.* Valencia (Spain). May 2023. Presentation.
- M. Casademont-Viñas, M. Gibert-Roca, Q. Liu, K. Vandewal, A. R. Goñi and M. Campoy-Quiles. RAINBOW Organic Solar Cells: Implementing Spectral Splitting in Lateral Multi-Junction Architectures. *EMRS Spring Meeting 2023.* València (Spain). May 2023. Poster.
- M. Casademont-Viñas, M. Gibert-Roca, Q. Liu, K. Vandewal, A. R. Goñi and M. Campoy-Quiles. RAINBOW Organic Solar Cells: Implementing Spectral Splitting in Lateral Multi-Junction Architectures. *European conference on molecular electronics (ECME2023).* Bari (Italy). October 2023. Poster.
- M. Casademont-Viñas, M. Gibert-Roca, Q. Liu, K. Vandewal, R. A. Goñi and M. Campoy-Quiles. RAINBOW Organic Solar Cells: Implementing Spectral Splitting in Lateral Multi-Junction Architectures. *Materials for Sustainable Development Conference (MATSUS24).* València (Spain). March 2024. Presentation.

ACKNOWLEDGMENTS

Recordo un dia a l'institut que en Jaume, el professor de física que em va marcar en els meus inicis, em va dir alguna cosa com: "a vegades quan les coses no van com volem ens canvien la vida cap a bé de forma inesperada". Crec que aquesta idea defineix bastant bé com et vaig conèixer a tu, Mariano. Y des del momento que decidí hacer el TFG contigo he descubierto a una persona y una forma de hacer de las cuales estoy enamorado y contento de haber conocido, y supongo que esto ha hecho que a día de hoy esté defendiendo mi tesis a tu lado. Y muy de cerca, sobre todo estos años de doctorado, he tenido el placer de escuchar y gozar de un argentino parlanchín, valga la redundancia, con las ideas muy claras. ¡Por si no lo habías adivinado, estoy hablando de ti Alejandro! A los dos os quiero agradecer el esfuerzo y confianza que siempre habéis depositado en mí y la pasión por la ciencia que me habéis transmitido. Sois dos personas muy creativas, con muchas ideas y brillantes científica y humanamente. Espero que podáis seguir transmitiendo esta pasión y energía a toda la gente que conozcáis en el futuro porque, por experiencia propia, puedo decir que hacéis que la gente de vuestro alrededor esté más feliz.

També vull agrair a tothom de NANOPTO a qui he conegut a llarg d'aquests anys a l'ICMAB, i especialment als dos supervisors que he tingut en les dues etapes a l'ICMAB prèvies a la tesi (TFG i TFM). Primero de todo a ti, Bernhard, que fuiste un referente de correctitud y método científico des del primer día que te conocí. Aleksandr Perevedentsev, your name is also important in my scientific career. I think your character is like your surname, it may seem complicated and strange at the start, but after working hard you end up learning it "by heart". Your unique approach to life is something that I admire. Un altre pilar important ha estat el Dr. Gibert-Roca. Martí, trobaràs moltes vegades el teu nom escrit a la tesi (si algun dia te la llegeixes) i és que es podria dir que al teu costat vaig començar-la tant en la vida quotidiana com en els laboratoris, i això m'ha donat experiències que no oblidaré mai. Si algun dia tornem a compartir la vida, estic segur que ho celebraré. Jose, moltes gràcies per estar sempre al meu costat disposat a donar un cop de ma i fer broma del que calgués. T'has convertit en un amic meu i per això espero no perdre't mai la pista. Illy y Leo, muchas gracias por tomar el relevo de "los italianos de NANOPTO". Creo que no habeis defraudado a nadie con vuestro humor y vuestra siempre amigable sonrisa. Me habeis hecho sentir de vuestra

família des del primer dia. Putu Pau, quan vas marxar em vaig adonar del bon humor que aportaves al laboratori (i a la pista de pàdel), moltes gràcies per fer-ho sempre. Ana, espero que te vaya muy bien en esta nueva etapa de madre y que sepas que estas invitada a probar una fideuá de mi padre cuando quieras! (no solo un lunes de mi tupper). Osnat, tienes un corazón inmenso, siempre me has dado consejo cuando lo he necesitado. Espero que te pase lo mejor en tu futuro con Fendy, los dos sois lo más bonito y dulce que he conocido. Eulàlia, ets la millor roomescapista d'europa i no ho dic per les tantes scape rooms que has probat sinó per les mil gestions en les que m'has salvat el cul. T'ho agraeixo de tot cor. Albert, per mi ets el gran hereu del know-how del grup i t'estic mol agraït per respondre'm sempre els dubtes absurds. Vam compartir junts el nostre primer congrés i sempre me'n recordaré. Luis, la calma, la homogeneidad en el tamaño de tus pelos y el buen sentido del humor han sido características que sempre he admirado de ti. Kai, thanks for sharing screws with me and for your efforts in the development of "my" lovely SOLS. Adrián, compartimos unos meses de duro trabajo con el Raman donde lo único que sacamos fueron buenos momentos, pero ¡que nos quiten lo bailado! Alfonsina, des del primer día me sorprendieron tus habilidades en el laboratorio y tu carácter siempre alegre. Ha sido un placer compartir un proyecto tan bonito como el RAINBOW con una persona tan brillante como tú. Francesc, moltes gràcies pel carácter obert i trempat que tens, el futur del RAINBOW está en molt bones mans! Crec que mai oblidaré els teus pasos de ball prohibits el día de l'helio (estaves a primera fila jeje). Arianna, des del primer minuto no has dejado de compartir sonrisas y buenas palabras con todo el mundo. Eres una gran persona y espero seguir viendo tu sonrisa como hasta ahora. Jiali, we have shared so many moments as PhD students. I wish that out thesis defense is not the last. Manan, at some point I regretted to share with you my phone number, but then I realized that you are a magnific person and a very critic and talented scientist. I wish you use glasses the next time you filter anything, just in case. Xabi y Quique, habéis sido referentes para mí en lo personal y en lo científico. Espero no perderos nunca la pista. Jana i Dani, vau estar a l'altura el poc temps que us vaig tenir com a estudiants. Us agraeixo molt la paciència que vau tenir amb mi i les bones maneres de comunicarnos. Espero poder mantenir el contacte amb vosaltres. Sergi, me'n recordo dels primers dies que vam compartir a l'ICMAB on discutíem (sempre amb bona actitud i des de l'amistat) qualsevol cosa. T'agraeixo molt tot el que m'has ensenyat. Sebas, raramente encontrarás un momento para leer esta frase porque siempre andas

liado compartiendo conocimiento y buenos momentos con todo el mundo. I would also like to thank to the people I meet in Jülich, specially to Benjamin, Markus and Thomas for your help during my days in Jülich. També a la gent de l'EURECAT. Ignasi i Paula, moltes gràcies per acullir-me amb els braços oberts i per tenir paciència amb mi. I also acknowledge all the other people that have been part of NANOPTO at some point and that shared moments with myself and my colleagues in and outside the lab: Muhamad, Theo, Sunghwan, Eric, Carlota, Afroditi, Martin, Shima, Videsh, Xiaoyu, Minghua, Jinhui, Rana, Camilla, José, Gail, Mayte, Valentina, Cristiano, Agustín, Miquel, Isabel, y muchos otros que me olvido.

I have always been a "open software" kind of person, thus I have to aknowledge all the people that have developed resources that I used during the thesis. Everyone that collaborates in online Q&A pages like Stack Overflow. Thanks to André Miede, for the development of Classic Thesis LaTeX template, which I have used to write the manuscript. També vull agraïr a tothom qui fa possible el finançament derrera la ciència, tant a nivell català i espanyol com a nivell europeu.

També vull agrair als amics que la vida m'ha regalat al llarg dels anys per distreure'm els caps de setmana i incloure'm en qualsevol pla. Genís, Pere, Martí, Guillem i Arnau, us vull agrair que feu que l'esforç que significa compartir un projecte com Classe B amb vosaltres sigui més lleuger. També a tota l'altre gent que fa que Classe B sigui un lloc on gaudir de bons moments: Bernat, Alec, Kel, Lara, etc... Joan, finalment (si tot va be) deixaré que em diguis "doctor" i espero que m'ho diguis moltes més vegades. Lili, Ari i Judit, us agraeixo la vostra eterna confiança en mi (i en el meu cervellet). I a tot els altres amics i coneguts que m'han aguantat durant aquests anys, també us ho agraeixo tot.

Cris, et vull agrair també tota la paciència que has tingut amb mi especialment en el temps que he estat escrivint la tesi. Em sap greu que la incertesa del futur et sigui complicada d'assumir però t'estimo molt i m'agradaria que sempre tinguessis clar que la única certesa és que vull que el futur sigui al teu costat. També vull agrair-los als meus pares, Narís i Pepita, per tota la paciència que heu tingut amb mi. Des de que vaig marxar de casa sé que m'heu trobat a faltar i que sempre heu desitjat el millor per mi i heu fet tot el possible per aconseguir-ho. Vull que sapigueu que ho heu aconseguit i que us estic mol agraït per tots els esforços que feu dia rere dia per mi. Us estimo molt. Als meus avis, que m'agradaria haver pogut compartir aquests moments. A la Maria petita, que es mereix el títol de doctora més que jo, i a la seva

família per la força que han tingut en tot moment. Als meus tius Clara i Francesc per la inspiració professional que involuntàriament han tingut en mi. I a la resta de la meva família.

Finally, I would like to thank you for taking a look at my thesis. I hope you enjoy it as much as I did during these years. I am always open to discussing and chatting about anything related (or unrelated) to the thesis.

CONTENTS

LIST OF FIGURES

LIST OF TABLES

ACRONYMS

- **AL**: Active layer
- **AM1.5G**: Air mass 1.5 Global
- **CAS**: Chemical abstract services
- **CB**: Chlorobenzene
- **CF**: Chloroform
- **CCT**: Correlated color temperature
- **CV**: Cyclic voltametry
- **DMD**: Digital micromirror device
- **DSSC**: Dye-sensitized solar cell
- **EVS**: Electrochemical voltage spectroscopy
- **EL**: Electroluminesence
- **ETL**: Electron transport layer
- $\boldsymbol{E_{bg}}$: Energy band-gap

- E_{ph}: Photon energy
- **FoM**: Figure of merit
- FF: Fill factor
- **GISAXS**: Grazing incident small angle X-ray scattering
- **GIWAXS**: Grazing incident wide angle X-ray scattering
- **HOMO**: Highest occupied molecular orbital
- **HTL**: Hole transport layer
- **IoBC**: Increase over the best cell
- **CIE**: International commission on illumination
- **IEA**: International Energy Agency
- **IUPAC**: International union of pure and applied chemistry
- **IoT**: Internet of things
- **LED**: Light emiting diode
- **LCD**: Liquid crystal display
- **LUMO**: Lowest unoccupied molecular orbital
- **MO**: Molecular orbital
- **NFA**: Non-fullerene acceptor
- V_{sc}: Open-circuit voltage
- **OPV**: Organic photovoltaic
- **PCR**: Partial coverage radial
- **PSC**: Perovskite photovoltaic
- **PV**: Photovoltaic
- EQE_{PV}: Photovoltaic external quantum efficiency
- PCE: Power conversion efficiency
- **RCoBC**: Relative change over the best cell
- **R2R**: Roll-to-roll
- **SQ**: Shockley-Queisser
- J_{sc}: Short-circuit current density

- **SOLS**: Spectrum on-demand light source
- **TRL**: Technology readiness level
- **VASE**: Variable-angle spectroscopic ellipsometry

1 INTRODUCTION

1.1 MOTIVATION

1.1.1 *Environmental scenario*

Humankind is facing one of its most challenging technological problems: the increasing energy consumption and the environmental impact of its production. The global economy, centered on high consumption of resources, has increased the global energy demand by more than 50% in the last 50 years. 80% of this increase came from emerging markets and developing economies.[1] The increase is even higher for the electricity production market, which has increased fourfold during the last 50 years, reaching a production near 29000 TWh. Fossil fuels have been the main source of energy production, representing 75% of electricity production 50 years ago. Nowadays, they are responsible for 60% of electricity production, which is still a high value compared with the need for the Net Zero Emissions scenario. Due to the utilization of fossil fuels, the concentration of greenhouse gases in the Earth's atmosphere has increased, intensifying the greenhouse effect and contributing to the global warming phenomenon. As a result, an alarming climate change is present in our daily lives. Last year (2023) was the hottest recorded year in the history of modern humankind.

In this scenario, we need to replace fossil fuel energy sources with renewables, a goal known as Net Zero Emissions Scenario.[2] The International Energy Agency (IEA) expects that in 2030 electricity production from renewable energy sources will grow from the current 30% to 50%, reducing fossil fuel sources from 60% to 40%. The latter will be mainly driven by significant investment and production of photovoltaic (PV) technologies.[3]The last report on renewable energies from the IEA states that solar PV generation increased by a record 270 TWh (up 26%) in 2022, reaching almost 1300 TWh.[3] It demonstrated the largest absolute generation growth of all renewable technologies in 2022, surpassing wind for the first time in history. This generation growth rate matches the level envisaged from 2023 to 2030 in the Net Zero Emissions by 2050 Scenario. Continuous growth in the economic attractiveness of PV, massive development in the supply chain, and increasing policy support, especially in China, the United States, the European Union, and India, are expected to accelerate further capacity growth in the coming years.[3]

With the current policies, this increase in PV energy production and change in the energy market will not be enough to keep global warming below the critical 1.5°C.[1] Nonetheless, the IEA reports that this is still open thanks to the growth of green energies.[2] For this to happen, policies must drastically change to a greener world. It is still in our hands to learn from the mistakes of the past humankind to have the best possible future.

1.1.2 *Photovoltaic technologies*

In the current scenario, the energy produced by solar PV represents 4% of all energy production.[1] Crystalline silicon (c-Si) modules (aka. first generation PV) account for over 95% of global PV production.[4] During the last years, commercial silicon modules have drastically improved. Today, electricity-intensive solar PV manufacturing is mostly powered by fossil fuels, but solar panels only need to operate for 4-8 months to offset their manufacturing emissions.[4] This payback period compares with the average solar panel lifetime of around 25-30 years. The relatively short energy payback times are due to the improved efficiency, which reached values between 18 and 23% depending on the different existing technologies. The price of PV modules has decreased significantly over the past decade. Around 2014, the cost of PV modules was approximately $0.70 to $0.80 per watt. By contrast, prices in recent years have dropped to as low as $0.20 to $0.30 per watt.[4]

Nonetheless, there are certain disadvantages associated with first-generation photovoltaic (PV) technology. These include the weight and lack of flexibility of the devices, which result from the requirement for thick components to ensure maximum light absorption and thick glass encapsulation. These limitations result in silicon PV modules being restricted to solid rooftops, facades, and dedicated solar farms and do not integrate aesthetically into the urban environment. As a result, silicon is not a good candidate for photovoltaic light harvesting for the upcoming generation of internet of things (IoT) electronic devices.[5] Small, portable, and independent energy sources need to be incorporated into different systems and designs, functioning effectively under indoor lighting conditions, at a low cost, and with minimal maintenance.[6] All such requirements are mostly accomplished by emerging PV technologies such as organic photovoltaics (OPV), dye-sensitized solar cells (DSSC), or perovskite solar cells (PSC) modules, which have been demonstrated to surpass the 20% efficiency milestone under AM1.5G illumination and the 35% under indoor light-emitting diode (LED) lighting conditions.[7, 8, 9, 10]

1.2 ORGANIC PHOTOVOLTAICS

Organic photovoltaics (OPV) is the field that explores the use of semiconducting organic polymers and small molecules to convert light into electrical power through the photovoltaic effect. OPV has seen increasing interest in recent years as an alternative to silicon PV because it offers a suite of promising properties. For example, the organic chemistry to synthesize different molecules and polymers is well-studied and has already been implemented on an industrial scale for various processes.[11, 12, 13] The capability of synthesizing molecules with a wide variety of properties opens the possibility for the improvement of devices and widens their applications, such as integrated architecture,[14] curved surfaces,[15, 16, 17] or integration in textile fabric.[18] One of the most important properties of tuning on-demand is the energy band gap (E_{bg}), i.e., the absorption profile can be varied along the visible spectrum by designing and synthesizing molecules with different molecular orbital energy levels.[19, 20, 21] In this direction, one can design an OPV system optimized for harvesting the solar spectrum (AM1.5G) as described by the Shockley-Queisser limit.[22] Nevertheless, the same materials may not be the best for harvesting the energy from other light sources, such as an indoor LED bulb. The latter may be done more efficiently by another material system. Thus, OPV is a suitable technology for harvesting light sources differing from the 1-Sun standard.

One of the key advantages of OPV is its compatibility with roll-to-roll (R2R) processes: all layers of an OPV device can be coated from a precursor ink compatible with industrial R2R systems.[23, 24, 25] The latter enables the fabrication of modules with velocities from 60 to 300 m min^{-1}, comparable to those used to print plastics in industrial R2R systems.[26] Post-processing conditions are not energy-intensive since annealing is generally below 150°C for a few minutes.[26] As a result, OPV promises to have a low energy payback time. Krebs et al. showed that the energy payback time of an OPV solar farm in 2014 could be around 277 days.[26] Nowadays, with the improved efficiency in the OPV field, it can be reduced to just a few days.[27, 28, 29] In the future, the fabrication cost of OPV is expected to be below that of silicon PV.[30, 31]

Nevertheless, the fabrication cost is not the only indicator to compete with the silicon PV market.[32] Efficiency is another important indicator to consider. The latter has been increasing during the last 25 years of research (see Figure 1.1), starting from the 2-3% achieved in the early century for the archetypal MDMO-PPV:$PC_{60}BM$ blend,[33] up to the current certified 20.0% PCE record obtained by a ternary

blend with the new-generation of non-fullerene acceptors (NFAs) derivatives of Y6.[34] The efficiency increase was partly due to the continuous development of active layer materials, in the first instance, by chemical modifications of donor polymers (side chains and co-polymers) blended with functionalized fullerenes.[35] In recent years, the employment of novel NFAs (with ITIC and Y6 as important milestones) yielded even higher *PCE*s and changed the focus of organic semiconductor developments.[36, 37, 38] Lately, Y6 and its derivatives are responsible for the actual high *PCE*s reaching 20%.[39, 40] Key findings on processing conditions (choice of solvents, solvent additives, aggregation control) were similarly crucial as the development of the light-harvesting semiconductors themselves to adjust the bulk-heterojunction morphology and to yield high *PCE*s.[41, 42]

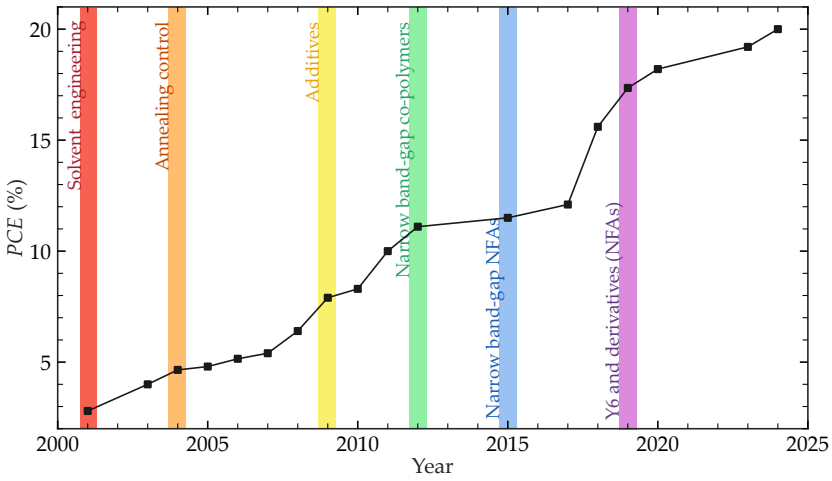

Figure 1.1: Power conversion efficiency evolution of organic photovoltaics since the start of this century. The different vertical regions show key advances in knowledge and synthesis of new materials that triggered the increase in PCE. Adapted from references [43, 44, 45]

1.2.1 *Working principles*

The phenomenon behind any photovoltaic technology is the photovoltaic effect, which was first described by Becquerel in 1839. Becquerel observed that an electrical current and a voltage were generated upon illumination of platinum electrodes coated with silver chloride.[46] It was decades after that the physics of the photovoltaic effect was understood. It involves exciting an electron to a high energy state by photon absorption and then extracting charge carriers to an external circuit. In order to convert the energy of excited charge carriers into electricity, the charge carriers need to maintain their excited state until

they reach the external load, at which point their energy is released and converted into useful work. Semiconducting materials are ideal candidates for this purpose because of their energy level band gap and good electrical conductivity, which results in long charge carrier diffusion paths, enabling excited charge carriers to escape the material before releasing its energy.[47] This is unlike metals, where charge carrier relaxation is almost immediate,[48] and insulators, where charge mobility is too low for efficient charge extraction.[49] Because of this, solar cells are conventionally made out of semiconducting materials, with a series of layers with different electrical properties engineered to maximize excited charge carrier extraction, thus maximizing light power conversion.

Inorganic semiconductors present an electronic band structure composed of a valence band (low energy states) and a conduction band (high energy states) with an energy range in between without electronic states named energy band gap (E_{bg}), as represented in Figure 1.2. Each of the mentioned bands are composed of electronic states that extend along the material due to the crystalline structure of the latter. For an intrinsic semiconductor (without dopants), most of the electrons (free charges) are at the valence band. When a photon with energy higher than the E_{bg} of the semiconductor reaches the material, it can promote the excitation of an electron from the valence band to a state of the conduction band, leaving an electron hole (positively charged) in the conduction band. Since they originated physically close, the electron and hole remain bounded by coulomb attraction in a quasiparticle named exciton (referring to the bound electron-hole pair). Due to the high dielectric constant of inorganic semiconductors, the medium screens the coulomb attraction, reducing it to a few meV. Thus, at

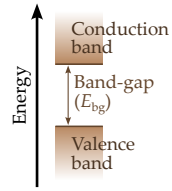

Figure 1.2: Band diagram of an inorganic semiconductor. The majority of electrons are occupying states of the valence band.

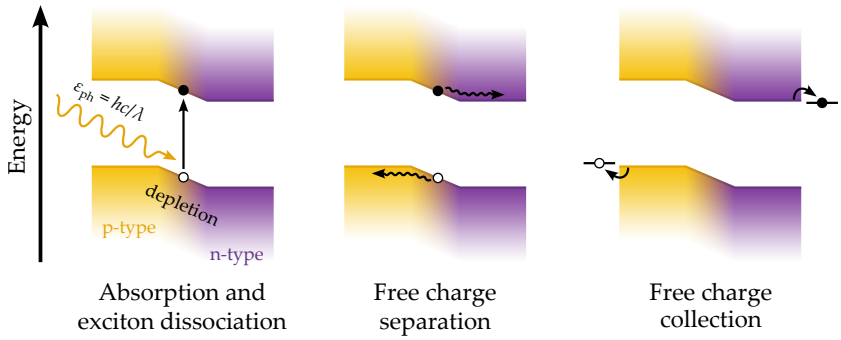

Figure 1.3: Basic processes in an inorganic p-n junction for PV electricity generation. First, light is absorbed, creating an exciton which dissociates immediately due to the thermal energy. The absorption can happen at any point of the material, charges will only effectively separate if one reaches the depletion region. After separation, free charges are collected from the contacts.

room temperature (300 K), the thermal energy (26 meV) is enough to rapidly dissociate the exciton, effectively generating a free electron and a free hole readily after absorption. The device is engineered to drive them to separate contacts so that an electric field inside the material originates, driving the different charge carriers to opposite contacts. The latter is commonly achieved by a p-n junction, which consists of a bilayer-like structure that combines a positively doped semiconductor (p-type) with a negatively doped semiconductor (n-type). The junction of both materials creates a depletion region, where electrons and holes introduced by the dopants recombine. In the depletion region, the semiconductor bands bend, generating the electric field that drives the charges to separation. Figure 1.3 depicts the band diagram of an inorganic p-n junction and the basic processes described for electricity generation.

1.2.2 *Organic semiconductors*

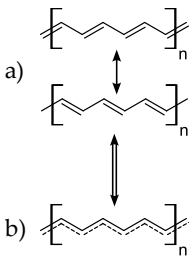

Figure 1.4: Chemical draw of conjugated carbon chain. The conjugated nature can be drawn in resonant structures (a) where single and double bonds are alternated or as in (b) where the dashed line denotes conjugation.

The photovoltaic process for OPV differs from that in inorganic photovoltaics. The first difference concerns the nature of the material and, thus, its electronic states. While organic semiconductors still have an energy band gap within the range of a semiconductor (which is why they behave as semiconductors), their electronic states are molecular orbitals (MO) confined in certain regions of the organic molecules rather than electronic states that extend over the active layer material. Thus, although molecular orbitals in an organic semiconductor can be simplified as conduction and valence bands analogously to inorganic semiconductors, their nature is different. The semiconductor nature arises from the great degree of conjugation within their chemical structures, where carbon atoms bond in an alternating single-double bond configuration, as depicted in Figure 1.4. This bond distribution leads to the delocalization of their p_z orbital electrons, forming two new molecular orbitals, a bonding π orbital, and an antibonding π^* orbital (see Figure 1.5). The latter, repeated as many times as carbon atoms have the single-double backbone, originates a group of bounding MO populated with electrons and a group of antibonding MO empty of electrons, with an energy band gap in between. Thus, one can simplify the scenario by attributing to those MO the naming of valence and conduction bands, respectively, as in the case of inorganic semiconductors (see Figure 1.5). Nevertheless, they are not "bands" but, instead, molecular orbital states with close lying energies. Two of those MO are especially important for the optical and electronic properties of the semiconductors: the highest occupied molecular orbital (HUMO), corresponding to the MO with higher energy in the valence band; the lower unoccupied molecular orbital (LUMO), corresponding to the MO with lower energy in the conduction band.[50]

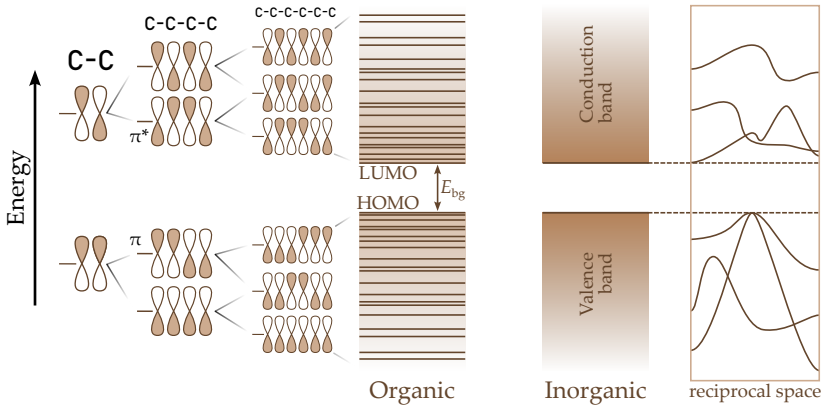

Figure 1.5: Nature of organic semiconductor behavior concerning inorganic. The origin of semiconductor nature of organic materials comes from the bonding and antibonding (π and π^*) orbitals that originate from the hybridization of p_z orbital electrons.

1.2.3 *Active layer morphology*

Another fundamental difference between organic and inorganic semiconductors is their dielectric constant, being much lower for organic materials. The latter has a direct impact on the working principles of the device. In an organic semiconductor, the photogenerated exciton (electron-hole pair) exhibits a binding energy higher than the thermal energy (at 300 K). Thus, the exciton does not dissociate due to thermal energy and would recombine, unless one engineers a driving force to promote its dissociation. The latter is done by combining (at least) two materials in the active layer, known as electron donor and electron acceptor (a.k.a. donor and acceptor, respectively). To achieve exciton dissociation, the exciton must reach a donor-acceptor interface where the it will dissociate through a charge-transfer (CT) state where orbitals from both materials are involved.[51, 52, 53] The latter is a phenomenon still under study to understand and optimize properly.[51, 52, 53] To achieve high-efficiency devices, efficient exciton dissociation and the lowest possible energy loss are crucial. Nonetheless, a certain amount of energy has to be lost since, to promote electron transfer from the donor to the acceptor, $LUMO_{acceptor}$ must be deeper than the $LUMO_{donor}$. On the other hand, to promote hole transfer from the acceptor to the donor, $HOMO_{donor}$ must be shallower than $HOMO_{acceptor}$. The latter description forms a staggered (type-2) hetero-junction, as depicted in Figure 1.6.

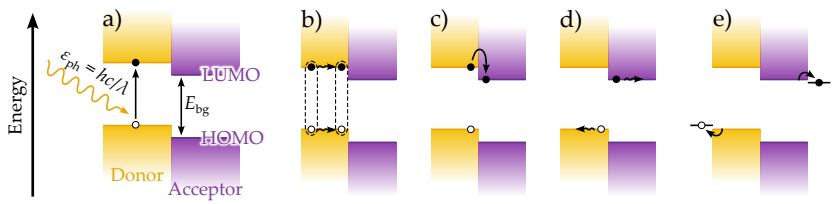

Figure 1.6: Schematics working principles of organic photovoltaics. A photon is absorbed, promoting an electron transition to an excited state (a). The photogenerated electron-hole pair (exciton) reaches a donor:acceptor interface (b), where one of the charges (in this case, the electron) is transferred to the other material through the charge transfer state (c) and the exciton is dissociated. The free charges diffuse to the contacts (d) where they get collected (e).

During the history of the OPV field, it has been accepted that for efficient exciton dissociation, the difference between $HOMO_{donor}$ and $HOMO_{acceptor}$ (ΔHOMO) as well as the difference between $LUMO_{donor}$ and $LUMO_{acceptor}$ (ΔLUMO) has to be at least 0.3 eV. Devices with lower values suffered from not efficient enough exciton dissociation seen as a low external quantum efficiency values (EQE_{PV}) and J_{sc}.[52, 54] Nevertheless, in recent years this idea has proven not to be universal, as various donor:NFAs systems appear to exhibit high efficiencies (i.e., efficient exciton dissociation) with ΔHOMO and/or ΔLUMO below 0.3 eV.[55, 56, 57, 58] Other factors like the delocalization of the CT state seems to be important to achieve efficient exciton dissociation at the donor:acceptor interface.[51, 52, 53, 58, 59, 60, 61]

As discussed before, photogenerated excitons can only dissociate at the donor:acceptor interface. This, together with the rather small exciton diffusion lengths (a few tens of nm in the best cases) results in the need for a finely tuned active layer morphology to achieve the best possible exciton generation, dissociation, and free charge extraction. To consider the ideal active layer morphology, one first needs to know that the typical mean free path of an exciton in an organic semiconductor is on the order of a few tens of nanometers, let's assume 20 nm.[62, 63, 64, 65] Thus, only excitons photogenerated at 20 nm far from the donor-acceptor interface will reach the interface to have the chance to dissociate. The excitons photogenerated at distances longer than the mean free path will end up recombining in a geminate recombination process.

The name "geminate" means that the electron-hole pair that recombines comes from the same photogenerated exciton.

Consider an active layer with a bilayer structure, as depicted in Figure 1.7 (a). In this scenario, the thickness of both layers should be of the order of the exciton diffusion length of each material since thicker films will result in excitons that recombine before reaching the donor-acceptor interface. The dissociated free charges would have a

straightforward path to their corresponding contact, with all electrons being collected at the ETL and all holes being collected at the HTL, thus achieving *a-priori* a high fill factor. Nevertheless, due to the low absorption of thin organic layers, most of the light will not be absorbed and the number of photogenerated charges will be small. As a result, the bilayer structure is not generally the ideal morphology. Nevertheless, some materials exhibiting large exciton diffusion lengths can benefit from this geometry. This is generally achieved with materials with a high crystalline order.[66]

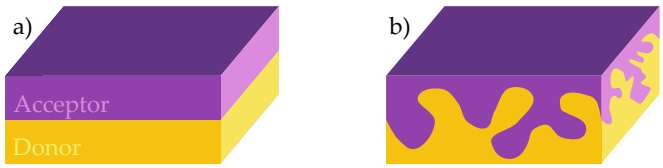

Figure 1.7: Schematis of bilayer and bulk heterojunction active layer morphologies. The donor and acceptor regions are depicted in yellow and purple, respectively.

To mitigate the problem of short exciton diffusion length and at the same time having a thick enough active layer to absorb most of the light, one needs to think of more complex geometries. In that direction, there has been a large investigation effort on a geometry named bulk heterojunction (BHJ).[67] This type of junction consists of a partially intermixed blend of donor-acceptor materials with domain sizes of the order of a few tens of nanometers, as depicted in Figure 1.7 (b). These nanoscopic domains result from partial phase segregation within the blend, during solution deposition from a single solution containing both materials, which leads to an increased donor-acceptor interfacial area. The larger donor-acceptor area, evenly spread throughout the bulk of the heterojunction, reduces exciton-interface distance, resulting in increased exciton dissociation efficiency, even with short exciton diffusion lengths. Shorter exciton-interface distances allow for thicker active layers, without sacrificing exciton dissociation efficiency, increasing light absorption in the photoactive layer, thus leading to higher-efficiency devices.[68]

Bulk heterojunctions are usually manufactured with solution processing techniques, such as spin coating or blade coating, by simultaneously depositing the donor and the acceptor thoroughly mixed in solution.[69] There is a large variety of parameters that affect the final active layer geometry, such as donor:acceptor composition, solvent, cosolvents, additives, deposition technique, deposition temperature or post-treatment annealing, just to name a few. For this reason, the

processing conditions usually need to be optimized to find the proper active layer morphology for each active layer material.[70, 71, 72, 73] Additionally, active layer thickness is an important parameter. Too thick active layer will reduce effiency extraction of charge carriers due to higher recombination rates, while a too thin active layer will exhibit suboptimal light harvesting..

1.2.4 *Device structure*

To achieve high-performing devices, active layer materials and morphology are important. Nonetheless, a solar cell is composed of other layers that also play an important role. The active layer is typically sandwiched in between two charge carrier selective layers. They are in charge of blocking the opposite sign charge carriers from reaching the incorrect contact. Thus, there are two types of selective contacts. The electron transport layer (ETL), sometimes named hole blocking layer, is a material that can selectively carry electrons (negative charges) while blocking holes (positive charges). This is achieved with a material whose conduction band is aligned with the $\mathrm{LUMO_{acceptor}}$, i.e., it has empty electronic states at the energy of free charge excited electrons, while keeping its valence band deeper than the $\mathrm{HOMO_{donor}}$ to prevent injection of excited holes from the donor. Conversely, the hole transport layer (HTL), sometimes named electron blocking layer, is a material that can selectively carry holes while blocking electrons. The latter is achieved with a material whose valence band is aligned with the $\mathrm{HOMO_{donor}}$, i.e., it has empty hole states (electronic states populated with electrons) at the energy of free-charge excited hole, while keeping its conduction band shallower than the $\mathrm{LUMO_{acceptor}}$ to prevent injection of excited electrons from the acceptor.

Notice that the described band alignment of ETL and HTL with respect to active layer materials imposes their E_{bg} to be substantially higher than the E_{bg} of the active layer materials. Therefore, ETL and HTL are typically insulators with E_{bg} above 3 eV. The latter is also mandatory from an optical point of view since layers with its E_{bg} in the visible range would compete with the active layer for light absorption, increasing optical losses.

The ETL/AL/HTL sandwich has to be contacted from the selective transport layers with conductive materials to transport the free-charge carriers to the external circuit. It is important to notice that at least one of the contacts has to be transparent to visible light, since light has to reach the active layer, while maintaining the electrically conductive behavior, a pair of requisites that are challenging to be

achieved simultaneously. The transparent electrode is usually made of conductive glasses such as ITO (Indium-doped Tin Oxide) or FTO (Fluorine-doped Tin Oxide). Gridded or thin metal electrodes can also work as transparent electrodes provided that a certain level of transparency does not strongly impact its conductivity.[74, 75] The other contact does not necessarily have to satisfy the transparency condition, thus finding a material candidate is easier. Nonetheless, band alignment has to be taken into account. In this case, contact materials should have a band structure equivalent to metals, with valence and conduction bands overlapping (no energy band gap). The energy levels of a metal are defined by the work function, which is the energy needed to extract the higher energy electron from the solid to the vacuum, i.e., the minimum energy of an unoccupied electronic state. The latter has to be aligned with its corresponding selective transport layer. For example, the work function of the electrode contacting the ETL should be slightly deeper than the lowest energy state of the conduction band of the latter, to ensure free electronic states in the contact material. On the other hand, the work function of the electrode contacting the HTL should be slightly shallower than the highest energy state of the valence band of the latter, to ensure accupied electronic states where the excited holes can jump.

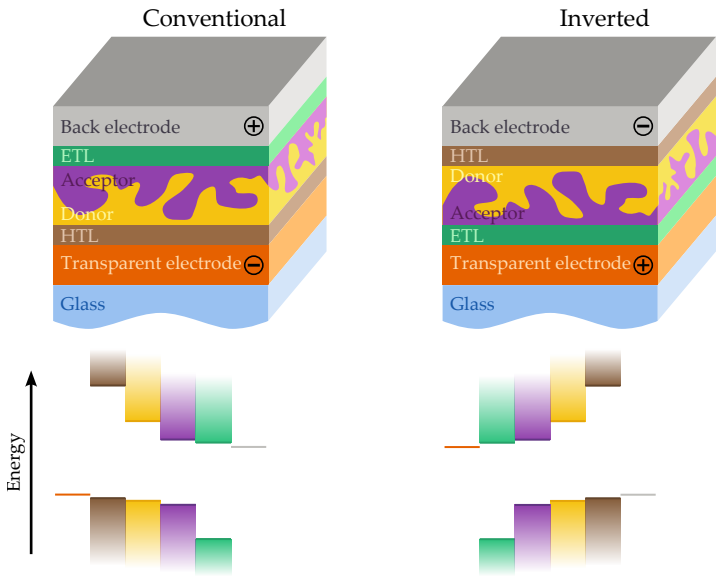

Figure 1.8: Normal and inverted device structure. Layer structure in the top panels with its example of band alignmen in the bottom panels. The inverted structure was invented after the normal structure, explaining its namings.[76]

Depending on the relative position of all these different layers, the convention is to refer them as conventional or inverted architectures

(see Figure 1.8). The conventional architecture uses the transparent electrode as the anode (positive electrode), usually deposited on top of the substrate. HTL is deposited on top of the anode, followed by the active layer, ETL, and finally, the top electrode (cathode). The latter is usually a low work function metal, typically aluminum or calcium.[76] On the other hand, the inverted architecture has the same layer stack structure but upside down, as the name implies, swapping places between the two charge-selective layers. In this case, the transparent electrode acts as a cathode, and the top electrode acts as an anode. The latter is typically a high-work function metal such as silver or gold. The inverted architecture tends to offer longer lifetimes than the conventional one, because of the better electrode corrosion resistance of high work function metals,[77] as opposed to lower work function metals, by definition.[78]

1.2.5 *Figures of merit*

To compare the performance of solar cells, one has to measure their efficiency for converting solar light energy into electrical energy. This is a basic procedure in solar cell characterization through a $J-V$ curve measurement. The cell is illuminated with a light source which spectrum and instensity are close to the standard AM1.5G spectrum, which is the calculated spectrum recieved at Earth's surface with an equivalent air mass of 1.5. Under illumination, a voltage sweep is performed to the device while measuring the current, which is divided by the device's area to obtain the current density (J), as illustrated in Figure 1.9. The electrical output power density corresponds to the product $P_{\mathrm{D,out}} = -J \cdot V$. The negative sign is introduced to represent the output power density of the solar cell. The output power density as a function of voltage defines three regions (see Figure 1.9). The output power density ($P_{\mathrm{D,out}}$) is negative in the first and the last regions, indicating that the device consumes power. Nevertheless, in the middle region, the cell generates energy since the current flows in the direction opposite to the applied voltage. The maximum power density that the cell can output ($P_{\mathrm{D,max}}$) is named maximum power (density) point (MPP), which happens at a certain current density (J_{mpp}) and voltage (V_{mpp}). Thus, the maximum power conversion efficiency of the device (PCE) is calculated as the ratio between the MPP and the input power density ($P_{\mathrm{D,in}}$).

Further details on AM1.5G conditions can be found in references [79, 80]

$$PCE = \frac{P_{\mathrm{D,max}}}{P_{\mathrm{D,in}}} = \frac{J_{\mathrm{mpp}}\ V_{\mathrm{mpp}}}{P_{\mathrm{D,in}}} \tag{1.1}$$

$P_{\mathrm{D,in}}$ for the AM1.5G spectrum corresponds to 1000 W m^{-2}. Now, we have the most important figure of merit in photovoltaics, the PCE.

While the MPP gives important information about the efficiency and the electrical conditions at which this efficiency is achieved, J_{mpp} and V_{mpp} do not have an interesting physical meaning. Instead, the points at which $P_D = 0$ correspond to physical situations related to the processes inside the cell, although their output power density is null. The current density at which $V = 0$ is named short-circuit current density (J_{sc}) because the voltage that drops across the contacts of the device is null (like in short-circuit). J_{sc} corresponds essentially to the photogenerated charges. Thus, it represents parameters such as absorption profile, exciton dissociation efficiency, or charge extraction efficiency. The voltage at which $J = 0$ is named open-circuit voltage (V_{oc}) because the current flowing through the device is null as if the cell was not connected to anything. V_{sc} corresponds essentially to the energy of the charges extracted and is proportional to the energy difference between $LUMO_{acceptor}$ and $HOMO_{donor}$. The V_{oc} compared to E_{bg} gives an idea of energy losses inside the device influenced by many parameters, such as the arrangement of electronic states or non-radiative voltage losses. Notice that to express J_{mpp} and V_{mpp}, we are missing a factor, which relates the area defined by the $J_{sc} \cdot V_{oc}$ product and the one defined by the $J_{mpp} \cdot V_{mpp}$ product. The latter figure of merit is the fill-factor (FF). The latter is a measure of the squareness of the $J - V$ curve, so that higher FF implies square-like curves. In OPV, the parameters affecting the FF are mainly related to active layer morphology and leakage current in the device (through pin-holes).

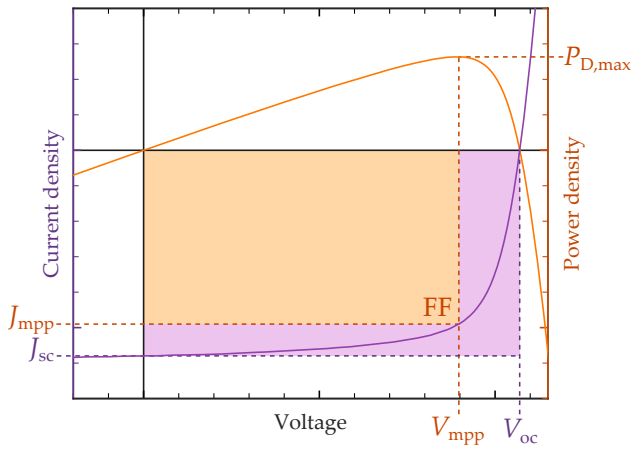

Figure 1.9: Example of a $J - V$ cruve measurement and its derived figures of merit. The $J - V$ curve (purple) and the output power density (orange). The FF is defined as the ratio between the orange and the purple rectangular areas.

Thus, Equation 1.1 can be rewritten as a function of V_{oc}, J_{sc} and FF:

$$PCE = \frac{P_{D,max}}{P_{D,in}} = \frac{J_{mpp}\ V_{mpp}}{P_{D,in}} = \frac{J_{sc}\ V_{oc}\ FF}{P_{D,in}} \tag{1.2}$$

1.2.6 *Equivalent electronic circuit*

A common practice to model, understand, and represent the behavior of certain physical systems is with an electronic circuit. The analogy can also be used for photovoltaic devices. Figure 1.10 (a) shows the equivalent electronic circuit of a solar cell which is composed of a current source, a diode, a resistance connected in parallel, and a second resistance connected in series. The current source represents the photogenerated charges related to the J_{sc}, the diode represents the rectifying behavior of the solar cell, and the two resistances represent different loss mechanisms. The shunt resistance (R_{sh}) in parallel represents non-rectifying current leakage losses. It includes all possible electrical paths between the solar cell contacts, from pinholes within the active layer to poor electrode insulation. For an ideal cell, R_{sh} is infinite; thus, in real devices, the higher the R_{sh}, the better. The series resistance (R_s) represents all possible ohmic losses that arise from the non-zero resistance of every electrical circuit component in the solar cell. For an ideal cell, R_s is null; thus, in real devices, the lower the R_s, the better. From this model we can derive two more figures of merit: R_s and R_{sh}, representing loss mechanisms of the device. R_s is calculated as the inverse of the $J-V$ curve slope at the V_{oc} point, while R_{sh} is calculated as the inverse of the $J-V$ curve slope at the J_{sc}, as depicted in Figure 1.10 (b). R_s and R_{sh} have a strong impact on FF. Their values are usually not reported since FF is a more representative figure of merit.

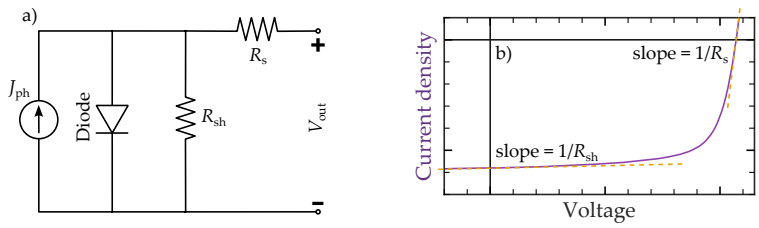

Figure 1.10: Solar cell equivalent electronic circuit. (a) The electronic circuit model including, from left to right, a current generator, a diode, a shunt resistance and a series resistance. (b) The representation of R_{sh} and R_s on a measured $J-V$ curve.

1.3 MULTI-JUNCTION ORGANIC SOLAR CELLS

Up to now, the described photovoltaic working principles apply to single-junction devices. The latter are composed of only one junction that receives the solar spectrum and converts it to electrical energy. Single-junction solar cells cannot effectively capture the whole solar spectrum, and absorption and thermalization losses from a fundamental point of view limit their efficiencies. This section aims to explain the fundamentals of the limitations and describe some proposed technological solution to overcome these limitations, with the focus on RAINBOW mutli-junction structures.

1.3.1 *Spectral mismatch: the Shockley-Queisser limit*

As stated below, single-junction solar cell efficiencies are limited by absorption and thermalization losses. The efficiency limit arises from the spectral mismatch between the energy band-gap (E_{bg}) of the semiconducting junction and the solar spectrum. Photons with energies $E_{ph} < E_{bg}$ pass through the material unabsorbed (absorption losses) and photons with energies $E_{ph} > E_{bg}$ dissipate their excess energy as heat (thermalization losses). Both losses limit the theoretical maximum efficiency of a single-junction on a fundamental level.

The Shockley-Queisser limit is a theoretical thermodynamic limit that relates the theoretical maximum efficiency of a single-junction solar cell with its energy band gap (E_{bg}). The model assumes a perfect solar cell that converts all received photons with $E_{ph} > E_{bg}$ to excitons with an energy equal to E_{bg}, while $E_{ph} < E_{bg}$ are not absorbed. All abosrbed photons are converted to electricity and only radiative losses

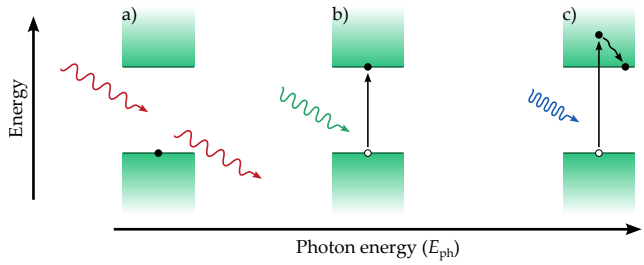

Figure 1.11: Schematics of the spectral mismatch problem resulting in the Shockley-Queisser limit. In the first situation (a), the photon energy (E_{ph}) is smaller than the energy band gap (E_{bg}), thus the photon is not absorbed by the material (absorption losses). In the last situation (c), $E_{ph} > E_{bg}$ and the photon gets absorbed, but part of this energy is lost during thermalization to the lowest energy level of the conduction band (thermalization losses). In the middle situation (b), $E_{ph} \simeq E_{bg}$, the photon gets absorbed without thermalization losses.

are considered. The latter is represented as electrons being extracted at a V_{oc} lower than the E_{bg}. Radiative losses have a thermodynamical nature coming from the difference in solid angles between the incoming light (solar light) and the radiation emitted by the cell as a black body, also known as *étendue* expansion.[81, 82] Figure 1.12 shows the dependency of V_{oc}, J_{sc}, FF and PCE as a funtion of E_{bg} in the Shockley-Queisser limit. The maximum efficiency is 33.16% with a E_{bg} of 1.34 eV.[22]

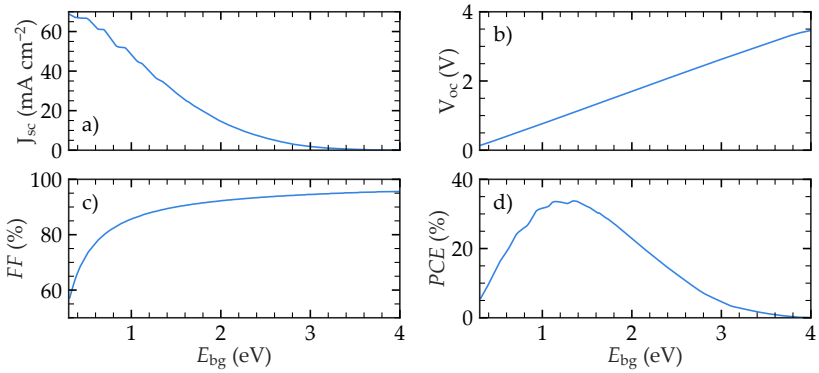

Figure 1.12: Sockley-Queisser limit for the different figures of merit. The thermodinamic maximum limits of V_{oc}, J_{sc}, FF and PCE are plotted against the energy band gap of the semiconductor material, (a), (b), (c), and (d), respectively.[82]

The literature proposes different technological approaches to overcome the spectral mismatch. We could divide them into two generic groups. In the first group, we encompass solutions based on decreasing thermalization or absorption losses but still using single junction. For example, the latter can be done by manipulating sunlight before conversion, like in the case of luminescent concentrators[83, 84], photon up- and down- converters,[85, 86] or thermophotovoltaic devices[87, 88]. Alternatively, by higher-order absorption processes that involve the energy from multiple photons to excite one electron (i.e, achieving sub-bandgap absorption)[89, 90] or one photon exciting multiple electrons (surpassing 100% external quantum efficiency).[91, 92, 93]. Within the second group, we can enclose all approaches using multiple junctions, named multi-junction geometries.

1.3.2 *Multi-junction solar cells geometries*

So far, the most promising strategy to overcome the Shockley-Queisser fundamental limit consists of combining multiple junctions with different E_{bg} that attempt to match the energy of incoming photons, so to minimize thermalization and absorption losses.[94, 95] The device

optics are engineered so that each photon reaches the PV converter that harvests it more efficiently. The latter is known as multi-junction solar cells. As a result, the theoretical maximum efficiency increases from 33.2% to 45.8% when adding just one junction (i.e., for two-junction geometries). With infinite junctions, the limit is 68% under AM1.5G illumination and 86% with solar concentration.[94, 95] These theoretical limits are calculated with the same Shockley-Queisser (detailed balance) model.

Multi-junction geometries have been widely studied for inorganic semiconductors. Multi-junction devices based on III-V semiconductors surpassed the single-junction limit more than twenty years ago, and since their invention, they have been in the top-most part of the NREL efficiency chart.[44] They hold the actual efficiency record with certified 47.6% with a four-junctions device (under concentrated light). To date, the most common implementation of such multi-junction solar cells consists of vertically stacked devices. In this configuration, the topmost junction absorbs the shortest wavelength range, while unabsorbed photons, with $E_{ph} < E_{bg}$, go through to the next sub-cell where this partial spectral absorption is repeated, resulting in a complementary absorption along the entire multi-junction stack (Figure 1.13 (a)).[94, 96, 97, 98, 99, 100, 101, 102] The tandem approach is also the most studied, and until recently, the unique studied multi-junction approach for OPV. Despite the large material library available, with widely varying band gaps, organic multi-junction tandem have, thus far, shown modest success, not yielding more than a few percentages improvement over the best single-junction efficiency.[44] This is, in part, due to the difficulty of fabricating such geometries from solution[103, 104] and further complicated by the need for current matching between sub-cells in two-terminal devices,[105, 106] as well as the availability and implementation of transparent interconnecting layers (ICLs).

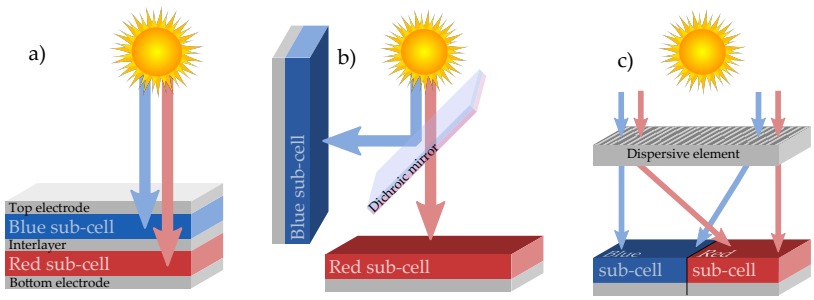

Figure 1.13: Schematics of different multi-junction geometries. Vertical tandem (a), spectral splitting with a dichroic mirror (b), and RAINBOW in-plane configuration (c).

In this direction, an alternative configuration for multi-junction cells is the spectral beam-splitting geometry.[107, 108] This involves spectrally separating the solar spectrum and redirecting the spectral fractions to different sub-cells,[109] as shown in Figure 1.13 (b). This approach has yielded promising results in various systems, such as high-efficiency III-V material multi-junctions,[110, 111] hybrid inorganic perovskite multi-junction solar cells,[112, 113] as well as hybrid silicon thermal absorbers[114, 115, 116] and thermoelectrics.[117, 118, 119] Having physically separated cells makes fabrication simple and sub-cell connection straightforward. The implementation of such systems, however, has proven to be rather cumbersome, as the most common configuration consists of placing each sub-cell at 90°, with a dichroic mirror at 45° spectrally redistributing sunlight, resulting in an awkward form factor that gets significantly more complex when increasing the junction count.[107]

1.3.3 *The RAINBOW geometry*

During this thesis, we investigate an alternative beam-splitting configuration consisting of a forward wavelength spreading element located over a horizontal stack multi-junction solar cell, so-called RAINBOW solar cell, as illustrated in Figure 1.13 (c). This geometry has already been explored with III-V inorganic semiconductors.[109, 110, 120] With a monolithic in-plane geometry, manufacturing solutions for the RAINBOW approach can be based on advanced deposition techniques such as slot die coating.[122, 123, 124, 125]

It is important to clarify that we are not referring to RAINBOW solar cells as those based on layered stacks of Quantum dots of different diameters as in reference [121]

On the other hand, the lateral distribution of each sub-cell allows for easy implementation of electrically independent contacts, eliminating the need for current or voltage matching on a device level.[126, 127] Additionally, a RAINBOW cell based on organics uses the same amount of material for electrodes, active layer, transport layers and substrate as a single junction cell without significantly complicating production. Thus, the sustainability and cost of this architecture will be competitive, provided that the dispersive element can be manufactured easily, sustainably, and cheaply. Finally, tandem solar cells show current losses due to spectral variations because of the current matching condition.[128, 129, 130] The latter is expected to reduce the efficiency limit to approximately 90% of the thermodynamic limit.[131] This restriction is expected to be less critical in RAINBOW solar cells. Nevertheless, the need for optical elements introduces other restrictions, such as optical losses and geometry constraints.[131] Table 1.1 sumarizes the comparison between the tandem and the RAINBOW multi-junction geometries.

Property	Tandem	RAINBOW
Sub-cells stack direction	Vertical	Horizontal, monolithic
Compatibility with R2R processes	Complex (layer thickness control and solvent orthogonality)	Easily compatible with slot die and lateral patterning approaches
Optical constrains	No constrains when no concentrating the light	Spectral splitting optics (optical losses and directionality constraints)
Effect of spectral deviations	Heavily affected by spectral deviations	Slightly affected by spectral deviations
Electric contacts	Two (or more) contacts device	Separated contacts for each sub-cell added by a DC-DC converter
Active layer material usage	As much as the number of sub-cells	Equivalent to one single-junction cell with the same area
Complexity when increasing number of junctions	Increases drastically	Does not necesarilly increases drastically

Table 1.1: Comparison between tandem and RAINBOW multi-junction geometries. The main properties defining each multi-junction geometry is compared to understand the advantages and disadvantages of each gometry.

Given the extensive material catalog and their ease of processing, organic semiconductors are chosen to investigate their potential as active layer materials for RAINBOW solar cells in this thesis. It is worth noting, however, that the geometry studied here could be used in combination with other photovoltaic technologies provided that they exhibit a wide range of possible band gap energies and are also suitable to be processed into stripes of different materials (either by solution processing or evaporation through a shadow mask). This would be the case for perovskites, but also for quantum dots, kesterites and more recently for oxide-based photovoltaics.

1.4 THESIS OBJECTIVES AND STRUCTURE

The thesis focuses on RAINBOW solar cells to explore their possibilities as a multi-junction approach alternative to tandem. To the best of our knowledge, there were very few reports on RAINBOW multi-junction geometries at the initial stage of this thesis. Thus, the first objective was to develop theoretical and characterization tools to understand the particular needs of the RAINBOW geometry in terms of active layer materials and spectral splitting requirements. Defining figures of merit of RAINBOW systems was also an important objective in comparing different systems and evaluating them with well-defined parameters. Another objective we defined was validating the RAINBOW's working

principles (based on the multi-junction approach) with a proof of concept device. Finally, the last objective of the thesis was to develop active layer materials in the direction that we found important for the improvement of RAINBOW solar cells.

The first chapter introduces the thesis's motivation, the field of organic photovoltaics, and the RAINBOW multi-junction approach. The second chapter describes the materials and methodologies used during the thesis, aiming to help the reader to reproduce the experiments performed during the thesis.

In the third chapter, we have designed and built the first prototype of a spectrum on-demand light source (SOLS) setup, which enables the characterization of solar cells as RAINBOW sub-cells. The SOLS resulted in more versatile equipment with potential in the photovoltaic field as a custom spectra light source.

The fourth chapter centers on the developments in the RAINBOW multi-junction geometry during this thesis. It comprises simulation tools that can predict RAINBOW efficiency with a standard external quantum efficiency (EQE) and J-V curve characterization of its sub-cells; and characterization tools to experimentally validate the RAINBOW multi-junction approach. This was further explored by the fabrication and characterization of two proof of concept devices.

The fifth chapter explores wide energy band-gap materials to be applied as sub-cells in the RAINBOW geometry. We conducted a thorough combinatorial screening of wide band-gap materials to identify novel donor:acceptor active layer materials. In this study, voltage losses of the cells were studied during a stay at Forschungszentrum Jülich. This led us to the PTQ10:O-IDFBR combination as a promising blend that enhances the performance of multi-junction solar cells and shows potential for indoor light harvesting. The blend was further studied for up-scaling at a stay at EURECAT mataró.

2

MATERIALS AND METHODS

This chapter describes the general procedures used in the fabrication and characterization of the various devices manufactured within this thesis. More specifically, it focuses on solar cell fabrication and characterization, including used materials, manufacturing techniques, and characterization equipment.

2.1 ORGANIC SOLAR CELL FABRICATION

The fabrication of organic solar cells is a fundamental procedure during the development of this thesis. In this scope, the knowledge of the NANOPTO group is a valuable resource. All solar cells fabricated during the thesis have the inverted geometry, i.e. the electron transport layer (ETL) is near the transparent electrode while the hole transport layer (HTL) is at the back reflective contact side. This section describes the standard procedure of device fabrication at the NANOPTO group. Materials and methodologies that differ from the standard in certain parts of this thesis manuscript are described in their corresponding place.

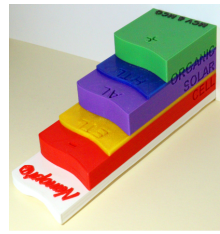

Figure 2.1: 3D-printed model of the inverted geometry structure. I made this design for educational purposes.

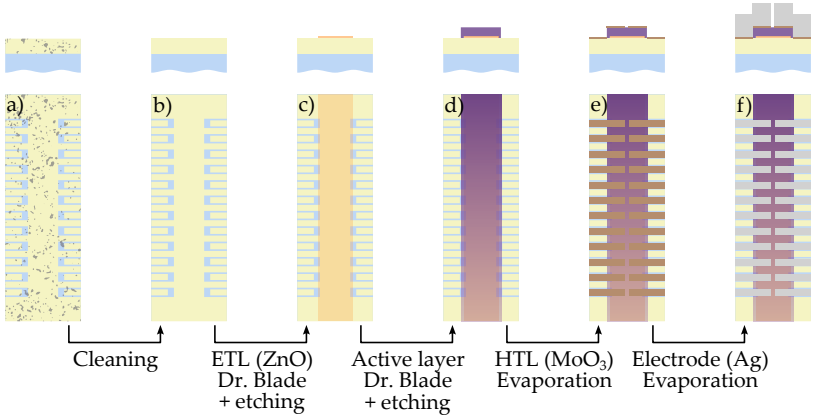

Figure 2.2: Organic solar cell fabrication procedure schematics. Cross section (top) and top-view (bottom) of the substrate as bought (a), cleaned (b), ETL deposition (c), AL deposition (d), HTL deposition (e), and back electrode deposition (f).

2.1.1 *Substrate cleaning protocol*

The fabrication starts with ITO-coated glass substrates from Ossila with a specific ITO pattern, as depicted in Figure 2.2 (a) and (b). This patterning defines a total of 24 cells, 12 on each side of the substrate. To identify the substrates afterward, they are manually scratched from the glass side with a diamond tip. These marks have to be done outside the area of the working devices and would be unique for every substrate one may ever fabricate. Afterward, substrates are cleaned by sequentially sonicating them in acetone, 2% vol% Hellmanex© soap solution in H_2O, isopropanol and 10% sodium NaOH solution in H_2O; during 5, 5, 5, and 10 minutes respectively. The first three baths aim to clean the surface from any organic moiety. The last bath aims to activate the surface of the ITO to improve wettability for the blade coating deposition of the ETL. Afterward, the samples are submerged in H_2O to clean any remaining NaOH, and the H_2O is blown away from the substrate with compressed air. In this last step, it is important to avoid the evaporation of the water on the substrate surface since it could lead to the deposition of any impurity present in the water. On the contrary, compressed air has to be used to push the water to one side of the substrate where a cleanroom wipe can absorb it.

All H_2O used is Milli-Q ultrapure grade

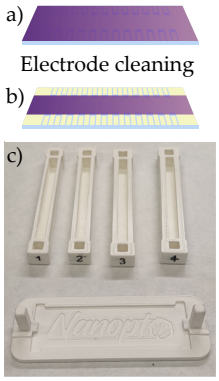

Figure 2.3: 3D-printed tool for electrode cleaning after blade coating. Schematics of a substrate before (a) and after (b) electrode cleaning. Photograph in (c) shows the 3D-printed tool used. The four guides (on top) have different etching widths.

2.1.2 *Electron Transport Layer (ETL)*

The first layer deposited is the electron transport layer (ETL). In the standard procedure, a solution of ZnO nanoparticles (Avantama N10) is deposited via blade coating with a constant blade speed of 5 mm s^{-1}, a blade gap of 50 µm, and a temperature of 40°C. Afterwards, the layer is cleaned on the sides of the substrate to avoid electrical shortcuts of the contacts to form the desired device structure, as shown in Figure 2.2 (c). This is done with the help of a 3D-printed guide and a cleaning wipe wetted with isopropanol, as depicted in Figure 2.3. Finally, the sample is annealed at 110°C during 10 min to evaporate all remaining solvent and form a compact 30 to 35 nm thick layer.

2.1.3 *Active Layer (AL)*

The desired O_2 and H_2O concentration levels inside the glovebox are are below 1.5 parts per million (ppm)

The active layer (AL) is generally deposited inside the glovebox, where the controlled low levels of O_2 and H_2O prevents degradation of the organic semiconductors. For this reason, it is also recommended to store and prepare the solutions for the AL deposition inside the glovebox. The solutions are generally prepared at 1:1.5 donor:acceptor ratio with a

concentration in between 15 and 20 mg mL^{-1}. Nevertheless, the solution composition (donor:acceptor ratio and total concentration) cannot be generalized to any material combination since it is one of the most important parameters affecting the final efficiency.

The solutions are kept in stirring for at least 4 hours to ensure proper dissolution of the materials. Generally, applying temperature helps the dissolution process. However, the temperature can never be higher than the solvent's boiling point to avoid its evaporation, which would cause a change in the solution concentration.

In most cases, the active layer is deposited with a thickness gradient along the long side of the substrate to evaluate the effect of thickness on the device performance, resulting in 12 device pairs of different thicknesses. This is achieved by the deacceleration of the blade during the deposition of the active layer, which is controlled by an Arduino electrically connected to the blade moving motor. This modification was done by Dr. Bernhard Dörling during his PhD thesis.[132] To achieve a thickness gradient between 250 and 40 nm approximately, the blade speed is linearly decreased from 90 mm s^{-1} to 10 mm s^{-1} between the first and the last cell of the substrate, respectively. Figure 2.4 shows the linear velocity profile that the Arduino applies as a function of the position. To align the blade speed gradient with the sample, one sacrificial glass is added before the substrate. Additionally, a sacrificial glass is used after the substrate to avoid the evaporation of the remaining solution at the edge of the substrate. Finally, similarly to the case of the ETL, the active layer is cleaned in the long axis edges to build the proper cell geometry and avoid any possible electrical leakage, as shown in Figure 2.2 (d). At this point, annealing treatment (if desired) can be done before the evaporation of the hole transport layer (HTL) and the back electrode. The latter can affect active layer morphology having an impact on device performance.

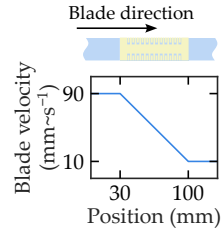

Figure 2.4: Typical speed profile for a thickness gradient deposition. The latter usually produces a thickness gradient from 250 to 40 nm.

2.1.4 *Active Layer materials*

During the thesis, we have used a large amount of different active layer materials (donors and acceptors). Their chemical structures are drawn in Figure 2.5 with donors and acceptors highlighted in yellow and purple, respectively. Table 2.1 and Table 2.2 shows the CAS (Chemical Abstract Services) identification number for each compound as well as its provider. The materials were processed as received without any additional purification steps. Next, we list the IUPAC (International Union of Pure and Applied Chemistry) names of the donors and acceptors used:

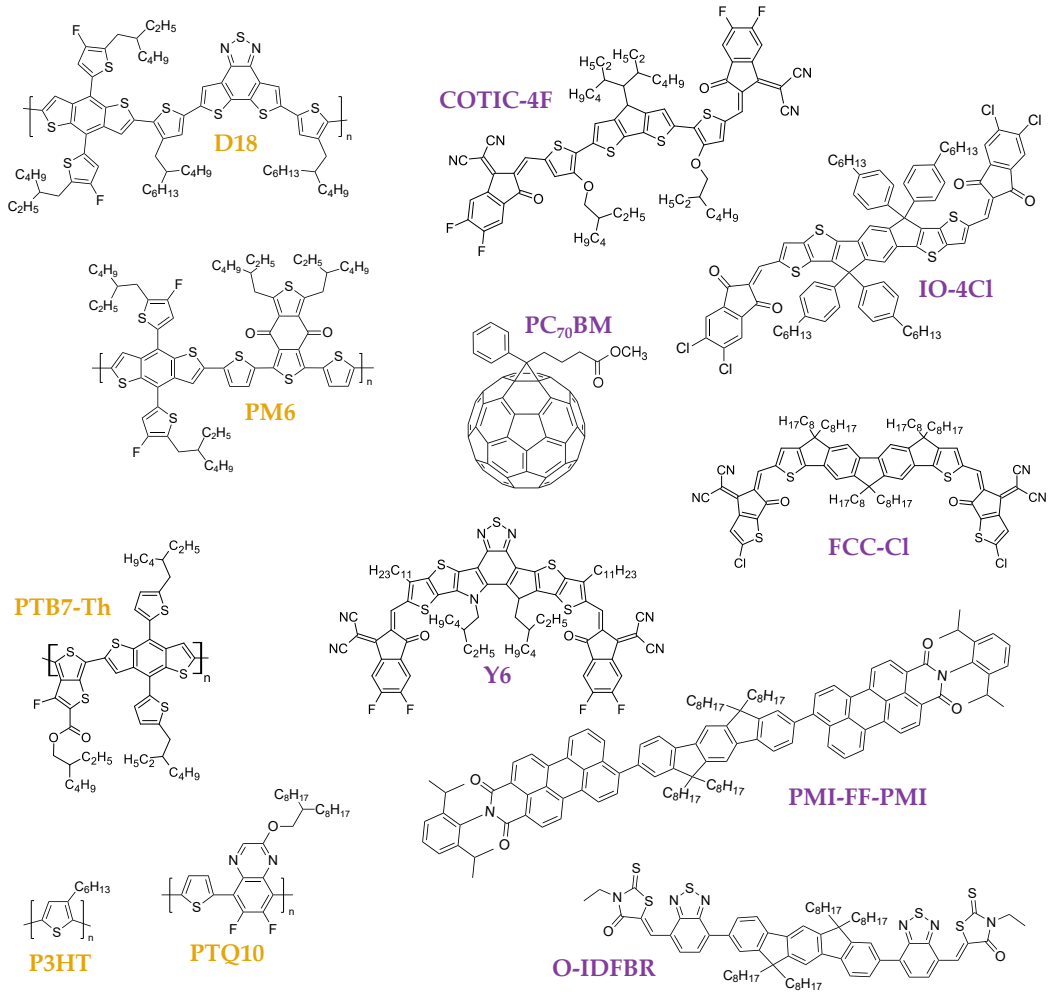

Figure 2.5: Chemical structures of donors and acceptors used in the thesis. The donors (left side, yellow) and acceptors (right side, purple) extra information can be found in Table 2.1 and Table 2.2, respectively.

- **PTQ10:** Poly[(thiophene)-alt-(6,7-difluoro-2-(2-hexyldecyloxy)quinoxaline)]
- **PM6:** Poly[(2,6-(4,8-bis(5-(2-ethylhexyl-3-fluoro)thiophen-2-yl)-benzo[1,2-b:4,5-b′]dithiophene))- alt-(5,5-(1′,3′-di-2-thienyl-5′,7′-bis(2-ethylhexyl)benzo[1′,2′-c:4′,5′-c′]dithiophene-4,8-dione)]
- **D18:** Poly[(2,6-(4,8-bis(5-(2-ethylhexyl-3-fluoro)thiophen-2-yl)-benzo[1,2-b:4,5-b′]dithiophene))-alt-5,5′-(5,8-bis(4-(2-butyloctyl)thiophen-2-yl) dithieno[3′,2′:3,4;2″,3″:5,6]benzo[1,2-c][1,2,5]thiadiazole)]
- **PTB7-Th:** Poly[4,8-bis(5-(2-ethylhexyl)thiophen-2-yl)benzo[1,2-b;4,5-b′]dithiophene-2,6-diyl-alt-(4-(2-ethylhexyl)-3-fluorothieno[3,4-

DONORS		
Material	**CAS number**	**Provider**
PTB7-Th	1469791-66-9	Ossila
PTQ10	2270233-86-6	1-Material
D18	2433725-54-1	Ossila
P3HT	104934-50-1	Sigma-Aldrich
PM6	1802013-83-7	1-Material

Table 2.1: Information of polymer donors used. The chemical structures can be found at Figure 2.5

ACEPTORS		
Material	**CAS number**	**Provider**
COTIC-4F	2328118-91-6	1-Material
IO-4Cl	-	1-Material
Y6	2304444-49-1	1-Material
PC70BM	609771-63-3	Ossila
PMI-FF-PMI	-	*
O-IDFBR	2088628-64-0	1-Material
FCC-Cl	2681341-29-5	1-Material

Table 2.2: Information of small molecules acceptors used. The chemical structures can be found at Figure 2.5. * PMI-FF-PMI was provided by our collaborators from Prof. Gergor Trimmel's group.[133]

b]thiophene-)-2-carboxylate-2-6-diyl)]

- **P3HT:** Poly(3-hexylthiophene-2,5-diyl)
- **O-IDFBR:** (5Z,5′Z)-5,5′-((7,7′-(6,6,12,12-Tetraoctyl-6,12-dihydroindeno[1,2-b]fluorene-2,8-diyl)bis(benzo[c][1,2,5]thiadiazole-7,4-diyl))bis(methanylylidene))bis(3-ethyl-2-thioxothiazolidin-4-one)
- **PMI-FF-PMI:** 8,8′ (6,6,12,12-tetraoctyl-6,12-dihydroindeno[1,2-b] fluorene -2,8-yl)-bis(N-(2,6-diisopropylphenyl)-perylene-3,4-dicarboximide)
- **COTIC-4F:** 2,2′-((2Z,2′Z)-(((4,4-bis(2-ethylhexyl)-4H-cyclopenta[2,1-b:3,4-b′]dithiophene-2,6-diyl)bis(4-(heptan-3-yloxy)thiophene-5,2-diyl))bis(methanylylidene))bis(5,6-difluoro-3-oxo-2,3-dihydro-1H-indene-2,1-diylidene))dimalononitrile
- **IO-4Cl:** 3,9-bis[5,6-dichloro-1H-indene-1,3(2H)dione]-5,5,11,11-tetrakis (4-hexylphenyl)-dithieno[2,3-d:2′,3′-d′]-s-indaceno[1,2-b:5,6-b′]dithiophene
- **Y6:** 2,2′-((2Z,2′Z)-((12,13-bis(2-ethylhexyl)-3,9-diundecyl-12,13-dihydro-[1,2,5]thiadiazolo[3,4-e]thieno[2″,3″:4′,5′]thieno[2′,3′:4,5]pyrrolo[3,2-g]thieno[2′,3′:4,5]thieno[3,2-b]indole-2,10-diyl)bis(methanylylidene))bis(5,6-difluoro-3-oxo-2,3-dihydro-1H-indene-2,1-diylidene))dimalononitrile
- **$PC_{70}BM$:** [6,6]-Phenyl-C71-butyric acid methyl ester

2.1.5 *Hole Transport Layer (HTL) and back electrode*

The last step of the device fabrication is the evaporation of the hole transport layer (HTL) and the back electrode. An evaporation shadow

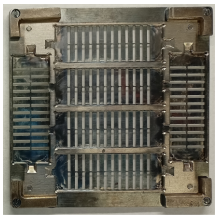

Figure 2.6: Photograph of the mask used to define the HTL and back electrode during evaporation. The masks fit up to 6 substrates, which is the maximum number that we fabricate in each batch.

mask is used to define the desired pattern of the evaporated layers (see Figure 2.6), defining the top contacts as seen in Figure 2.2 (e) and (f). The standard procedure consists of depositing between 10 and 15 nm of molybdenum (VI) oxide (MoO_3) as HTL. In general, a thick MoO_3 would increase the selectivity of the HTL, increasing the fill factor (FF) of the resulting solar cell at the expense of the number of free charges reaching the contacts (i.e. less photocurrent (J_{sc})). The latter also results in a lower dark current, generally desired for photodetectors. A thin MoO_3 will have the opposite effect, increasing J_{sc} at expenses of FF. Finally, a minimum of 150 nm of silver (Ag) is deposited as the reflective back electrode to ensure an electrically conductive contact. Figure 2.6 shows a top-view photograph of the mask used for evaporation.

2.1.6 *Encapsulation*

Due to the organic nature of active layer materials, OPV degrades when exposed to oxygen and moisture. To prevent this degradation, we can perform a last step in device fabrication called encapsulation. During the thesis, most of the fabricated substrates have been encapsulated to increase the lifetime of the devices. The latter was important since some characterization techniques used during the thesis, such as the RAINBOW characterization performed with the SOLS or the EQE_{PV}, can take a long time to perform (some hours). After encapsulation, the main degradation mechanisms should be light-driven and thermodynamic morphological changes.

The encapsulation consists of gluing a glass coverslip on top of the substrate with an epoxy resin. In the first instance, the resin (in a liquid phase with high viscosity) is sandwiched between the substrate and the coverslip to spread it, covering the surface between the substrate and the coverslip. Ideally, the resin should not interact with the active layer. Nevertheless, although the device's active layer is protected by the top electrode, due to the organic nature of the resin and the active layer, the resin may interact to some extent, affecting the device's performance. The next step is resin curing, which, in our case, is triggered with UV light illumination. The latter may also affect the active layer to some extent, although the resin and the top electrode may protect the active layer from direct UV light illumination.

For the discussed effects, the encapsulation may affect the initial performance of the devices, generally decreasing it.[134, 135] Nevertheless, the improved stability is the reason for device encapsulation which is especially important for the characterization techniques used in the work. I want to remark that I have regularly checked the performance

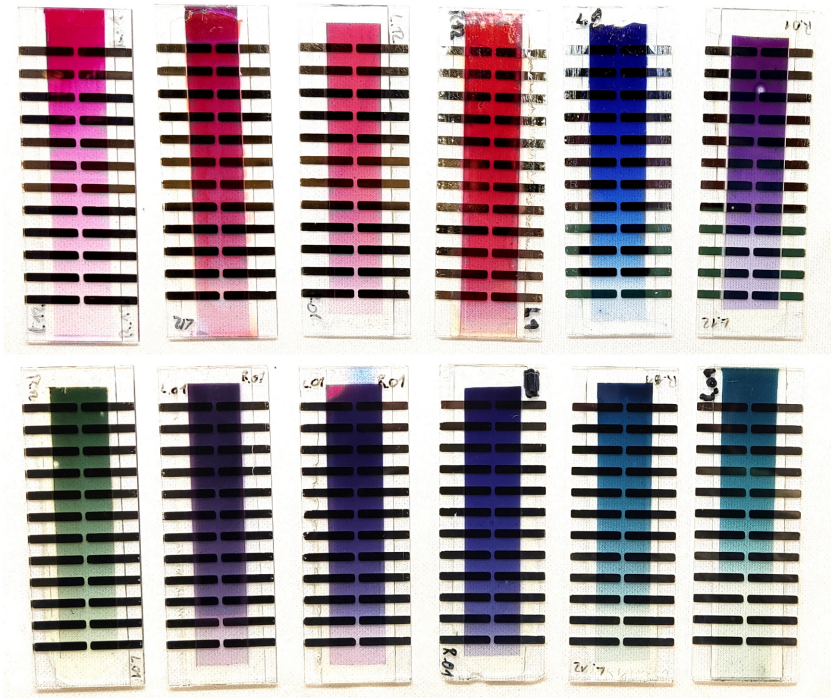

Figure 2.7: Compilation of OPV samples fabricated during the thesis. The active layer materials of the top row (from left to right) are: D18MI-FF-PMI; PTQ10:O-IDTBR; P3HT:PC_{60}BM; P3HT:O-IDFBR; PM6:IO-4Cl; PTQ10:PC_{60}BM. The active layer materials of the bottom row (from left to right) are: PTB7-Th:PC_{60}BM; P3HT:O-IDTBR; P3HT:EH-IDTBR; PTQ10:Y6; PTB7-Th:Y6; PTB7-Th:COTIC-4F. The IUPAC name and chemical structures of some of the materials are not included in the active layer materials since they are not included in any results of the thesis. This figure is only for the sake of art.

of some devices that were fabricated during the early stages of the thesis (about 3 years now), and thanks to being encapsulated and stored inside the glovebox in the dark, they in most cases retain more than 60% its initial efficiency.

The epoxy was sourced from DELO, and the type is KATIOBOND LP655.[136] The resin was cured with a UV lamp of 365 nm for 5 to 10 minutes.[137] The encapsulation slides were 0.5 mm thick glass coverslips from Ossila compatible with the ITO-covered substrates from the same provider.[138]

2.2 DEPOSITION TECHNIQUES

2.2.1 *Blade coating*

Blade coating (a.k.a. Dr. Blade) is a coating technique widely used in the field of organic electronics, and especially in organic photovoltaics thanks to its upscaling potential.[139, 140] The technique is considered a step in between the lab-scale fabrication, usually based on spin coating, and the industrial-scale fabrication, usually done using slot-die coating machines.[141, 142] In the thesis, blade coating is the technique used for depositing the solution-processed materials for most of the devices prepared.

Figure 2.8 shows a simplified schematics to represent the working principles of the technique. A certain amount of solution is placed between the surface and the blade, creating a meniscus in between. Afterward, the blade (or the substrate) moves in one direction guiding the meniscus and spreading the solution over the surface. This creates a liquid film whose thickness depends on blade velocity. A faster blade speed will deform the meniscus so that the wet film thickness gets thicker, as depicted in Figure 2.9 (a) and (b). The latter is due to the shear forces developing in the meniscus. Afterwards, the wet film dries, creating the thin-film.

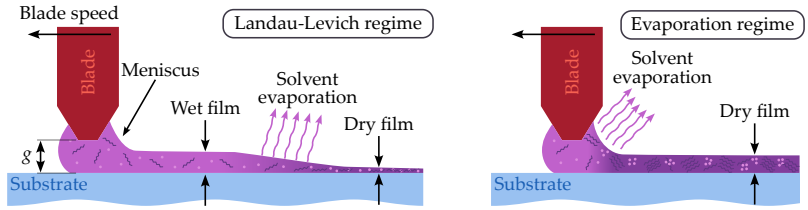

Figure 2.8: Schematics of blade coating working principle. In the Landau-Levich regime (a), a wet film originates while the solvent finally dries to define the solid film. In the evaporation regime (b), evaporation happens in the meniscus region, and the solid film is directly created following the meniscus (without a wet film formation). g corresponds to the gap between the blade and the substrate. More insights on thickness dependence can be found in Figure 2.9.

There have been several studies relating the resulting layer thickness to the various parameters involved during the blade coating process.[143, 144] However, from a practical point of view, blade gap, concentration and blade speed usually have the most significant effect on the final film thickness, the latter being the one with the strongest influence. There is an empirical formula describing the effect of gap and concentration on thickness for a certain velocity:

$$t = \frac{1}{2}\left(g\,\frac{c}{\rho}\right) \tag{2.1}$$

where t is the thickness, g is the gap distance between the substrate surface and the blade, c is the concentration of the solute in the solvent, and ρ is the final density of the film.[144]

The described thickness dependence (higher blade speed resulting in thicker films) happens in the regime known as Landau-Levich,[145, 146] where the rate of solution bladed is higher than the evaporation rate of the solvent. As a result a wet thin film originates before the complete evaporation (see Figure 2.8 (a)). Nevertheless, when evaporation happens faster, the solid film is created directly on the edge of the meniscus (see Figure 2.8 (b)). In this regime, named evaporation regime, the effect of blade speed on thickness is the opposite: lower velocities produce thicker films (see Figure 2.9). The latter is because, with a certain evaporation rate, a slower velocity will deposit the same amount of material per unit time at a higher velocity deposition but in a shorter length, therefore increasing its thickness.[146] The regime depends on the evaporation rate of the solvent which can be controlled mainly by the temperature applied to the substrate (and to the solution).

For the conditions that we use in the lab, the Landau-Levich regime is usually the regime that we work on, and we take advantage of the thickness dependence on velocity to create a thickness gradient. The latter is done by an Arduino modification designed and implemented by the NANOPTO member Dr. Bernhard Dörling that controls the speed of the blade during the deposition. More details about the process are described in the previous Section 2.1.3.

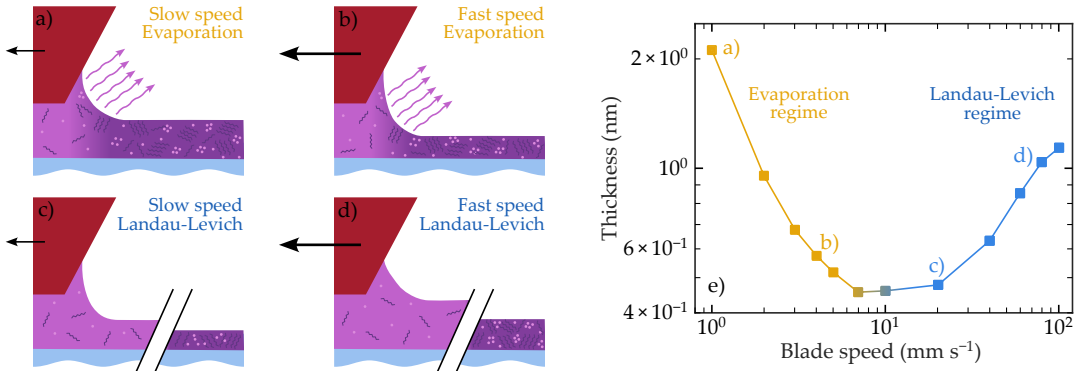

Figure 2.9: Thickness dependence on blade coating speed. Schematics of the evaporation regime happening at lower coating speeds (a) and (b) and the Landau-Levich regime happening at higher speeds (c) and (d). (e) shows an example of the full thickness dependence on blade speed with data from reference [147], with the different situations from (a) to (d) being marked in the corresponding speed range.

2.2.2 *Spin coating*

Spin coating deposition is a technique that produces thin homogeneous films with a high degree of control and reproducibility, making it the most widely used deposition technique in the field of OPV.[43, 139] In this thesis, spin coating is used only for a few devices, which appear in Chapter 4.

In this deposition technique, the substrate is attached to a rotating platform, usually by means of vacuum. The typical process involves depositing a certain volume of solution on top of the substrate, ideally wetting the entire substrate surface. Since the substrate is not moving while depositing the solution, the technique is known as static spin coating. The substrate rapidly accelerates to a certain spin velocity, typically expressed in revolutions per minute (r.p.m.). The adhesive forces at the liquid/substrate interface and the centrifugal forces acting on the rotating liquid result in strong sheering forces on the liquid layer, causing a radial flow in which most of the deposited solution is rapidly ejected from the substrate. Eventually, these two forces equilibrate, resulting in a thin liquid film, with a highly homogeneous thickness over the entire substrate. As one may expect for Newtonian fluids, the higher the speed, the higher the sheering forces and the thinner the liquid film. The substrate is kept spinning at a constant speed while most of the solvent evaporates, creating a homogeneous solid film. Figure 2.10 schematically shows the process. Spin coating has a variant in which the ink is introduced while the substrate is already rotating at the desired r.p.m. The latter is called dynamic spin coating and is typically done for volatile solvents, like chloroform or dichloromethane.

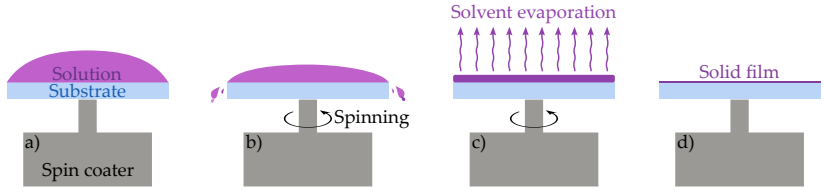

Figure 2.10: Working principles of spin coating. Schematics of a static spin coating deposition where the ink solution is placed on top of the substrate (a). When the substrate starts to spin, the majority of the solution fly off the substrate (b) creating a thin wet film which evaporates while spinning (c), creating the homogeneous thin film (d).

Various works have studied the effect of different parameters on the layer thickness.[148, 149, 150] Some of them include the solution volume, the history of angular velocity from start to end (acceleration) or the total rotating time. Nevertheless, the parameters with a higher impact on the layer thickness are angular velocity, solution viscosity

and solution concentration. The latter is reflected in the following empirical formula:[149]

$$t = k\,\eta_0^{\beta}\,\omega^{\alpha} \tag{2.2}$$

where t is the thickness of the film, η_0^{β} is the initial solution viscosity, ω is the angular velocity, and β, α, and k are empirical constants.[149] For various systems studied in the literature, α has been observed to be close to -0.5 for polymer solutions.[149, 151, 152, 153] Figure 2.11 shows the thickness dependence on angular velocity with α=-0.5 and its concentration dependence (higher concentrations resulting in thicker films).

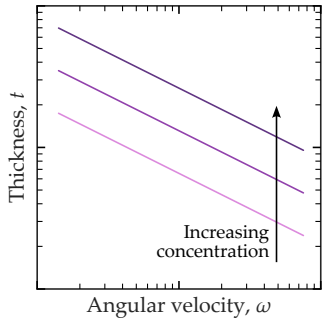

Figure 2.11: Spin coating thickness dependence on angular velocity and concentration. The different lines represent solutions with different concentrations, increasing with color darkness. The figure represents the dependence between the three parameters with α=-0.5.

2.2.3 *Partial coverage radial (PCR) spin coating*

This technique consists in depositing the solution only in one half of the substrate, and regulating the amount of liquid, maximum angular velocity and acceleration, to reliably cover half of the substrate, leaving the other half completely untainted (Figure 2.12). Consequently, we have named this technique Partial Coverage Radial (PCR) spin coating. The working principle of this technique relies on the fact that the liquid will only move outwards within the substrate due to centrifugal forces, preventing the uncovered side from getting deposited.

The main disadvantage of the technique is that the precision of the partial coverage greatly depends on the steady hand of the operator during the deposition. To mitigate this, we have 3D-printed a guide that guarantees a straight line every time, as depicted in Figure 2.12(a). Additionally, one needs to correctly tune the spin coating parameters to achieve optimal deposition conditions For a small 20 $\times$ 15 mm^2

substrate we typically use around 25 µl, with angular accelerations as low as 100 rpm s^{-1}. Figure 2.12 (d) shows some examples of films prepared with the PCR spin coating technique.

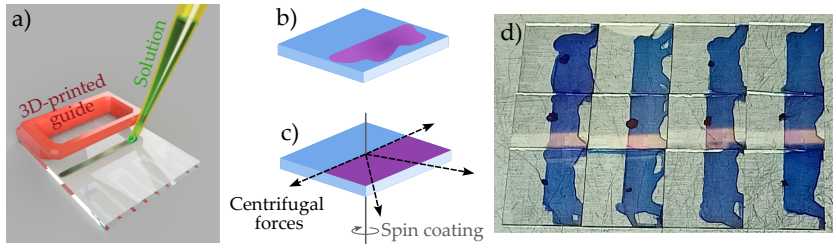

Figure 2.12: PCR spin coating working principle and examples. (a) shows a render (made by Dr. Martí Gibert-Roca) of the 3D-printed guide used to define the central line, which is the firs step of the PCR spin coating. The solution is deposited covering the wanted half of the substrate (b), before starting the spin of the substrate (c). If the center is placed correctly, the centrifugal forces avoid that the solution spreads only in one half of the substrate. (d) shows some examples of PCR spin coating films done by Dr. Martí Gibert-Roca.

The technique was used to fabricate the active layer of monolithic RAINBOW proof of concept devices shown in Section 4.2.3. For these devices, half of the substrate is coated with an active layer material and the other half with the other material. The latter can be achieved by using PCR spin coating for both materials, i.e., first covering one half of the substrate and then the other half. Notice that, in the latter, both active layers need to be deposited in static mode (i.e., depositing the ink before starting to spin). This was done for the PM6:Y6 and PTB7-Th:COTIC-4F 2-J RAINBOW device.

Since some active layers achieve higher efficiencies with dynamic spin coating, the monolithic devices can also be fabricated by first spin coating full surface substrate with one of the materials (in static or dynamic); clean half of the substrate with a wipe towel; and use the PCR spin coating technique to deposit the other half substrate.

2.2.4 *Physical evaporation*

Physical evaporation (or simply evaporation) is a physical vapor deposition (PVD) technique versatile and widely used in materials science, particularly for creating thin films and coatings. The process involves the transition of material from a condensed phase to a vapor phase and then back to a condensed phase as a thin film on a substrate. Physical evaporation stands out as a fundamental technique, offering precision and control over film properties such as thickness,

composition, and morphology. In this thesis physical evaporation is used to deposit the HTL (MoO_3) and the back reflective electrode of (Ag).

Physical evaporation is integral to the development of advanced materials in industries ranging from electronics and optics to protective coatings and decorative finishes. Its ability to deposit materials with high purity and uniformity makes it indispensable in applications requiring precise control over film characteristics. For instance, in the semiconductor industry, physical evaporation is crucial for depositing metal contacts and dielectric layers, where even minor deviations in film quality can significantly impact device performance.[154]

At the core of physical evaporation is the principle of converting a solid or liquid material into a vapor by supplying sufficient thermal energy. The vaporized atoms or molecules then travel through a vacuum environment and condense on a substrate to form a thin film. The process can be broken down into three main stages:

EVAPORATION The source material is thermally heated until it vaporizes. In the setup available in our lab, the material is placed on a molybdenum boat which heats by Ohm's law when an electrical current is passed through. The heat is transferred to the material until it vaporizes. In the case of silver, it melts before evaporation, thus it is evaporated from a liquid phase.[155] Nevertheless, MoO_3 behaves differently compared to Ag due to its specific thermal properties. It sublimes rather than melts before it evaporates without passing through a liquid phase in between.[156, 157, 158]

TRANSPORT The vaporized atoms or molecules migrate from the source to the substrate. In vacuum, the mean free path of the particles is long, allowing them to travel without significant scattering, with a ballistic trajectory. This defines a technique with low conformality, meaning that the position and orientation of the surfaces relative to the source influence the deposited film uniformity and thickness. This enables to pattern the deposited film thanks to a mask. In our application, the mask defines the area of the top electrode while it provides a proper contact for its electrical connection.

CONDENSATION The vaporized material condenses on the substrate, forming a thin film. The film's properties, such as grain size, adhesion, and microstructure are influenced by factors like the substrate temperature, deposition rate, and vacuum conditions.The deposition rate used for MoO_3 and Ag is 0.05 and 0.2 nm s^{-1}, respectively.

The vacuum levels that one needs to achieve for proper evaporation are below 10^{-4} Pa because of the low vapor pressure of the materials to evaporate.[155, 158] To achieve such high vacuum levels, a combination of a mechanical and a turbomolecular pump is used, which are capable of maintaining stable vacuum levels throughout the deposition process, pumping out any adsorbed gas released during evaporation.

2.3 ELECTICAL CHARACTERIZATION

2.3.1 *J − V curves*

Current density-voltage ($J - V$) curves have been measured using a custom-made $J - V$ characterization setup, consisting of a demultiplexing board in combination with a LabVIEW application. This system was developed by Dr. Martí Gibert-Roca during his PhD thesis.[159] I was involved a part of the development and the construction of the last version. The substrate is fixed into a 3D-printed support that connects each substrate contact to the demultiplexer board with a pogo-pin (a pin with a spring inside to ensure proper contact). The 3D-printed part needs to be mechanically robust and avoid deformation over a long time. The most used material for 3D-printing, polylactic acid (PLA), even when printed in white color to avoid heating of the piece, deforms and breaks over time. On the opposite, we found transparent polyethylene terephthalate glycol-modified (PETG), to be a better solution for this application. The bottom contact of cells are electically connected in the multiplexer. This reduces and equalizes any possible difference in series resistance introduced by different path lengths between the cell and the conctact. The multiplexer system consists of a series of relays connected in a pyramid-like structure that is able to connect to each of the 24 cells top contacts thanks to a signal triggered by an Arduino.

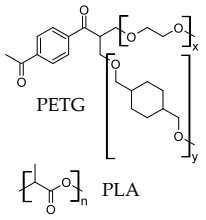

Figure 2.13: Chemical strucutre of PLA and PETG materials used in 3D-printing. Taken from references [160, 161]

The top and bottom contacts are connected to a Keithley 2400 source meter that performs high-precision current vs. voltage measurements. The LabVIEW program controls the Arduino of the demultiplexer (connecting the Keithley to each cell individually); the Keithley (automatically measuring $J - V$ curve on each cell); and finally treats and stores the data to save time for the user. The described procedure reduces characterization time by a factor of 90% according to Dr. Martí Gibert-Roca calculations.[159]

To illuminate the devices, under AM1.5G and 1000 W m^{-2} we use a solar simulator (XES-100S, SAN-EI Electric). The latter combines a xenon arc lamp and a filter to get the spectrum as close as possible to the AM1.5G standard. The simulator is AAA class, in an area of

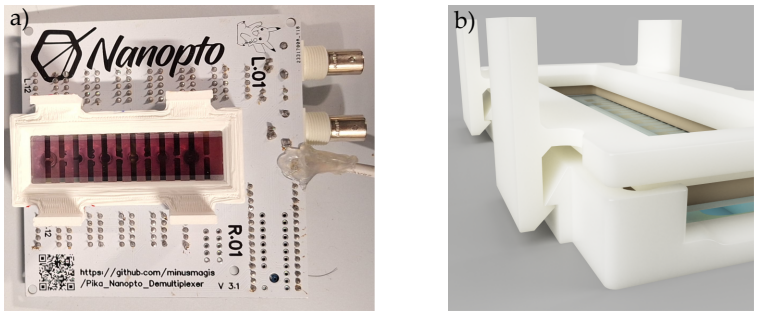

Figure 2.14: Demultiplexer used to electrically contact devices in blade-coated substrates. (a) Photograph of the demultiplexer with a cell in the 3D-printed holder (in this case, in white PLA). (b) Close-look render of the 3D model of the holder (courtesy of Dr. Martí Gibert-Roca).

10×10 cm^2. The solar simulator power density is calibrated before each $J-V$ measurement to ensure reliability, using a certified reference silicon solar cell (Oriel, Newport).

Besides the xenon arc lamp solar simulator, we also have an LED solar simulator from Wavelabs (SINUS 70). The latter is not our general illumination source for 1-sun $J-V$ measurements. However, it has been used in Chapter 4 of this thesis to generate custom spectra (appart from the AM1.5G spectrum) for the characterization of the proof of concept RAINBOW devices. The spectra were achieved by modulating the different LEDs intensities.

2.3.2 *Photovoltaic external quantum efficiency (EQE_{PV})*

The photovoltaic external quantum efficiency EQE_{PV} (also tipically referred as EQE), is the ratio between the number of extracted electrons and the number of incoming photons as a function of the wavelength (or energy) of the photons. During the thesis, EQE_{PV} has been measured in the NANOTPO labs and in the Forschungszentrum Jülich labs, i.e. with different equipment.

The light source of the setup at the NANOPTO labs consists of a supercontinuum pulsed laser coupled to a computer-controlled monochromator (LLTF contrast, Fianium). The monochromated light is further filtered to avoid unwanted diffraction orders. The substrate is placed in a multiplexer unit attached to a computed-controlled moving stage, which is able to align each device with the light beam automatically. With this setup, we can illuminate the sample with light ranging from 400 to 1100 nm, a range which can be further extended into the infrared by changing the monochromator. The light

beam power is previously calibrated with a photodiode power sensor (Thorlabs S120C). Current measurements were made with a Keithley 2450 source meter. All the components are controlled with a custom-made LabView program developed by Dr. Martí Gibert-Roca during his PhD thesis.[159]

The EQE_{PV} setup used in Forschungszentrum Jülich labs consists of a Xenon-arc lamp as a light source, which is collimated before being monochromated. The light beam splits in half to illuminate a reference photodetector and the measured solar cell simultaneously. The light is chopped, and the solar cell current is measured through a lock-in amplifier to reduce the signal-noise ratio (SNR). The spotlight directed to the solar cell was adjusted to fit inside the device, which was electrically connected through the multiplexer. The equipment was set up by Mr. Wilfried Reetz, who helped me during the measurements.

2.4 OPTICAL CHARACTERIZATION

2.4.1 *Raman spectroscopy imaging*

Raman spectroscopy is based on the physical phenomenon of inelastic scattering of photons known as Raman scattering. In the technique, the sample is illuminated with a monochromated light from a laser. A big fraction of the light gets scattered elastically through a phenomenon known as Rayleigh scattering, while a small fraction of the light scatters inelastically. The latter is known as Raman scattering and is the product of the interaction of the incoming photons with the molecular vibrations (phonons) of the sample, which adds or subtracts energy to the scattered light. The Rayleigh scattered light is typically filtered with a notch filter, to reduce its intensity which is much higher than the Raman scattered light. The intensity of the latter increases when the incoming light energy matches an electrical absorption transition. In this case, we say that the system is in Raman resonance. Thus, to obtain a higher Raman response, one needs to choose a laser wavelength at which the material to study has a high absorption peak. The resulting Raman spectrum, which is plotted as the spectral shift of the scattered light (typically in cm^{-1}), is a fingerprint of the vibrations (phonons) of the material, unique to each material.

Raman imaging is built upon the combination of Raman spectroscopy and microscopy. The latter generates images with both spectral and spatial information on Raman response. Due to the fingerprint characteristics of Raman scattering, one can have compositional maps. In the thesis, the latter was used to study the boundary between two

active layer sub-cells deposited side-by-side using the partial coverage radial spin coating methodology. The equipment used is a WITec Alpha300RA (1200 lines per mm grating) with a 40×, NA = 0.6 Zeiss objective.

2.4.2 *Variable-angle spectroscopic ellipsometry (VASE)*

Variable-angle spectroscopic ellipsometry (VASE) is a non-destructive, non-contact, and non-invasive optical technique that is based on measuring the change in the polarization state of a linearly polarized light beam as it is reflected obliquely from (or transmitted through) a thin film sample over a defined spectral range (see Figure 2.15).[162, 163, 164] The name ellipsometry comes from the fact that polarized light becomes elliptical upon light reflection. The change in polarization is measured by two varaibles: the amplitude ratio (Ψ) and the phase difference (Δ) between the p-polarized and the s-polarized lightwave components.[162, 163] The p-polarized is named after parallel and corresponds to the component parallel to the plane formed by the incident and reflected light. Conversely, the s-polarized component is named after the German word "*senkrecht*" referring to its perpendicularity to the incidence beam plane. Ψ and Δ are measured in a certain spectral range (typically from 300 to 1100 nm) at different incident angles. The measured data are introduced in a model of the sample, which contains its different layers with their properties like refractive index (n), extinction coefficient (k), film thickness, and/or film roughness.[164, 165] The model is fitted to the experimental data to deduce the parameters. This data treatment is complex since there exist many models, each one best suited for different situations.

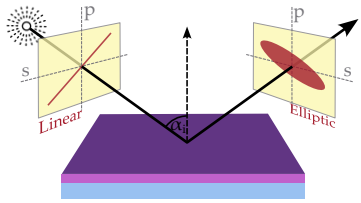

Figure 2.15: Schematics of spectroscopic ellipsometry measurement. The linearly polarized input light (left part) is directed to the substrate at a certain angle with respect to the normal of the substrate (α_i). The reflected light polarization changes due to its interaction with the sample becoming elliptical polarized light.

In this thesis, spectroscopic ellipsometric and data treatment was carried out by Ms. Arianna Quesada-Ramírez, while the substrates prepared for the measurements were made by myself. The equipment used for the VASE measurements was a SOPRA GES5E with a rotating

polarizer in reflection mode. The ellipsometry data were analyzed using WinElli 3.04, a commercial software supplied by SOPRA. A model based on Tauc-Lorentz oscillators was implemented, as it leads to accurate fits of the optical functions of our materials.

2.4.3 *Electroluminesence (EL)*

Electroluminescence is a phenomenon in which a material emits light when an electrical current passes through it. It is essentially the opposite process of photovoltaic generation. The characterization technique is based on applying a current to a photovoltaic cell and measuring the emitted spectrum. Ideally, the injected holes and electrons should recombine in the active layer of the solar cell in a radiative way, elucidating the radiative electronic transitions enabled in the active layer material. Nevertheless, part of the injected current can also recombine through non-radiative paths. In this thesis, electroluminescence was carried out at Forschungszentrum Jülich labs with the help of Mr. Markus Hülsbeck. The current density applied to the devices was equal to the previously measured short-circuit photocurrent under 1-Sun illumination (J_{sc}). The electroluminescence light was captured by a lens system and directed to a spectrometer with a Si photodetector.

2.5 TOPOLOGICAL CHARACTERIZATION

2.5.1 *Profilometry*

Profilometry was used to measure the thickness of different layers. To measure the active layer thickness of a device, we generally scratch a line in between cells, to avoid destroying the device. The tip of the profilometer is scanned perpendicular to the scratched line. Here one has to consider whether the scratch also affects the ETL (ZnO) transport layer on the bottom, if any. The latter is generally seen as a small stair in the scanned profile. Nevertheless, it is recommended to perform the scratch and the scan in a region where ETL was cleaned previously to active layer deposition. To get the thickness gradient of the hole sample one may need to repeat this process in between sub-cells. Nevertheless, just having a few points (4 or 5 at least) is enough to interpolate the values of the devices in between. The used profilometry equipment is a Dektak 150, Bruker. The thickness is measured for selected substrates.

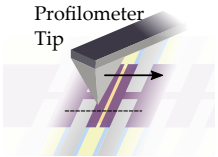

Figure 2.16: Schematics of the methodology to measure thickness with profilometry.

To know the thickness of encapsulated samples, one needs to prepare a non-encapsulated sample of the active layer on top of a glass substrate with the same processing conditions (materials, concentration, solvent,

coating conditions, etc...). The latter is used as a reference to find points that have a similar color intensity either by eye comparison or by means of transmission spectroscopy. At those points, the thickness of the reference film is measured, and its value is assumed in the corresponding similar point of the substrate. This is an approach with less accuracy than the direct measurement of the thickness in the substrate, nevertheless, it is the easiest option available once the substrate is encapsulated.

2.5.2 *Grazing Incidence X-Ray Scattering Characterization*

Grazing Incidence X-ray Scattering is a characterization technique that consists of shining an X-ray beam on a substrate at a very shallow incoming angle, typically below 1°, and collecting the light scattered with a 2D detector. This technique is further subdivided into Grazing Incidence Wide Angle X-ray Scattering (GIWAXS) and Grazing Incidence Small Angle X-ray Scattering (GISAXS), where their only difference is the distance between the detector and the sample. In GIWAXS, the detector is close to the sample (around 10 cm), therefore capturing a wide range of exiting angles, while in GISAXS the photodetector is placed further from the sample (around 2 to 3 m), capturing a smaller exiting angles range (see Figure 2.17).

As happens in X-ray scattering techniques, we get information about repeating patterns of electronic density in the sample by the observation of diffraction peaks at certain angles defined by the scattering vector q. The relation of q with the repeating unit distance is inverse, with q typically being expressed in $Å^{-1}$. Thus, since GIWAXS captures

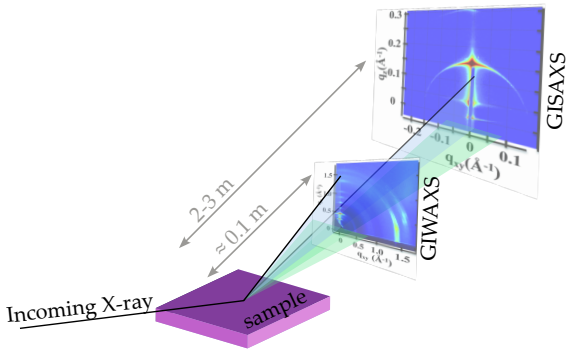

Figure 2.17: Schematics of GIWAXS and GISAXS characterization techniques. The detector in GIWAXS is placed closer to the sample than GISAXS. The GIWAXS and GISAXS spectra shown are taken from reference [166], and correspond to a block copolymer.

higher angles (i.e. q up to 3 $Å^{-1}$) the information obtained relates to the intermolecular arrangement, while GISAXS, capturing lower q values (below 0.1 $Å^{-1}$), gives information about the intramolecular arrangement.

In this thesis, we studied the morphology of some active layer materials using GIWAXS. Dr. Matteo Sanviti and Dr. Jaime Martín from Universidade da Coruña and POLYMAT performed the measurements and data treatment in the ALBA Synchrotron (Campus UAB, Barcelona). The GIWAXS experiments were performed in grazing-incidence geometry, using a beam of 50 µm in width and energy of 12.4 keV, with the Pilatus detector at a distance of 21 cm. The incidence angle of the X-ray radiation was fixed at 0.12° with respect to the sample plane for all the experiments, and an acquisition time of 1 second was used. The background for all samples was acquired on the empty sample holder, and half of its intensity was subtracted from the measurements in order to obtain better-defined diffractograms. The images were obtained in the full q range by overlapping three displaced images acquired consecutively.

3 SPECTRUM ON DEMAND LIGHT SOURCE (SOLS)

This chapter describes a setup named Spectrum On demand Light Source (SOLS) which was developed during the first stages of the thesis and has been improved throughout the whole thesis.[167] Although the motivation behind SOLS was the characterization of RINABOW sub-cells, its posterior development led to a setup with more potential. For this reason, SOLS application examples are present in other thesis chapters. Moreover, intellectual property was protected by a patent.[168] The latter was a great opportunity to be conscious of the importance of technology transfer inside the academic environment. It was also a good opportunity to learn more about this complex field. This chapter first introduces the state of the art and motivation behind SOLS development. Afterward, it describes the setup embodiment used in the lab and its working principles. The most important parts are explained in depth in order to provide a better description of the setup and its possibilities. The output light is also classified as a solar simulator following ASTM standards. Finally, the chapter proposes ideas to improve the setup and describes the next steps to produce a first pre-industrial prototype.

3.1 STATE OF THE ART

Developing and optimizing materials for emergent photovoltaic technologies to work in different conditions and environments increasingly calls for novel light sources capable of adapting the irradiance conditions to the targeted application. Examples include modules placed on vertical walls (e.g. for building integrated PV),[169] at different altitudes (and thus different UV amounts),[170] different air masses and turbidities,[171] underwater photovoltaics[172] or for indoor applications.[173, 174, 175] Moreover, multi-junction solar cells based on the spectral splitting concept have recently attracted renewed attention.[107, 131, 176, 177] In this case, an optical element separates the sunlight into a number of beams exhibiting different spectral ranges that match the bandgap of each sub-cell. For optimizing this geometry, each sub-cell should be investigated as a function of a fraction of the sun spectrum. Sources capable of producing tunable low and high-wavelength pass and band-pass filters would be needed. While promising results have been obtained for different applications, we believe the field would greatly benefit from novel characterization tools that could help to adapt studies to specific geometries and applications.

See Figure 3.1 for spectra examples of different air masses (a), artificial indoor light (b), underwater (c), and tunable filter (d).

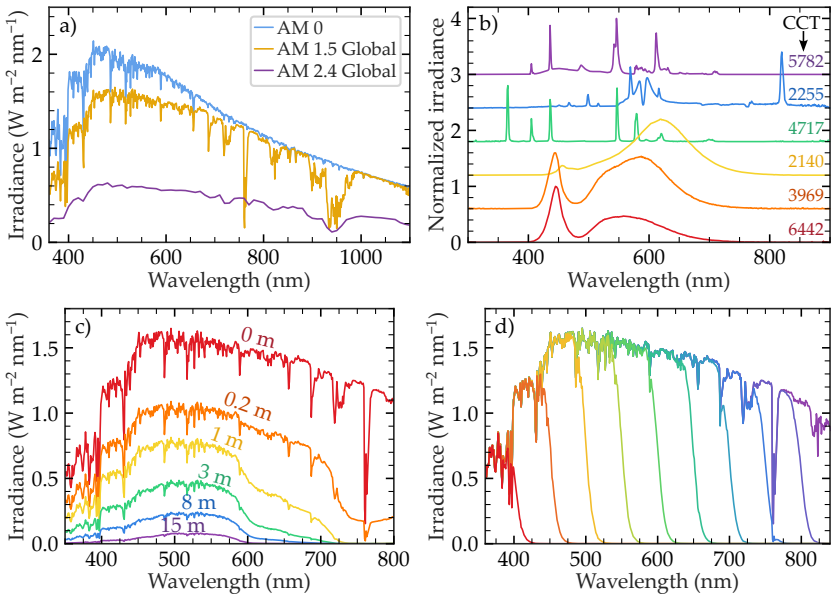

Figure 3.1: Examples of useful spectra for novel applications of OPV. (a) Spacial AM 0 spectrum (blue) and terrestrial AM 1.5 Global (yellow).[79] Purple spectrum is calculated using [80] at my hometown (Torrella de Montgrí) on day 2024/05/24 at 17 h corresponding to an air-mass of 2.42. (b) Examples of artificial light sources measured in Madrid city corresponding to compact fluorescent (pruple), sodium (blue) and mercury vapor (green) lamps as well as different LEDs (yellow, orange, and red).[178, 179] Correlated color temperaure (CCT) is indicated in the right side of the plots. (c) Downwelling spectra irradiance as a function of water depth at geographical latitude 46.0053° and longitude -8.1543° between Majorca and Algeria.[180, 181] (d) Example of spectra resulting from a low-wavelength-pass tunable filter useful for RAINBOW solar cells characterization.

The standard and most used characterization procedure in PV is the measurement of the power conversion efficiency (PCE) under 1 Sun illumination (the standard terrestrial AM1.5G broad-band spectrum).[7, 182] Another essential characterization is the photovoltaic external quantum efficiency (EQE_{PV}), which provides information on the photon-to-electron conversion effectiveness.[7] More advanced measurements are used to investigate solar cells besides PCE and EQE_{PV} measurements. For instance, the dependence of the photocurrent and open circuit voltage with illumination intensity has been used to investigate different recombination mechanisms in organic [183, 184, 185] and hybrid-based photovoltaics.[186]

Currently, these measurements rely on the use of different filters and/or different light sources and/or different setups. Importantly, a recent attractive method its to have a light source whose light

spectrum can be modified in shape and intensity by using an array of individually addressable light-emitting diodes (LEDs). These devices are particularly useful for producing different broad-band spectra (e.g. AM0 and AM1.5G) as well as different narrow-band spectra.[182, 187, 188] Having a single piece of equipment for testing many conditions is advantageous. However, LED illumination has several intrinsic limitations, such as poor spectral resolution. Typical systems have less than 20 LEDs to cover a spectral range of more than 900 nm; therefore, the LEDs used for these devices have FWHMs of several tens of nanometers. Another problem is the non-linear response of LEDs with current, which strongly limits the dynamic range of the illumination source. The latter implies that LED-based solar simulators may not be well fitted for experiments requiring a large dynamic range (e.g., the recombination studies mentioned earlier) or to reproduce indoor illumination conditions unless a combination of (non-automatic) filters is used. Finally, it seems that the most critical aspect is that achieving spatial homogeneity for large areas is complex and expensive.

Regarding beam characteristics, all the discussed characterization techniques require the beam to be homogeneous in terms of intensity and spectrum, apart from being stable over time. Therefore, different light sources are set up to meet these criteria. One notable exception to this requirement is the mentioned multi-junction solar cells based on the spectrally split (RAINBOW) concept, which is the main focus of this thesis.[176] In this case, a spectrally split beam is required to illuminate each sub-cell with the appropriate fraction of the sun spectrum.

With the latter being our primary motivation, we have developed a spectrum on-demand light Source (SOLS) capable of providing a tunable light spectrum, which can be spectrally shaped in intensity and wavelength range with respect to a primary light source. The distinctive features that differentiate the SOLS light source from the current state of the art are:

1. It offers two types of spectrally shaped output: A spatially homogeneous beam over its cross section with the demanded spectral shape, used for homogeneous areal illumination, and a spatially and spectrally split beam divided into different wavelength components, a unique capability for illuminating lateral-tandem (RAINBOW) solar cells.

2. It provides a high light throughput and a large spectral window (at least from 380 to 1100 nm) by implementing a dispersive optical element based on refraction instead of diffraction.

3. It can output a highly tunable broad-band spectrum shaped to suit a extensive range of applications, e.g. AM1.5, AM0, indoors,

building integrated PV, agrivoltaics, tunable low/high pass filter for spectral splitting PV, stability measurements, etc. At the same time, it can output narrow-band spectra with a broad tunability of the central wavelength and FWHM, suitable for EQE_{PV} measurements, among others.

4. SOLS has a large intensity dynamic linear range (about two orders of magnitude) realizable without the need for optical density filters, which could compromise the broad-band spectral filtering uniformity. The intrinsic linearity dependence and its wide dynamic range lead to a much simpler and less time-consuming procedure to spectrally shape the output spectrum, as compared to LED solar simulators.

5. The first implementation of SOLS already exhibits excellent temporal stability in terms of intensity and spectrum (e.g., <2%, type A solar simulator) and fairly good spatial (e.g., <5%, type B) and spectral (e.g., <2%, type A) homogeneity over the output illuminated area.

Hence, SOLS offers great versatility with the mentioned features, such that it can be used to test different PV properties like PCE, EQE_{PV}, efficiency under specific illumination conditions, tandem optimization, automatic light intensity scans, etc., adapting simultaneously the output spectrum to match the illumination requirements of a particular application.

3.2 SOLS SETUP EMBODIMENT

This subsection describes the working principles of the SOLS and focuses on the actual embodiment of the setup. Figure 3.2 shows a sketch and a photograph of SOLS setup. We can divide the underlying concept for the proposed setup into three main blocks. In the first block (green in Figure 3.2), white light from a broad-band lamp is dispersed into its constitutive wavelengths with a dispersive optical element. The choice of optical element is discussed later in the section. After this stage, the light beam is spectrally split into its composing wavelengths in the direction perpendicular to light propagation.

A second block (blue in Figure 3.2) is placed in the beam's path to partially mask it, controlling the transmitted light at each wavelength. This block is the part of the SOLS that shapes the output spectrum, being able to produce any spectrum by subtraction of the original light. We have implemented two different masking systems in the SOLS

setup, which will be discussed afterward. Implementing other masking systems is also discussed for a future setup upgrade.

Finally, a third block (red in Figure 3.2) is responsible for reconcentrating the spectrally split beam. At any point during this path, the beam light is spectrally split. To our knowledge, the latter is a novel feature not present in any setup available on the market. Nevertheless, for most of the applications, a homogeneous spot is needed. For this reason, some optical elements can be added at the focal point of the spectrally split beam to spatially and spectrally homogenize the light beam. Additionally, the output light has to be characterized in terms of its power and spectrum to quantify the effect of the masking systems and the overall setup. Unless specified, all spectra and output characterization shown in this chapter are measured at position (6) of Figure 3.2. The latter also applies to SOLS spectrum shown throughout the whole thesis.

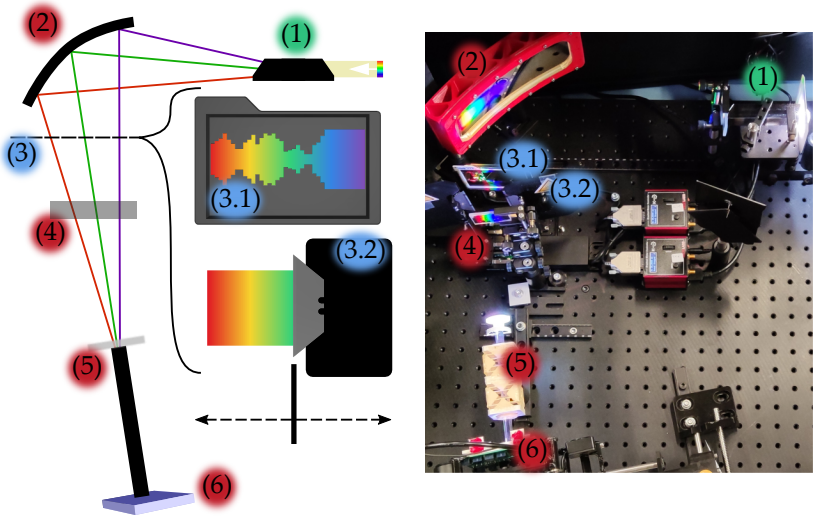

Figure 3.2: SOLS setup schematics. (a) Schematic of the SOLS setup. (b) Photograph of the actual SOLS setup. The main parts composing the setup are labeled as (1) double Amici prism, (2) custom mirror to concentrate spectrally split light, (3) masking plane, (3.1) 3D-printed mask, (3.2) motorized guillotines, (4) cylindrical lens to concentrate light in the vertical direction, (5) light pipe homogenizer, and (6) light output and cell holder. The three main blocks are differentiated with green (dispersive element), blue (filtering elements), and red (reconcentration and homogenizing elements) background in the numbering.

3.2.1 *Dispersive element*

Dispersive optical elements based on a combination of diffraction and refraction have advanced functionalities. Nevertheless, they are unsuitable for this setup

A dispersive element is an optical element that physically separates an input light, typically broad-band, into its composing wavelengths (colors). The latter can be done thanks to diffraction and/or refraction of light. Diffraction-based dispersive elements generally have better light separation than refractive-based ones due to a higher wavelength resolution and a more homogeneous dispersion dependence on wavelength. Nevertheless, their optical window is limited due to overlapping multiple diffraction orders of different wavelengths. Additionally, the latter is a source of light loss, reducing light output. Although modern monochromators use diffractive gratings as dispersive elements, their disadvantages are incompatible with the SOLS application. The overlapping of diffraction orders of different wavelengths limits the spectral range of operation of the device: the ratio between the maximum and the minimum wavelengths has to be between 1 and 2. For example, suppose the maximum wavelength that we want to achieve is 1000 nm. The second dispersion order of 500 nm will appear in the same direction as the first diffraction order of 1000 nm, limiting the spectral range between 500 and 1000 nm. Additionally, the diffraction efficiency has a strong wavelength dependence, drastically dropping for wavelengths far from the wavelength at which the grating is optimized. The latter reduces the light output intensity and strongly impacts the spectral shape of the diffracted light. On the other hand, refraction-based dispersive elements have no spectral limitations except from the transparency range of the materials composing the optical element. Since these are typically optical-grade SiO_2 (fused silica and similar optical glasses), their operation range is approximately 300 nm to 3 µm. Additionally, the transparency in that range is near 100%, and the main losses are due to reflection at the interfaces. Although *a priori* refraction-based dispersive elements have the worst dispersion because they heavily rely on the dispersion of the refractive index, they can be designed to satisfy a wide range of applications.[189, 190, 191]

Refraction-based dispersive elements typically are geometrical blocs of glass, thus referred to as prisms.

The discussed advantages and disadvantages between diffraction and refraction-based dispersive elements resulted in the choice of refraction-based for the SOLS equipment. Among all possible dispersive prisms, we chose the double Amici prism as the dispersive element.[192, 193] The double Amici prism consists of three triangular prisms in contact, with the first and the last typically being made from a medium-dispersion crown glass, and the middle one made from a higher-dispersion flint glass (see Figure 3.3 (a)). The main advantage of the double Amici prism compared to other types of dispersive prisms is that a certain wavelength of the incoming beam (≈550 nm for our

prism) remains in the optical axis of the input light, facilitating the geometric design of optical setups.[194] This prism can be optimized and designed to achieve dispersion comparable to gratings.[189, 191]

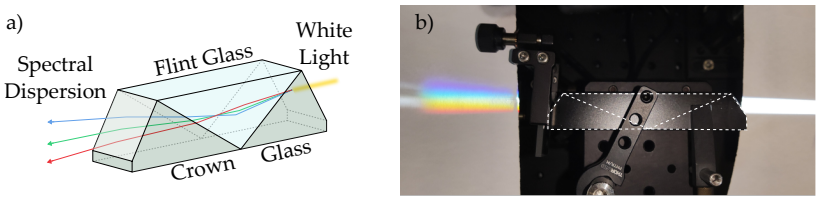

Figure 3.3: White light dispersion in a double Amici Prism. (a) Schematics of the geometry of the double Amici prism and (b) photograph of the double Amici prism used in the SOLS setup with the three different glass slabs marked with dashed white lines.

In our implementation, the light source is a Xenon arc lamp (150 W). In general, it can be any (broad-band) light source; nevertheless, some aspects have to be considered for a better light separation (i.e. wavelength resolution). The incoming beam should be as collimated as possible since any degree of divergence or convergence of the input light will result in different incoming light angles and, therefore, different exit angles for the same wavelength, resulting in poorer color separation. The width of the incoming light beam also affects the latter since a wider collimated input light will result in a wider spatial distribution of the same wavelength that exits the prism with the same angle. We had to improve the collimation of the Xenon arc lamp before the double Amici prism to increase wavelength resolution at the expense of light power. The latter is further discussed in the last section of this chapter. The actual implementation of the double Amici prism with the corresponding input light source can be seen in Figure 3.3 (b). The photograph shows the dispersion introduced by the prism to the broad-band input light (right side), which produces the rainbow pattern observed at the output of the prism (left side).

3.2.2 *Filtering element: 3D-printed masking cards*

The second block (blue in Figure 3.2) corresponds to the filtering elements placed in the beam's path where the beam is spectrally separated. These filtering elements are crucial components that enable simple and versatile spectral shaping. For demonstration, we have implemented the use of 3D-printed "cards" (element (3.1) in Figure 3.2), such that by insertion of a card with a given slit height versus wavelength profile, a predefined spectrum is obtained. The shadow mask encodes the intensity-wavelength information in the form of slit height as a function of lateral position as shown in Figure 3.4.

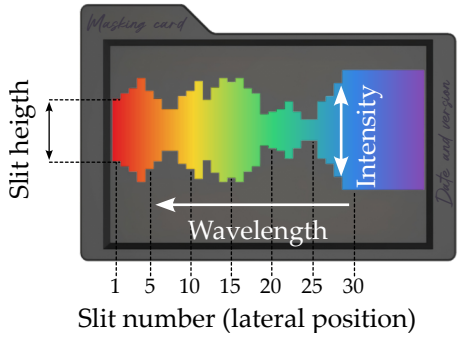

Figure 3.4: 3D-printed masking card schematics. Example of the design of a 3D-printed masking card wherein the lateral position is discretized as slit number, and the height of each slit tune the light intensity transmitted.

The plane where the mask element is placed can be defined by two orthogonal directions, the one in which light becomes spectrally separated (wavelength) and the direction corresponding to the actual size of the light beam (intensity), as depicted in Figure 3.4. This plane contains a continuous distribution of wavelengths along the wavelength direction. Nevertheless, for simplification, one can discretize this distribution by considering a set of N contiguous vertical slits equally distributed along the wavelength direction. The slits correspond to masks that transmit light along the intensity direction but only in a defined wavelength range. In our case, we implemented a total of 40 slits of 2 mm width, adopting consecutive positions throughout the wavelength direction. Figure 3.5 (a) shows a photograph of four consecutive vertical slits, while Figure 3.5 (b) shows the color resulting from other four slits when placed into the SOLS setup. During the thesis, I have experimented colors that I had never seen before. Unfortunately, the difficulty of capturing them in a photograph makes the endless possibilities of output colors a unique beauty of the setup in live.

The spectrum that emerges from each vertical slit, $\varphi_i(\lambda)$ measured at the sample position, can be used as basis vectors for expressing any spectrum as a linear combination of the latter, with coefficients, a_i, ranging from 0 to 1.

$$\theta_{calc} = \begin{bmatrix} a_1 & \cdots & a_i & \cdots & a_N \end{bmatrix} \cdot \begin{bmatrix} \varphi_1(\lambda) \\ \vdots \\ \varphi_i(\lambda) \\ \vdots \\ \varphi_N(\lambda) \end{bmatrix} = \vec{a} \cdot \vec{\varphi}(\lambda) \qquad (3.1)$$

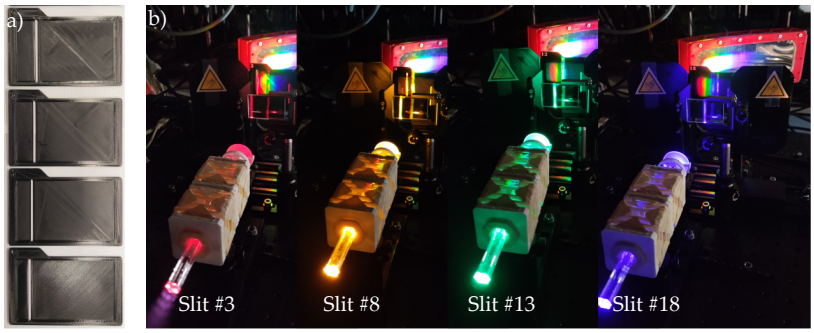

Figure 3.5: Examples of the slits system for the calibration of 3D-printed masks. (a) 3D-printed slits of the slits mask system from slit number 6 (bottom) to slit number 9 (top), wherein the complementarity of the slits is apparent. (b) Photograph of different slits acting as a unique mask system in the SOLS setup. The different colors show the SOLS's ability to act as a monochromator.

Figure 3.6 shows a set of slits spectra used for the calibration of the 3D-printed masking cards. Although the plane is discretized with 40 slits, the spectrally split beam does not pass through all of them because its width is smaller than the width of all 40 slits, resulting in a null spectrum for some of the slits at the extremes. Their position is maintained fixed with respect to the other parts. Therefore, small changes in light directions due to re-calibrations or movements of other parts of the setup results in a change of the slits spectrum. The actual vector basis is reduced to about 26 spectra. Assuming that each slit spectrum is uniformly distributed along the intensity direction, the a_i coefficients ($\vec{a}$) correspond to the relative height of each slit in the intensity direction. The latter is a reasonable assumption for a homogeneous and collimated beam incident at the entrance of the double Amici prism since the dispersive element does not affect the vertical direction of the rays that pass through it. A minimization function like Scipy.optimize.minimize from the *scipy* library in Python can rapidly find the coefficients vector, $\vec{a}$, to best fit the target specturm.[195, 196] The integrated spectral difference between the fitted and the target spectrum is the function to minimize and $\vec{a}$ is the vector parameter to fit. Afterwards, the coefficients are introduced in a parametric 3D design of the masking card, resulting in a model for 3D printing that matches the target spectrum.

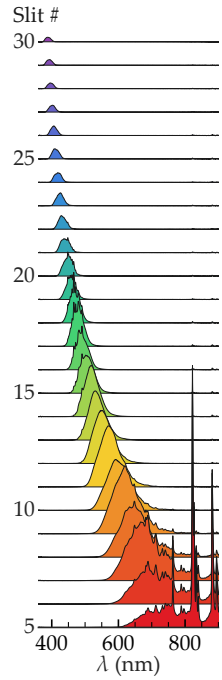

Figure 3.6: Spectra basis vectors for 3D-printed masks. Series of spectra from vertical slits used as basis vectors to calibrate the 3D-printed masks.

If the slits were complementary and the light distribution along the intensity direction was homogeneous, the designed mask should result in the exact calculated spectrum. Nevertheless, this is not the case in the actual SOLS setup. The distribution along the intensity direction is not homogeneous but more concentrated in the central part. The latter is shown in Figure 3.7 (a), wherein the slit spectrum was measured as a function of slit height. The measured spectra were

integrated along the slit peak, and its total power density, normalized with the full slit spectrum, is plotted as a function of the slit height. The latter is decreased linearly for slits in the blue (425 nm), green/yellow (550 nm), red (650 nm) and infrared (900 nm) regions of the spectrum. The experimental points fall slightly above the expected trend for an ideal homogeneous distribution, indicating that light is not entirely homogeneously distributed along the intensity direction, being more concentrated in the central region. Moreover, Figure 3.7 (b) shows that the linear combination with $\vec{a} = \vec{1}_N$ for all slits (solid line) results in a spectrum lower than the measured spectrum without masks (dashed line). The combination of both effects results in the measured spectrum being slightly different than the calculated for a masking card. Therefore, a few extra optimization steps were needed to fabricate a masking card for each target spectrum.

$\vec{1}_N$ *is a vector of length* N *containing ones:* $\begin{bmatrix} 1 & \cdots & 1 & \cdots & 1 \end{bmatrix}$

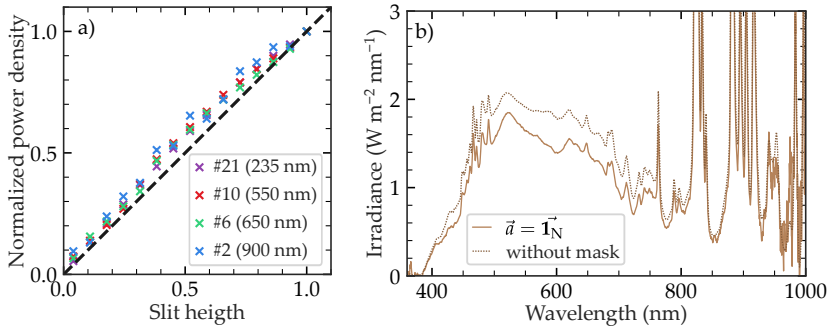

Figure 3.7: Slits calibration system imperfections. (a) Power density transmitted as a function of slit height for slits at different spectral regions (central wavelength indicated in brackets). The ideal homogeneous distribution (grey dotted line) is also plotted for comparison. (b) Spectrum measured without a mask (dashed line) and spectrum resulting from the linear combination with $\vec{a} = \vec{1}_N$ (solid line).

Table 3.2 of Section 3.3.2 shows the spectral match evaluation of all spectra shown in Figure 3.8

For demonstration, Figure 3.8 shows four examples of different target spectra (solid lines) and their corresponding SOLS output spectra (shaded curves). The first targeted spectrum (Figure 3.10 (a)) corresponds to the AM1.5G. It can be seen that the SOLS output spectrum closely reproduces the target spectrum. The latter is evaluated in Table 3.2 of Section 3.3.2, resulting in a Class A qualification between 400 and 1000 nm. Therefore, the SOLS is suitable for standard PV characterization under 1 Sun illumination. To confirm the good spectral match, we used three different OPV systems with energy band-gaps across the visible spectrum as a reference. We measured their efficiency with SOLS using the AM1.5G mask and with a commercial AAA solar simulator based on a xenon arc lamp. Figure 3.10 (a) shows less than 5% difference for each measurement, corroborating the good spectral match.

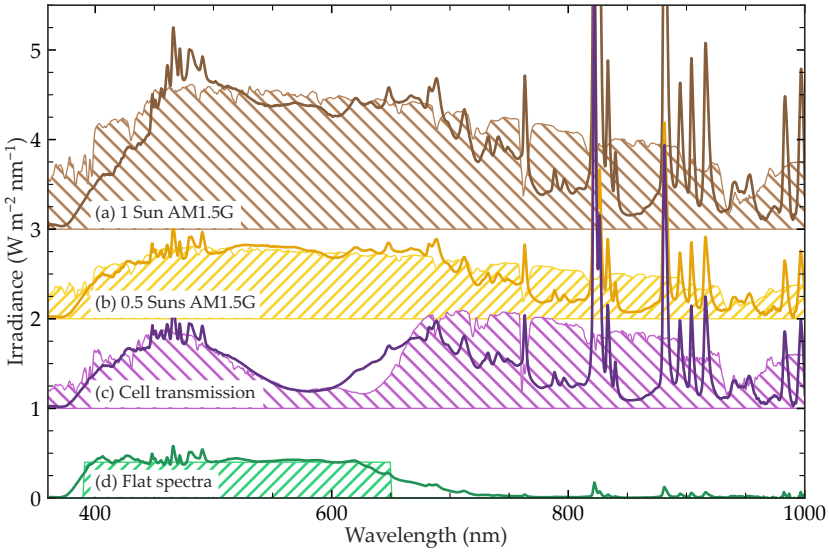

Figure 3.8: Spectra from 3D-printed masking cards examples. Example of four different target spectra (filled area) and their corresponding SOLS output spectra (solid line) made with the slits calibration system. The physical masks that encode each spectrum are shown in Figure 3.9, while their spectral match evaluation can be found at Table 3.2.

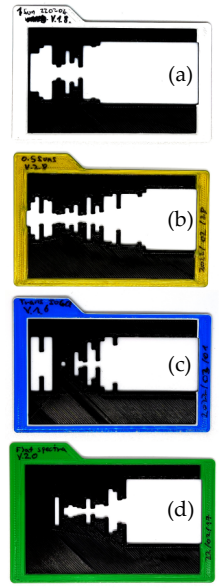

Figure 3.9: Masking cards encoding the fitted spectra from Figure 3.8. The 3D-printed masks were designed using the fitting procedure explained in this section.

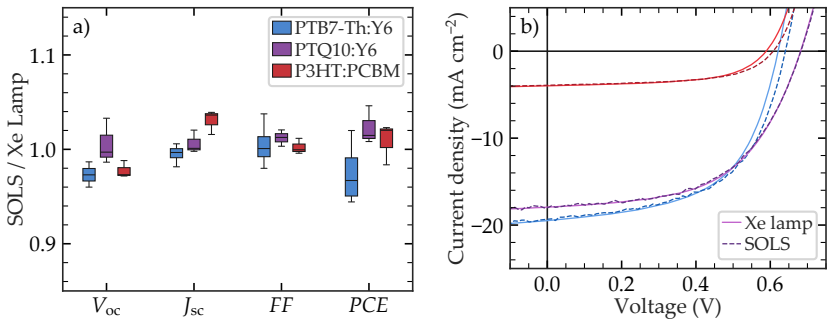

Figure 3.10: Comparison of OPV performance under 1 Sun measured with SOLS and with Xenon arc lamp solar simulator. (a) Statistical comparison between SOLS and Xenon lamp J-V measurements. (b) J-V curves of single organic solar cell measured with SOLS (dashed) and standard Xenon arc lamp (solid). Each box plot comprises four cells with different thicknesses and overall PCE.

Figure 3.8 (b) corresponds to the 0.5 Sun AM1.5G spectrum exhibiting a Class A qualification as well, between 400 and 1000 nm (see Table 3.2). It demonstrates the setup's ability to perform light intensity-dependent PV characterization. By scaling the slit height profile of a mask card but maintaining the same spectral shape, the integrated spectral intensity can be substantially varied at least two orders of magnitude, as also shown in Figure 3.7 (a). Thus, the dynamic range of the SOLS is

larger than that of currently available spectral shaping alternatives, like the LED-based solar simulator, enabling the study of light intensity-dependent phenomena in greater detail. Additionally, it has a linear dependence on slit height, which facilitates the 3D-printed mask design procedure. For example, this feature would be handy for studying the nature of recombination processes in the photoactive layer, which requires measuring multiple J-V curves with a range of light intensities while maintaining the same spectral shape.

The SOLS is not limited to uniform intensity variations. By varying the relative intensity of each wavelength component, we can emulate the transmission spectrum of semitransparent solar cells, which can be an interesting feature in the thickness and blend composition optimization of tandem PV. For example, in Figure 3.8 (c), we emulate the transmission spectrum of a thin PBDBT-2F:IO-4Cl organic solar cell, which would act as the tandem top cell with a band gap around 700 nm. With this "filtered" transmission spectrum, one can study the performance of multiple bottom cells before manufacturing the actual tandem device.

Besides simulating the pure or "filtered" solar spectrum, the SOLS is capable of producing entirely custom-shaped spectra, like the one shown in Figure 3.8 (d) (green curve), which targets a top-hat flat spectrum with an intensity of 0.4 W m^{-2} nm^{-1}, between 400 and 650 nm, and 0 W m^{-2} nm^{-1} in every other wavelength. The resulting SOLS spectrum is also Class A within the relevant wavelength range, fitting the target spectrum quite well (see also Table 3.2). This custom output spectra capability expands the possible applications of the SOLS beyond PV characterization. For example, this custom spectra could be used for calibration purposes that require a flat spectrum.

An important part of the versatility of this filtering element relies on the use of 3D printing. This introduces some limitations which are directly related to the intrinsic properties of this fabrication technique. Fused deposition modeling (FDM) 3D printing has resolutions on the order of a few hundred of µm in the plane where slits are created. This resolution is more than enough for the vast majority of applications. For example, the slits of the vertical slits system are 2 mm in width and 50 mm in height. And typical values for slit height in Figure 3.5 varies between 50 mm and 10 mm. Therefore, for most applications, the resolution of FDM 3D printing is enough. Nevertheless, if one wants to reproduce spectra comprising vertical slit height below 1 mm (corresponding to a relative slit height of 0.02), some problems may occur due to the 3D printing process. Then, the solution may require the fabrication of the mask with other methods such as printing the

mask in black ink on transparent plastic film or using CNC machinery of metals. Another solution could be the use of optical elements (such as filters) to reduce the light intensity and therefore increase the relative slit height needed. Nevertheless, we have not found problems with these resolutions, and 3D printing was the easiest choice in this case. Another limitation is time-related, since 3D printing a mask is far from an automated process. This could be mitigated with automated systems, as discussed in the last section of this chapter.

3.2.3 *Filtering element: guillotines*

As a part of the second block, we have introduced a partial automatization of the filtering process for more advanced experiments. This is a motorized filtering stage composed of two guillotines. Each guillotine masks the spectrum entirely above or below a given wavelength, producing the function of a tunable high-pass or low-pass filter. Figure 3.11 shows the blue guillotine acting as a high wavelength pass filter as an example. These filtering elements are designed to characterize and optimize solar cells in spectral-splitting multijunction geometries.

Additionally, the combined effect of both guillotines corresponds to a band-pass filter which can be tuned in width and central wavelength.

To perform these measurements, a previous calibration needs to be done. The calibration aims to determine mathematically the effect of each guillotine on the output spectrum by associating the position of the guillotine with a mathematical function. For this reason, we first modeled the masking effect of the blue guillotine masking the blue fraction of the spectrum on the spectral shape when performing a red sweep. For each position of the guillotine motor, the measured spectrum φ_{out} is divided by the full spectrum φ_{TOT} and the resulting ratio is fitted with an edge function $H(\lambda)$, following:

The blue guillotine masks the blue fraction of the spectrum. Therefore, it generates a red sweep because the resulting spectrum contains the red fraction.

$$\frac{\varphi_{\text{out}}(\lambda)}{\varphi_{\text{TOT}}} = H(\lambda) \tag{3.2}$$

The edge function is a step function given by the Fermi-Dirac distribution (Equation 3.3), where h is the height, λ_{d} is the edge central wavelength and FWHM is the full width at half maximum of the edge:

$$H(\lambda) = \frac{\text{h}}{1 + e^{\frac{\lambda_{\text{d}} - \lambda}{\text{FWHM}}}} \tag{3.3}$$

Notice that the first derivative of the Fermi-Dirac distribution is symmetric with respect to the central wavelength λ_{d}. Nevertheless, due to the non-linear dispersion of the double Amici prism, the first derivative of the measured spectrum when a guillotine is acting as a

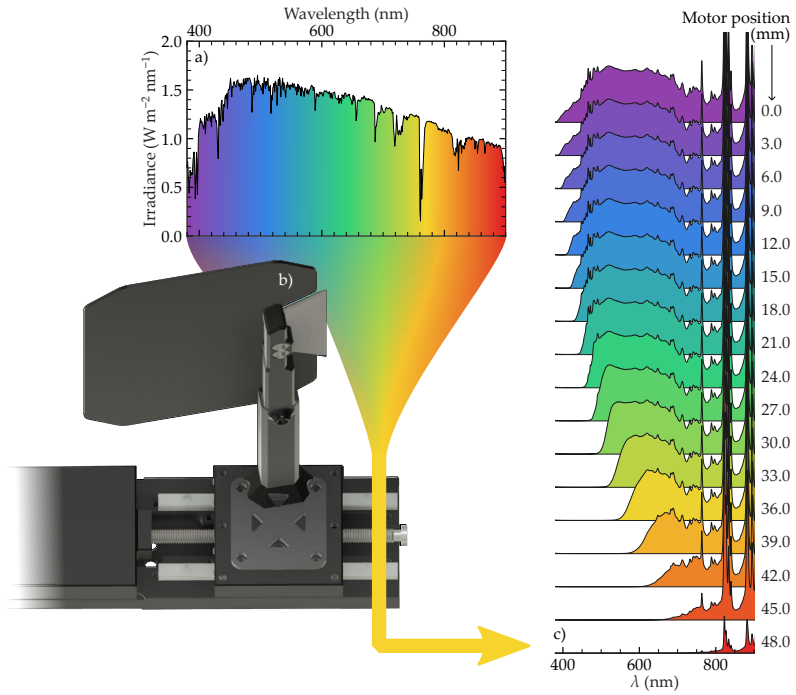

Figure 3.11: Schematics of the motorized blue guillotine. (a) Solar spectrum spectrally split at the masking plane. (b) Motorized blue guillotine masking the blue fraction of the spectrum. (c) Individual spectra resulting from the movement of the blue guillotine (red sweep), which acts as a high wavelength pass filter. This set of spectra is used to calibrate the motor positions.

filter is not totally symmetric. Nevertheless, this effect is very small in most of the spectral range, and the Fermi-Dirac distribution is enough to describe the effect of the guillotines. Figure 3.12 (a) show three examples of the described and in all cases except for the red line corresponding to λ_d in the IR region, the fit is close to the spectrum.

The dependence of λ_d and FWHM on the motor position for the blue guillotine is fitted to a spline to smooth the results. Figure 3.12 (b) shows the fitted λ_d and FWHM as a function of blue motor position. To calibrate the red motor position (i.e. the guillotine that performs the blue sweep), we search for the best complementary blue sweep spectrum for each red sweep spectrum. As a result, for each position of the blue motor, we have an associated λ_d and FWHM resulting from the fitting using Equation 3.3, and a red motor position with a complementary spectrum. λ_d is considered as the wavelength at which the spectrum is divided in the blue and the red part by the guillotines. For this reason, λ_d is named as the dividing wavelength along the thesis.

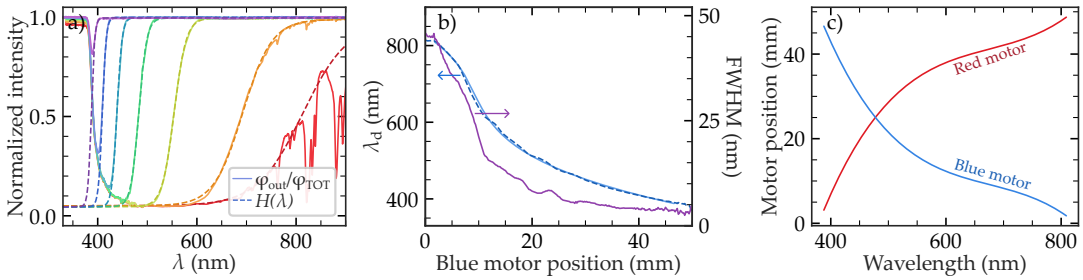

Figure 3.12: Results of the motorized guillotines calibration (a) A few examples of fitting the H function to the red-sweep data. (b) λ_d and FWHM as a function of the blue motor position resulting from the 250 spectra fitted. (c) The final calibration result shows the relation between motor position and dividing wavelength for the red and the blue motors.

In the scope of this thesis, the guillotines were used to characterize organic solar cells as sub-cells in a RAINBOW two-junction geometry, namely "blue" and "red" sub-cells with higher and lower bandgaps, respectively. Under AM1.5G illumination and in spectral splitting geometry, the red sub-cell receives the lower energy part of the solar spectrum, from ca. 1100 nm up to the dividing wavelength, λ_d. In contrast, the blue sub-cell receives the complementary part, i.e. between λ_d and 390 nm. The corresponding chapter (Chapter 4) explains all the experimental details of the RAINBOW characterization and results.

3.2.4 *Reconcentrator and homogenizer*

The third block of the setup (red in Figure 3.2) consists of an optical element that corrects the divergence applied by the prism to reconcentrate the spectrum (different colors) into a spot. The best and simplest option we found is a custom-made mirror, whose size and curvature must be designed according to the output of the double Amici prism. Dr. Martí Gibert-Roca did the design and first fabrication of the custom-curvature mirror.[159] Besides considering the measured light divergence after the double Amici prism, the calculation also considers the distance the spectrally split beam is forced to travel. The latter is to guarantee a correct spatial wavelength separation to attain the desired wavelength resolution. In our implementation, the distance between the prism and the curved mirror is designed to be about 30 cm. The mirror consists of a 3D-printed structure that provides the calculated curvature to an evaporated silver-coated 0.5 mm thick rectangular polyethylene terephthalate glycol-modified (PETG). The first two mirrors fabricated had the Ag exposed to air. The latter resulted in a decrease in reflectivity over time, especially in the UV

region. Appart from that, the degradation was obvious to the naked eye (Figure 3.13 (a)). Trying to protect the Ag surface with a 40 nm thick LiF film was insufficient to avoid degradation over time. Nevertheless, the Ag/PETG interface barely showed degradation, as seen in Figure 3.13 (b). For this reason, in the successive iteration (evaporated mirror shown in Figure 3.13 (c)), we inverted the PETG sheet to reflect the light at the Ag/PETG interface. In that configuration, the Ag is sandwiched between the PETG and the 3D-printed frame, decreasing its possibility of degrading. This modification increased the durability of the mirror. The mirror is currently about two years old, and we have not observed any decrease in reflectivity yet, nor is degradation visually noticeable (Figure 3.13 (d)).

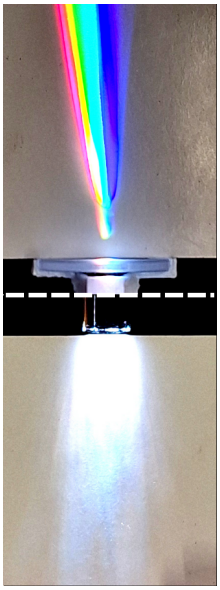

Figure 3.14: Effect of the homogenizing apparatus. Spectrally split light beam entering the homogenizing apparatus through the diffuser (top image) and exiting the homogenizing apparatus through the light pipe (bottom image).

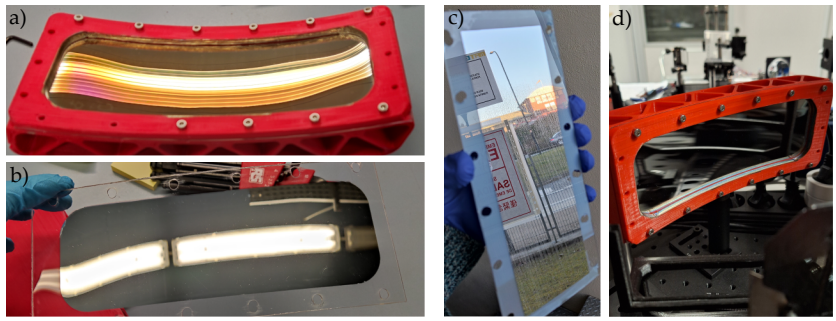

Figure 3.13: Degradation of the custom mirror Ag surface. Custom mirror showing degradation only in the Ag/air surface after approximately 6 months mounted on the SOLS from the front side (a) mounted on the 3D-printed frame, and from the rear side (b). (c) Mirror from the front side right after evaporation. (d) Show the same mirror mounted in the SOLS after 2 years (nowadays photo).

The reconcentration applied by the custom 3D-printed mirror is in the horizontal direction (wavelength direction in Figure 3.4). In addition, a cylindrical lens concentrates the beam along the vertical direction (intensity direction in Figure 3.4) to provide a tight focus on the next optical element. The focal length matches the mirror's focus in the horizontal direction to be in focus simultaneously in both directions to ensure minimal light losses.

The equipment delivers a focused but spectrally split beam in the path and at the focal plane where light is concentrated (where element (5) is placed in Figure 3.2). The latter could be used to characterize a multi-junction RAINBOW solar cell by placing the device at the correct distance before or beyond that focal plane. Nevertheless, this has not been implemented yet in the SOLS. In all the reported experiments, a homogenizing apparatus is placed at the focal point of the mirror and the cylindrical lens. It consists of a diffusing element in front

of a homogenizing light pipe. In this way, the diffusing element introduces significant randomness in the direction of the incoming light. Together with the homogenizing light pipe, the output beam produces a homogeneous illumination area, both spectrally and intensity-wise. The latter is shown in Figure 3.14. Moreover, an analysis of the non-homogeneity of the output is done in Section 3.3.3, wherein the effect of the diffuser on the output homogeneity is also discussed. In our current implementation, the resulting illuminated area ((6) in Figure 3.2) is about 50 mm^2 (a 4 mm inner radius hexagon).

3.3 OUTPUT LIGHT CHARACTERIZATION

To use the SOLS as a solar simulator, we need to characterize its output following a standardized definition of a solar simulator. We chose the standard ASTM E-927 10, although other standards exist. This standard assesses the spectral match, the spatial non-uniformity of irradiance, and the temporal stability of the light produced by a light source that approximates the illumination of natural sunlight. A solar simulator gets a classification for each aspect, following Table 3.1. The classification is Class A for the best scenario and Class C for the worst. Therefore, the classification of a solar simulator is defined by three letters. This section explains in detail the SOLS characterization according to the ASTM E-927 10 standards. But first of all, we need to explain the setup and methodology used to measure the output spectrum.

	Spectral Match*	Spatial non-uniformity SNU	Temporal instability TI
Class A	0.75 - 1.25	2 %	2 %
Class B	0.6 - 1.4	5 %	5 %
Class C	0.4 - 1.2	10 %	10 %

Table 3.1: Class A, B and C Standards and Specifications Defined by ASTM E 927-10.
* Acceptable range ratio of ideal % according to related table values for Ideal Spectral Match standards for ASTM E 927-10.

3.3.1 *Measuring the output spectrum*

To determine which is the spectrum delivered by the SOLS, we perform a direct measurement at the output of the light homogenizer. This corresponds to exchanging the sample at position (6) in Figure 3.2 by the following contraption: a 1" tube containing a diffuser, a concentrator lens, and a glass fiber connected to a Flame spectrometer, as shown in

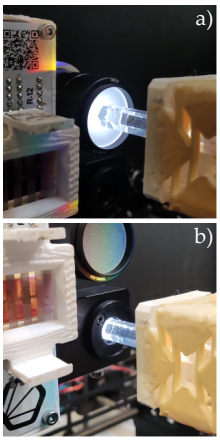

Figure 3.15: SOLS output spectrum measurement. Photograph (a) shows the measurement contraption while acquiring a spectrum, while photograph (b) shows a power measurement with the thermopile during calibration.

Figure 3.15 (a). Here, the purpose of the (second) diffuser is to measure the spectrum independently of the tube's position with respect to the light pipe. The spectral response of the combined elements of the contraption, including the CCD and the Flame spectrometer, is unknown, but *a priori*, not flat (i.e. it has an unknown dependence on wavelength). Hence, first of all, one needs to calibrate the contraption response. The calibration is performed by illuminating the contraption with an input light with a well-known irradiance spectrum, $E_{\text{ref}}(\lambda)$. We used an LEDs solar simulator with a calibrated built-in spectrometer. By dividing $E_{\text{ref}}(\lambda)$ by the Flame spectrometer data expressed in CCD counts for a certain integration time t_{int}, $\text{CCD}_{\text{cts}}^{t_{\text{int}}}(\lambda)$, we obtain the spectral response function, $k(\lambda)$; apart from a scaling factor, $A(t_{\text{int}})$, which only depends on t_{int}:

$$\frac{E_{\text{ref}}(\lambda)}{\text{CCD}_{\text{cts}}^{t_{\text{int}}}(\lambda)} = A(t_{\text{int}})k(\lambda) \tag{3.4}$$

The scaling factor $A(t_{\text{int}})$ is calculated only for 1 ms integration time since this is the limit of the Flame spectrometer, right below saturation for the AM1.5G spectrum. $A(t_{\text{int}})$ calculation is done by matching the power density integrated across the whole spectrum with that measured with a thermopile placed at the output of the light pipe (as in Figure 3.15 (b)) instead of the contraption for measuring the spectrum (as in Figure 3.15 (a)). Figure 3.16 (b) shows the product $A(t_{\text{int}})k(\lambda)$ resulting from the calibration. In principle, this calibration must be performed only once. Afterward, when a spectrum is measured with the contraption, we obtain the $\text{CCD}_{\text{cts}}^{t_{\text{int}}}(\lambda)$ spectrum (Figure 3.16 (a)). By applying Equation 3.4 with the calibration curve, we can get the measured spectra in terms of irradiance ($E_{\text{out}}(\lambda)$), as in Figure 3.16 (c).

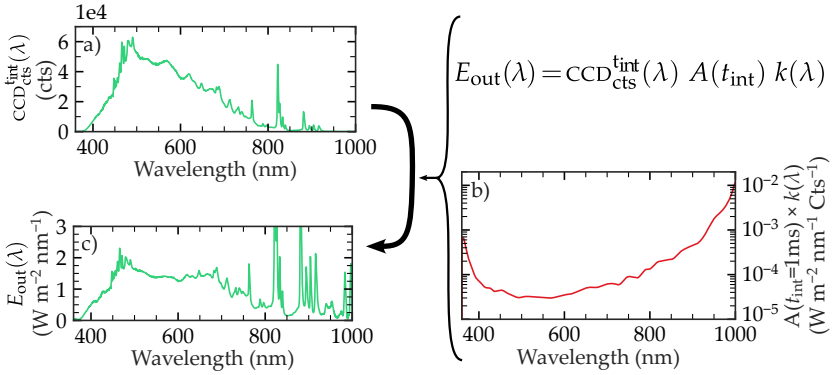

Figure 3.16: Workflow diagram for the measurement of a SOLS spectrum. In the first instance, a CCD cts. vs. wavelength spectrum is acquired (a). Using Equation 3.4 and the calibrated $A(t_{\text{int}})k(\lambda)$ (b), the acquired spectrum is converted to irradiance vs. wavelength (c).

3.3.2 *Spectral match*

To assess the spectral match, we designed a 3D-printed masking card with the AM1.5G standard as target spectrum. Figure 3.8 (a) shows the target AM1.5G spectrum and the output spectrum of the SOLS achieved with the 3D-printed mask (Figure 3.9 (A)). The first row of Table 3.2 shows the classification according to the ASTM standards. The results indicate that the SOLS achieves a Class A between 400 and 1000 nm.

	400-500 nm	500-600 nm	600-700 nm	700-800 nm	800-900 nm	900-1000 nm
Spectrum A 1 Sun AM1.5G	Class A (-10.06 %)	Class A (-4.80 %)	Class A (1.80 %)	Class A (-21.16 %)	Class A (6.78 %)	Class A (-2.71 %)
Spectrum B 0.5 Sun AM1.5	Class A (-2.51 %)	Class A (3.65 %)	Class A (8.67 %)	Class A (-22.45 %)	Class A (-1.4 %)	Class A (-12.26 %)
Spectrum C Cell transmission	Class A (-0.51 %)	Class A (1.49 %)	Class C (52.12 %)	Class C (-44.38 %)	Class B (-25.34 %)	Class B (-32.65 %)
Spectrum D Flat spectrum	Class A (8.04 %)	Class A (4.93 %)	Class B (28.85 %)	*	*	*

Table 3.2: Classification following the ASTM E927-10 standards of the four spectra shown in Figure 3.8. * Corresponds to spectra data which cannot be evaluated with the standards since the target spectra irradiance is 0, therefore the percentage difference cannot be calculated.

3.3.3 *Spatial non-uniformity*

For the measurement of the spatial non-uniformity (SNU), we mounted a 500 μm in diameter pinhole at the entrance of the spectra measuring contraption. This pinhole collects only a small part of the light that exits the homogenizing light pipe.The spectra was measured in front of the homogenizing light pipe in a grid of 10 by 9 pixels, every pixel of 1×1 mm^2 in size. Because the output light spreads relatively fast, this measurement is very sensitive to the distance between the light pipe and the pinhole. Additionally, the small dimensions of the output light made it difficult to ensure parallelity between the light pipe output facet and the mesh measurement plane. As a result, the measurement had a gradient offset. The latter was corrected by fitting the data to an offset plane, which corrects for the non-parallelity between the light pipe output facet and the mesh measurement plane. Additionally, the scaling factor $A(t_{\text{int}})$ was corrected by the relation between the measuring area with and without the pinhole.

SNU of a certain area is calculated considering the pixels with the maximum and minimum power values (P_{max} and P_{min}, respectively), and following:

$$\mathrm{SNU}(\%) = 100\,\frac{P_{\max} - P_{\min}}{P_{\max} + P_{\min}} \tag{3.5}$$

The resulting spatial power density distribution, Figure 3.17 (a), shows that the spatial non-uniformity is 4.16% in a large area over the central part enclosed by the yellow dashed line. It corresponds to a Class B spatial non-uniformity according to ASTM standards. Nevertheless, if we consider a lower area, such as the one enclosed by the green dashed line, the non-uniformity can be reduced to 1.56%, achieving a region with Class A spatial non-uniformity. Figure 3.17 (b) shows the spectra from 3 different pixels, highlighted with solid lines in Figure 3.17 (a), to show that the spectral shape over the whole output plane is consistent. The former indicates that the small changes in the integrated power of Figure 3.17 (a) are mainly related to a change in the intensity of the spectrum rather than a change in its shape.

The same procedure was carried out without the initial diffuser to understand the diffuser's role in homogenizing the light output. It is

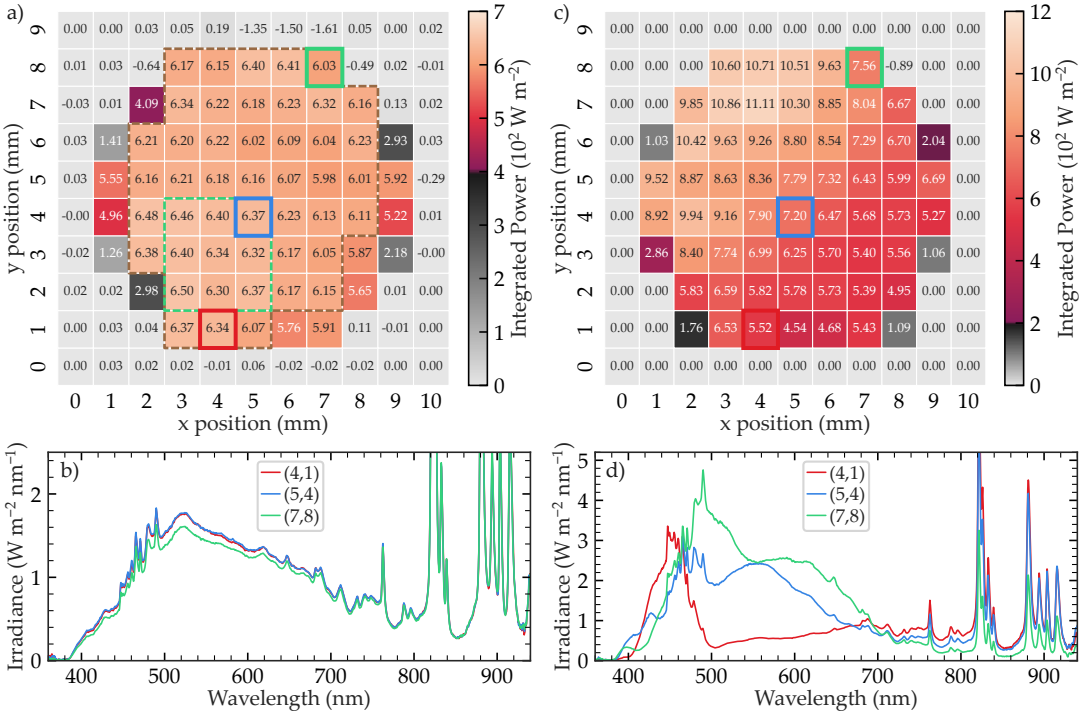

Figure 3.17: Spatial non-homogeneity classification. (a) Spatial distribution of SOLS output light plane with a 1 mm by 1 mm pixel grid. The dashed brown line encloses a large Class B region with 4.16% spatial non-uniformity, while the green dashed region has a 1.56% spatial non-uniformity corresponding to a Class A. The green, blue, and red solid squares highligth the pixels whose spectrum is shown in (b). (c) and (d) correspond to the same measurement and analysis performed respectively in (a) and (b) but without the diffuser element before the homogenizing light pipe. The lack of diffuser drastically affects the non-homogeneity of the output light.

worth mentioning that the difference is obvious to the eye, making the output much more homogeneous when using the diffuser. Additionally, the measurements showed higher intensity, indicating null losses due to scattered light before the homogenizing light pipe. The results of this experiment are shown in Figure 3.17 (c). In this case, the spatial distribution is less homogeneous than the case with the diffuser (Figure 3.17 (a) and (b)). The differences are especially notorious when considering the spectra in different pixels, as shown in Figure 3.17 (d). The different pixels show completely different spectral shapes when the diffuser is not used. Conversely (when the diffuser is used), spectral shapes are very similar. Finally, the spatial inhomogeneity classification is poorer than Class C for most of the area. Thus, the need for the diffuser is justified and mandatory when comparing the spatial distribution of the output light with (Figure 3.17 (a) and (b)) and without (Figure 3.17 (c) and (d)) the diffuser. Although it comes at the expense of light intensity.

The diffuser which was taken out for this measurement is the one corresponding to the homogenizing apparatus shown in Figure 3.14

3.3.4 *Temporal instability*

We expect the temporal instability of the setup to be defined by the temporal stability of the input light source since none of the SOLS parts is moving while a fixed spectrum is given at the output of the equipment. To verify this hypothesis, we have measured the temporal instability of the light entering the SOLS as well as its output light. To do that, the light power time dependence was measured with a silicon photodetector, and Equation 3.6 was used to calculate the temporal instability. While JIS C and IEC standards differentiate between short-term and long-term temporal instability (STI and LTI respectively), ASTM standards do not. Nevertheless, it is useful to differentiate between short-term and long-term instability. In this case, we will be considering the measurement of *I-V* curves, which takes around 5 seconds. In that case, STI is understood as the temporal instability between data points in the same *J-V* curve. For STI, data was acquired every 10 ms for a total of 5 seconds. Analogously, LTI represents the temporal instability between different *J-V* curve measurements. In that case, LTI data was acquired every 1 second for 50 seconds. Analogous to spatial non-uniformity, STI or LTI are calculated taking into account the maximum and the minimum power measured for each data set (P_{max} and P_{min}, respectively) and following:

$$\text{STI or LTI}(\%) = 100\,\frac{P_{max} - P_{min}}{P_{max} + P_{min}} \tag{3.6}$$

The results in Table 3.3 show that both input and output STI averages are statistically the same value, while in the case of LTI, average

values are statistically different, with the LTI of the output the smaller value. These observations indicate that the SOLS setup does not introduce temporal instability to the light source used, a xenon-arc lamp, confirming the starting hypothesis. We can also deduce from the results that with the light source employed in this embodiment, the temporal stability is Class A according to ASTM standards since STI and LTI are significantly lower than 2%.

Measurement	STI (%)		LTI (%)	
	Input	Output	Input	Output
1	0.73	0.88	0.30	0.22
2	0.88	0.81	0.38	0.20
3	0.69	0.62	0.28	0.27
4	0.80	0.56	0.31	0.24
5	0.78	0.88	0.39	0.21
Average	0.78 ± 0.07	0.75 ± 0.15	0.33 ± 0.05	0.23± 0.03

Table 3.3: Short-term instability (STI) and long-term instability (LTI) of the input and output light of the SOLS. 5 measurements were done for each situation and the average and standard deviation are shown in the last row.

3.4 LIMITATIONS, CONCLUSIONS, AND OUTLOOK

3.4.1 *Spectral resolution*

The main advantage of SOLS with respect to other light sources is the spectrum customizability. This is strongly linked to the wavelength resolution, and thus to the wavelength distribution/separation along the masking plane wherein the filtering systems act. To distinguish between two wavelengths, their intensity distributions in that plane need to be sufficiently separated in the lateral (wavelength) direction. This is directly related to the way the dispersive element, the double Amici prism, separates the light.[189] In any refractive optical element, the separation between two adjacent wavelengths is determined by the difference in the deviation angles for the two wavelengths and the distance they travel. The former is governed by the wavelength variation of the refractive index (a.k.a. dispersion) of the two materials composing the double Amici prism. In the visible spectral range, and as a rule of thumb for any glass combination, this angle is higher for shorter wavelengths. Therefore, the wavelength resolution of the SOLS setup is higher in the blue than in the red part of the spectrum. The wavelength resolution or color separation can also be improved

by increasing the distance between the prism and the mirror at the expense of increased equipment size.

Moreover, other factors directly impact the resolution, namely the degree of collimation (how paraxial the incident beam is) and the lateral extension (width) of the beam at the entrance of the double Amici prism. Ideally, if the input light is perfectly collimated and enters the prism only in an infinitesimally thick vertical line, every photon with the same wavelength would have the same optical path through the prism, exiting throughout the same point and with the same angle. Thus, one would expect an infinitesimally narrow Gaussian peak for each wavelength, perfectly separated from the others. A departure from this ideal situation corresponds, for example, when light, though collimated, enters through a finite thickness slit. The resulting distribution is expected to be a sum of various Gaussian functions corresponding to each infinitesimal slit inside the slit width. In that situation, the different wavelengths overlap at a given position in space. In that case, wavelength resolution improves moving further from the prism. However, we have found that the effect of a poor collimation of the beam is still more critical. For example, if one focuses the beam at the entrance of the double Amici prism, there would be a distribution of incoming angles for photons with the same wavelength, and therefore, even if they enter the double Amici prism from exactly the same point, they would escape the prism with different angles. Therefore, one expects a broadening effect of the Gaussian distribution and a certain degree of color mixing. In that case, the wavelength resolution does not necessarily improve far from the prism. Both effects are detrimental to the spectral resolution and are mainly dependent on the input light beam: the thinner and the more collimated it is, the better the color separation at the plane of the mask systems, thus improving the wavelength resolution. Nevertheless, the latter comes at the expense of light intensity.

As usual, there is a tradeoff between spectral resolution and the throughput of the SOLS setup. It is clear that if the primary light source is not properly collimated, whatever the optics used for its collimation, there will be a certain penalty in light intensity, which is even higher when a slit is placed in front of the prism. The latter can also be observed in Figure 3.18, wherein the spectra from (b) and (c) were scaled 5 and 10 times, respectively.

The mentioned dependence in spectral resolution is best observed in the cascades of slit spectra as shown in Figure 3.18. The Figure displays the spectra resulting from consecutive 2 mm slits masks when the light enters the double Amici prism directly from the Xenon arc lamp (a),

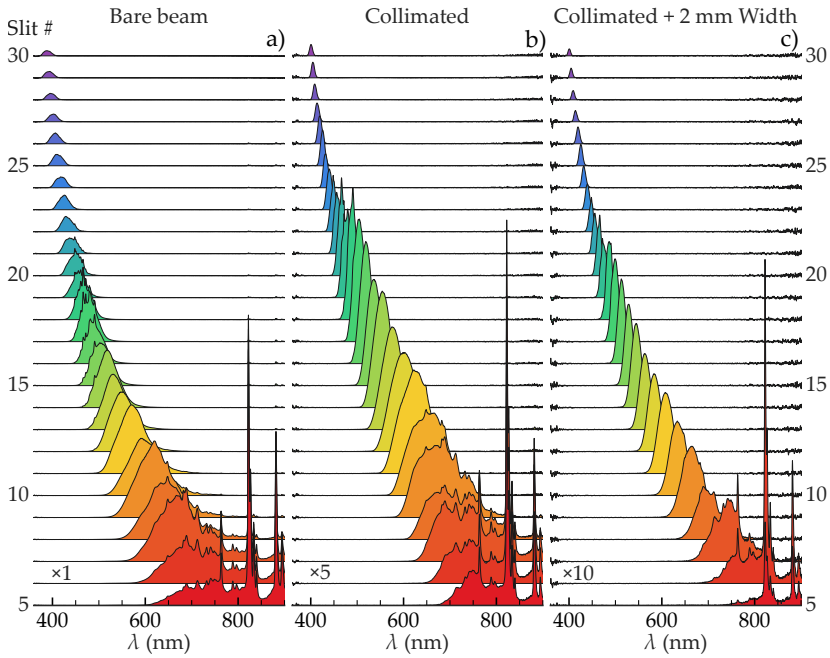

Figure 3.18: Effect of input light collimation and width reduction to wavelength resolution. Series of spectra corresponding to vertical slits used in Section 3.2.2 for different treatment of the light entering the double Amici prism: (a) bare beam, (b) collimated beam, and (c) collimated and laterally-reduced beam width. Spectra from (b) and (c) is amplified by 5 and 10 times, respectively, with respect to spectra shown in (a) for clarity porpoises.

when it is collimated in between (b), and when apart from collimated it is also width reduced with a 2 mm width slit at the entrance of the double Amici prism (c). The data clearly shows that the resulting measured spectra are much narrower when collimation and width-reduction are implemented to the light entering the prism, showing a better wavelength resolution for the same slit width.

The Split-Gussian is a Gaussian that has a different HWHM at each side of the central wavelength.

Each spectrum of Figure 3.18 was normalized and fitted to a Split-Gaussian function. In this case, due to the observed non-symmetry of the slits spectra, we obtained a better fit with a Split-Gaussian. Figure 3.19 shows the values of the fitted HWHM Split-Gaussian as a function of the central wavelength from spectra shown in Figure 3.18. Figure 3.19 demonstrates that collimating and width-reducing the light beam before the double Amici prism (green data points) improves up to 5 times the spectral resolution compared with the bare beam case (red data points), where light does not receive any treatment prior to being separated by the prism. When light is only collimated (blue data points), the spectral resolution is in between the other cases, being similar to

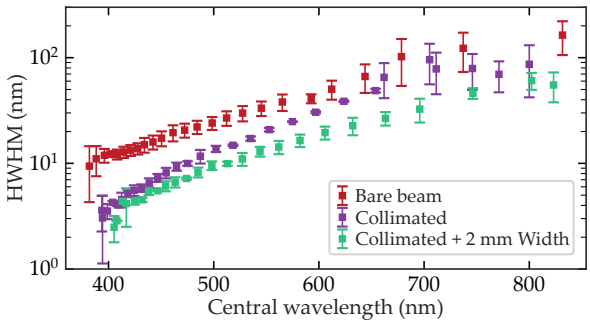

Figure 3.19: Half width at half maximum (HWHM) as a function of the central wavelength for the slit spectra shown in Figure 3.18. The normalized slit spectra were fitted using a Split-Gaussian curve. The figure data squares shows the average of the two HWHM fitted values (which are shown as errorbars) as a function of the central wavelength for the three different light treatments.

the bare beam at the infrared region and similar to the collimated and width-reduced beam for the low wavelength region. This means that reducing the width is particularly effective at long wavelengths while collimation improves the resolution at short wavelengths.

3.4.2 *External Quantum Efficiency*

One of the capabilities of the SOLS setup, as mentioned in Section 3.1, is to measure the photovoltaic external quantum efficiency (EQE_{PV}). This functionality still needs improvement in terms of automatization, better analysis tools, and improved wavelength resolution in the infrared region in order to become a feature of a future SOLS prototype. Nevertheless, this subsection shows the potential of SOLS for measuring EQE_{PV} with different methodologies. EQE_{PV} is a common and useful characterization in photovoltaics that quantifies the spectral contribution to the short-circuit current density J_{sc}.[7] Mathematically, EQE_{PV} is related to J_{sc} as follows:

$$J_{sc} = \int \frac{\varphi(\lambda)}{\varepsilon_{ph}(\lambda)} EQE_{PV}(\lambda)\, q\, d\lambda \tag{3.7}$$

Here, $\varphi(\lambda)$ is the spectral irradiance (in units of energy/second/area), $\varepsilon_{ph}(\lambda)$ is the photon energy, and q is the electron charge. By dividing $\varphi(\lambda)$ by $\varepsilon_{ph}(\lambda)$ we obtain the number of photo-generated electrons per unit time and area, which multiplied by the EQE_{PV}, the charge of an electron, and integrated over the entire spectrum yields the current density J_{sc}. The standard EQE_{PV} characterization involves the measurement of the photocurrent under narrow-band monochromatic wavelength illumination, typically in short-circuit conditions ($J_{sc,\,\lambda}$), for

different central wavelengths in the range between 350 and 1100 nm.[7] Narrow-band illumination is typically obtained by spectrally filtering a broad-band source, for example using a monochromator. In that direction, the EQE_{PV} can be calculated for each narrow-band illumination condition as follows:

$$EQE_{PV}(\lambda) = \frac{\frac{J_{sc,\,\lambda}}{q}}{\frac{P_{in}}{\varepsilon_{ph}}} \tag{3.8}$$

where P_{in} is the power of the monochromic light reaching the device. Equation 3.8 corresponds to the ratio between the number of collected electrons and the number of incoming photons at a given wavelength. The narrower the light source, i.e. the more monochromatic it is, the better the resolution of the EQE_{PV}. Notice that SOLS also includes a slit system, comprising a set of complementary slits masks of 2 mm each centered at different wavelengths (see Figure 3.5 and Figure 3.18), with which SOLS transforms into a narrow-band tunable light source. In this case, the power density of the spectrum resulting from each slit (P_{in}) is measured with the thermopile (Figure 3.15 (b)) or by integrating the slit spectrum, and the wavelength is given by the central wavelength of each slit spectrum. Figure 3.20 shows EQE_{PV} measurements made with the slit system of SOLS (slits-EQE_{PV} measruements) compared to those attained with our custom made EQE_{PV} rig, which includes a broad-band laser and a monochromator (blue curves). The results were obtained for OPVs with different E_{bg}. When light is collimated before entering the double Amici prism (purple data crosses in Figure 3.20), the slits-EQE_{PV} resolution is similar to that of the reference system

The tunable narrow-band source can also be achieved automatically with the synchronous movement of the motorized guillotines.

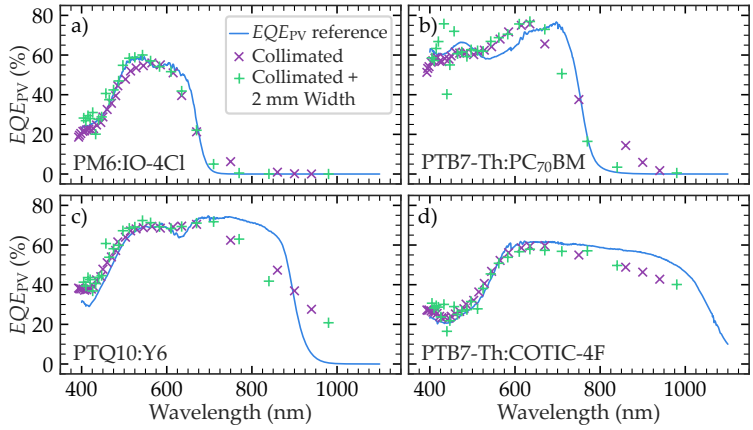

Figure 3.20: Slits-EQE_{PV} measurements with different input light treatments. Slit-EQE_{PV} measurements with SOLS for collimated input light and collimated with lateral width reduced (purple and green data crosses, respectively) compared with results obtained with a standard white laser coupled to a monochromator (purple solid line).

in the spectral range between 400 and 600 nm approximately. For longer wavelengths, though, the wavelength resolution decreases drastically resulting in a broadening effect of the slits-EQE_{PV}. This can be improved by enhancing the wavelength resolution, for example, by collimating the input light of the double Amici prism and reducing its lateral size (green data in Figure 3.20). Although wavelength resolution can still be improved in the infrared, in our current implementation the agreement between the slits-EQE_{PV} curves and those of the custom-made rig is excellent.

See Section 3.4.1 for more details on spectral resolution of the SOLS

Interestingly, EQE_{PV} can also be extracted from a red or a blue sweep measurement using the motorized guillotines (like Figure 3.11). In this characterization mode, we can consider that the difference between measurements for two consecutive dividing wavelengths, λ_d, is analogous to a narrow-band measurement using a slit with a width equal to the spatial difference between the positions of the guillotine during the red or the blue sweep. The measurement proceeds as follows: first either a red or blue sweep is performed and the $J-V$ characteristics of the cell are recorded as a function of λ_d. From this set of data, one computes the solar cell figures of merit J_{sc}, V_{oc}, FF, and PCE as a function of λ_d. In analogy to a slit spectrum, $J_{sc,\,\lambda}$ of Equation 3.8 is computed by taking the difference of the J_{sc} obtained for two consecutive λ_d. The corresponding (pseudo-slit) power density P_{in} is then obtained from a previous calibration of the incident spectrum, which consists of separately measuring the spectrum and the power density at each λ_d. This calibration is equipment-dependent and thus only needs to be performed once, saving valuable measurement time. Hereafter, the sweep-EQE_{PV} is computed using Equation 3.8, as in the

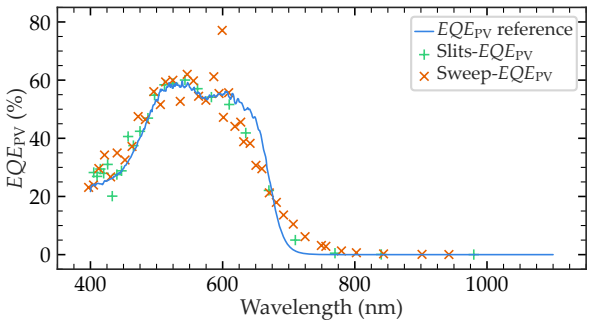

Figure 3.21: Sweep-EQE_{PV} measurement of a PM6:IO-4Cl solar cell. Sweep-EQE_{PV} of a PM6:IO4-Cl cell (same cell as Figure 3.20 (a)) calculated from a red sweep of a RAINBOW measurement (orange data crosses). The agreement with the reference EQE_{PV} measured with a white laser and a monochromator (blue curve) is very good, as well as with the slit-EQE_{PV} measurement with collimated and slit-reduced width (green data crosses).

Notice that, as far as we know, this methodology of measuring EQE_{PV} from a red (or a blue) sweep is a unique capability of the SOLS setup.

case of slits-EQE_{PV}. As can be appreciated in Figure 3.21, the agreement between the sweep-EQE_{PV} obtained with the red sweep procedure and the more conventional monochromator-like mode with the slits system (slits-EQE_{PV}) is very good. The sweep-EQE_{PV} could also be obtained from a blue-sweep measurement since the pseudo-slit resulting from both sweeps is analogous.

3.4.3 *Conclusions and outlook*

In summary, we presented a novel spectral shaper illumination device with facile tunability, which can be used to perform standard photovoltaic tests like efficiency and EQE_{PV} with the same equipment, thus helping to accelerate material screening. This enables the discovery and optimization of novel multi-component materials for emergent PV technologies like organic PV, metal halide perovskites PV, all oxides PV, or kesterites. The same equipment can also be used as a light source for more advanced characterizations requiring intensity-dependent PV characterization, which is the case for the study of recombination processes in photovoltaics. The SOLS also enables the development of many photovoltaic applications far from the standard sunlight harvesting, including agrivoltaics, indoor PV, building integrated PV (windows, sunshades, etc.), semitransparent PV, etc.

One particularly attractive novel application of the SOLS light source is in the field of materials science for the development of multi-junction solar cells, both spectrally split as well as conventional tandem cells, aimed at highly efficient light-to-electricity conversion. This is the application for which the SOLS was initially intended. To the best of our knowledge, there is no other light source capable of addressing the full characterization (multi-junction and single sub-cell characterization) of multi-junction solar cells. In view of the fact that tandem and spectrally split solar cells can increase power conversion efficiency by up to two to three times more than that of single-junction cells, this is a very promising implementation area of the SOLS system.[107, 131, 176, 177]

The combination of intensity and spectral tailoring capabilities offered by SOLS leads to novel characterization methodologies that could help to better understand charge generation and loss mechanisms inside solar cells, especially in the case of OPV, where at least two materials (donor and acceptor) are involved in the dynamics of the charge-generation process.

Technology readiness levels (TRLs) are a method for estimating the maturity of a technology from basic research to commercialization.

We now consider SOLS to be at TRL4 since we have proved all its capabilities in the lab. Nevertheless, we still need to improve some important aspects to develop a product to transfer to the industry. One of them is the automatization. Currently, custom spectra done with the 3D-printed masks are far from automatic. To automatize the spectra tunability, we need to implement some masking elements that can change fast and in a controlled way. One alternative is the use of liquid crystal displays (LCD). Nevertheless, the transmission of LCDs is typically poor (around 20% in the best scenario) and, therefore, would limit the equipment's intensity. Another option is the use of a digital micro-mirror display (DMD). The spatial resolution of DMD arrays is more than enough for our application (around 10×10 μm^2). Nevertheless, they are much smaller than the spectrally split beam, and their implementation requires optimizing the dispersive element.

The wavelength resolution is also an essential part of the equipment, and it may need improvement to find a niche in the market. The enormous impact of the input light's characteristics on the wavelength resolution is a bottleneck for the equipment. It implies the equipment's need for a specific light source, increasing its price. Nevertheless, we are working on these improvements. If we can find a solution for them, the commercialization of SOLS can help discover new materials and geometries in the PV field.

4 RAINBOW SOLAR CELLS

While multi-junction geometries have the potential to boost the efficiency of organic solar cells, the experimental gains yet obtained are still very modest. In this chapter, we explore an alternative spectral splitting device concept in which various individual semiconducting junctions with cascading band gaps are laid side by side, thus the name RAINBOW. Each lateral sub-cell receives a fraction of the spectrum that closely matches the main absorption band of the given semiconductor. We first show the developed toolkit for the investigation of RAINBOW solar cells. Using the active layer blends PTB7-Th:COTIC-4F, PM6:Y6, and PM6:IO-4Cl as examples we show the agreement between a simple simulation model and two different characterization setups, the SOLS (described in Chapter 3) and a commercial LEDs solar simulator. With these examples we show that this geometry can lead to a reduction in thermalization losses and an improvement in light harvesting, which results in a relative improvement in efficiency of 46.6% with respect to the best sub-cell. Two proof of concept monolithic devices consisting of two sub-cells deposited from solution on the same substrate are fabricated, thus demonstrating the feasibility and the potential of the RAINBOW solar cell concept. The effect of active layer thickness on RAINBOW efficiency is discussed and studied for the most efficient RAINBOW combination.

4.1 THE RAINBOW CONCEPT

The RAINBOW solar cell concept consists of two main parts: a light-dispersive element and a horizontal multi-junction array. The first, located above the multi-junction solar cell, spatially redistributes the solar spectrum into all its composing wavelengths. This combination results in a rainbow of colors, as shown in Figure 4.1, where each sub-cell is illuminated with the optimal wavelength range. The main advantage of the RAINBOW configuration relies on its ability to reduce both thermalization and absorption losses while avoiding the limitations of vertical stack manufacturing, such as defect accumulation and optical transparency loss,[127, 131, 197] and the awkward form factor of other beam splitting geometries,[107, 108] thanks to its planar lateral deposition configuration. While the RAINBOW geometry is not as simple as a single-junction device, in this novel configuration one can increase the number of sub-cells from two to N junctions without

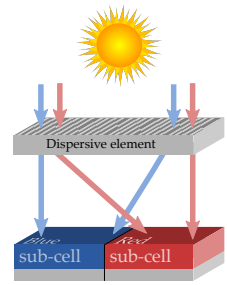

Figure 4.1: Schematics of RAINBOW geometry configuration.

changing the form factor. Nevertheless, Peters et al., have already shown that the optimal number of junctions may be below ten juntcions.[131]

The SOLS setup, shown in Chapter 3, can potentially be the light-dispersive part of a RAINBOW solar cell configuration. Nevertheless, while it can be used for characterization, it is not optimal for this application. This is because an optical element with a big light input area is needed. Additionally, the double Amici prism is too big and heavy, and does not have a high enough dispersion. Thus, one needs to consider other options for the light-dispersive optical element. The latter is not in the scope of this thesis, however, such elements have been previously reported, with multiple solutions available. For example, the dispersive lens proposed by Thio et al.,[198] the holographic solution proposed by Vorndran et al.,[199] or the the diffractive optical element proposed by Lin et al.[200] These solutions take advantage of a combination of diffraction and refraction of light to physically separate different fractions of the spectrum. The latter is not only applicable to RAINBOW solar cells but also to silicon photovoltaics for avoiding overheating of the modules due to IR radiation.[107, 201, 202]

This thesis focuses on the optimization of the horizontal multi-junction array throughout the choice of materials and the fabrication conditions of each sub-cell as well as the optimization of the spectral split light. We want to point out that the device used to achieve a certain spectral split light is not in the scope of this thesis.

4.2 TOOLKIT FOR RAINBOW OPTIMIZATION

4.2.1 *RAINBOW simulation model*

One of the objectives of the thesis is to develop tools to facilitate the development of RAINBOW multi-junction geometries. For this reason, we first developed a simulation model to predict the RAINBOW performance considering the more important parameters:

DIVIDING WAVELENGTH In the simplest scenario, a RAINBOW configuration consists of two sub-cells. Thus, the optical splitting element divides the solar spectrum into two fractions: a "blue fraction" containing the shorter wavelengths, and a "red fraction" containing the longer wavelengths. These spectral fractions are redirected to each of the two sub-cells, which are consequently named "blue sub-cell" and "red sub-cell", respectively (see Figure 4.2). The performance of the RAINBOW device greatly depends on how the solar spectrum is divided. The wavelength at which the spectrum is divided is named

"dividing wavelength" (λ_d). The latter defines the fraction of the spectrum that each sub-cell receives. Therefore, λ_d is one of the most important parameters to consider for the optimization of RAINBOW solar cells.

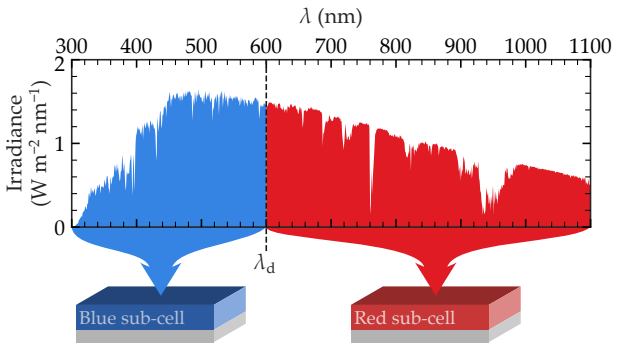

Figure 4.2: Graphical definition of dividing wavelength for a 2-J RAINBOW solar cell. The solar spectrum is divided into two halves at a wavelength equal to the dividing wavelength, λ_d. The blue fraction of the spectrum, comprising the high-energy photons, is redirected to the blue sub-cell, while the red fraction, comprising the low-energy photons, is redirected to the red sub-cell.

EXTERNAL QUANTUM EFFICCIENCY The materials used in each sub-cell are also one of the key parameters. Their spectral photon-electron conversion response (i.e., the photovoltaic external quantum efficiency (EQE_{PV})) is key for the choice of materials. EQE_{PV} is a parameter that summarizes many processes happening in the solar cell, such as photon absorption, exciton dissociation, or free-charge conductivity to the contacts. Among all of them, the most relevant for the RAINBOW configuration is the photon absorption since it defines at which spectral region the EQE_{PV} will have its maximum. The choice of materials with certain EQE_{PV} spectra is key to reduce absorption losses.

$J-V$ CHARACTERISTICS Finally, the FoM derived from the $J-V$ curve are key to predicting the RAINBOW efficiency. The V_{oc} is crucial because it is directly linked to the energy of the extracted electrons from each sub-cell and, subsequently, to the thermalization losses at the different sub-cells. The FF is important to reach high efficiencies. It depends on active layer thickness and light intensity, which is important to consider when fine-tuning the RAINBOW device. Finally, J_{sc} considers the number of extracted electrons and, consequently, is directly related to λ_d and EQE_{PV}.

4.2.1.1 *Description of the simulation model*

The simulation model focuses on the solar cells and their composing materials assuming, to start with, lossless light redistribution of the spectral splitting optical element, and lossless DC-DC conversion of the electronic component converting the multiple-terminal device into a two-terminal solar cell. We are aware that those two assumptions may be far from reality. The spectral splitting element always has a certain white background (unsplit background light) and the spectral division may not be as sharp as desired. Furthermore, it is important to note that DC-DC converters consume power.

With these conditions, the RAINBOW efficiency (PCE_R) is calculated as the sum of the output electric power density of each sub-cell ($P_{out,\ cell}$) divided by the input power density of the AM1.5G spectrum (P_{in} = 1000 W m^{-2}). The lattter can be interpreted as a sum of the partial contribution of each sub-cell ($PCE_{p,cell}$) to the PCE_R as described by Equation 4.1. Notice that, in this case, $PCE_{p,cell}$ is different from the power conversion efficiency of each sub-cell ($PCE_{p,cell} \neq PCE_{cell}$) since the input power density considered corresponds to that within the

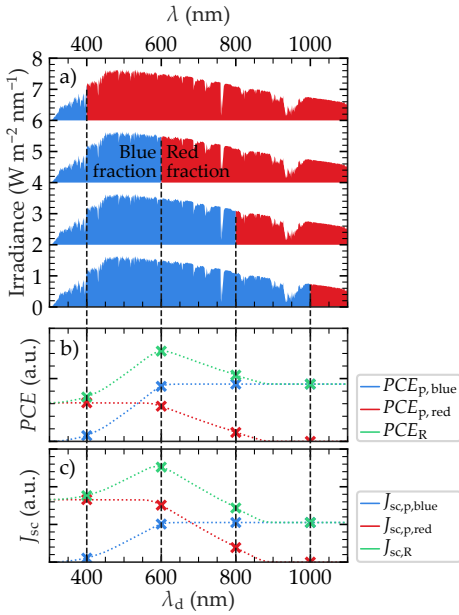

Figure 4.3: Concept of the RAINBOW simulations. Example of spectral distribution to the blue and red sub-cells for four different dividing wavelengths (λ_d = 400, 600, 800, and 1000 nm) (a). The $PCE_{p,blue}$ and $PCE_{p,red}$ as well as $J_{sc,p,blue}$ and $J_{sc,p,red}$ corresponding to each λ_d are marked with crosses in (b) and (c), respectively. PCE_R and $J_{sc,R}$ are also marked with green crosses. The full λ_d dependence is shown as dashed lines for both sub-cells and the RAINBOW combination.

RAINBOW device and not to the power density each sub-cell recieves. We use the total power instead of the incident power because we are interested in the final multi-juntion efficiency and not in the efficiency of each sub-cell under a truncated solar spectrum, which would tend to be higher, as it is the case for indoor photovoltaics.

$$PCE_{\mathrm{R}} = \frac{\sum P_{\mathrm{out,\,i}}}{P_{\mathrm{in}}} = \sum \frac{P_{\mathrm{out,\,i}}}{P_{\mathrm{in}}} = \sum PCE_{\mathrm{p,\,i}} \tag{4.1}$$

In the simplest 2-J RAINBOW solar cell scenario with red and blue sub-cells, Equation 4.1 can be rewritten as:

$$\begin{aligned} PCE_{\mathrm{R}} &= \frac{P_{\mathrm{out,\,red}} + P_{\mathrm{out,\,blue}}}{P_{\mathrm{in}}} \\ &= \frac{P_{\mathrm{out,\,red}}}{P_{\mathrm{in}}} + \frac{P_{\mathrm{out,\,blue}}}{P_{\mathrm{in}}} \\ &= PCE_{\mathrm{p,\,red}} + PCE_{\mathrm{p,\,blue}} \end{aligned} \tag{4.2}$$

$P_{\mathrm{out,\,cell}}$ is calculated as the multiplication betwen V_{oc}, J_{sc}, and FF of each sub-cell. Theoretically, all three parameters will depend on the spectrum that each sub-cell receives (φ_{cell}). Nevertheless, the model considers that the only parameter that depends on φ_{cell} is the J_{sc}. The model considers that the other parameters (V_{oc} and FF) are equal to the values measured under 1-Sun illumination. This assumption will be evaluated later on in the chapter when looking at the actual measurements.

$$P_{\mathrm{out,\,cell}} = J_{\mathrm{sc}}(\varphi_{\mathrm{cell}}) \cdot V_{\mathrm{oc,\,AM1.5G}} \cdot FF_{\mathrm{AM1.5G}} \tag{4.3}$$

$J_{\mathrm{sc}}(\varphi_{\mathrm{cell}})$ is calculated following:

$$J_{\mathrm{sc}}(\varphi_{\mathrm{cell}}) = \mathrm{A} \int_0^{\infty} \frac{\varphi_{\mathrm{cell}}(\lambda)}{\varepsilon_{\mathrm{ph}}(\lambda)}\, EQE_{\mathrm{PV}}(\lambda)\; q\; d\lambda \tag{4.4}$$

$\varepsilon_{\mathrm{ph}}(\lambda)$ is the energy of a photon, and $\varphi_{\mathrm{cell}}(\lambda)$ is the spectrum that the sub-cell receives from a certain spectral splitting configuration. A is a normalization factor used to match the measured and calculated J_{sc} at 1-Sun ($A = J_{\mathrm{sc}}^{\mathrm{measured}} / J_{\mathrm{sc}}(\varphi_{\mathrm{AM1.5G}})$). As happens for the moving guillotines of the SOLS (see Section 3.2.3), one can express φ_{cell} as the product between the full spectrum ($\varphi_{\mathrm{AM1.5G}}$) and an edge function which depends on the dividing wavelength ($H(\lambda_{\mathrm{d}})$). In the simplest 2-J scenario:

$$\varphi_{\mathrm{red}}(\lambda) = \varphi_{\mathrm{AM1.5G}}(\lambda)\; H_{\mathrm{red}}(\lambda,\, \lambda_{\mathrm{d}}) \tag{4.5}$$

$$\varphi_{\mathrm{blue}}(\lambda) = \varphi_{\mathrm{AM1.5G}}(\lambda)\; H_{\mathrm{blue}}(\lambda,\, \lambda_{\mathrm{d}}) \tag{4.6}$$

where $H_{red}(\lambda,\ \lambda_d)$ and $H_{blue}(\lambda,\ \lambda_d)$ are the edge functions for the red and the blue sub-cells, respectively. The only requirement that H_{red} and H_{blue} have to satisfy is complementarity: the sum of both has to be equal to 1 for all wavelengths. In the simplest spectral division scenario (which is the case in all simulations of the thesis except otherwise specified) H_{red} and H_{blue} are sharp edge functions, defined as:

$$H_{red}(\lambda,\ \lambda_d) = \begin{cases} 0 & \text{if } \lambda < \lambda_d \\ 1 & \text{if } \lambda \geq \lambda_d \end{cases} \tag{4.7}$$

$$H_{blue}(\lambda,\ \lambda_d) = \begin{cases} 1 & \text{if } \lambda < \lambda_d \\ 0 & \text{if } \lambda \geq \lambda_d \end{cases} \tag{4.8}$$

With the presented mathematical expressions, we can calculate the RAINBOW efficiency as well as the partial contribution of each sub-cell for a certain λ_d. The next step is to study the RAINBOW efficiency as a function of the λ_d. The latter is done by repeating the simultion with λ_d values sweeping along the AM1.5G spectrum, tipically from 300 to 1100 nm. As a result, a simulation of a 2-J RAINBOW solar cell gives the PCE_R, the $PCE_{p,\ red}$, and the $PCE_{p,\ blue}$ as a function of λ_d (an example of the latter is shown in Figure 4.3). Additionally, we also get the λ_d dependence of J_{sc} for both sub-cells ($J_{sc,p,red}$ and $J_{sc,p,blue}$) which sum gives the RAINBOW short-circuit photocurrent ($J_{sc,R}$, as in Equation 4.9). The RAINBOW equivalent of V_{oc} and FF is not straightforward to define. A possible interpretation is given later in this chapter.

$$J_{sc,R} = J_{sc,red} + J_{sc,blue} \tag{4.9}$$

4.2.1.2 *RAINBOW figures of merit*

Figure 4.4 shows an example of a RAINBOW simulation wherein we can define three important figures of merit of the RAINBOW multi-junction configuration. The first one is the maximum RAINBOW efficiency ($PCE_{R,max}$) which corresponds to the maximum efficiency that the RAINBOW device achieves comparing all possible λ_d values. The latter corresponds to an optimized spectral distribution, defined by $\lambda_{d,opt}$ (Equation 4.10).

$$PCE_{R,max} = PCE_R(\lambda_d = \lambda_{d,opt}) \tag{4.10}$$

The last FoM to consider is the increase over the best cell (IoBC) which is defined as the percentual increase of the $PCE_{R,max}$ with respect to the best single junction (see Equation 4.11). With these three FoM,

we can compare the RAINBOW performance between different sub-cell materials in order to find material candidates suitable for the RAINBOW multi-junction geometry.

$$IoBC = \frac{PCE_{\mathrm{R,max}}(\lambda_{\mathrm{d}} = \lambda_{\mathrm{d,opt}}) - PCE_{\mathrm{AM1.5G,best\ sub-cell}}}{PCE_{\mathrm{AM1.5G,best\ sub-cell}}} \tag{4.11}$$

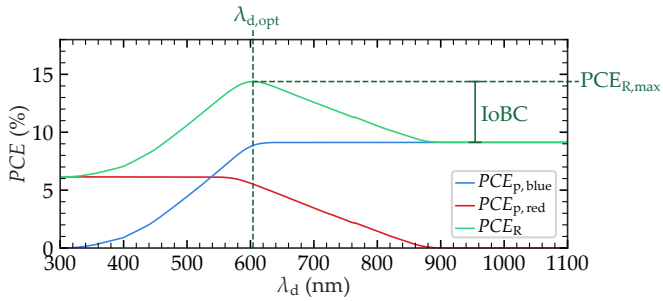

Figure 4.4: Graphical description of RAINBOW figures of merit. The three RAINBOW FoM are the maximum RAINBOW PCE ($PCE_{\mathrm{R,max}}$), the optimized dividing wavelength ($\lambda_{\mathrm{d,opt}}$), and the increase over the best cell (IoBC).

4.2.1.3 *Simulations with ideal EQE_{PV} curves*

To establish a basic set of guidelines for material combination selection in RAINBOW solar cells we first employed the simulation model to evaluate the performance of a series of sub-cell material combinations, with idealized top hat EQE_{PV} curves, sigmoid edges and varying widths and heights. The edge of the EQE_{PV} curves was used to calculate E_{bg}, from which the V_{oc} was obtained combining the Shockley-Queisser limit and a polynomial fit from the data published in reference[203]. The FF was assumed to be constant at 65% for all sub-cells. These $J-V$ parameters, along with the EQE_{PV} curves, were fed into the model to evaluate the RAINBOW performance of every possible ideal EQE_{PV} combination. In the following paragraphs, we discuss some of the most relevant simulation cases, which give us an intuitive sense of the parameters that ultimately determine RAINBOW performance and their relative contribution.

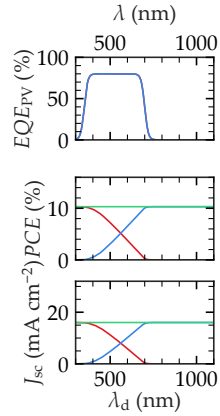

Figure 4.5: RAINBOW simulation with equal sub-cells. PCE_{R} is constant for all λ_{d} and the resulting IoBC is 0%.

To do so, we begin by the trivial case, where the red and blue sub-cells have exactly equal EQE_{PV} curves, both are effectively the same cell (Figure 4.5). In this case, as we shift the dividing wavelength, the combined efficiency stays constant, since the changes in the partial efficiencies of each sub-cell are perfectly complementary, resulting in a 0% IoBC. This result is perfectly logical, since, having the same E_{g} and equal EQE_{PV} curves, each sub-cell is competing for the same light.

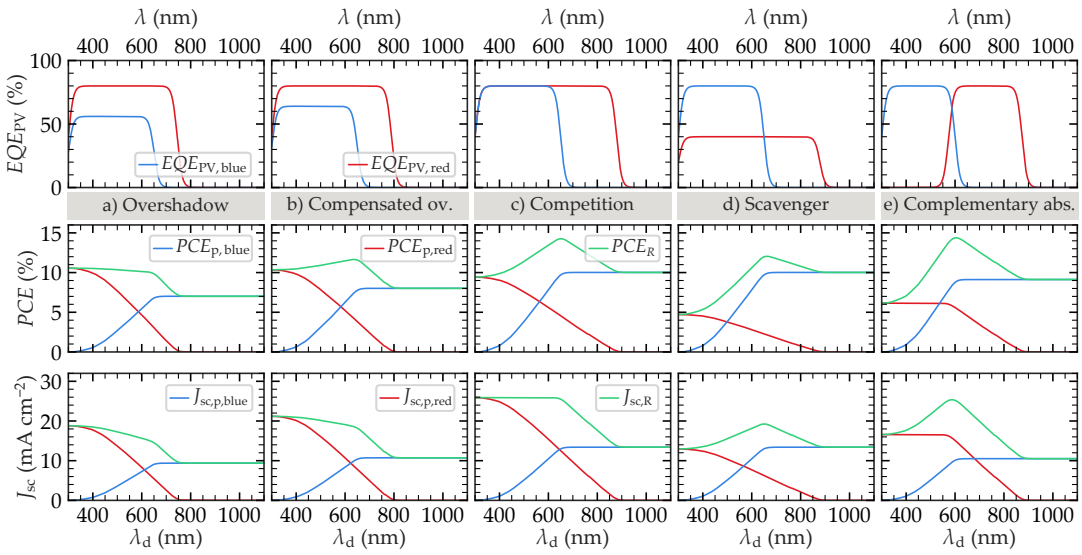

Figure 4.6: Relevant examples of RAINBOW simulations with top-hap EQE_{PV}. Simulation results are shown in columns (EQE_{PV}, PCE, and J_{sc} in top, middle, and bottom panels, respectively) for cases named overshadow (a), compensated overshadow (b), complementary competition (c), photon scavenger (d), and complementary absorption (e). The resulting increase over the best cell (IoBC) is 0%, 12%, 42%, 20%, and 58%, respectively; and the maximum RAINBOW efficiency ($PCE_{R,max}$) is 10.56%, 11.66%, 14.26%, 12.05%, and 14.38%, respectively.

As a result, they both absorb the same amount of photons in the same spectral range with equal thermalization losses, so there is no benefit in redistributing the light spectrum between the two.

Figure 4.6 (a) shows a RAINBOW combination where the red sub-cell completely outperforms the blue sub-cell. In this case, the combined efficiency never rises above the efficiency of the red sub-cell, resulting in a 0% IoBC. That is because the blue sub-cell's lower thermalization losses cannot compensate for its low EQE_{PV} values (i.e., low J_{sc}). As a result, any photon we take from the red sub-cell to illuminate the blue sub-cell will result in a lower combined efficiency. For this reason, we name this case "overshadow". A variant of the latter can be seen in Figure 4.6 (b), where EQE_{PV} of the red sub-cell is still overshadowing that of the blue sub-cell but because the EQE_{PV} of the latter is a little bit higher than in the previous case, the lower thermalization losses of the blue sub-cell are able to compensate for its lower EQE_{PV} values. As a result, the RAINBOW multi-junction exhibits a positive but moderate IoBC.

The third case, named "complementary competition" (Figure 4.6 (c)), is closer to the ideal combination, with both sub-cells having equal maximum EQE_{PV} values, but with a much wider absorption spectrum

for the red sub-cell, arising from a lower E_{bg}. In this scenario, the two sub-cells compete for light in the shorter wavelength range of the spectrum while complementing each other on the longer wavelength range. On the spectral region where they overlap, the blue sub-cell is able to convert light energy more efficiently, having lower thermalization losses and equal EQE_{PV} values. The red sub-cell will efficiently convert the lower energy fraction of the spectrum since the blue sub-cell cannot absorb those photons below its E_{bg}, resulting in one of the highest IoBC values.

In a variation of this case, named "photon scavenger" (Figure 4.6 (d)), the red sub-cell is set to have a lower maximum EQE_{PV} values compared to the blue sub-cell and a significantly lower E_{bg}. In this case, since the blue sub-cell cannot absorb photons below its E_{bg}, even if the red sub-cell has significantly lower EQE_{PV} values, the IoBC will always be greater than zero because the red sub-cell is "scavenging" the photons that the blue sub-cell cannot make use of.

Finally, the ideal case in terms of IoBC, named "complementary absorption" (Figure 4.6 (e)), is the one in which the EQE_{PV} of the red and blue sub-cells do not significantly overlap in any part of the spectrum. This case is similar to the complementary competition (Figure 4.6 (c)), but in this case there is no competition between the two sub-cells, resulting in a greater IoBC. We want to note that even though the IoBC is greater for this case, the maximum theoretical efficiency is equal for the two cases. However, achieving high absorption values along the entire spectrum is generally difficult, especially in OPV,[204] we considered this case relevant enough to treat it separately.

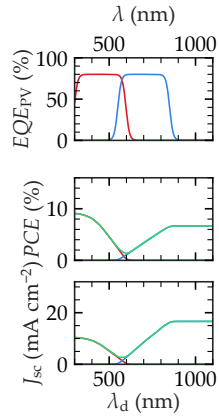

Figure 4.7: RAINBOW simulation of an inversed complementary absorption. The sub-cells are illuminated with the wrong spectral fraction, showing a decrease in PCE_R.

As a side curiosity, if we have a RAINBOW system with a positive IoBC and we shine the wrong fraction of the spectrum to each sub-cell, the resulting graph will look like the one in (Figure 4.7 (b)), where the combined efficiency goes below that of the lowest-performing cell. This is a clear indication that we have swapped the sub-cells order and that the system is a good RAINBOW combination.

In the examples shown here as ideal EQE_{PV} curves (i.e., lossless sub-cells with top hat-shaped EQE_{PV} curves) the optimal λ_d coincides with the E_{bg} of the blue sub-cell, as one may expect. Nonetheless, in real devices with spectrally irregular EQE_{PV} curves and different total voltage loss (ΔV_{oc}^{total}) values, the optimum light splitting should be determined case by case. This is the reason why simulations are done sweeping λ_d along the spectrum.

4.2.1.4 *Material selection criteria*

From the examples shown in Figure 4.6 and other simulations not shown here, we can identify the following guidelines for material selection in order to maximize PCE_R:

LOW V_{OC} LOSSES To reduce thermalization losses, each sub-cell needs to have inherently low voltage losses, ΔV_{oc}^{total}, particularly the blue sub-cells. Otherwise, even with higher band gaps, thermalization losses will not be reduced. This is similar to any other multi-junction configuration.

SIMILAR EQE_{PV} VALUES AROUND THEIR RESPECTIVE E_{BG} In a RAINBOW configuration, each sub-cell will likely recieve the spectral region closer to its E_{bg}, where most organic materials have their strongest absorption band. If there is a spectral region where red and blue EQE_{PV}s overlap, the EQE_{PV} of the blue sub-cell should be, at least, as high as that of the red sub-cell, otherwise, there will be a compromise between better V_{oc} and worse J_{sc}. Interestingly, in this configuration, materials should be maximum EQE_{PV} matched, a condition easier to achieve than the current matching required in series connected tandem stacks.

HIGH SUB-CELL EFFICIENCIES Generally speaking, the RAINBOW efficiency is directly related to the achievable individual efficiency of each sub-cell, which must be as high as possible. However, the cell parameters for maximum PCE_R can differ from the optimal values of the individual cells. In particular, we may expect optimal RAINBOW sub-cells to be thinner than their single junction counterparts. That is because each sub-cell is only illuminated around its absorption maximum, where thin films are capable of absorbing most light, with the added benefit of thinner cells often exhibiting a higher FF. Compared to a tandem stack, the thickness of each sub-cell can be optimized independently, as no filtering effects occur.

Moreover, in order to maximize IoBC, additional selection criteria arise:

HIGH COMPLEMENTARITY To maximize IoBC, it is ideal for the absorption and EQE_{PV} curves of each sub-cell to have minimal overlap while spanning as wide a fraction of the solar spectrum as possible when combined, i.e., to be complementary. The first condition maximizes the ratio between $J_{sc,R}$ and $J_{sc,cell}$, while the second increases $J_{sc,R}$ due to a wider absorption range.

SIMILAR MAXIMUM PCE VALUES To have a large IoBC, each sub-cell within a RAINBOW combination should have similar PCE values. Note that the highest IoBC does not necessarily lead to the highest PCE.

4.2.2 *RAINBOW characterization with SOLS*

The spectrum on-demand light source (SOLS) presented in the previous chapter (Chapter 3) was developed for the characterization of RAINBOW solar cells. It is another tool that enables us to predict RAINBOW efficiency from measurements. It is recommended to the reader to take a look at Chapter 3, especially at Section 3.2.3 where the masking element in charge of RAINBOW characterization (the automatized guillotines) is explained.

4.2.2.1 *RAINBOW characterization procedure*

In general, the RAINBOW characterization is done for a 2-J device with blue and red sub-cells with higher and lower E_{bg}, respectively. Under AM1.5G illumination and in spectral splitting geometry, the red sub-cell receives the lower energy part of the solar spectrum, i.e., from $\approx$1100 nm up to the dividing wavelength λ_d, whereas the blue sub-cell receives the complementary part, i.e., between λ_d and $\approx$390 nm. The aim of the measurement is to determine the RAINBOW figures of merit i.e., $PCE_{R,max}$, $\lambda_{d,opt}$, and IoBC. The measurements are performed with the card mask of 1 Sun AM1.5G spectrum (shown in Figure 3.8 (a) and Figure 3.9 (a)) and then moving the motorized guillotines (Section 3.2.3). The $J-V$ response of the single-junction cell is measured at each guillotine position (i.e., for each λ_d). Typically, λ_d stepsize is 5 nm.

The measurement procedure is as follows: each sub-cell is subsequently placed at the end of the homogenizing light pipe for homogeneous illumination. Then, the response of the red sub-cell is determined for a so-called "red sweep", for which the starting position of the guillotine is at $\lambda_d = \lambda_{d,min}$, where the red sub-cell is illuminated with the full spectrum, and then moves to the red up to $\lambda_d = \lambda_{d,max}$. On the contrary, for the blue sub-cell, illumination proceeds as a "blue sweep", in which the opposite guillotine starts at $\lambda_d = \lambda_{d,max}$, again allowing full spectrum illumination, but moves to the blue toward $\lambda_d = \lambda_{d,min}$.

The values of $\lambda_{d,min}$ and $\lambda_{d,max}$ can vary slightly depending on the position of the beam with respect to the guillotines, which is considered in the calibration of the motors. $\lambda_{d,max}$ is limited by the low color separation in the red and IR regions and corresponds to a spectrum with almost no light for a red sweep and a full spectrum for a blue

sweep. On the other hand, the limitation of $\lambda_{d,min}$ comes from a too-large dispersion, resulting in some blue light being already blocked by the limits of the guillotines. It corresponds to a null spectrum for the blue sweep and the full spectrum for the red sweep. Additionally, the blue and UV region intensity at the output of the homogenizer is weak due to absorption in the different components. In the current guillotine calibration of the setup, $\lambda_{d,max}$ is 810 nm while $\lambda_{d,min}$ is 390 nm.

Additionally, red and blue sweeps have another descriptor regarding the direction of the sweep: "closing" refers to starting the measurement with the full spectrum and ending it in dark; while "opening" refers to starting the measurement in dark and ending it with the full spectrum. We have not seen an important difference between closing or opening sweeps if the devices are stable enough. For this reason, the direction of the sweep is generally not specified in the SOLS measurements.

4.2.2.2 *Choice of materials*

With the selection rules described in the previous subsection, we searched for possible combinations of materials for the first RAINBOW architecture demonstration. We selected three commercially available active layer blends, covering a broad range of E_{bg}: PM6:IO-4Cl,[205, 206] PM6:Y6,[39, 56] and PTB7-Th:COTIC-4F.[207, 208, 209] Their chemical structures are shown in Figure 2.5 of Chapter 2. The wide E_{bg} of 1.8 eV of the PM6:IO-4Cl blend makes it more suitable for the blue sub-cell, as we can see from its EQE_{PV} curve (Figure 4.8 (a) purple curve), whereas the extremely narrow gap of 1.12 eV of PTB7-Th:COTIC-4F is more adequate for the red sub-cell (Figure 4.8 (a) orange curve). Conversely, PM6:Y6, which has an intermediate gap value of 1.4 eV, can function either as the blue or the red sub-cell (Figure 4.8 (a) yellow curve), depending on which of the other two blends is used in the 2-J RAINBOW combination. We note that even if the reported efficiencies of PM6:IO-4Cl and PTB7-Th:COTIC-4F are not amongst the highest in OPV. These materials exhibit extreme E_{bg} on opposite sides of the spectrum, with relatively low voltage losses within organic materials ($\Delta V_{oc}^{total} \approx 0.6$ V, Table 4.1), which makes them ideal for testing the feasibility of the RAINBOW solar cell concept.[39, 205, 207, 210]

	PTB7-Th:COTIC-4F	PM6:Y6	PM6:IO-4Cl
E_{bg} (eV)	1.15	1.41	1.85
V_{oc} (V)	0.56	0.82	1.22
ΔV_{oc}^{total} (V)	0.59	0.59	0.63

Table 4.1: V_{oc} losses of the blends studied. E_{bg} was measured with the inflection point of the EQE_{PV} edge.

Using these materials, we manufactured and characterized well-performing solar cells, from which we obtained the EQE_{PV} and $J-V$ curves (Figure 4.8 (a) and (b), respectively) that were fed into the simulation model. In this case, the cells were prepared by spin coating instead of blade coating. The spin coating substrates used are smaller, and each one contains eight cells with an area of 2 mm$\times$2 mm. Since the

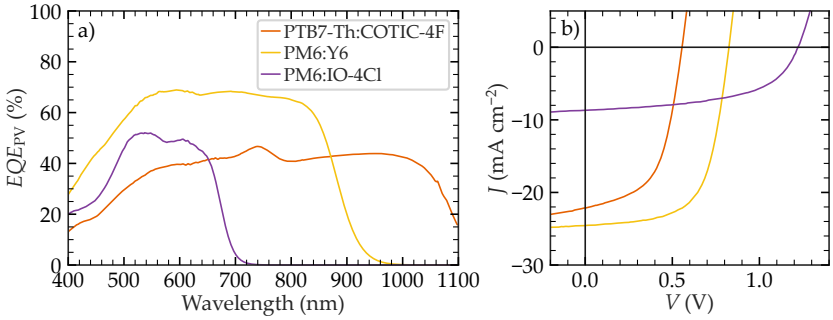

Figure 4.8: EQE_{PV} (a) and $J-V$ curves (b) of the selected materials used for the simulation model.

Active layer blend	V_{oc} (V)	J_{sc} (mA cm^{-2})	FF (%)	PCE (%)
PTB7-Th:COTIC-4F	0.56	22.14	55.65	6.84
PM6:Y6	0.82	24.55	63.99	12.93
PM6:IO-4Cl	1.22	8.67	54.94	5.83

Table 4.2: FoM of the active layer materials selected for the RAINBOW study. The FoM corresponds to the $J-V$ curves shown in Figure 4.8 (b).

deposition technique used for ETL and AL is spin coating, the devices are homogeneous in thickness. In this case, different thicknesses were tested by spin coating at different velocities, and the best-performing cells were selected. In this way, the theoretical PCE_R was calculated for the three 2-J RAINBOW combinations between the materials blends.

We first consider the wide-narrow gap combination, using PM6:IO-4Cl as the blue cell and PTB7-Th:COTIC-4F as the red cell (Figure 4.9 (a)). This combination yields the best results in terms of increase over the best cell, with a value of 41% (see Table 4.3), and a $PCE_{R,max}$ of 10.1%. The latter happens at a $\lambda_{d,opt} = 570$ nm, slightly below the band gap of the blue sub-cell. Even if the resulting combined efficiency is not amongst the highest in OPV, this combination is a remarkable example of a better final PCE_R due to a reduction in thermalization and absorption losses. For this combination, the complementary competition example shown in Figure 4.6 (c) is the closest case.

The other functional RAINBOW cell is the intermediate-narrow gap combination, using PM6:Y6 as the blue sub-cell and PTB7-Th:COTIC-4F as the red sub-cell (Figure 4.9 (b)). The latter yields a positive IoBC of 10.5% and a maximum combined efficiency of 13.7% (see Table 4.3). In this combination, the optimal λ_d, $\lambda_{d,opt}$, is located just below the band gap of the blue sub-cell, most likely because of its high performance

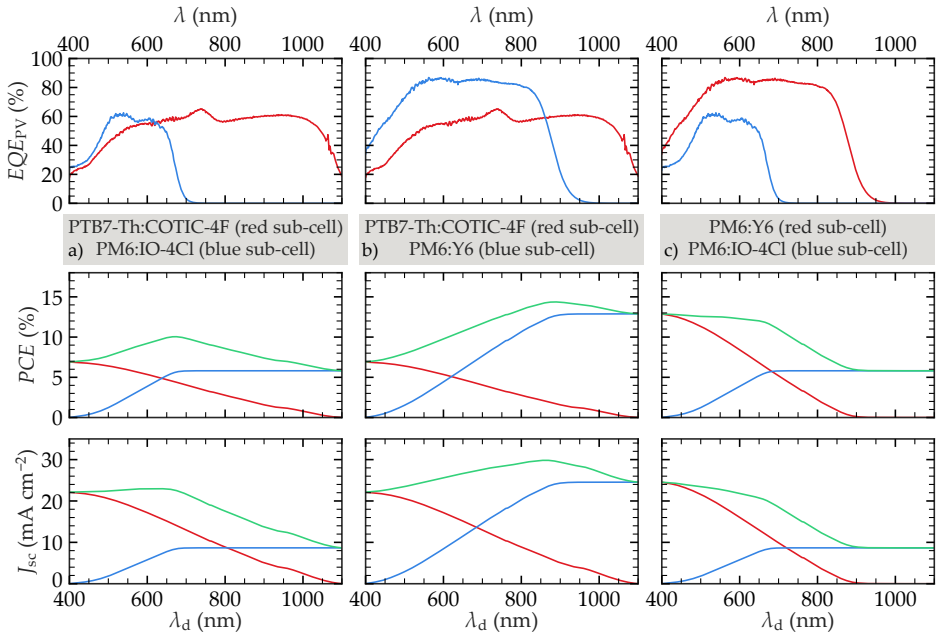

Figure 4.9: RAINBOW simulations with solar cells fabricated with the selected materials. Simulation results are shown in columns (EQE_{PV}, PCE, and J_{sc} in top, middle, and bottom panels, respectively) for 2-J RAINBOW geometries with PTB7-Th:COTIC-4F as red sub-cell and PM6:IO-4Cl as blue sub-cell (a), PTB7-Th:COTIC-4F as red sub-cell and PM6:Y6 as blue sub-cell (b), and PM6:Y6 as red sub-cell and PM6:IO-4Cl as blue sub-cell (c). Red, blue, and green lines refer to the red sub-cell, blue sub-cell and RAINBOW, respectively. The RAINBOW figures of merit are summarized in table Table 4.3.

Simulation in Figure 4.9	Active layer materials		RAINBOW figures of merit		
	Red sub-cell	**Blue sub-cell**	$\boldsymbol{PCE_{,max}}$ **(%)**	**IoBC (%)**	$\boldsymbol{\lambda_{d,opt}}$ **(nm)**
(a)	PTB7-Th:COTIC-4F	PM6:IO-4Cl	10.05	45.71	670
(b)	PTB7-Th:COTIC-4F	PM6:Y6	14.37	11.54	885
(c)	PM6:Y6	PM6:IO-4Cl	12.88	0.00	-*

Table 4.3: RAINBOW FoM for materials simulations shown in Figure 4.9. *The third combination (c), do not show any RAINBOW efficiency increase. For this reason, IoBC is 0, and $\lambda_{d,opt}$ do not has a value.

when compared with the red sub-cell. In this case, the red sub-cell (PTB7-Th:COTIC-4F), even with its significantly lower EQE_{PV} values, is able to capture the lower energy photons that the blue sub-cell (PM6:Y6) cannot absorb, resulting in a higher photocurrent for the RAINBOW combination. This material combination behaves similarly to the photon scavenging example presented in Figure 4.6 (d).

On the opposite, the wide-intermediate gap combination between PM6:IO-4Cl as the blue sub-cell and PM6:Y6 as the red sub-cell (Figure 4.9 (c)) exhibits null IoBC (see Table 4.3). This is because the EQE_{PV}

curve of the blue sub-cell (PM6:IO-4Cl) is entirely overshadowed by that of the red sub-cell (PM6:Y6). As a result, the lower thermalization losses of the blue sub-cell cannot compensate its lower photocurrent, resulting in a non-functional RAINBOW combination, where the maximum combined efficiency is equal to that of the best-performing sub-cell (the red). This is a case similar to the overshadowing presented in Figure 4.6 (a).

Notice that the EQE_{PV}s shown in the top panels of Figure 4.9 have higher values than the corresponding EQE_{PV}s in Figure 4.8 (a). The latter is because the EQE_{PV}s shown for a RAINBOW simulation, are already mupliplied by the normalization factor A described in Equation 4.4. The latter is because the normalized EQE_{PV} is the actual tool to compare with the simulations, and when EQE_{PV}s are shown in the thesis inside an environment of a RAINBOW simulation, the corresponding EQE_{PV} is always multiplyed by the A factor. We have always found $A > 1$, whith typical values between 1.1 and 1.3. The latter indicates that the J_{sc} calculated from the measured EQE_{PV} is between 10 and 30% below the expected value. The origin of this difference is out of the scope of this thesis. Nevertheless, we could attribute it to inaccuracies when measuring the EQE_{PV}; or to J_{sc} overestimation due to collection of charges generated far from the contacs or due to diffued and reflected light.[211, 212]

4.2.2.3 *Model validation via RAINBOW characterization with SOLS*

To validate the model we have chosen to perform SOLS RAINBOW measurements of the two successful RAINBOW combinations by measuring red and blue sweeps of the sub-cells. The individual SOLS characterization of the red and blue sub-cells (shown in Figure 4.10) provides us with insights to assess the validity of the model assumptions. For the red sub-cell (PTB7-Th:COTIC-4F) we notice that PCE behaviour is mainly driven by the J_{sc} component, where the V_{oc} and FF rapidly saturate, with minor variations throughout the entire λ_d range (Figure 4.10). This behavior is consistent with the model initial assumptions (constant V_{oc} and FF), where the rapid saturation can be attributed to the relation of V_{oc} and FF with increasing illumination intensity, a phenomenon well reported in the literature.[213, 214, 215, 216] Notice that this saturation behavior observed with the SOLS is likely to begin at λ_d closer to the extremes in a real RAINBOW device since, due to spectral redistribution, light power density is higher (spectrally concentrated) for each sub-cell than it is in the SOLS measurement. The latter is because, in the SOLS setup, the varying spectrum is achieved by masking the unwanted half of the spectra but not by

spectral reconcentration. We see that, above a certain light intensity threshold, the λ_d dependence of these two parameters seems to play a minor role in determining the final partial efficiency of each sub-cell, being eclipsed by the λ_d dependence of J_{sc}. This figure suggests that a minimum of illumination power would be needed for each cell for the RAINBOW to work well. Without considering the concentration that may occur, from Figure 4.10 one can say that the fraction of the spectrum that needs to hit each sub-cell would be somewhere between 50 and 100 nm for FF and V_{oc} to be already stable. This points towards a maximum number of subcells of about $(1100 - 400)/100 = 7$. This number is not too far from what the theoretical paper from Peters et al. found due to optical losses (below 10 junctions),[131] and it would be a lower limit as with concentration, the number may increase.

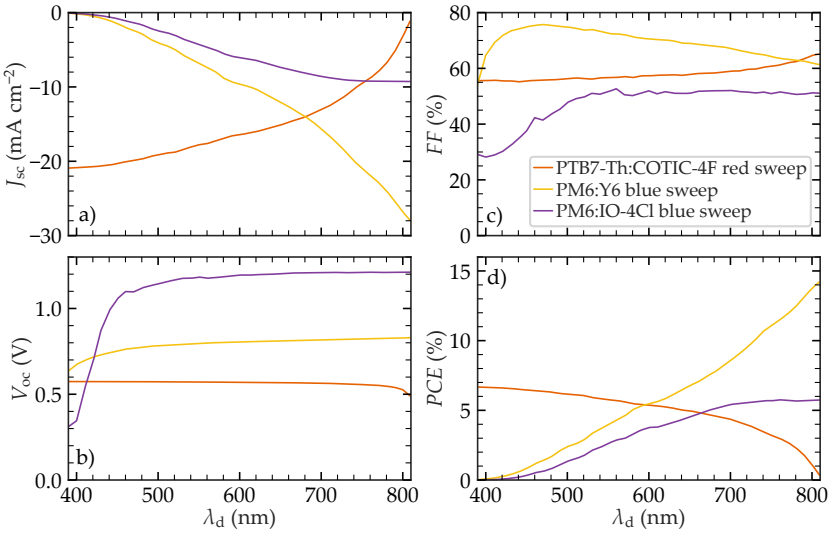

Figure 4.10: Results of RAINBOW characterization with SOLS. V_{oc}, J_{sc}, FF and PCE are plotted in panels (a), (b), (c), and (d), respectively as a function of λ_d. The orange line corresponds to a red sweep performed on the PTB7-Th:COTIC-4F device, the yellow line corresponds to a blue sweep performed on the PM6:Y6 cell, and the purple line corresponds to a blue sweep performed on the PM6:IO-4Cl cell.

Intuitively, we can see that the J_{sc} of each sub-cell is proportional to the fraction width of the illuminating spectrum, as wider spectral fractions will encompass a higher amount of photons. However, we notice that for the blue sub-cell (PM6:IO-4Cl), the J_{sc} slope changes suddenly after the dividing wavelength sweep surpasses 700 nm, bringing the current increase almost to a halt (Figure 4.10 (a)). This sudden slope change can be attributed to the lack of photon absorption below 700 nm, which corresponds to the E_{bg} of PM6:IO-4Cl. Meanwhile,

Measruement in Figure 4.11	Active layer materials		RAINBOW figures of merit		
	Red sub-cell	Blue sub-cell	$PCE_{,max}$ (%)	IoBC (%)	$\lambda_{d,opt}$ (nm)
(a)	PTB7-Th:COTIC-4F	PM6:IO-4Cl	9.78	46.6	700
(b)	PTB7-Th:COTIC-4F	PM6:Y6	14.93	5.0	790

Table 4.4: RAINBOW FoM of the SOLS characterization of Figure 4.11.

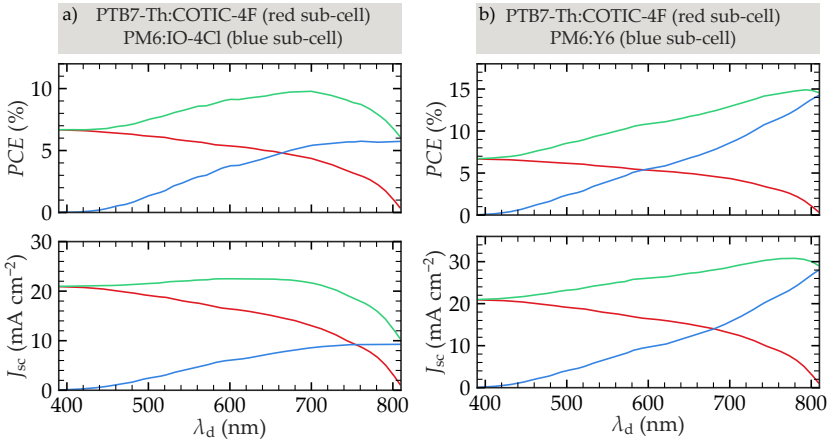

Figure 4.11: RAINBOW analysis with SOLS characterization. PTB7-Th:COTC-4F // PM6:IO-4Cl (a) and for PTB7-Th:COTIC-4F // PM6:Y6 (b) 2-J RAINBOW systems are evalutated by merging the RAINBOW characterization of each sub-cell shown in Figure 4.10. Table 4.4 shows the RAINBOW FoM.

with a E_{bg} well below the measuring range of the SOLS setup, the PTB7-Th:COTIC-4F red sub-cell has a J_{sc} component that constantly increases with wider spectral fractions.

By merging these two measurements as a function of the dividing wavelength, we can calculate the RAINBOW performance of the wide-narrow gap combination (PM6:IO-4Cl and PTB7-Th:COTIC-4F, respectively) resulting in a high IoBC of 46.6% (Figure 4.11 (a)) and a $\lambda_{d,opt}$ = 700 nm. This high IoBC agrees with previous simulations and calculations, where the significant reduction of thermalization and absorption losses results in a functional RAINBOW combination. Moreover, in these measurements, we also see that the optimal wavelength range is wider than predicted by the simulations. This could be partly due to the SOLS setup's lack of sufficient spectral resolution. As seen in Figure 3.12 (a) and (b) of the previous chapter, the edge of the red and the blue spectra have a full width at half maximum (FWHM) at λ_d of approximately 30 nm. Therefore, there is a certain wavelength range where light is not fully redirected to its best photovoltaic converter. The latter is also seen in Figure 4.12 where we

simulate the effect of increasing the FWHM from 0 to 80 nm. As a result, the IoBC decreases, and the RAINBOW peak becomes wider. In turn, this has important implications for the design of the optical element, where a clear separation of the wavelengths around the optimum λ_d is desirable.

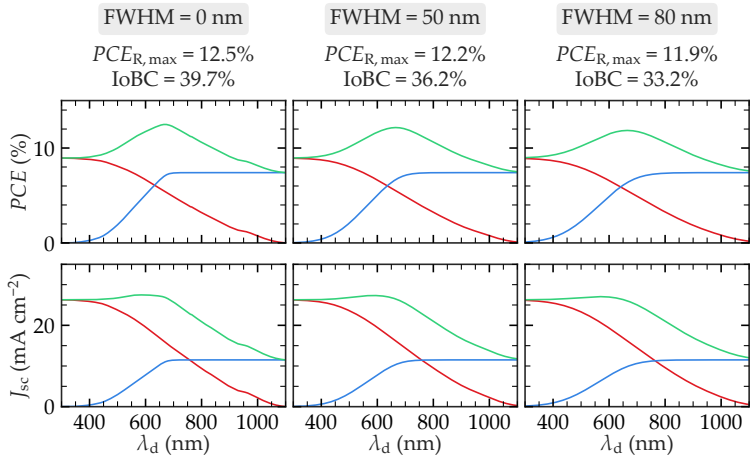

Figure 4.12: Simulations to determine the effect of the spectral resolution of the SOLS setup on RAINBOW performance. The spectral division is calculated using a Fermi-Dirac distribution function with full width at half maximum (FWHM) of 0, 50 and 80 nm. The broadening effect of the RAINBOW device is appreciable. It explains the small differences between the simulations and the measurements using the SOLS setup and the need for a dispersion element with sharp light separation for the real application of RAINBOW solar cells.

The intermediate-narrow gap combination between PM6:Y6 as the blue sub-cell and PTB7-Th:COTIC-4F as the red sub-cell was also characterized with the SOLS. Since we already have the measurement of the red sub-cell we only need to add the characterization of the PM6:Y6 device with a blue sweep (Figure 4.10 green line). In this case, since PM6:Y6 has a flat EQE_{PV} between 900 and 500 nm, as seen in Figure 4.8 (a), the slope of the J_{sc} dependence on λ_d is almost constant. The latter dependence is also reflected on PCE. According to the simulation results (Table 4.3) the intermediate-narrow gap combination shows the maximum IoBC at a $\lambda_{d,opt} = 885$ nm with a value of 11.50%. The RAINBOW measurement analysis (Figure 4.11 (b)) shows a maximum IoBC of 5.0% at $\lambda_{d,opt} = 790$ nm. The significant differences can be explained by considering the limitations of the SOLS setup. First of all, the theoretical $\lambda_{d,opt}$ is outside the λ_d range of the equipment, which can measure up to $\lambda_{d,max} \approx 805$ nm. Additionally, the commented low spectral separation at high λ_d also introduces some differences as in the previous case.

4.2.3 *Monolithic proof of concept devices*

Having validated our simulation model with the SOLS measurements, we proceeded to manufacture monolithic proof of concept devices that includes two junctions deposited side by side on the same substrate, representing the simplest embodiment of a RAINBOW solar cell.

To manufacture the monolithic proof of concept device, we selected the same two combinations as in the characterization with SOLS, i.e. the wide-narrow and the intermediate-narrow gap combinations. To fabricate such a device on a small scale we developed a technique that we named partial coverage radial (PCR) spin coating, which is able to deposit half of the substrate. This technique is easy to reproduce without specialized equipment and allows us to sequentially deposit two junctions side-by-side in a single substrate, making it a useful technique in RAINBOW solar cell lab scale optimization. Section 2.2.3 shows more details on the technique.

The monolithic device of the RAINBOW system composed by PM6:Y6 and PTB7-Th:COTIC-4F as blue and red sub-cells, respectively, was manufactured using the PCR spin coating technique for both active layer materils. In this case, PTB7-Th:COTIC-4F was deposited first on one side of the substrate and PM6:Y6 was deposited on the other side afterwards, in both cases using the PCR spin coating technique. For the other monolithic device composed of PM6:IO-4Cl and PTB7-Th:COTIC-4F as blue and red sub-cells, respectively, the PM6:IO-4Cl was deposited first covering the whole substrate with dynamic spin coating. This is because we observed a significant decrease in device performance when depositing PM6:IO-4Cl in static spin coating (which is necessary for the PCR spin coating technique) compared to dynamic mode. Prior to PTB7-Th:COTIC-4F deposition using the PCR spin coating, half of the substrate was cleaned with a wipe towel with toluene. Figure 4.13 shows a photograph of both monolithic samples. Notice that the PM6:IO-4Cl active layer looks more homogeneous under the microscope compared with the others deposited with PCR spin coating.

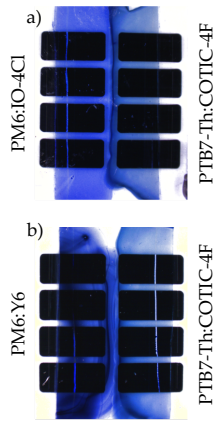

Figure 4.13: Photos of monolithic substrates. Wide-narrow (a) and intermediate-narrow band-gap combinations.

To asses the quality of the deposition using the PCR spin coating method we used Raman scattering imaging for the monolithic RAINBOW device of PM6:IO-4Cl and PTB7-Th:COTIC-4F, as illustrated in Figure 4.14. Two excitation wavelengths were used to selectively probe the two systems, namely 785 nm for PTB7-Th:COTIC-4F and 488 nm for PM6:IO-4Cl. The Raman peak centered at 1322 cm^{-1} corresponds to the signal of PTB7-Th:COTIC-4F. By integrating the intensity of this peak over the scanned region, we can see that this blend only appears

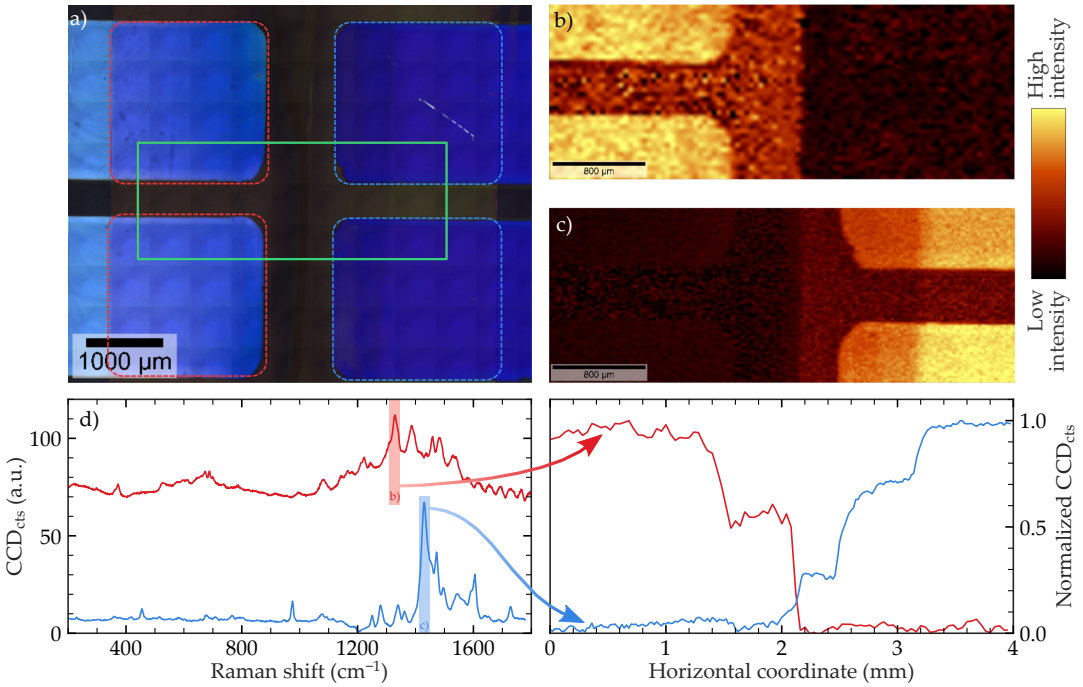

Figure 4.14: PCR spin coating Raman characterization. Raman characterization of the RAINBOW monolithic proof of concept device of PTB7-Th:COTIC-4F (red sub-cell) and PM6:IO-4Cl (blue sub-cell) which corresponds respectively to the left and right half of the substrate. (a) Stitching image of the measured sample where 2 red sub-cells and 2 blue sub-cells (discontinuous red and blue squares, respectively) are shown as well as the region where Raman spectra was measured (green rectangle). (b) Raman intensity map corresponding to peak at 1322 cm^{-1} acquired with 785 nm laser excitation (spectrum shown in (d) panel in red). (c) Raman intensity map corresponding to peak centered at 1428 cm^{-1} acquired with 488 nm laser excitation (spectrum shown in (d) panel in blue). (d) Raman spectrum of PTB7-Th:COTIC-4F when excited with 785 nm laser (red) and PM6:IO-4Cl when excited with 488 nm laser (blue). Panel (e) corresponds to the integrated intensity of panels (b) and (c) in the horizontal direction and shows that the step between the two materials is on the order of tenths of µm.

on the left part of the device (Figure 4.14 (b)). Similarly, by monitoring the peak centered at at 1428 cm^{-1} we can see the signal of PM6:IO-4Cl, and how this material is only distributed on the right-hand side of the sample (Figure 4.14 (c)). The absence of any significant intermixing between the materials of two adjacent sub-cells sequentially deposited with the PCR spin coating method is demonstrated by the sharpness and negligible overlap of the Raman profiles shown in Figure 4.14 (e), each one corresponding to a characteristic Raman peak of each organic blend.

The EQE_{PV} and $J-V$ curves of the monolithic devices were measured and fed into the numerical model to calculate the optimal dividing wavelength ($\lambda_{d,opt}$) and the expected $PCE_{R,max}$ and IoBC. As we can see in Figure 4.15, both combinations exhibit a positive IoBC and

relatively good combined efficiencies. In the case of PM6:Y6 as the blue sub-cell and PTB7-Th:COTIC-4F as the red sub-cell (Figure 4.15 (a)), we see that the EQE_{PV} curves are highly complementary, resulting in a great calculated $PCE_{R,max}$ of 13.25% with an IoBC of 11.39% at a $\lambda_{d,opt}$ of 885 nm. On the other hand, we see that the RAINBOW combination with PM6:IO-4Cl as the blue sub-cell and PTB7-Th:COTIC-4F as the red sub-cell (Figure 4.15 (b)) is expected to exhibit an excellent performance with a calculated IoBC of 47.64% and a $PCE_{R,max}$ of 9.91% at a $\lambda_{d,opt}$ of 670 nm. This is a consequence of the highly complementary EQE_{PV} curves of each sub-cell.

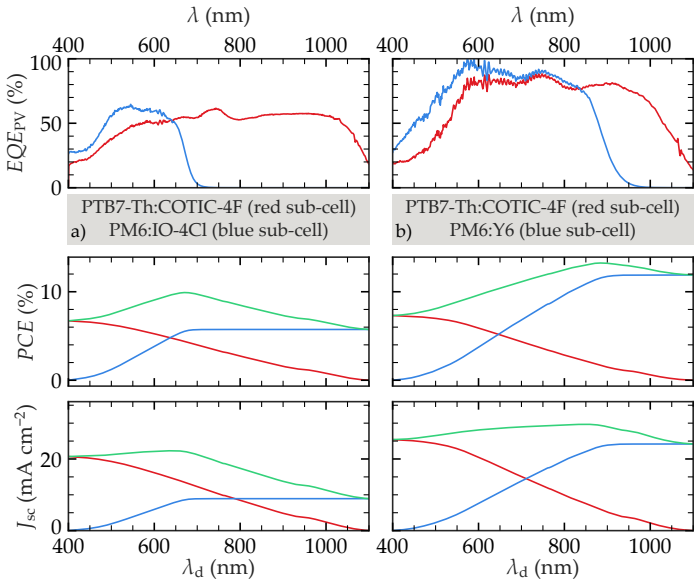

Figure 4.15: RAINBOW simulations of the monolithic devices. PM6:IO-4Cl as the blue sub-cell and PTB7-Th:COTIC-4F as the red sub-cell (a), PM6:Y6 as the blue sub-cell and PTB7-Th:COTIC-4F as the red sub-cell (b). The differences in PTB7-Th:COTIC-4F data between (a) and (b) is because they are different devices, each one monolithic with its corresponding blue sub-cell. The EQE_{PV} used for each material is plotted on the top panels and the $J-V$ FoM can be found at Table 4.6 for RAINBOW combination (a) and Table 4.6 for RAINBOW combination (b) in the "1 Sun" row. The RAINBOW FoM for both simulations can be found at Table 4.7.

In this case, instead of using the SOLS setup, to further validate the simulation results we used a more accessible solution to characterize the sub-cells: an LED-based solar simulator, which consists of an array of 21 individually addressable LEDs. This setup is capable of providing homogeneous illumination with discrete fractions of the solar spectrum by varying each LED intensity. We used our simulations to set the dividing wavelength on the LED solar simulator to be as close as possible to the optimal simulated $\lambda_{d,opt}$ for each RAINBOW

Material	spectral fraction	V_{oc} (V)	FF (%)	J_{sc} (mA cm^{-2})	PCE (%)
PM6:IO-4Cl (blue sub-cell)	1 Sun	1.20	53.6	8.92	5.75
	Blue fraction	1.20	51.8	8.60	5.32
PTB7-Th:COTIC-4F (red sub-cell)	1 Sun	0.58	55.96	20.68	6.71
	Red fraction	0.56	60.66	11.97	4.04
RAINBOW	Combined	0.83	-	20.57	9.36
	RCoBC (%)	42.69	-	-0.53	39.50*

Table 4.5: Monolithic RAINBOW device performance, with PM6:IO-4Cl as the blue sub-cell and PTB7-Th:COTIC-4F as the red sub-cell. The RAINBOW characterization is measured with the LED solar simulator with various spectra (see Figure 4.16 (a)), simulating the behavior of the SOLS setup for a single λ_d of approximately 690 nm. The result is a PCE_R of 9.36% corresponding to 39.50% increase over the best cell (IoBC) marked with *. RCoBC refers to the combined RAINBOW values compared to the best-performing single junction device.

combination, namely at ∼860 nm and ∼690 nm for the intermediate-narrow and wide-narrow gap cell combinations respectively. Figure 4.16 shows the red and blue spectra used for the characterization of the wide-narrow (a) and the intermediate-narrow (b) band gap RAINBOW combinations.

Table 4.5 and Table 4.6 summarize the monolithic RAINBOW cell characterization results. The upper table section shows the $J-V$ parameters obtained for each sub-cell under full sun illumination, and using only the corresponding fraction of the solar spectrum (red or blue). For the RAINBOW device (bottom table section), the rainbow

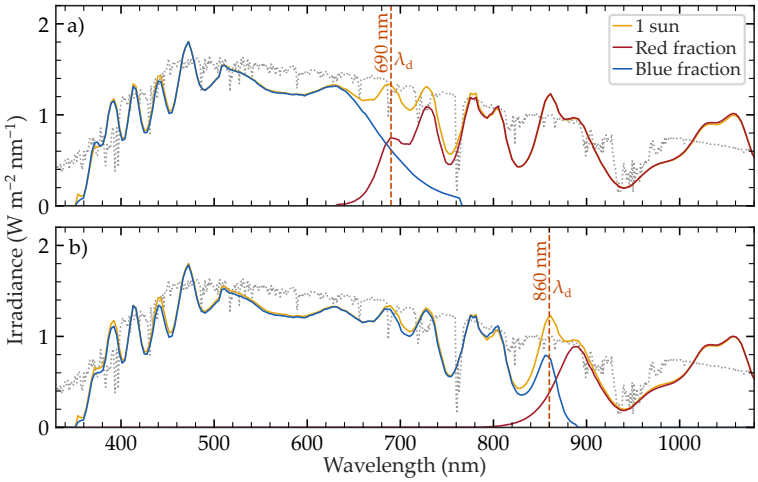

Figure 4.16: LED solar simulator spectra used for monolithic RAINBOW characterization. Blue and red fractions are shown in blue and red solid lines, respectively, while the 1 Sun spectrum in shown in yellow. The two λ_d of 690 and 860 nm were used to characterize the two RAINBOW systems studied.

Material	spectral fraction	V_{oc} (V)	FF (%)	J_{sc} (mA cm^{-2})	PCE (%)
PM6:Y6 (blue sub-cell)	1 Sun	0.81	60.8	24.18	11.94
	Blue fraction	0.81	61.0	22.31	11.05
PTB7-Th:COTIC-4F (red sub-cell)	1 Sun	0.57	50.7	25.39	7.35
	Red fraction	0.54	58.6	7.09	2.26
RAINBOW	Combined	0.74	-	29.40	13.31
	RCoBC (%)	-8.04	-	21.59	11.47*

Table 4.6: Monolithic RAINBOW device performance, with PM6:Y6 as the blue sub-cell and PTB7-Th:COTIC-4F as the red sub-cell. The RAINBOW characterization is measured with the LED solar simulator with various spectra (see Figure 4.16 (b)), simulating the behavior of the SOLS setup for a single dividing wavelength of approximately 860 nm. The result is a PCE_R of 13.31% corresponding to 11.47% increase over the best cell (IoBC) marked with *. RCoBC refers to the combined RAINBOW values compared to the best-performing single junction device.

PCE (PCE_R) and the increase over the best cell (IoBC) are calculated from the measurements of the sub-cells following Equation 4.2 and 4.11, respectively.

The first observation is that all of the sub-cells at 1 Sun operate with efficiencies similar to those of single-junction devices made by conventional deposition, i.e., without monolithic integration (see Table 4.2, Table 4.5, and Table 4.6). The latter suggest that the PCR spin coating technique does not significantly affect the performance of the devices. For the wide-narrow gap combination (PM6:IO-4Cl as the blue sub-cell and PTB7-Th:COTIC-4F as the red sub-cell), we have obtained an IoBC of 39.50% with a PCE_R of 9.36% (Table 4.5), in good agreement with the simulations in Figure 4.15 (a), which predicted an IoBC of 46.34% with a PCE_R of 9.82% at λ_d = 690 nm (see Table 4.7).

For the the intermediate-narrow gap combination (PM6:Y6 as the blue sub-cell and PTB7-Th:COTIC-4F as the red sub-cell), we have obtained an IoBC of 11.41% with a PCE_R of 13.31% (Table 4.6), in very good agreement with the simulations of Figure 4.15 (b), with values of 10.49% and 13.14%, respectively, at a λ_d of 860 nm (see Table 4.7). Table 4.7 summarizes the comparison between the simulations and the characterization of the two studied monolithic RAINBOW solar cells.

We next try to estimate the importance on these RAINBOW cells of the two main mechanisms that operate in multi-junction solar cells, i.e., the reduction in the thermalization losses and the increase in absorption. In all cases, comparisons are made with respect to the best-performing single junction amongst sub-cells for a given monolithic device. To address the changes in absorption, we use as proxy the photocurrent density. In particular, we compare the J_{sc} of the best sub-cell with that of the RAINBOW device following Equation 4.9. Clearly, this is only

Blue sub-cell	Red sub-cell	Kind	Reference	PCE_R (%)	IoBC (%)	λ_d (nm)
PM6:IO-4Cl	PTB7-Th:COTIC-4F	Simulation	Figure 4.15 (a)	9.91	47.64	670
				9.82	46.38	690
		Measurement	Table 4.5	9.36	39.50	$\sim$ 690
PM6:Y6	PTB7-Th:COTIC-4F	Simulation	Figure 4.15 (b)	13.25	11.39	885
				13.14	10.49	860
		Measurement	Table 4.6	13.31	11.47	$\sim$ 860

Table 4.7: Comparison between the RAINBOW characterization with LEDs solar simulator and the simulations for the two RAINBOW systems studied.

an approximation, since, besides being proportional to the absorption, charge transport and collection also affect the J_{sc}. In any case, as the materials and device stack being compared are the same, we use as a first approximation the changes in J_{sc} as being mainly related to changes in absorption.

On the other hand, thermalization of charges is often reflected in the energy of the extracted charges, and thus we use, again as proxy, the difference in V_{oc} between the best-performing single junction cell and that of the RAINBOW devices. Being an N-terminal device, the V_{oc} of the latter is not well-defined. To approximate an effective (or averaged) V_{oc} for the combined cells, we take into account that a fraction of the charges will be collected at the V_{oc} of the blue sub-cell, and the rest with the V_{oc} of the red sub-cell. A simple way of factoring this in, is by calculating the RAINBOW V_{oc} ($V_{oc,R}$) through the J_{sc}-weighted average of the corresponding sub-cell values (following Equation 4.12). This expression uses the photocurrent fraction as an approximation of the P_{in} average that each sub-cell receives, and it assumes that the FFs of both sub-cells are approximately equal.

$$V_{oc,R} = \frac{V_{oc,red} \cdot J_{sc,red} + V_{oc,blue} \cdot J_{sc,blue}}{J_{sc,R}} \tag{4.12}$$

The last two rows in Table 4.5 and Table 4.6 show the parameters of the corresponding RAINBOW cells following Equation 4.2, Equation 4.9 and Equation 4.12, as well as the relative change of the combined V_{oc}, J_{sc} and PCE ($V_{oc,R}$, $J_{sc,R}$ and PCE_R, respectively) concerning the best-performing single junction cell (RCoBC). Note that the RCoBC for the PCE corresponds to the aforementioned overall figure of merit IoBC (%). While being only estimates, the RCoBC can be used to give an idea of the origin of the IoBC or, in other words, whether thermalization and/or absorption losses are reduced.

For the wide-narrow gap combination (Table 4.5), the RCoBC analysis shows that this improvement basically comes from the V_{oc} RCoBC (42.69%), so in this case, the RAINBOW device does minimize thermalization losses. This is simply due to the high V_{oc} of the blue sub-cell, which is more than twice that of the red sub-cell.

On the other hand, for the intermediate-narrow gap combination (Table 4.6) the increase in efficiency is mainly related to an improvement in J_{sc} from the contribution of the red sub-cell (21.59% of RCoBC), which absorbs photons well below the E_{bg} of the blue sub-cell, showing a reduction on absorption losses. In fact, this even overcompensates the lower V_{oc} of the electrons extracted from the red sub-cell, which yields a worsening of the open-circuit seen as a negative V_{oc} RCoBC of -8.04% (notice that the best-performing cell is the blue sub-cell). Hence, this is an example of a RAINBOW combination that minimizes optical absorption losses.

4.3 EFFECT OF ACTIVE LAYER THICKNESS

One parameter to consider in the optimization of RAINBOW solar cells is the active layer thickness. The latter has an impact on the FoM of organic solar cells such as J_{sc} or FF as well as on its EQE_{PV}. To study this, we have prepared two blade-coated samples of PTB7-Th:COTIC-4F and PM6:IO-4Cl blends with active layer thickness gradients. Apart from measuring the $J-V$ curves of each cell under AM1.5G illumination, we have also measured EQE_{PV}. Figure 4.17 shows the resulting thickness dependence for both blends. Notice that, for simplicity, only one side of each substrate is selected. The PTB7-Th:COTIC-4F blend (Figure 4.17 (f)-(j)) shows the typical thickness dependence. Too thin devices (the first two cells) do not work due to short-circuits (i.e., low shunt resistance) and low amounts of absorbed photons. After a certain threshold, short-circuits are reduced, and the device efficiency starts to increase. At this point, there is a trade-off between thin devices offering short percolation paths to the contacts but a low amount of absorbed photons (i.e., favoring FF); and thick devices offering longer percolation paths but a high amount of absorbed photons (i.e., favoring J_{sc}). As a result, FF thickness dependence shows its maximum at thinner devices ($\approx$100 nm Figure 4.17 (h)) compared to the maximum shown by J_{sc} ($\approx$150 nm in Figure 4.17 (g)). The V_{oc} typically shows a weak dependence on thickness due to its logarithmic dependence on J_{sc}. Only extreme thickness (too thin or too thick) decreases its value drastically. As a result, the thickness dependence of the PCE (Figure 4.17 (i)) shows its maximum at a thickness of $\approx$ 130 nm, in between 100 nm and 150 nm.

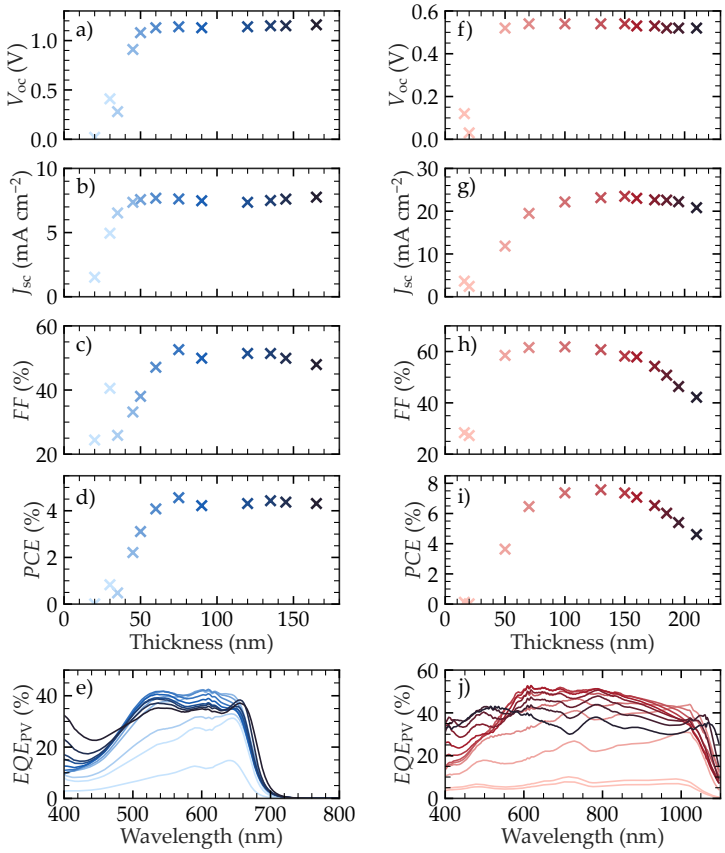

Figure 4.17: FoM and EQE_{PV} thickness dependence for PM6:IO-4Cl and PTB7-Th:COTIC-4F blends. FoM (a)-(d) and EQE_{PV} (e) thickness dependence for PM6:IO-4Cl blend, and FoM (f)-(i) and EQE_{PV} (j) thickness dependence for PTB7-Th:COTIC-4F blend. In (e) and (j), thickness is represented with the color darkness. The corresponding cell number for the different thicknesses (which other parts of the section refer to) is 1 for the thinner cell and increases to 12 following thickness order.

The wide band-gap blend PM6:IO-4Cl (Figure 4.17 (a)-(e)) do not show the same FF and J_{sc} trend. Its FF peaks at a thickness of approximately 75 nm while J_{sc} shows already a first maximum at approximately 60 nm. However, the J_{sc} trend appears to have a higher maximum at an active layer thickness surpassing 165 nm. The thickness gradient of the sample did not reach thick enough devices to see the full picture.

Additionally, the thickness has an important effect on EQE_{PV} shape. For thin cells, the EQE_{PV} curve is expected to have a profile similar to the absorption of the active layer material. The latter is generally shown as a high peak at the first absorption band of the donor and acceptor components (lighter curves in Figure 4.17 (e) and (j)). This

absorption increases as the thickness increases, increasing the EQE_{PV} value. Nevertheless, due to the exponential nature of the absorption, the charge generation is inhomogeneous in the vertical direction for thicker films. The latter is more prominent for the spectral regions where the material's light absorption is the strongest (i.e., around the E_{bg} of the active layer components). In these regions, the EQE_{PV} gets reduced because the charges are not produced homogeneously; therefore, one type of free charge can not reach its contact. The latter would happen for holes in the inverted geometry. On the contrary, the spectral regions with lower absorption absorb more light still homogeneously enough to increase their EQE_{PV} (darker curves in Figure 4.17 (e) and (j)). As a result, the EQE_{PV} changes its shape with increasing thickness. For thick films, this effect is known as energy filtering.[217]

4.3.1 *Considering active layer thickness on EQE_{PV}*

Due to energy filtering, thick cells generally show EQE_{PV} resembling top-hat curves, while thin cells show EQE_{PV} closer to absorption profiles (i.e., peak- and valley-like profiles). Considering that sub-cells in the RAINBOW geometry are likely to receive only photons in the spectral region near its E_{bg}, we do expect thinner cells to present an EQE_{PV} more suitable for RAINBOW. The higher FF that generally thinner cells often exhibit may also be an advantage.

To study the effect of thickness on RAINBOW performance, we have simulated every RAINBOW pair of the thickness-dependent data acquired for PM6:IO-4Cl (as blue sub-cell) and PTB7-Th:COTIC-4F (as red sub-cell). As a result, we obtained the RAINBOW FoMs thickness-dependence combination for both blends. The results for IoBC and $PCE_{R,max}$ are shown in Figure 4.18 (a) and (b), respectively, with the PTB7-Th:COTIC-4F in the horizontal axis and the PM6:IO-4Cl in the vertical axis. As discussed before, the best-performing single-junction device (thickness optimized) for the blue and the red blends are cells numer 6 and 7, respectively (see Figure 4.17 (i) and (d)). The simulations comprising these cells are highlighted with blue and red rectangles in Figure 4.18.

As discussed before, we expect cells thinner than the ideal single junction thickness to perform better in the RAINBOW configuration. However, we observe that the maximum $PCE_{R,max}$ (highlighted with a light-green square) is achieved for the single junction thickness optimized devices. We attribute this to the importance of the efficiency of each sub-cell at the $PCE_{R,max}$. First, we must consider that in a 2-J RAINBOW geometry, the blue sub-cell will most likely receive all the

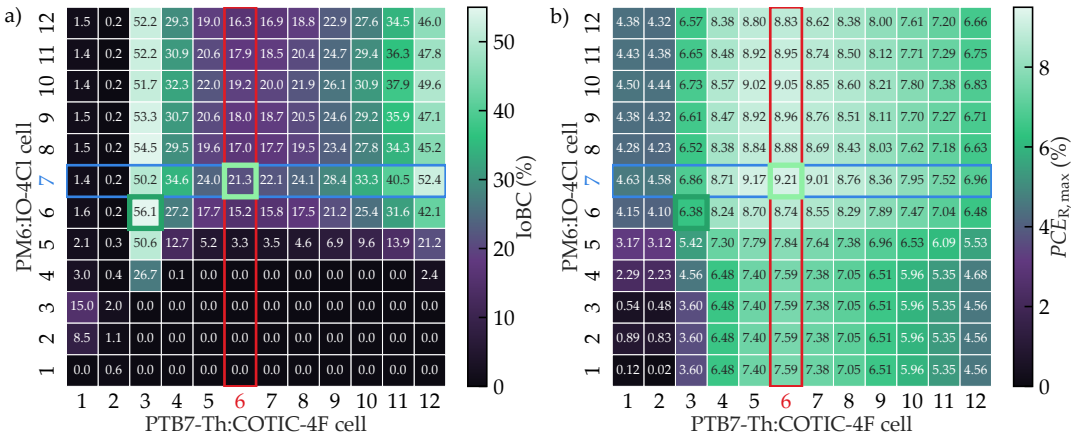

Figure 4.18: RAINBOW FoM for simulations with active layer thickness dependent sub-cells. The IoBC (a) and the $PCE_{R,max}$ (b) are plotted as heatmaps with the blue sub-cell (PM6:IO-4Cl) and the red sub-cell (PTB7-Th:COTIC-4F) in the vertical and horizontal axis, respectively. The data used for the simulation is shown in Figure 4.17, with cells number 1 and 12 corresponding to the thinner and the thicker devices, respectively. The best-performing single junction PM6:IO-4Cl cell is highlighted with a blue horizontal rectangle, while the analogous for the PTB7-Th:COTIC-4F blend is highlighted with a red vertical rectangle. The maximum IoBC and $PCE_{R,max}$ calculated are highlighted with dark and light green squares, respectively.

spectral region it is absorbing. Thus, we should not be surprised that the blue sub-cell best-performing thickness at 1-sun is close to the ideal thickness for the 2-J RAINBOW geometry. Conversely, the red sub-cell will be illuminated with a fraction of the spectrum it can absorb. In this case, the E_{bg} of the red sub-cell is far from the $\lambda_{d,opt}$, reducing the impact of energy filtering in EQE_{PV} shape. A wider spectral fraction compensates for differences in EQE_{PV} shape that generally happens around E_{bg}. Therefore, this effect may be more important in RAINBOW configurations with more junctions.

Nevertheless, the maximum IoBC is achieved when both cells are thinner than their best-performing thickness as single junctions. If we compare column-wise the values on the left and on the right of cell number 6 of PTB7-Th:COTIC-4F (in Figure 4.18 (a)), we notice that thinner cells (left) have considerably higher IoBC altough having similar $PCE_{R,max}$. This is the case for example of device 3 and 12, or the device 4 and 9 of PTB7-Th:COTIC-4F. This is because the complementarity of two sub-cells directly impacts IoBC, while it does not necessarily have an impact on $PCE_{R,max}$. The latter has a direct implication from the energy filtering effect of EQE_{PV}. Thinner red-cells will have an EQE_{PV} larger at their E_{bg}, a spectral region where the blue sub-cell cannot absorb. On the opposite, the increased EQE_{PV} of thicker devices at lower wavelengths will compete with the EQE_{PV} of the blue sub-cell, decreasing its complementarity. However, the thickness dependence

studied for this 2-J RAINBOW system can not be extrapolated to a general rule, and more systems should be studied to better understand the thickness dependence in RAINBOW devices.

4.4 CONCLUSIONS AND OUTLOOOK

In this chapter we have proved the feasibility of the RAINBOW solar cell multi-junction architecture which consists of a lateral (horizontal) array of solar cells, illuminated with spectrally split sunlight. The individual junctions, with distributed band gaps, are laid out so that each sub-cell is illuminated with a wavelength range that closely matches the band gap of the semiconductor in that particular position. The main advantages of this architecture include its relatively flat form factor, high compatibility with roll-to-roll technologies, no stacking defect accumulation, lower active layer material consumption compared to any other multi-junction geometry and, finally, the simple implementation of an N-terminal configuration.

Using simulations, we defined design rules for the selection of materials and devices. The RAINBOW device is optimized when choosing materials with maximum EQE_{PV} value matching (rather than current matching) as well as low thermal losses particularly in the blue sub-cells. We used these criteria to select three active layer blends, namely, PM6:IO-4Cl, PM6:Y6 and PTB7-Th:COTIC-4F, with band gaps that cover a wide range of the solar spectrum. Theoretically, the efficiency increase over the best cell (IoBC) that we could obtain for two-junction cells with the selected materials is up to 46%. We then used a purposely made experimental setup (SOLS) that helped us validate the simulations, thus providing a theoretical tool for material and device screening. With the SOLS setup, we achieved an IoBC of close to 46% for the wide-narrow band gap RAINBOW combination which has PM6:IO-4Cl as blue sub-cell and PTB7-Th:COTIC-4F as red sub-cell.

We manufactured two proof of concept monolithic RAINBOW devices using the partial coverage deposition technique. The combination between PM6:IO-4Cl and PTB7-Th:COTIC-4F yielded an IoBC of 39.50% arising from reduced thermalization losses, while RAINBOW combinations based on PM6:Y6 and PTB7-Th:COTIC-4F, resulted in an 11.47% IoBC, in good agreement with simulations that explain this improvement in terms of enhanced photocurrent arising from a significant reduction in absorption losses. We have also quantified the thermalization and absorption losses for each RAINBOW system, understanding the nature of the improvement in the lateral

multi-junction geometry. Our results demonstrate the feasibility and significant potential of the RAINBOW concept, inviting the community to explore novel combinations, demonstrate multi-junctions with more than two sub-cells, and design efficient dispersive elements.

Finally we performed some simulations to understand the role of active layer thickness on RAINBOW performance. We expected that the higher FF and narrower EQE_{PV} range of thin layers benefited the RAINBOW efficiency. Nevertheless, for the material system studied (PM6:IO-4Cl and PTB7-Th:COTIC-4F as blue and red sub cells respectively) we found that thiner sub cells were not specially favouring higher RAINBOW efficiencies since the highest RAINBOW efficiency was achieved for the best-performing single-junction devices. Thinner sub-cells had a higher IoBC compared to thicker devices attributed to its EQE_{PV} having a higher complementarity degree.

5 WIDE BAND-GAP ORGANIC PHOTOVOLTAICS

As seen in Chapter 4, having a good-performing wide band gap sub-cell in a RAINBOW configuration is crucial for achieving higher efficiencies. Nevertheless, the field lacks studies on active layer materials that are able to achieve efficiencies as close to the theoretical limit as those exhibited by mid- and low-band-gap cells. In this chapter, we have explored different donor:acceptor combinations in a combinatorial screening manner. The donors used are PM6, PTQ10, and D18, while the acceptors used are IO-4Cl, PMI-FF-PMI, and O-IDFBR. The latter led to 9 different donor:acceptor combinations processed from 2 solvents, chloroform (CF) and chlorobenzene (CB). These combinations achieved remarkably high V_{oc} with values between 1.1 and 1.4 V, and in most cases being higher than 1.25 V. The novel blend PTQ10:O-IDFBR is the most promising active layer because of its high V_{oc} (1.35 V) is accompanied by one of the highest efficiency achieved in the combinatorial study (6.87 %). Selected devices were also studied regarding voltage loss characterization during a two-month stay at Prof. Thomas Kirchartz's labs in Forschungszentrum Jülich.

The developed wide band-gap materials were studied in different applications such as indoor light harvesting and RAINBOW geometries. As indoor light harvesters, the PTQ10:O-IDFBR blend reached an efficiency of 22.6% with a V_{oc} of 1.21 V. The same blend used as blue sub-cell in a RAINBOW geometry promises to lead to high efficiencies, with a predicted $PCE_{R,max}$ of 13.12% and 14.50% in 2-J and 3-J configuration, respectively. Finally, a research stay at EURECAT technological center, in Mataró, under the supervision of Dr. Ignasi Burgués Ceballos was done to investigate on the up-scalability of the PTQ10:O-IDFBR blend.

5.1 INTRODUCTION

Organic photovoltaics (OPVs) have recently surpassed 20% efficiency, mainly thanks to the development of non-fullerene acceptors (NFAs) during the last years.[44, 55, 218, 219, 220, 221] These molecules exhibit stronger absorption and broader energy level tunability compared to the fullerene acceptors used since the early days of OPV technology.[222] The increased color tunability, as a result of the development of NFAs, together with the advantages of organic solar cells, such as their light weight, flexibility, and up-scalability, have expanded the range of applications of organic photovoltaics.

In this context, wide energy band-gap (E_{bg}) OPV (here meaning cells with photo-active layer energy band-gaps E_{bg} > 1.8 eV) are promising for harvesting light whose spectrum and conditions differ from the AM1.5G solar spectrum. This is the case, for example, for underwater light harvesting. Depending on water depth, sunlight becomes increasingly filtered in color.[172, 206] In general, this results in a blue-shift of the Shockley-Queisser optimum bad-gap as as a function of depth, from the well-known 1.34 eV to values higher than 2 eV, depending on water depth and geographical area.[22, 172] Yang et al. have already shown 23.11% efficiency with the wide E_{bg} blend PM6:IO-4Cl at a depth of 5 m.[206] Another relevant application of wide E_{bg} OPV is the harvesting of indoor light, in which the benchmarck efficiency reached 36%.[9] Other works also achieve high efficiencies with different materials and strategies, therefore showing the potential of OPV for indoor light harvesting.[8, 173, 205, 223, 224, 225, 226] For this application, wide E_{bg} cells are needed since the light source to be harvested is typically a light-emitting diode (LED), emitting between 400 and 700 nm with a variable spectrum depending on the LED bulb.[182, 227] Therefore, devices with E_{bg} < 1.8 eV are expected to suffer from unnecessarily high thermalization losses.

An example of the spectrum dependence on water depth is shown in Figure 3.1 (c)

Few examples of the LED spectra are shown in Figure 3.1 (b).

In this thesis, the application that motivated the study of wide E_{bg} OPV are RAINBOW multi-junction solar cells. During the previous chapters, we have demonstrated the importance of the wide E_{bg} sub-cell in multi-junction devices as well as the need for an efficient sub-cell with low voltage losses to reduce thermalization losses. Wide E_{bg} sub-cells are essential not only for RAINBOW devices but also for tandem multi-junction, where the current matching condition imposes J_{sc} to be similar to the other sub-cells.[133, 197, 218, 219, 228, 229] Therefore, wide E_{bg} sub-cells need special attention due to the fewer investigations performed as compared to narrow E_{bg} sub-cells.[7, 220]

As demonstrated in the literature, organic solar cells exhibit higher voltage losses compared to other photovoltaic technologies such as perovskites or silicon solar cells, resulting in a lower open-circuit voltage (V_{oc}).[7, 133, 230] The latter is understood as one of the main factors limiting the efficiency of organic solar cells. Precisely, non-radiative voltage losses (ΔV_{oc}^{nr}), due to the low emissivity nature of the charge-transfer state, are responsible for the high voltage loss compared with other technologies.[231, 232] Nevertheless, literature also shows that as charge-transfer state energy increases, non-radiative voltage losses decrease.[52, 59] Therefore, wide E_{bg} organic solar cells, prone to having higher charge-transfer state energies, a lower ΔV_{oc}^{nr} should be expected. Nonetheless, their efficiency is still far from the ther-

modynamic limit. In this case, the photo-generated current seems to be the bottleneck.[7, 52] Due to the different methodologies used for characterizing voltage losses, the field lacks of a systematic comparison of voltage losses to understand better the efficiency limitation of wide E_{bg} solar cells.[52, 231, 233, 234]

Additionally, the fast development of NFAs is generating a vast library of materials, thus opening enormous possibilities for active layer blends. Although efforts have been invested in developing a material selection and efficiency prediction algorithm, this is still an unsolved question for organic photovoltaics.[21, 235, 236] In this scenario, high-throughput and combinatorial screening approaches are needed to discover efficient donor:acceptor blends faster.

5.2 COMBINATORIAL SCREENING

5.2.1 *Active layer materials*

5.2.1.1 *Materials selection and benchmarcking*

Figure 2.5 of Chapter 2 shows the chemical structure of the materials serving as electron-donors (D18,[237, 238] PTQ10,[239, 240] and PM6[56, 206]) and electron-acceptors (O-IDFBR,[51, 241, 242] PMI-FF-PMI,[133] and IO-4Cl[176, 205, 237]) used as components in the different active layers. The chosen materials are all wide band-gap materials, with E_{bg} between 1.78 and 2.07 eV ($\approx$ 700 and 600 nm, respectively) as discussed in Section 5.2.1.3.

The main goal of this combinatorial screening study was to test novel donor:acceptor materials combinations to find promising wide E_{bg} candidates. D18 was chosen as a donor with a relatively wide E_{bg}, which has shown a high efficiency of nearly 18% when blended with the benchmark non-fullerene acceptor Y6.[238, 243] Hofinger et al. also demonstrated that D18:Y6 cells exhibit a low ΔV_{oc}^{total} of 0.51 V with especially low ΔV_{oc}^{nr} of 0.20 V.[237] The donor polymer PTQ10 is a promising donor due to its low synthetic complexity and high efficiency, surpassing 16% when blended with Y6.[239, 244] The other donor material is PM6, whose efficiency, when blended with Y6, can surpass 17%.[39, 56] It is the donor exhibiting the lowest band-gap, but it has already demonstrated very high efficiencies also for indoor applications, surpassing 26% when blended with IO-4Cl,[205] and reaching up to 36% in combination with Y6 and 2PACz.[9] PM6:IO-4Cl blend is used in this work as a reference therefore IO-4Cl is also included as NFA. PMI-FF-PMI is an NFA synthesized by J. Hofinger et al. which has shown V_{oc} over 1.4 V when blended with D18 and deposited by spin

coating. Therefore, this blend possesses one of the highest V_{oc} reported in organic solar cells, with an efficiency of 5.34%.[133] The third NFA used is O-IDFBR, first synthesized by Baran et al. in 2017, achieving an efficiency of 11% in a ternary blend with PTB7-Th.[242] Afterwards, few studies address this NFA.[51, 241, 245] To the best of our knowledge, most of the tested donor:acceptor combinations have not been explored in literature. The only two exceptions are PM6:IO-4Cl and D18:PMI-FF-PMI, as shown in Table 5.1.

	PTQ10	D18	PM6
IO-4Cl	*	*	[205, 206]
O-IDFBR	*	*	*
PMI-FF-PMI	*	[133]	*

Table 5.1: State of the art of the wide E_{bg} blends explored. To the best of our knowledge, * denotes donor:acceptor combinations which are not explored in literature

5.2.1.2 *Fabrication*

The materials and methods section (Chapter 2) presents the solar cell fabrication process within the NANOPTO group. Nevertheless, here we describe some active layer composition and fabrication details that are essential for this chapter because of the number of conditions tested.

Each donor:acceptor combination was prepared from chlorobenzene (CB) and chloroform (CF) solutions separately, therefore giving a total of $3\times3\times2 = 18$ different solutions and active layers. The solutions were prepared in a 1:1.5 donor:acceptor ratio, except for the case of PMI-FF-PMI solutions, where the donor:acceptor ratio was 1:1 according to reference [133]. Almost all active layer materials were dissolved attaining the same concentration of 20 mg/mL, irrespective of the solvent. D18-based solutions were diluted down to 10 mg/mL due to their observed high viscosity at 20 mg/mL. The solutions were maintained in continuous stirring at 40°C and 80°C for CF and CB, respectively, for a minimum of 4 h to ensure proper dissolution of the solutes. The active layers were deposited via blade coating with a velocity varying from 90 mm/s to 10 mm/s along the substrate, achieving a thickness gradient from 200 to 50 nm, approximately.[241] Finally, all samples were encapsulated to increase its stability.

Figure 5.1 contains images of all 18 substrates prepared, showing the thickness gradient along the samples. It is interesting to see the variety of colors of the active layers even though all its components have similar E_{bg}. The color the human eye perceives is mainly affected by the spectrum reaching the eye between 400 and 700 nm.[246] Therefore,

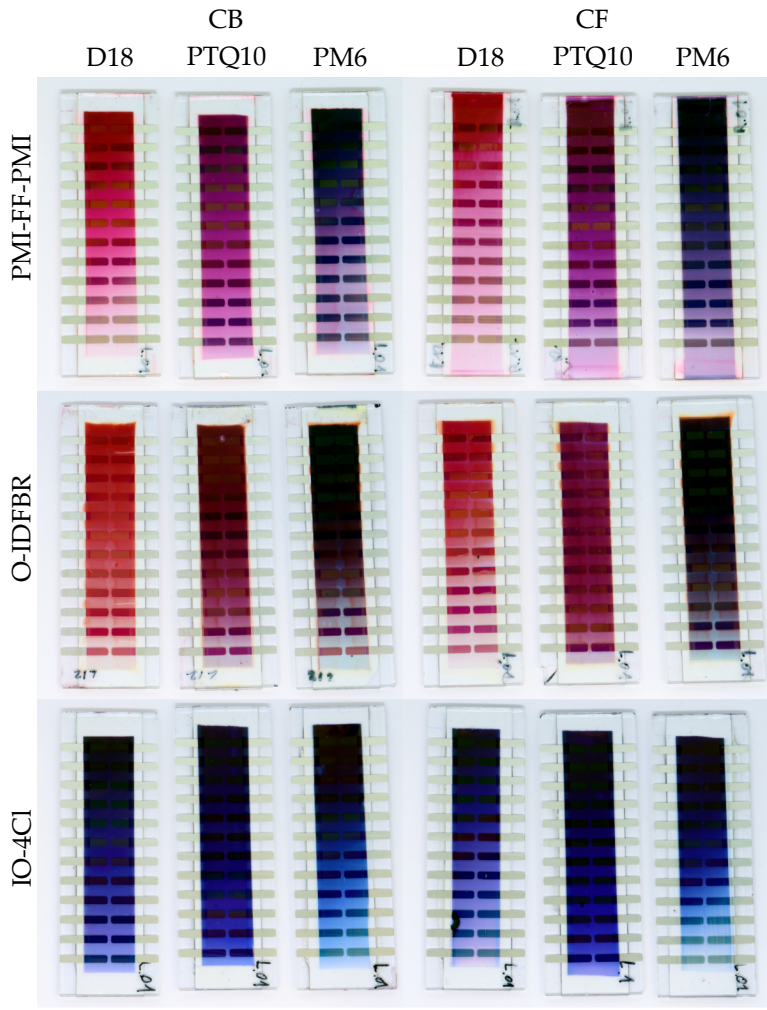

Figure 5.1: Photographs of the 18 samples prepared in the wide E_{bg} combinatorial screening. The color gradient in each sample corresponds to the thickness gradient of the active layer. The different colors of different active layers denote the different band-gaps and absorption profiles of donors and acceptors used.

we attribute the different colors to the fact that the E_{bg} of the materials is in between 600 and 700 nm, where small differences in E_{bg} and absorption spectrum shape strongly impact the perceived color. These color differences are also interesting to consider for applications like semi-transparent OPV, where color is meaningful.

5.2.1.3 *Optical properties*

Figure 5.2 shows the HOMO and LUMO energy levels for the active layer materials. The values correspond to cyclic voltammetry (CV) measurements taken from literature [205, 239, 242, 243] except for the case of PMI-FF-PMI, whose literature energetic levels were measured using electrochemical voltage spectroscopy (EVS).[133] According to the HOMO and LUMO levels, all donor-acceptor combinations form staggered (type-2) hetero-junctions (i.e., $LUMO_{donor} > LUMO_{acceptor} > HOMO_{donor} > HOMO_{acceptor}$) meaning that they could work as organic solar cells. Additionally, due to the similar E_{bg} between all materials, the difference between $HOMO_{donor}$ and $HOMO_{acceptor}$ (ΔHOMO) as well as the difference between $LUMO_{donor}$ and $LUMO_{acceptor}$ (ΔLUMO) lay between 0.2 and 0.4 eV, being similar offsets compared to the standard value of 0.3 eV for efficient exciton dissociation.[52] However, note that some materials have shown high efficiencies (and therefore efficient enough exciton dissociation) with ΔHOMO or ΔLUMO lower than 0.3 eV.[55, 56, 57] It is worth mentioning that since we have both donor and acceptor materials with similar E_{bg}, a low ΔHOMO implies a low ΔLUMO (and vice-versa). This is not the case for most of the literature works that study small ΔHOMO or ΔLUMO, for which, to achieve a broad absorption spectrum, the materials composing the active layer are chosen to absorb in different regions of the solar spectrum (i.e., significantly different E_{bg}).

Additionally, all six materials were characterized with ellipsometry to assess their refractive index, n, and extinction coefficient, k, (Figure 5.3). From the measured k, we have inferred the band-gap energy (E_{bg})

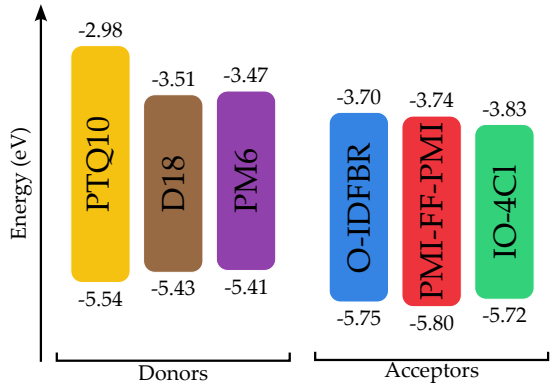

Figure 5.2: HOMO and LUMO energy levels of the materials selected for the wide E_{bg} combinatorial screening. The energetic levels values are taken from references [133, 205, 239, 242, 243] and are measured by cyclic voltammetry except for the acceptor PMI-FF-PMI that was measured by electrochemical voltage spectroscopy.

of each material as the inflection point of the extinction coefficient edge. Table 5.2 shows the resulting E_{bg}. Additionally, E_{bg} can also be calculated from the difference between the HOMO and LUMO values shown in Figure 5.2. Table 5.2 shows a comparison between both methodologies to measure E_{bg}. In that comparison, one can see that the PTQ10 has an exceptionally high HOMO-LUMO difference compared to the E_{bg} value calculated from k. The latter suggests that the reported LUMO for PTQ10 may be overestimated or that PTQ10 aggregation in the solid film significantly affects its LUMO energy (through the gas-to-solid shift). The same comparison for the other materials yields percentage differences lower than 7.5%, indicating a better agreement between the reported HOMO and LUMO energy levels and the measured extinction coefficient, k.

Material	E_{bg} (eV)		Difference	
	Ellipsometry	HOMO-LUMO	(eV)	(%)
D18	2.064	1.92	-0.144	-6.977
PTQ10	2.010	2.56	0.550	27.363
PM6	1.935	1.94	0.005	0.258
O-IDFBR	2.221	2.05	-0.170	-7.699
PMI-FF-PMI	2.127	2.06	-0.067	-3.150
IO-4Cl	1.888	1.89	0.002	0.106

Table 5.2: Comparison of E_{bg} of materials measured with different methods. Energy band gap of active layer materials calculated as the inflection point of the extinction coefficient (k) measured with ellipsometry compared to the difference between LUMO and HOMO found in the literature (Figure 5.2). The last two columns correspond to the difference between the two E_{bg} values in absolute and percentual values concerning the ellipsometric measurement.

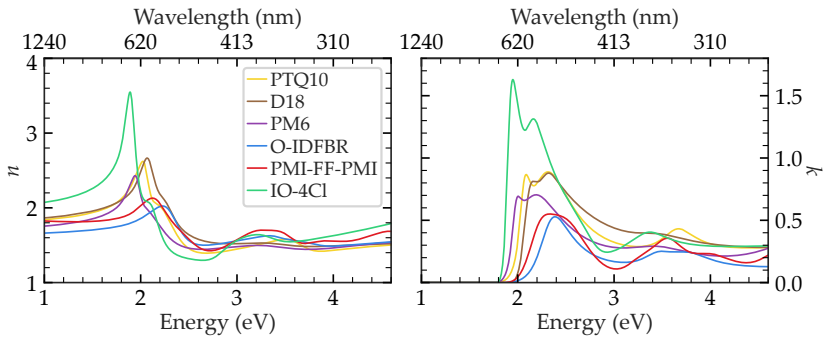

Figure 5.3: Refractive index n and extinction coefficient k of the wide E_{bg} donors and acceptors. n and k measured via ellipsometry by Ms. Arianna Quesada-Ramírez are plotted against energy in the bottom axis, and the corresponding wavelengths are shown in the top axis.

5.2.1.4 *Moprhology-related aspects*

The morphology of the active layer is a key parameter to achieve the best possible performance for any blend. There are many parameters related to device fabrication that can affect the active layer morphology: deposition technique, deposition temperature, or annealing conditions are just a few examples. Among them, the solvent is one of the most important because it directly affects the drying dynamics of the film during deposition. For example, a solvent with a higher boiling point, such as chlorobenzene (CB), will give donor and acceptor molecules more time to reorder before drying, typically resulting in more ordered films. On the contrary, a solvent with a lower boiling point, such as chloroform (CF), will tend to evaporate faster, quenching the disordered wet film and typically resulting in more amorphous domains. The different solubility of active layer components with the solvent is also an important factor during the formation of the thin film, which directly relates to the final morphology.

In order to evaluate the effect of the solvent on the morphology of PTQ10:O-IDFBR active layer we measured grazing incidence wide angle X-ray scattering (GIWAXS) with the help of Dr. Matteo Sanviti and Dr. Jaime Martín from Universidade da Coruña. We blade-coated O-IDFBR, PTQ10, and PTQ10:O-IDFBR films from CF and CB on silicon substrates. The results of the GIWAXS measurements performed by our collaborators are shown in Figure 5.4. PTQ10 exhibits a stronger crystalline signal when deposited from CB, due to the higher boiling point of the solvent. For O-IDFBR, there is no significant difference between CF and CB GIWAXS patterns. For the blend film, CB processing leads to higher long-range order than CF. This agrees with the previously discussed role of solvent evaporation during film drying. As we will show below, for PTQ10:O-IDFBR, the best performance is achieved with CB, which shows higher structural order than CF in its GIWAXS data. The latter is also in agreement with the previous assumption that the ideal morphology for any organic solar cell active layer is closer to the crystalline donor and acceptor domains rather than amorphous.

The same characterization was done for the blend PTQ10:IO-4Cl. The GIWAXS patterns (Figure 5.5) suggest packing motifs where NFA molecules pack into 1D-chain or multidimensional mesh-like structures.[247, 248] Because 1D- or mesh-like packing motifs feature continuous aromatic structures that are separated by aliphatic domains, many large d-spacing symmetry planes exist, which are expected to give rise to multiple diffraction peaks in the low-q region, as found in our patterns.[247, 248, 249] Nevertheless, when IO-4Cl is blended

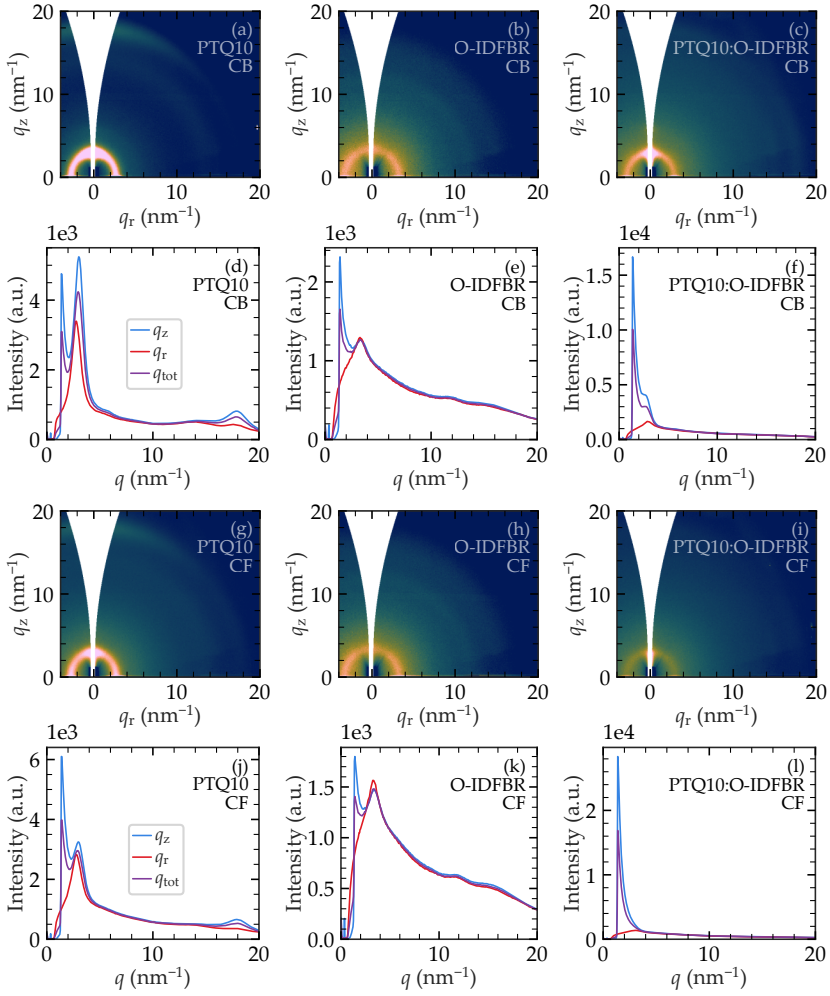

Figure 5.4: GIWAXS results for PTQ10:O-IDFBR material system deposited from CB and CF. (a)-(c) and (g)-(h) are the diffractograms for the neat materials and the blends.(d)-(f) and (i)-(k) are their corresponding in-plane (q_r, red), out of plane (q_z, blue), and total (q_{tot}, purple) integrated intensities.

with PTQ10, these reflections vanish and only the reflection from the lamellar-like packing of PTQ10 is observed. On the other hand, IO-4Cl deposited from CF shows a less defined (broader) GIWAXS signal, indicating less ordered crystalline domains. Nevertheless, the blend shows a GIWAXS signal preserving both donor and acceptor separately, indicating that both PTQ10 and IO-4Cl have a certain degree of crystallinity. Therefore, the assumption is also true since the blend with higher structural order (in this case deposited from CF) shows higher efficiency (see below).

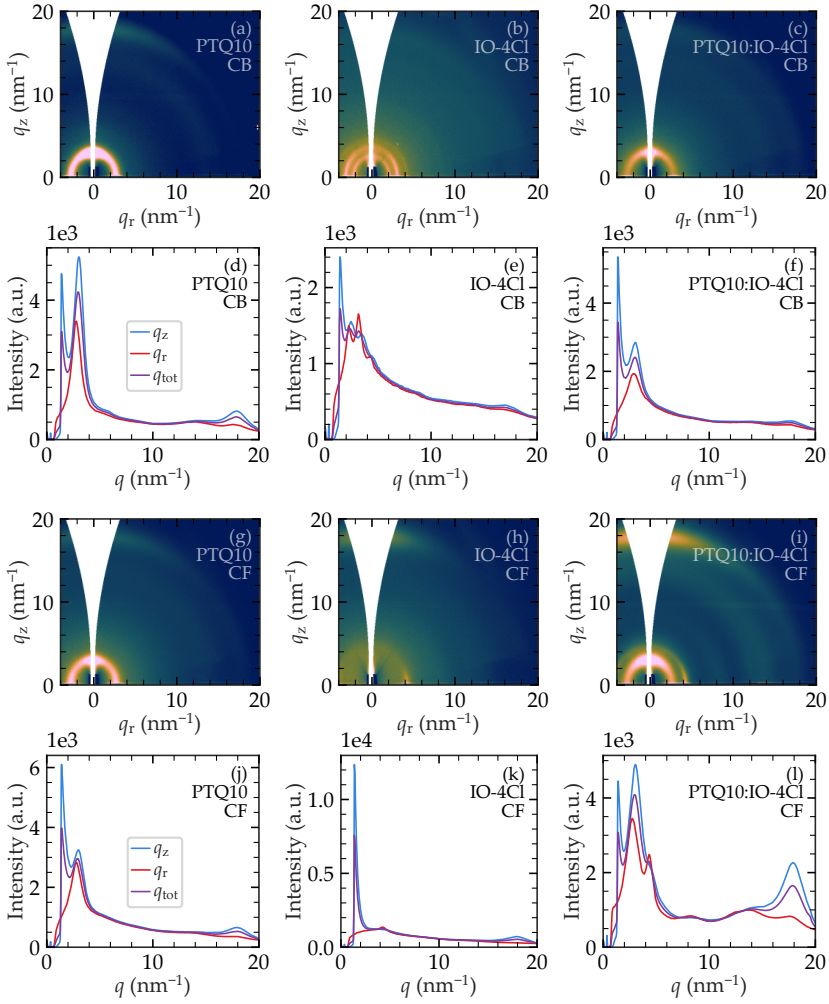

Figure 5.5: GIWAXS results for PTQ10:IO-4Cl material system deposited from CB and CF. (a)-(c) and (g)-(h) are the diffractograms for the neat materials and the blends. (d)-(f) and (i)-(k) are their correspondings in-plane (q_r, red), out of plane (q_z, blue), and total (q_{tot}, purple) integrated intensities.

The d-spacing, d, and the coherence length, L_c, were collected for all the samples from the 1D integrations of the GIWAXS diffractograms shown in Figure 5.4 and Figure 5.5. Table 5.3 summarizes lamellar stacking of the polymer donor, (100) planes, and other contributions, such as π - π stacking (010) as well as characteristic peaks from the acceptors at lower q values. Compared to the pure donor, the (100) planes of the blends seem to shift towards lower d values. Nevertheless, no direct correlation of such information with structural changes can be directly pointed out since the contribution from the acceptor at lower q can alter the peak position. Thus, it is hard to give reliable assessments of structural

changes of donor domains in the blend compared to the pure donor film.

Sample	Solvent	(100)		(010)		low q					
		d (nm)	L_c (nm)	d (nm)	L_c (nm)	d (nm)	L_c (nm)	d (nm)	L_c (nm)	d (nm)	L_c (nm)
PTQ10	CB	2.25	5.79	0.35	2.46						
	CF	2.24	5.48	0.35	2.49						
O-IDFBR	CB					1.90	6.44				
	CF					1.89	6.45				
PTQ10:O-IDFBR	CB	2.13	5.76	0.36	1.99						
	CF	2.09	4.46	-	-						
IO-4Cl	CB			0.38	6.13	2.78	20.44	1.99	8.87	1.49	4.88
	CF			0.35	3.25					1.49	10.91
PTQ10:IO-4Cl	CB	2.15	5.15	0.36	4.78						
	CF	2.07	5.76	0.35	3.07					1.46	14.82

Table 5.3: d-spacing (d) and coherence length (Lc) analysis for (100), (010) planes, and low q region. Data was calculated from GIWAXS diffractograms shown in Figure 5.4 and Figure 5.5.

In conclusion, the performance differences between CF- and CB-processed blends arise from their different microstructures. Additionally, the results show that the optimization of the latter cannot be predicted from the solvent choice because there is no clear tendency of one solvent to achieve better performance devices than the other for specific materials. This suggests that the boiling point is not the only parameter playing a role and other properties like solubility are also important.[250, 251]

5.2.2 $J-V$ characterization

All cells (24) for each of the 18 samples shown in Figure 5.1 were characterized by measuring their $J-V$ curve under a Xenon arc-lamp solar simulator. The latter can be done easily and rapidly thanks to the Pika demultiplexer developed by Dr. Martí Gibert-Roca and shown previously in Section 2.3.1. In this section, we discuss these results by analyzing the dependence of V_{oc}, J_{sc}, FF, and PCE on active layer composition. Figure 5.6 shows an example of the power conversion efficiency (PCE) dependence on thickness from the described measurement on the sample of PTQ10:O-IDFBR deposited from the CB solution. Not all 24 devices were completely operative. In this case, there were discrepancies in the two replicas (right and left) of cells number 1, 3, 11, and 12. Nevertheless, it is easy to recognize thickness-dependent tendencies.

The Pika demultiplexer reduces up to 90% the time spent in characterization.[159]

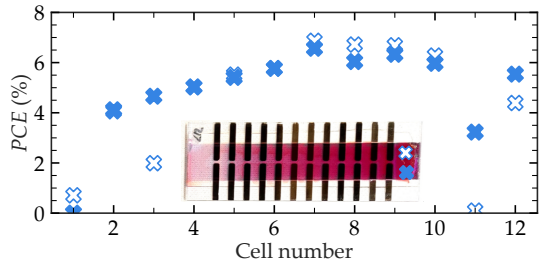

Figure 5.6: Dependence of PCE on active layer thickness. Power conversion efficiency (PCE) as a function of the cell pixel number (i.e., thickness) for a PTQ10:O-IDFBR cell deposited from chlorobenzene solution. The inset shows the substrate with a thickness gradient achieved by varying blade-coater speed. In the plot, thickness is increasing from cell number 1 to 12.

Donor	Acceptor	Solvent	V_{oc} (V)	J_{sc} (mA/cm^2)	FF (%)	PCE (%)
PTQ10	O-IDFBR	CF	1.33	8.05	50.85	5.44
PTQ10	O-IDFBR*	CB	1.35	9.06	56.05	6.87
PTQ10	PMI-FF-PMI	CF	1.38	3.63	39.52	1.98
PTQ10	PMI-FF-PMI	CB	1.36	1.70	37.80	0.87
PTQ10*	IO-4Cl*	CF	1.25	10.16	57.51	7.31
PTQ10	IO-4Cl	CB	1.22	8.09	56.37	5.55
D18	O-IDFBR	CF	1.29	5.16	47.08	3.15
D18	O-IDFBR	CB	1.33	3.92	50.49	2.62
D18	PMI-FF-PMI	CF	1.28	5.81	42.26	3.14
D18	PMI-FF-PMI*	CB	1.33	5.35	49.49	3.53
D18*	IO-4Cl	CF	1.24	8.32	57.13	5.91
D18	IO-4Cl	CB	1.21	8.13	51.85	5.10
PM6	O-IDFBR	CF	1.23	5.93	41.02	2.99
PM6	O-IDFBR	CB	1.24	4.91	48.95	2.98
PM6	PMI-FF-PMI	CF	1.26	2.20	43.07	1.19
PM6	PMI-FF-PMI	CB	1.26	2.48	52.49	1.64
PM6*	IO-4Cl	CF	1.18	9.29	57.03	6.23
PM6	IO-4Cl	CB	1.15	9.00	58.18	6.02

Table 5.4: Figures of merit from $J-V$ measurements. $J-V$ curves results of the best-performing devices for each combination tested. The * indicates the best-performing device for each of the tested active layer materials, which $J-V$ curves are shown in Figure 5.7.

In all cases, the best cell considered for each material and solvent combination was the one with the highest PCE within the thickness range, with its replica having a similar efficiency value. Therefore, we

can say that the thickness is an optimized parameter. Table 5.4 shows the figures of merit (FoM) of the best-performing devices. Additionally, Figure 5.7 shows the $J - V$ curves from the best-performing cells of each material (donors and acceptors) as an example of some of the best-performing cells of the combinatorial screening study.

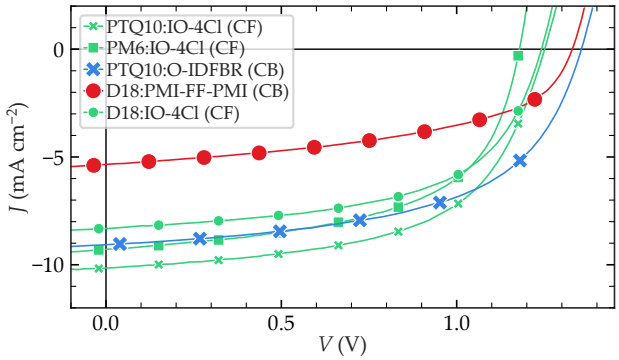

Figure 5.7: $J - V$ curves of the best-performing cells for each of the six materials tested (donors and acceptors). The corresponding FoMs of the measurements can be found at Table 5.4 marked with *.

5.2.2.1 V_{oc} and PCE

The results of the best-performing devices shown in Table 5.4 are summarized in Figure 5.8, where the *PCE* for each donor-acceptor combination deposited from CB and CF solvents is plotted against their V_{oc}. The colors (red, blue, and green) indicate the acceptor used (PMI-FF-PMI, O-IDFBR, and IO-4Cl, respectively). The colored ellipses are the central regions where the points of each cell with the same acceptor are located within a one standard deviation confidence range (σ). From these regions, it is clear that devices containing IO-4Cl achieve higher efficiencies but lower V_{oc} compared to O-IDFBR- and PMI-FF-PMI-based devices because the confidence ellipse is located more in the upper left part. Nevertheless, the PTQ10:O-IDFBR cells (both deposited from CF and CB) are an exception and, apart from being the only O-IDFBR devices with efficiencies comparable to those of IO-4Cl-based cells, its V_{oc} is among the highest measured in all combinations.

In Figure 5.8, another important tendency is that devices containing PTQ10 as the donor (cross-shaped points) achieve the highest V_{oc} observed for each acceptor. The latter is also shown in Figure 5.9, where V_{oc} is plotted as a heatmap for CF (a) and CB (b) processed blends. In Figure 5.9, all rows are darker in the PTQ10 column, indicating that PTQ10-based devices achieve always the highest V_{oc} regardless of

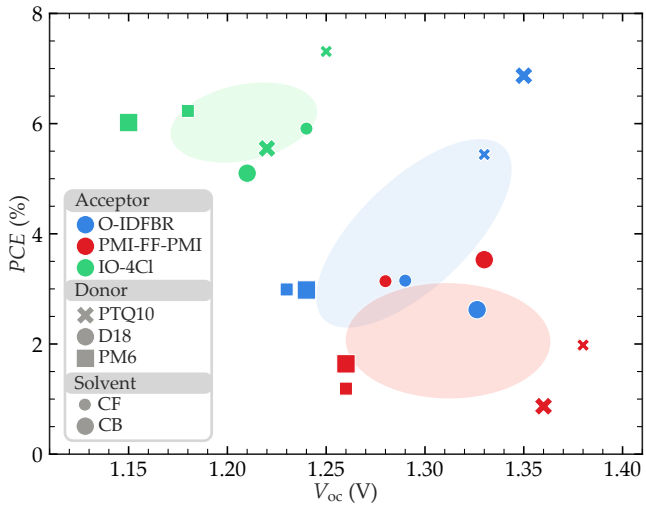

Figure 5.8: Best power conversion efficiency (PCE) values as a function of the corresponding V_{oc} achieved for each donor-acceptor-solvent combination. The 18 points are taken from a total of 432 devices where the thickness is optimized for each combination due to the thickness gradient. The colored ellipses represent confidence regions for the cells containing each acceptor with a σ confidence.

acceptor material or solvent processing. That is the case for PTQ10:PMI-FF-PMI deposited from CF where the V_{oc} of 1.38 V is the highest achieved; for PTQ10:O-IDFBR blend deposited from CB with a V_{oc} of 1.35 V; as well as for the IO-4Cl:PTQ10 blend deposited from CF with a V_{oc} of 1.25 V. On the contrary, the lowest V_{oc} for each acceptor occurs always for devices containing PM6, with V_{oc} of 1.15 V, 1.23 V and 1.26 V when blended with IO-4Cl, O-IDFBR, and PMI-FF-PMI from CB, CF, and CF, respectively. Devices based on D18 as the donor show V_{oc} values in between those of PTQ10 and PM6-based solar cells.

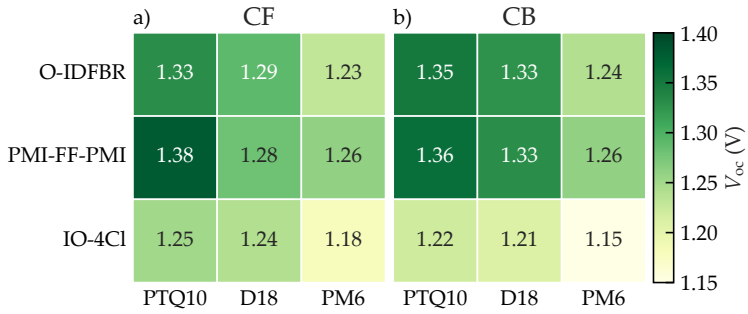

Figure 5.9: V_{oc} heatmap of all donor-acceptor-solvent combinations. The open circuit voltage of the best-performing devices deposited from CF (a) and the CB (b) is shown as a heatmap for each donor:acceptor combination.

The V_{oc} is directly related to the energetic difference between the $LUMO_{acceptor}$ and the $HOMO_{donor}$, therefore, when comparing blends with the same acceptor, the deeper the $HOMO_{donor}$, the higher the V_{oc} expected. This behavior agrees with the energy levels of the three donors shown in Figure 5.2, where the HOMO level of PTQ10 and PM6 are the deepest and the shallowest, respectively. Notice that, in this simplified scenario, we are assuming that $LUMO_{acceptor}$ and $HOMO_{donor}$ do not depend on the materials blended, which may not be valid due to differences in morphology of donor and acceptor regions in the blend compared to pure material films as well as compared to the conditions where energetic levels were measured (typically in solution for electrochemical methods). We also assume that V_{oc} losses are equal for all blends, which may not be true. When plotting the $HOMO_{donor}-LUMO_{acceptor}$ difference versus V_{oc} (Figure 5.10), we observe a strong linear correlation between both parameters with a slope near 1 and a high Pearson's correlation parameter (r = 0.84) indicating that this simplified scenario is valid, at least, for this study. Nevertheless, the difference in V_{oc} between CF and CB processing of the same blend material cannot be explained by this simple model.

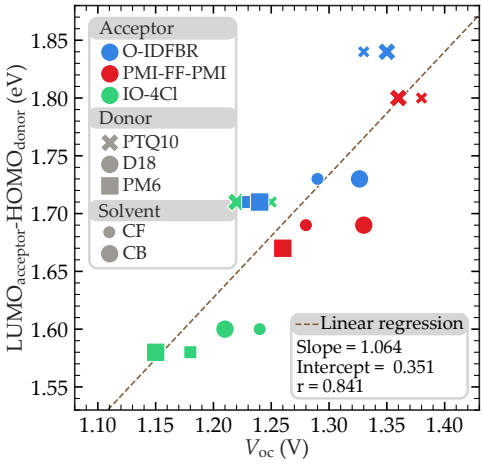

Figure 5.10: Energy difference between $LUMO_{acceptor}$ and the $HOMO_{donor}$ as a function of V_{oc}. The data points fit a linear regression with a slope of 1.06, suggesting the direct relation between the $LUMO_{acceptor} - HUMO_{donor}$ difference and the V_{oc}. The high Pearson's correlation coefficient (r = 0.84) is also a sign of the strong correlation between the two parameters.

For most of the donor:acceptor combinations, there is no literature to benchmark our results, highlighting the novelty of the tested donor:acceptor combinations. Nonetheless, we obtained somewhat lower efficiencies for the few cases where data are available (see Table 5.5). For example, Y. Cui et al. reached 9.80% efficiency for

Ref.	Active layer		Device geometry	Deposition technique	V_{oc} (V)	J_{sc} (mA/cm^2)	FF (%)	PCE (%)	Area (cm^2)
	Donor	Acceptor							
[205]	PM6	IO-4Cl	Normal	Spin coating	1.24	11.6	68.10	9.80	1
[206]	PM6	IO-4Cl	Normal	Spin coating	1.22	10.42	61.56	7.80	0.04
*	PM6	IO-4Cl	Inverted	Blade coating	1.15	9.00	58.18	6.02	0.08
[133]	D18	PMI-FF-PMI	Normal	Spin coating	1.41	6.09	60.9	5.34	0.1
*	D18	PMI-FF-PMI	Inverted	Blade coating	1.33	5.35	49.49	3.53	0.08

Table 5.5: Benchmark of PM6:IO-4Cl and D18:PPMI-FF-PMI active layer systems. Benchmark with literature for solar cells made with PM6:IO-4Cl and D18:PMI-FF-PMI deposited from CB as active layer materials. * in the reference column indicate the devices in this work.

PM6:IO-4Cl cells deposited from CB, with a V_{oc} of 1.24 V;[205] and Y. Yang et al. achieved 7.80% with a V_{oc} of 1.22 V for the same active layer material.[206] Nevertheless, when comparing these results to ours (PCE of 6.20% and V_{oc} of 1.15 V for PM6:IO-4Cl deposited from CB), it is important to consider that we are using the inverted architecture and depositing the active layer from blade coating. The latter is compatible with industrial roll-to-roll fabrication needed for up-scaling organic solar cells. On the other hand, the benchmark works use spin coating instead of blade coating, which is not a roll-to-roll-compatible coating technique. Additionally, the benchmark works use the standard architecture differing from our inverted devices (i.e., different ETL, HTL, and top electrode materials)

At this point, we want to comment on the IO-4Cl devices, which are the more efficient cells in the combinatorial screening study. We tested two different batches of IO-4Cl bought from the same provider. The results for the first tested batch of IO-4Cl are shown in Figure 5.11. In that case, the efficiency of the best devices did not exceed 5%. Furthermore, these results correspond to the best cells of a long optimization process where different processing conditions, such as donor:acceptor ratio, co-solvent addition, or ETL materials were optimized. In contrast, the second IO-4Cl batch tested improved all the previous cells on the first try with the conditions described in the experimental section (i.e., without further optimization), exceeding 5% when blended with all three donors regardless of the CB or CF solvent. With this insight, we want to highlight the importance of repeatable material fabrication processes for improved batch-to-batch repeatability. Furthermore, this is highly relevant for the commercialization of organic solar cell technologies.

The other combination found in the literature is D18:PMI-FF-PMI. J. Hofinger et al. achieved a PCE of 5.34% with a V_{oc} of 1.41 V.[133] These

values are considerably higher than our results (PCE = 3.53% and V_{oc} = 1.33 V). In this case, the reference work also used the standard architecture and deposited the active layer by spin coating compared to our blade-coated inverted devices. Table 5.5 shows a comparison of our devices with the benchmark works, where it can be seen that all the $J-V$ FoM are responsible for the efficiency difference between our devices and the literature.

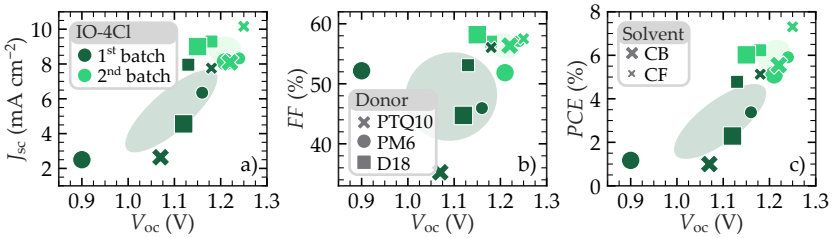

Figure 5.11: $J-V$ measurements results for the two IO-4Cl batches used. PCE (a), J_{sc} (b), and FF (c) as a function of V_{oc} for two different IO-4Cl batches. The performance of the 2nd batch (light green) is much better than the first altough both are bought from the same provider. The 2nd batch corresponds to the IO-4Cl used in the combinatorial screening study.

Owing to the important differences in device architecture between this study and the benchmark results, it is also worth comparing with the typical values obtained in our group. For example, FF is typically the weaker point of our cells, with typical values between 50 and 60%. J_{sc} is also a weak point, usually approximately 10% lower than that of the state of the art. In contrast, the V_{oc} that we obtain is generally in better concordance with the reported state of the art cells. Considering this and looking at Table 5.5, we can say that FF and J_{sc} are inside the expected values according to our experience. Nevertheless, V_{oc} is lower than what we would expect, which suggests that there is still room for improvement in all combinations to achieve higher PCE by improving the V_{oc}.

5.2.2.2 *FF and J_{sc}*

The PCE values are spread in a large range of almost one order of magnitude, from 0.82% for PTQ10:O-IDFBR in CB to 7.31% for PTQ10:IO-4Cl in CF. Nevertheless, not all figures of merit exhibit such large variations. For example, the fill factor (FF), shown as a function of V_{oc} in Figure 5.12, varies between 40 and 60% without a clear correlation with V_{oc}. IO-4Cl-based devices show a FF which is independent of the V_{oc} while O-IDFBR and PMI-FF-PMI show a positive and a negative correlation, respectively.

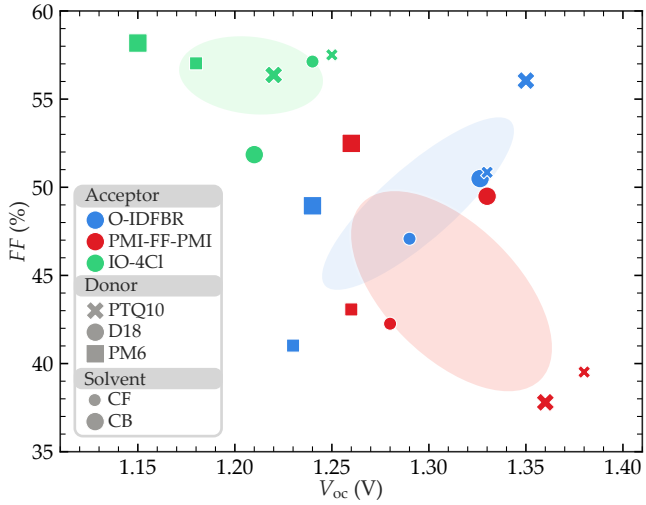

Figure 5.12: FF vs. V_{oc} for the 18 best-performing devices of the combinatorial screening. The coloured ellipses represent confidence regions for the cells containing each acceptor with a σ confidence.

The parameter which has the highest change and therefore affects more the PCE is the J_{sc}. Figure 5.13 (a) shows that J_{sc} varies almost one order of magnitude, between 1.35 mA/cm^2 and 10.16 mA/cm^2 (Figure 4 (a)). Similar to the PCE, the cells based on IO-4Cl as acceptor have the highest J_{sc} compared to PMI-FF-PMI and O-IDFBR devices. In other words, for every donor (different data-point shape in Figure 5.13 (a)) the cell containing IO-4Cl has the highest J_{sc}. The latter is in agreement with the extinction coefficients Figure 5.3, which show that IO-4Cl is the acceptor with the highest k at its absorption peak and, at the same time, the acceptor with the lowest energy band-gap (E_{bg}), being about 0.4 eV lower than O-IDFBR and PMI-FF-PMI. The latter is also highlighted in Figure 5.13 (b), where EQE_{PV} from IO-4Cl devices with the different donors (green lines) show a similar optical E_{bg}, while the others containing O-IDFBR (blue) and PMI-FF-PMI (red) have a higher E_{bg} than the IO-4Cl devices containing the same donor.

Although small, the E_{bg} difference between acceptors is in the spectral region where the flux of photons is the highest in all solar spectrum. Therefore, a small E_{bg} difference can make an important impact on the overall J_{sc}. This effect is clearly demonstrated by the Shockley-Queisser (SQ) limit, in which the EQE_{SQ} is considered to be zero for photons with energy lower than the E_{bg} and 100% for energies equal or higher than E_{bg}. However, the SQ limit assumes ideal, perfect absorption, exciton dissociation, and free-charge carrier transport to the contacts within the solar cells. The latter results in

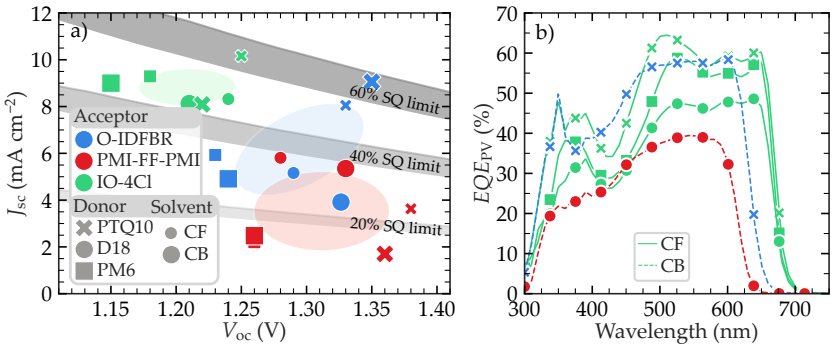

Figure 5.13: J_{sc} results. (a) J_{sc} as a function of V_{oc} for the best-performing cells of each donor-acceptor-solvent combination. The colored ellipses represent confidence regions for the cells containing each acceptor with a 1σ confidence. Fractions (60, 40, and 20%) of the Shockley-Queisser are plotted considering an E_{bg} of $V_{oc} + \Delta V_{oc}^{total}$ with $0.6 < \Delta V_{oc}^{total} < 0.7$ eV. (b) External quantum efficiency (EQE_{PV}) for some of the best-performing cells.

a J_{sc} decrease when increasing E_{bg}. For comparison, Figure 5.13 (a) also shows different fractions (60, 40, and 20%) of the SQ limit (grey areas) considering a total voltage loss of ΔV_{oc}^{total} = 0.6 V (upper limit) and ΔV_{oc}^{total} = 0.7 V (lower limit), with $E_{bg} = qV_{oc} + \Delta\ V_{oc}^{total}$. The IO-4Cl devices lay between 60 and 40% of the SQ limit, while O-IDFBR and PMI-FF-PMI devices (except for the PTQ10:O-IDFBR) have a J_{sc} between 40 and 20% of the SQ limit, in some cases even lower. This indicates that the decrease in J_{sc} is not only related to an increase in the E_{bg}, which would be related to absorption losses as described by the SQ limit, but also to a worse exciton separation and/or free-charge carrier extraction. Only PTQ10:O-IDFBR cells have a SQ limit J_{sc} percentage similar to PTQ10:IO-4Cl in CF, which indicates that the J_{sc} difference between those two cells is the expected from its E_{bg} difference. Nevertheless, the J_{sc} of the best devices being inside the 60% range shows that there is still room for improvement.

5.2.3 V_{oc} *loss analysis*

In general, the total voltage loss (ΔV_{oc}^{total}) is defined as the energy difference between the E_{bg} of the solar cell and the measured open-circuit voltage (V_{oc}) under AM1.5G illumination, therefore given by $\Delta V_{oc}^{total} = E_{bg}/q - V_{oc}$. E_{bg} is the optical band-gap of the cell, which can be defined in different ways, but typically, it is calculated as the inflection point of the EQE_{PV} edge. The V_{oc} is proportional to the natural logarithm of the ratio between the short-circuit current density

(J_{sc}) and the dark current density (J_0). The latter can be further divided into four quotients to give:[231]

$$V_{oc} = \frac{k_B T}{q} \ln\left(\frac{J_{sc}}{J_0}\right) = \frac{k_B T}{q} \ln\left(\frac{J_{sc}^{SQ}}{J_0^{SQ}} \frac{J_{sc}}{J_{sc}^{SQ}} \frac{J_0^{SQ}}{J_0^{rad}} \frac{J_0^{rad}}{J_0}\right) \tag{5.1}$$

Here J_{sc}^{SQ} and J_0^{SQ} correspond to the short-circuit and the saturation current density in the Shockley-Queisser limit, respectively, and J_0^{rad} corresponds to the saturation current density in the radiative limit. Equation 5.1 can be rewritten as a sum of four terms:

$$V_{oc} = V_{oc}^{SQ} - \Delta V_{oc}^{sc} - \Delta V_{oc}^{r} - \Delta V_{oc}^{nr} \tag{5.2}$$

Each term on the right side of Equation 5.2 has a different physical meaning.[231] The first term corresponds to the V_{oc} at the SQ limit (V_{oc}^{SQ}). The difference between E_{bg} and V_{oc}^{SQ} is understood as a thermodynamical loss due to the difference in solid angles between the incoming light and the radiation emitted by the cell as a black body, also known as *étendue* expansion.[81] The latter can be mitigated theoretically by equalizing both solid angle values, which can be done by sunlight concentration or by forcing the radiative emission to be at the same angle as the incoming light. We expect this difference to be constant in our cells since they have similar E_{bg} and we took all the measurements at the same temperature and light concentration conditions.

The short-circuit loss term (ΔV_{oc}^{sc}) in Equation 5.2 corresponds to the difference between the measured J_{sc} and the SQ value, J_{sc}^{SQ}. The main origin of this difference is the fact that the EQE_{SQ} is considered 100% for photons with energy higher than the E_{bg}, i.e., each photo-generated electron-hole pair is collected at the cell contacts. Nevertheless, this is never the case in a real cell, and the maximum EQE_{PV} is below 100%. Since J_{sc} is rarely lower than 10% of the J_{sc}^{SQ}, this loss is typically low. On the other hand, the radiative voltage loss (ΔV_{oc}^{r}) in Equation 5.2 can be more important. The latter is related to the energy difference between the emission peak and the E_{bg} of the cell. Even a small energy difference can result in a value of hundreds of millivolts. This is due to the exponential energy dependence of the spectrum emitted by the solar cell. The last term in Equation 5.2 is the non-radiative voltage loss (ΔV_{oc}^{nr}) which is the difference between the measured V_{oc} and the V_{oc} at the radiative limit, V_{oc}^{r}. ΔV_{oc}^{nr} considers all losses due to non-radiative recombination mechanisms such as trap-assisted (Shockley-Read-Hall) recombination.

For the V_{oc} losses analysis, V_{oc}^{SQ}, ΔV_{oc}^{sc}, and ΔV_{oc}^{r} were calculated using the current densities calculated as follows:

$$J_{sc}^{SQ} = q \int EQE_{SQ}(E)\ \varphi_{AM1.5G}(E)\, dE \tag{5.3}$$

$$J_{sc} = q \int EQE_{PV}(E)\ \varphi_{AM1.5G}(E)\, dE \tag{5.4}$$

$$J_{0}^{SQ} = q \int EQE_{SQ}(E)\ \varphi_{BB}(E)\, dE \tag{5.5}$$

$$J_{0}^{rad} = q \int EQE_{PV}(E)\ \varphi_{BB}(E)\, dE \tag{5.6}$$

Here $\varphi_{AM1.5G}$ and φ_{BB} are the 1 sun and black-body spectrum respectively. In the definition of φ_{BB}, we are considering the geometry of our solar cells, i.e., the active layer only emits to its front side due to the Ag electrode acting as a back reflector.[82] The Shockley-Queisser limit is well-known and studied, with values (V_{oc}^{SQ}, J_{sc}^{SQ}, FF^{SQ}, and PCE^{SQ}) being tabulated elsewhere (see Figure 1.12).[82] Therefore, the calculation of V_{oc}^{SQ} is a good opportunity to double-check the methodology used for calculating the different current density terms.

The Shockley-Queisser EQE (EQE_{SQ}) is a step-function that is 100% and 0% above and below E_{bg}

The integral for the determination of J_{0}^{rad} (Equation 5.6) is dominated by the lower energy tail of the EQE_{PV} spectrum due to the exponential nature of the black-body spectrum (φ_{BB}).[59, 237, 252] Therefore, to achieve a reliable J_{0}^{rad} value, one needs a highly sensitive EQE_{PV} with several orders of magnitude. The standard EQE_{PV} characterization (used in the cells of this section of the thesis) comprising an arc-lamp light source and a monochromator is not enough for the proper characterization of V_{oc} losses. For this reason, we need to improve the dynamic and spectral range of the measured EQE_{PV}. According to Rau,[252] the EQE_{PV} of a solar cell is equivalent to the quotient between the electroluminescence quantum efficiency (EQE_{EL}) and the black-body spectrum (φ_{BB}). EQE_{EL} is understood as the spectral distribution of the photons emitted by the cell when a current is applied to it. Its integral over the spectrum has to account for the total number of emitted photons per injected electron (expressed in %). This measurement is difficult to perform due to the challenge of collecting all emitted photons because their emission is generally omnidirectional. Nevertheless, assuming that the spectral shape is homogeneous in all directions and taking advantage of the relation between EQE_{EL} and EQE_{PV}, we can assess EQE_{EL} by measuring the EL spectrum (φ_{EL}) and the EQE_{PV}. This is done by assuming that $EQE_{EL} = a \cdot \varphi_{BB}$, where a is a factor that is fitted to the relation between EQE_{PV} and EQE_{EL}:

$$EQE_{PV} = \frac{EQE_{EL}}{\varphi_{BB}} = \frac{a \cdot \varphi_{EL}}{\varphi_{BB}} \tag{5.7}$$

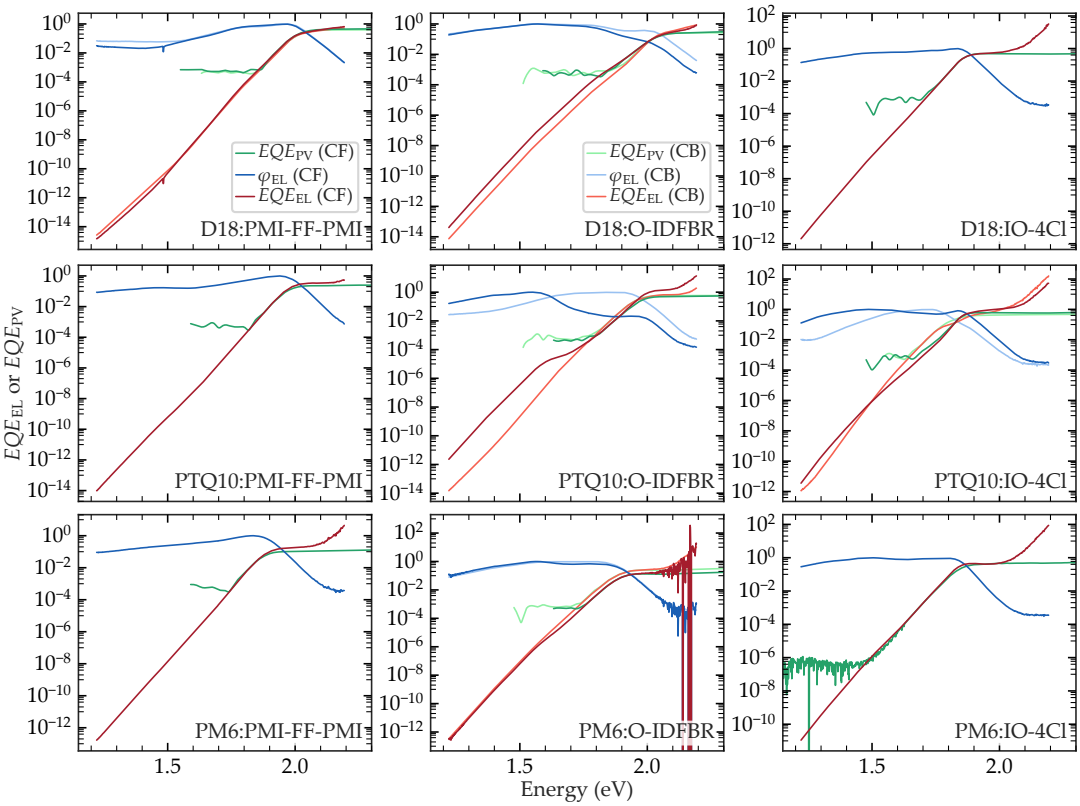

Figure 5.14: EL fits for extend the EQE_{PV} for V_{oc} losses calculations. The φ_{EL} divided by the φ_{BB} (red) is fitted to the EQE_{PV} (green) in low energy EQE_{PV} region where its edge shows a linear behaviour in the logarithmic scale. The plots also show the EL resulting from the fitted spectrum (blue). The light and dark colors stand for CF and CB processed devices respectively. The data from the blends D18:IO-4Cl, PTQ10:PMI-FF-PMI, PM6:PMI-FF-PMI and PM6:IO-4Cl prepared by CB is missing because they were not measured.

Figure 5.14 shows the EQE_{EL} (in blue) as well as the EQE_{PV} and the EQE_{EL}/φ_{BB}. The fitting of the factor a is done in the range where EQE_{PV} and φ_{EL} overlap. The latter occurs around the energy band gap of the material. The final extended EQE_{PV} used for the V_{oc} loss analysis is taken as EQE_{EL}/φ_{BB} for energies below the fit range, the measured EQE_{PV} for energies above the fit range and the average between both inside the fit range.

The non-radiative voltage loss term (ΔV_{oc}^{nr}) was calculated as the difference between the radiative open-circuit voltage, V_{oc}^{r}, and the measured V_{oc}. V_{oc}^{r} is the sum of the first three terms on the right side of Equation 5.1, which results in:

$$V_{oc}^{r} = \frac{k_B T}{q} \ln\left(\frac{J_{sc}}{J_0^{rad}}\right) \tag{5.8}$$

Table 5.6 shows the J_{sc} and the J_0^{rad} resulting from the extended EQE_{PV} using Equation 5.5 and Equation 5.6. It is interesting to compare the measured and the calculated J_{sc} to see the accuracy of the EQE_{PV} measurement. The theoretical and the measured values are close in all cases except for the PM6:O-IDFBR blend processed from CF, where EQE_{PV} is lower than expected (see also the corresponding plot in Figure 5.14). This could be due to a bad measurement of that device or due to device degradation. Table 5.6 also shows the calculated V_{oc}^{r}.

All values resulting from the V_{oc} loss analysis can be found at Table 5.7, while Figure 5.15 shows them in a bar plot manner. The overall voltage loss is around 0.6 to 0.7 V. Considering that voltage loss in literature lies between 0.5 and 0.8 V,[52] our results are in the middle range, without being especially low or high. The difference between V_{oc}^{SQ} and E_{bg}/q is maintained constant around 0.3 V. This is the value one may expect from the Shockley-Queisser limit,[22] especially considering that with the same illumination conditions, the only parameter that can affect this difference is the E_{bg}, which is similar for all devices.

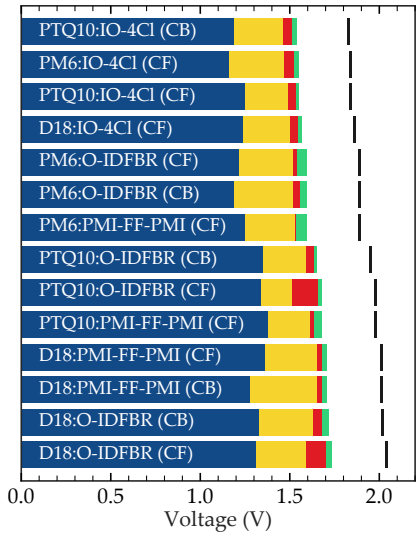

Figure 5.15: ΔV_{oc} loss analysis. Open-circuit voltage losses due to a nonideal short-circuit current density (ΔV_{oc}^{sc}, green), due to radiative recombination (ΔV_{oc}^{r}, red), and due to non-radiative recombination (ΔV_{oc}^{nr}, yellow) for the different solar cells studied. The cells are ordered in ascending order (from top to bottom) in E_{bg}/q, which corresponds to the black line.

In general, the largest voltage loss is ΔV_{oc}^{nr} (yellow boxes in Figure 5.15), which varies from 0.17 V for PTQ10:O-IDFBR in CF, up to 0.38 V for D18:PMI-FF-PMI in CB. The ΔV_{oc}^{nr} is especially interesting

Active layer materials			$J_{sc}^{calculated}$ (mA/cm^2)	V_{oc}^{r} calculations		
Donor	Acceptor	Solvent		J_{sc} (mA/cm^2)	J_0 (mA/cm^2)	V_{oc}^{r} (V)
D18	PMI-FF-PMI	CB	4.95	4.94	$7.60 \cdot 10^{-28}$	1.66
D18	PMI-FF-PMI	CF	5.05	5.59	$8.92 \cdot 10^{-28}$	1.65
D18	O-IDFBR	CB	3.85	3.34	$1.25 \cdot 10^{-27}$	1.63
D18	O-IDFBR	CF	4.48	3.76	$6.46 \cdot 10^{-27}$	1.59
D18	IO-4Cl	CF	8.32	7.65	$3.95 \cdot 10^{-25}$	1.51
PTQ10	PMI-FF-PMI	CF	3.44	3.12	$2.14 \cdot 10^{-27}$	1.62
PTQ10	O-IDFBR	CB	9.06	8.31	$1.37 \cdot 10^{-26}$	1.59
PTQ10	O-IDFBR	CF	7.97	7.27	$2.68 \cdot 10^{-25}$	1.51
PTQ10	IO-4Cl	CB	7.47	7.62	$2.01 \cdot 10^{-24}$	1.46
PTQ10	IO-4Cl	CF	10.53	10.16	$8.80 \cdot 10^{-25}$	1.49
PM6	PMI-FF-PMI	CF	2.16	1.94	$3.63 \cdot 10^{-26}$	1.53
PM6	O-IDFBR	CB	5.00	4.43	$1.35 \cdot 10^{-25}$	1.52
PM6	O-IDFBR	CF	5.93	2.38	$7.37 \cdot 10^{-26}$	1.52
PM6	IO-4Cl	CF	9.83	7.05	$1.32 \cdot 10^{-24}$	1.47

Table 5.6: Results of V_{oc}^{r} calculation. The good agreement between the measured J_{sc} and the calculated J_{sc} denotes that the measured EQE_{PV} is correct.

Active layer materials			V_{oc} values (V)				V_{oc} losses (V)			
Donor	Acceptor	Solvent	V_{oc}	V_{oc}^{r}	V_{oc}^{SQ}	$q\,E_{bg}$	ΔV_{oc}^{nr}	ΔV_{oc}^{r}	ΔV_{oc}^{sc}	ΔV_{oc}^{total}
D18	PMI-FF-PMI	CB	1.28	1.66	1.71	2.01	0.38	0.03	0.02	0.73
D18	PMI-FF-PMI	CF	1.36	1.65	1.71	2.01	0.29	0.02	0.03	0.65
D18	O-IDFBR	CB	1.33	1.63	1.72	2.02	0.30	0.04	0.05	0.69
D18	O-IDFBR	CF	1.31	1.59	1.74	2.04	0.28	0.03	0.11	0.73
D18	IO-4Cl	CF	1.24	1.51	1.57	1.86	0.27	0.02	0.04	0.62
PTQ10	PMI-FF-PMI	CF	1.38	1.62	1.68	1.98	0.24	0.04	0.02	0.60
PTQ10	O-IDFBR	CB	1.35	1.59	1.65	1.95	0.24	0.02	0.04	0.60
PTQ10	O-IDFBR	CF	1.34	1.51	1.68	1.98	0.17	0.02	0.15	0.64
PTQ10	IO-4Cl	CB	1.19	1.46	1.54	1.83	0.27	0.02	0.05	0.64
PTQ10	IO-4Cl	CF	1.25	1.49	1.55	1.84	0.24	0.02	0.04	0.59
PM6	PMI-FF-PMI	CF	1.25	1.53	1.60	1.89	0.28	0.06	0.01	0.64
PM6	O-IDFBR	CB	1.19	1.52	1.60	1.89	0.33	0.04	0.04	0.70
PM6	O-IDFBR	CF	1.22	1.52	1.60	1.89	0.30	0.05	0.03	0.67
PM6	IO-4Cl	CF	1.16	1.47	1.55	1.84	0.31	0.02	0.05	0.68

Table 5.7: Tabulated values of V_{oc} losses analysis. The V_{oc} values are the different V_{oc} calculated following the procedure described in this section. The difference between them (ΔV_{oc}) correspond to the different voltage losses associated to non-radiative (ΔV_{oc}^{nr}), radiative (ΔV_{oc}^{r}), and due to J_{sc} difference (ΔV_{oc}^{sc}). The total voltage loss is also shown (ΔV_{oc}^{total}).

since, a priori, it is the parameter that can be more affected by the engineering of materials and processing conditions. This is the case, for example, of the PTQ10:O-IDFBR blend. When the blend is processed from CB, the cell has a higher V_{oc} showing lower ΔV_{oc}^{total}. Nevertheless, the blend processed from CF shows the lowest ΔV_{oc}^{nr} of 0.17 V at expenses of the highest ΔV_{oc}^{r} of 0.15 V, which are significantly different from the values measured with the same blend processed from CB (0.24 and 0.04 V, respectively). This is directly related to the measured EL spectrum shown in the central panel of Figure 5.14 where it can be seen that the highest EL peak of the PTQ10:O-IDFBR blend processed from CB is centered at 1.95 eV while for the blend deposited from CF is approximately at 1.55 eV. The latter results in a difference of two orders of magnitude in the EQE_{PV} tail, yielding a J_0^{rad} ten times larger for the CF-processed device. Following Equation 5.8, the difference between both blends is approximately $k_B T/q \ \ln(10) = 0.06$ V which is roughly the difference between the V_{oc}^{r} of the CF and the CB-processed solar cells (1.51 and 1.59 V respectively). We attribute this considerable difference in EL spectrum to the different microstructure, as suggested by GIWAXS data discussed in Section 5.2.1.4. The increased intensity of the lower energy EL peak of the CF-processed cell indicates a higher recombination of injected electron-hole pairs through the charge-transfer state. On the other hand, the CB-processed cell shows a stronger emission of the singlet state of the donor and/or the acceptor materials (it is difficult to discern due to the overlap of both materials EL emission). The latter, together with GIWAXS data, suggests that the CF-processed blend has more donor-acceptor interfaces due to a more intermixed blend, while the CB-processed blend has larger domains of pure donor and acceptor.

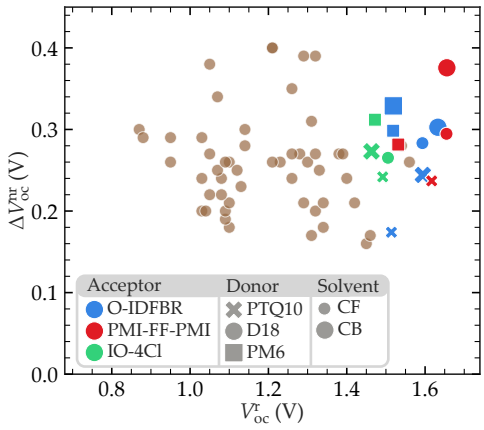

Figure 5.16: ΔV_{oc}^{nr} as a function of V_{oc}^{r} compared with literature from reference [52].

Figure 5.16 shows the ΔV_{oc}^{nr} as a function of the V_{oc}^{r}. We observe that, even for a systematic study like the case of this work, there is a big dispersion of values. The latter is also seen in the literature values (Figure 5.16, brown points), indicating the difficulty of predicting ΔV_{oc}^{nr}.[52] This study adds data points to the existing literature, especially in the high V_{oc}^{r} region. The ΔV_{oc}^{nr} lay between 0.25 and 0.35 V, similar to the literature values trend.

5.2.4 *FCC-Cl as a promising wide band-gap NFA*

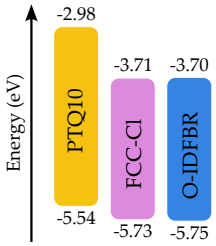

Figure 5.17: Energy levels of PTQ10, FCC-Cl, and O-IDFBR.

We have recently explored an interesting acceptor material, motivated by the various applications of wide band-gap photovoltaics such as indoor light harvesting or RAINBOW solar cells. In the work by Bai et al., they design and synthesize a non-fullerene acceptor (NFA) named FCC-Cl.[253] The HOMO and LUMO levels that they report are similar to those of O-IDFBR (see Figure 5.17). Nevertheless, they show a red shift of about 50 nm in the absorption spectrum of the FCC-Cl in film compared to solution. The latter is attributed to the high crystallinity of the NFA, a feature not present in O-IDFBR. Therefore, optical properties show that FCC-Cl blends are a good candidate for wide band-gap applications. They report blends of FCC-Cl with D18 and PM6 donors. As mentioned before, these donors are interesting candidates for wide band-gap photovoltaics. The D18:FCC-Cl devices were fabricated with the normal geometry with ITO/PEDOT:PSS/AL/PDI-NO/Al while PM6:FCC-Cl were fabricated with the inverted geometry (and the same ETL and HTL materials used in our labs). In both cases, the cells were prepared by spin coating. Under 1 sun illumination the D16:FCC-Cl blend achieves a PCE of 13.1% with a V_{oc} of 1.08 V, a J_{sc} of 16.04 mA cm^{-2} and a FF of 76.0%.[253] The PM6:FCC-Cl blend achieved similar values with a PCE of 13.0% with a V_{oc} of 1.02 V, a J_{sc} of 16.22 mA cm^{-2} and a FF of 78.1%.[253]

These results motivated us to do a first trial with the FCC-Cl. We choose to use PTQ10 as the donor since we have seen that it showed higher V_{oc} due to its deeper HOMO level compared to D18 and PM6. Only two substrates with the PTQ10:FCC-Cl were prepared from a solution of 1:1.5 PTQ10:FCC-Cl in chlorobenzene. The results of the $J-V$ characterization at 1 sun of one substrate are presented in Figure 5.18. The other substrate showed similar results. The best cell exhibited a PCE of 10.98% with a V_{oc} of 1.07 V, a J_{sc} of 14.49 mA cm^{-2} and a FF of 70.63%. The thickness dependence of the different parameters is expected, with FF its maximum at a thinner active layer than the maximum of J_{sc}. Nevertheless, in this case, the effect of FF on device performance is more important than the effect of J_{sc} since FF decreases almost half its peak value (from

∼70% to ∼40%). The decrease in FF is due to an increase of series resistance, R_s, as expected from thicker devices at 1 sun illumination. This initial preliminary results will be investigated further in the future, in particular, using ternary blends with the idea of increasing V_{oc}, and the best combination used for both, indoor PV, and RAINBOW solar cells.

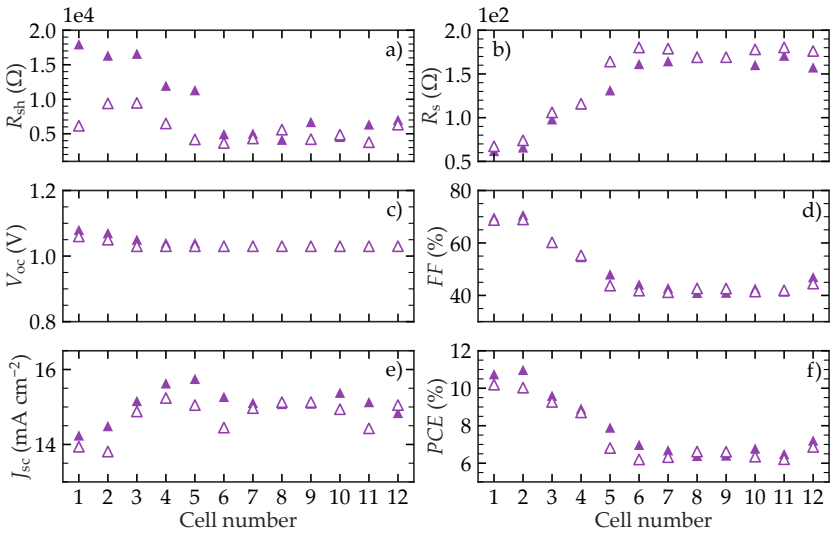

Figure 5.18: Thickness dependence FoM of PTQ10:FCC-Cl sample. Thickness increases with cell number. The different FoM are plotted against cell number. There is a good concordance between the right and the left side of the substrate (filled and empty triangle data points, respectively).

5.3 APPLICATION EXAMPLES OF WIDE BAND-GAP OPV

5.3.1 *Indoor light harvesting*

For indoor applications, wide band-gap active layer materials are especially interesting due to their E_{bg} matching indoor spectrum, which is especially true for the actual LEDs used in most modern indoor lighting. For the real application of OPV in indoor lighting, it is also worth mentioning the role of having a high V_{oc}, even if maintaining the efficiency results in lower J_{sc}. Imagine the case of two solar cells with the same efficiency and FF but different V_{oc} and J_{sc} values under AM1.5G illumination. Now, these cells are exposed to indoor light, which proportionally decreases J_{sc} by the same value (for example, three orders of magnitude). In this situation, the drop in efficiency due to the decrease in J_{sc} will be proportionally the same in both cells. Nevertheless, due to V_{oc} being proportional to the logarithm of J_{sc},

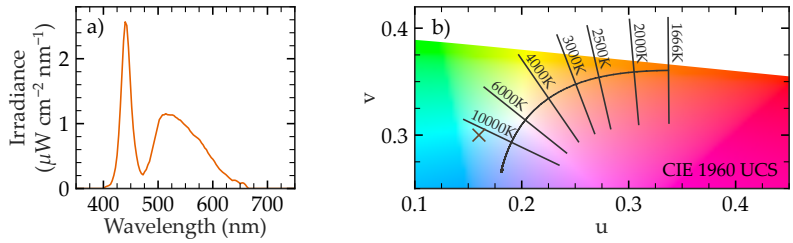

Figure 5.19: Characteristics of LED light source for indoor measurements Figure 5.20. (a) Irradiance spectrum of the LED light source used. (b) The corresponding color of the indoor spectrum in the CIE 1960 uniform chromaticity space (brown cross) at coordinates (u=0.16, v=0.30). The correlated color temperature of the spectrum is 12,200 K and the intensity is 560 Lux.

the 3 orders of magnitude drop in J_{sc} due to the reduced input light represents the same V_{oc} drop in absolute value regardless of the V_{oc} of the cell at AM1.5G. Therefore, a solar cell with a higher V_{oc} would benefit from a lower drop in efficiency percentage-wise, thus having a lower drop on the $V_{oc} \cdot J_{sc}$ product.

Due to its high E_{bg}, V_{oc}, and PCE, the PTQ10:O-IDFBR cells deposited from CB are good candidates for indoor light harvesting. This sample was measured under LED indoor light conditions, using a Wavelabs SINUS-70 LED solar simulator to generate a 560 Lux LED source with a correlated color temperature (CCT) of 12.200 K. The spectrum is shown in Figure 5.19 (a), and its color is plotted in the CIE 1960 uniform chromaticity space in Figure 5.19 (b). In the latter, we can see that the human eye sees the color of the tested spectrum as blueish, which is far from the D standard illuminants used as standards for commercial indoor lighting. Nevertheless, the closer point of the Planckian locus, which characterizes the CCT of the spectrum (Δ_{uv}), is lower than 0.05, $|\Delta_{uv}| < 0.05$. According to the CIE standards, the latter indicates that the calculated CCT is meaningful.[254]

Figure 5.20 (a) shows the thickness dependence of the measured efficiency under indoor lighting. The best-performing device corresponds to 4th pixel for both sides of the samples, achieving 22.6% on the right side (see the $J-V$ curve shown in Figure 5.20 (b)). The latter slightly differs from the measurement of the same sample under 1 sun illumination, which in that case corresponds to the 6th pixel. Thus, the optimum thickness for indoor is thicker than for AM1.5G illumination. This is due to different factors limiting efficiency at different light-intensity conditions.[184] For light intensities similar to the solar light, the main limiting factor is the series resistance, R_s.[184] The latter is proportional to J_{sc}, therefore, a thicker active layer, generally exhibiting higher J_{sc} due to an increased light absorption, will exhibit higher

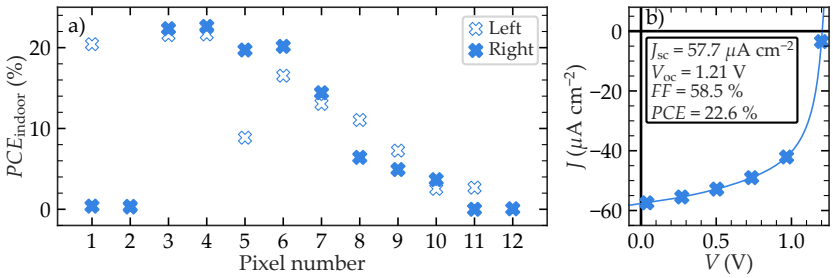

Figure 5.20: Indoor characterization of PTQ10:O-IDFBR deposited from CB sample. (a) efficeicny dependence on pixel (i.e., thickness) of the measured sample. (b) $J-V$ curve of the best performing device corresponding to the pixel number 4 of the right side.

R_s. The latter results in the maximum FF happening at a thinner active layer than the maximum J_{sc}. Thus, the optimal thickness is generally in-between. On the contrary, When the light intensity is a few orders of magnitude lower, i.e. similar to indoor conditions, R_s becomes negligible and the shunt resistance R_{sh} is the limiting factor. The latter depends on the leakage current of the device, which is mainly produced by active layer defects such as pinholes. The latter is reduced in thick films compared to thin. Therefore, the optimum FF generally moves to thicker active layers at low illumination. When the light power is reduced even more, the $J-V$ curve becomes a line without rectifying. The latter happens when R_{sh} is approaching the dark shunt resistance ($R_{sh,d}$). Therefore, a cell with a higher $R_{sh,d}$ can still work at lower light intensities.

In order to study the FF dependence on light intensity for the PTQ10:O-IDFBR system we have measured $J-V$ curves of two PTQ10:O-IDFBR devices at different light intensities in a wide dynamic range. The latter was done with the spectrum on demand light source (SOLS) explained in Chapter 3. The data points are the result of a red sweep measurement, as shown in Figure 3.11 (c). It means that different light intensities were achieved by blocking the blue part of the solar spectrum maintaining the red fraction constant. This implies that the spectrum at each data point does not have the same shape. Nevertheless, assuming that the generated charges thermalize before they are extracted, the shape variance of the spectrum is not an issue. As a first approximation, J_{sc} is the parameter analogous to the light intensity when the latter is maintained with a constant spectral shape. Figure 5.21 (a) shows the FF vs. R_{sh} for the red sweep of two PTQ10:O-IDFBR cells with different thicknesses (blue data crosses). The vertical lines show the $R_{sh,d}$ for both devices. As expected, the thicker device (dark blue) has a higher $R_{sh,d}$ due to lower leakage current. The latter results in a FF higher than the thin device (light blue) at lower

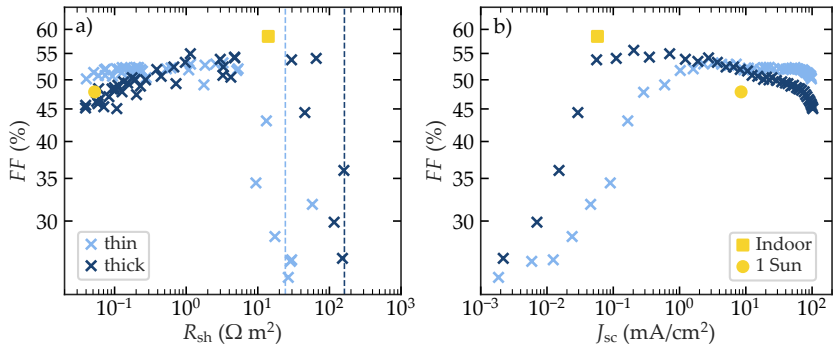

Figure 5.21: Evaluation PTQ10:O-IDFBR leakage with light-intensity dependent measurements. (a) Fill factor (*FF*) plotted against shunt resistance (R_{sh}) for a thin (light blue crosses) and a thick (dark blue crosses) measured at different light intensities during a red sweep using the custom Spectrum On Demand Light Source (SOLS). Dashed vertical lines correspond to the R_{sh} of both cells measured in dark $R_{sh,d}$. (b) *FF* vs. J_{sc} for the same data set. Yellow square in (a) and (b) corresponds to the data point of the solar cell measured under indoor conditions shown in Figure 5.20 (b). The yellow circle in (a) and (b) corresponds to the same cell measured under 1 sun.

intensities. On the opposite, at high intensities, the thin cell exhibits a higher *FF* due to its lower series resistance produced by a thinner active layer. The yellow squared and rounded data points correspond to the solar cell under indoor conditions for indoor illumination and 1 sun illumination, respectively. This cell at 1 sun has a *FF* in between the other two cells. Therefore, under indoor conditions, we expect this cell to behave between the blue data points, with a $R_{sh,d}$ in the middle. The corresponding square yellow data point is inside the expected trend, exhibiting a high *FF* at R_{sh} just below the $R_{sh,d}$ of the thinner device.

Similarly, Figure 5.21 (b) shows the *FF* vs. J_{sc} for the same red-sweep measurements. The tendency is expected since the thicker device (dark blue) exhibits a higher *FF* at low J_{sc} (i.e., low luminosity) while the thinner (light blue) shows higher *FF* at the J_{sc} region near 1 sun illumination. The yellow data points, corresponding to the cell characterized under indoor conditions for indoor illumination (yellow square) and 1 sun illumination (yellow circle), are also in between the behavior of the other two cells.

Figure 5.22 shows a comparison of the state of the art indoor organic photovoltaic devices in the literature according to references with LED-type light sources. To the best of our knowledge, the cell measured in this work made of PTQ10:O-IDFBR deposited from CB exhibits the highest V_{oc} achieved for indoor organic photovoltaics (V_{oc} = 1.21 V), and its indoor efficiency is among the best reported in the literature (*PCE* = 22.6%).

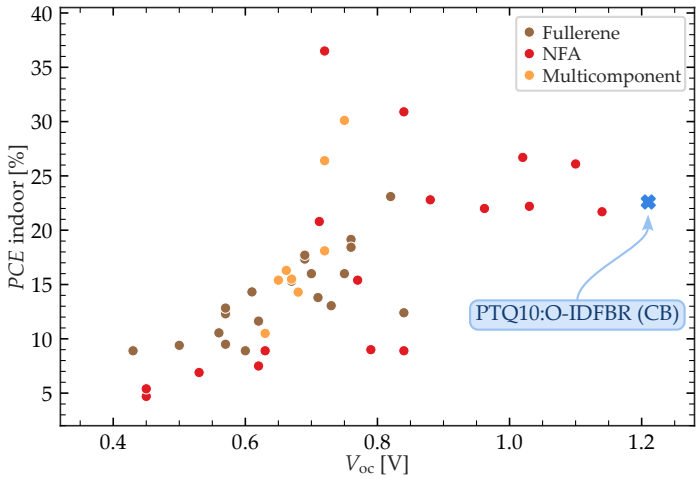

Figure 5.22: Comparison with the state of the art indoor organic solar cell efficiency. The state of the art data points are extracted from references [8, 9, 224, 225]. The record PTQ10:O-IDFBR cell has a V_{oc} of 1.21 V which is the highest reported for indoor cells, to the best of our knowledge.

5.3.2 *RAINBOW solar cells*

An application of wide E_{bg} solar cells is in multi-junction devices. The development and improvement of solar cells with E_{bg} higher than 1.8 eV directly impacts the efficiency of multi-junction PV. This is the case of the RAINBOW geometry studied in this thesis. In this subsection, we used the simulation model explained in Section 4.2.1 to study the potential of the materials tested in the combinatorial screening as blue sub-cells in 2-J and 3-J RAINBOW configuration.

5.3.2.1 *2-J RAINBOW solar cells simulations*

Red sub-cells data is taken from blends studied by Dr. Alfonsina Abat Amelenan Torimtubun, a post-doc colegue in my group. More details about the narrow band-gap materials can be found in reference [209]. Here we only considered the blends with PTB7-Th as donor, because they are the best-performing. Their efficiencies range from 7.42% for the PTB7-Th:SIOTIC-4F, to 10.45% for the PTB7-Th:Y6 blend.[209] As we have seen in Section 4.2.1.4, having similar efficiencies is a requisite for high IoBC. Therefore, the blue sub-cells data is taken from the materials studied in this chapter with efficiencies higher than 5%.

For these materials, we only have the EQE_{PV} of the best-performing cell and not its thickness dependence. Thus, we are considering only the best-performing device for each blend in the simulations. Additionally,

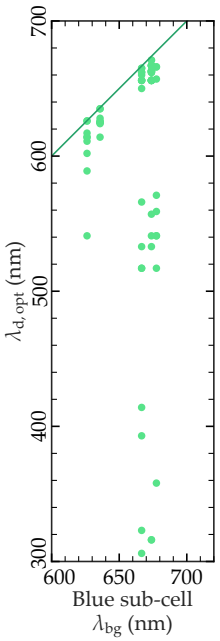

Figure 5.23: $\lambda_{d,opt}$ as a function of blue sub-cell's λ_{bg} of the 2-J RAINBOW simulations. The line corresponds to $\lambda_{d,opt} = \lambda_{bg}$.

λ_{bg} is the E_{bg} expressed in wavelength

for some of the CB processed blue sub-cells, we do not have the EQE_{PV}, and its corresponding CF processed data was used.

Figure 5.24 shows the RAINBOW FoM of the simulated 2-J RAINBOW solar cells. Red (horizontal axis) and blue (vertical axis) sub-cells are ordered by increasing efficiency as single junction. In Figure 5.24 (a) we see that the higher $PCE_{R,max}$ values are achieved in the top-right corner. The latter is in agreement with one of the selection criteria for high $PCE_{R,max}$, which states that high $PCE_{R,max}$ is achieved with high sub-cell efficiency. IoBC (Figure 5.24 (b)) maximum values are on the top-left corner. The latter agrees with the selection criteria for IoBC, saying that IoBC increases as sub-cells efficiencies get closer. The best-performing blue sub-cells (PTQ10:IO-4Cl in CF and PTQ10:O-IDFBR in CB) have efficiencies of 7.31 and 6.87%, respectively. These values are closer to the 7.42% of the PTB7-Th:SIOTIC-4F (the lowest-performing red sub-cell) than to 10.45% (the best-performing red sub-cell). The observed behaviour of $PCE_{R,max}$ and IoBC in Figure 5.24 (a) and (b) is another example showing that the highest IoBC does not necessarily lead to the maximum $PCE_{R,max}$, and viceversa. The simulations of the highest $PCE_{R,max}$ and the highest IoBC, highlighted in yellow squares in Figure 5.24, are shown in Figure 5.25 (a) in solid and dashed lines, respectively. The comparison highglights the importance of efficient sub-cells for maximizing $PCE_{R,max}$, and similar sub-cell efficiencies for achieveing high IoBC.

In a 2-J RAINBOW device, we would expect $\lambda_{d,opt}$ close to the E_{bg} of the blue sub-cell. Figure 5.23 shows that the latter is the general trend, with most of the data points being close to the $\lambda_{d,opt} = \lambda_{bg}$ straight line. Nevertheless, some RAINBOW combinations differ from the expected tendency. Figure 5.24 (c) shows the values of all combinations. IO-4Cl-based blue sub-cells show a $\lambda_{d,opt}$ for 2-J RAINBOW devices between 660 and 670 nm, while O-IDFBR-based blue sub-cells, with a wider E_{bg}, show a $\lambda_{d,opt}$ between 625 and 635 nm. Nevertheless, there are some exeptions showing $\lambda_{d,opt}$ considerably below E_{bg} of the blue sub-cell. We can divide those exceptions into two groups. The first group are those 2-J RAINBOW combinations with the highest difference between sub-cell efficiencies. The latter combines the best-performing red sub-cells with the worst-performing blue sub-cells (bottom right corner in Figure 5.24). The second group corresponds to specific red sub-cells blends which columns show a tendency to lower $\lambda_{d,opt}$. This is the case of PTB7-Th:$PC_{70}BM$ and PTB7-Th:O-IDTBR blends.

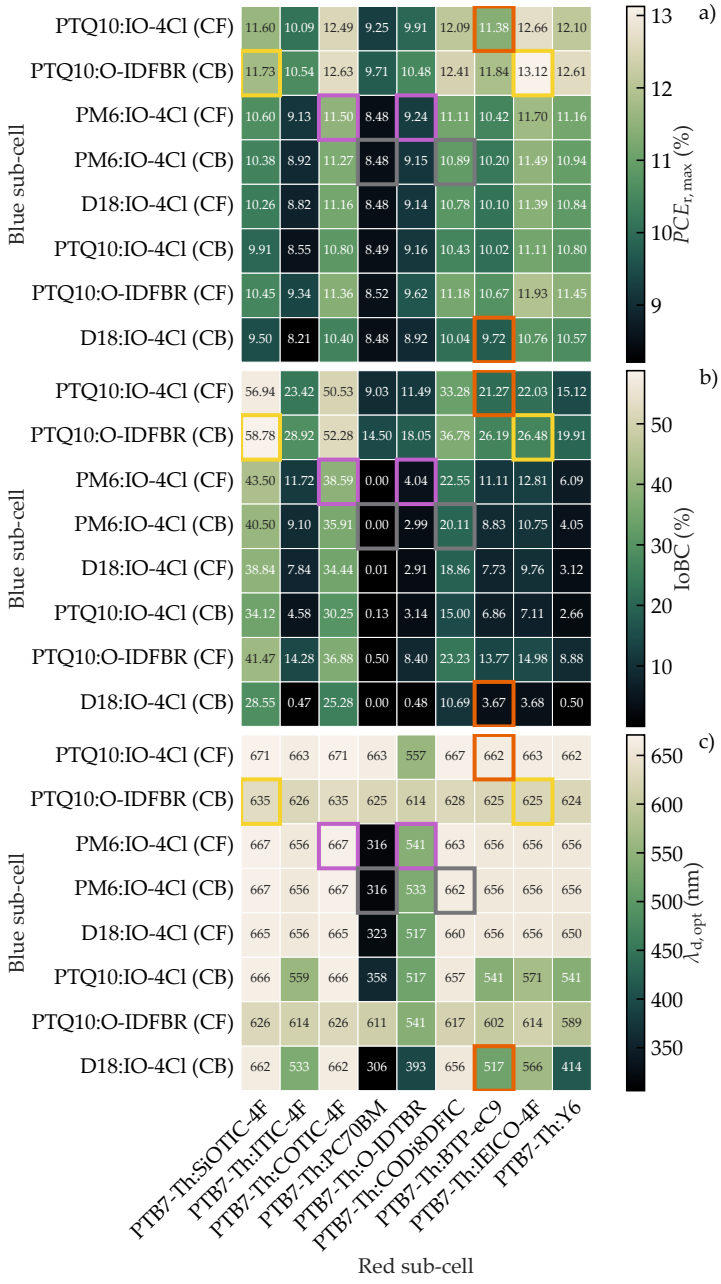

Figure 5.24: RAINBOW FoM of simulated 2-J RAINBOW devices with wide band-gap materials. The simulations are done at λ_d between 300 and 1100 nm with a λ_d step of 1 nm. $PCE_{R,max}$, IoBC and $\lambda_{d,opt}$ are ploted as heatmaps with the red and blue sub-cells blends in the horizontal and vertical axis respectively. The blends are ordered in increasing performance as single-junctions. The 2-J RAINBOW combinations highlighted with colors are plotted in Figure 5.25.

When the red and blue sub-cells EQE_{PV} overlap, PCE_R can typically show two local maximum points. The first one, with a smaller λ_d, corresponds to the optimized $J_{sc,R}$. In general, this maximum happens at λ_d in between $\lambda_{bg,blue}$ and the λ at which red and blue sub-cells EQE_{PV} cross, depending on the shape of both EQE_{PV}. The latter corresponds to minimized optical losses. On the other hand, thermalization losses are minimized when λ_d approaches the E_{bg} of the blue sub-cell ($\lambda_d \approx \lambda_{bg,blue}$). For $\lambda_d < \lambda_{bg,blue}$, some photons that the blue sub-cell could absorb are absorbed by the red sub-cell, increasing thermalization losses. On the other hand, for $\lambda_d > \lambda_{bg,blue}$ thermalization losses are maintained constant but absorption losses appear since photons that the red sub-cell could absorb cannot be captured by the blue sub-cell. In this scenario, $J_{sc,R}$ is far from its optimum. Due to the EQE_{PV} overlap, λ_d when thermalization or absorption losses are optimized can be significantly different. The latter strongly depends on the shape of EQE_{PV}, highlighting the importance of studying the λ_d dependence in organic RAINBOW solar cells.

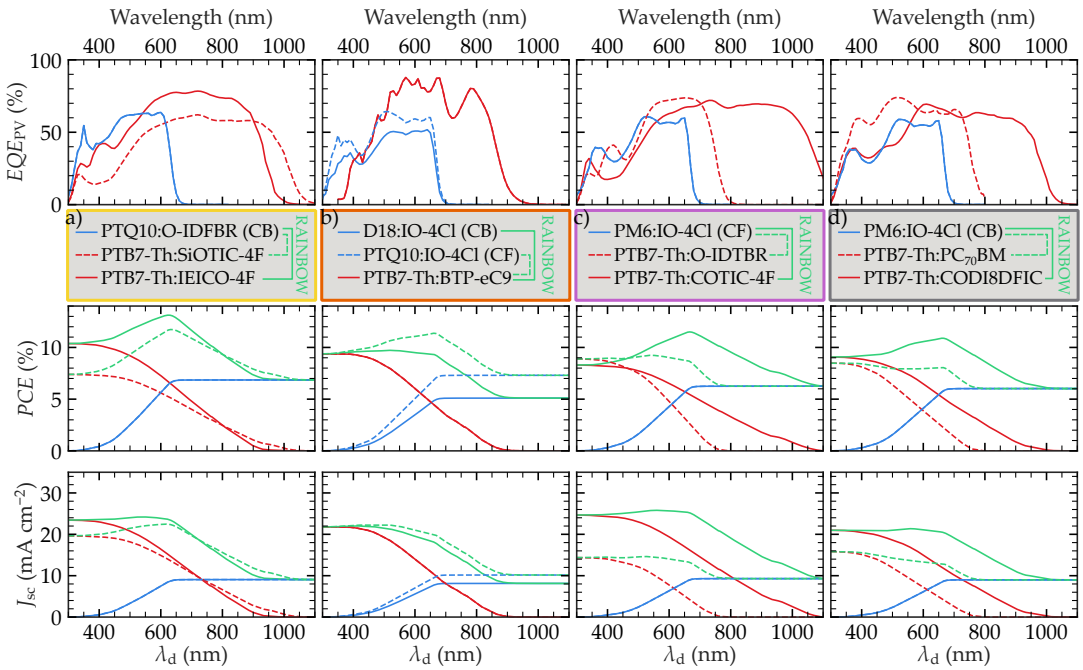

Figure 5.25: 2-J RAINBOW simulations of selected materials in Figure 5.24. (a) highest $PCE_{R,max}$ (solid) and IoBC (dashed) obtained in the simulations. (b) example of optimized absorption losses (solid) and optimizezd thermalization losses (dashed) competing in overlaping EQE_{PV}. (c) and (d) examples of red and blue sub-cells having similar EQE_{PV} (dashed) compared to a working 2-J RAINBOW (solid).

In this first group, due to the low efficiency of the blue sub-cell compared to the red counterpart, the absorption losses optimum wins over the thermalization losses optimum, showing a $\lambda_{d,opt} < \lambda_{bg,blue}$. Figure 5.25 (b) shows the simulation of the PTB7-Th:BTP-eC9 red sub-cell with D18:IO-4Cl in CB (solid) and PTQ10:IO-4Cl in CF (dashed). In the first RAINBOW combination, the absorption losses optimization peak is more important, lowering the $\lambda_{d,opt}$ to 517 nm. On the oposite, the thermalization losses optimum gets more important in the combination with the PTQ10:IO-4Cl in CF due to the higher efficiency of the latter.

PTB7-Th:$PC_{70}BM$ and PTB7-Th:O-IDTBR blends are part of the second group. In these cases, the E_{bg} of the red sub-cell is close to the blue sub-cell E_{bg}. When the blue sub-cell is a IO-4Cl-based blend, the difference in λ_{bg} is around 100 nm. The EQE_{PV} of both sub-cells are very similar (see dashed lines of Figure 5.25 (c) for PTB7-Th:O-IDTBR and (d) for PTB7-Th:$PC_{70}BM$). As a result, the PCE_R depencende on $\lambda_{d,opt}$ tends to be flat with small variations depending on the sub-cells EQE_{PV} shape. Therefore, IoBC is small compared to the other 2-J RAINBOW combinations and $\lambda_{d,opt}$ can vary significantly due to the small fluctuations of PCE_R. The example of PTB7-Th:$PC_{70}BM$ is more extreme (see Figure 5.25 (d)). The fullerene acceptor's absorption overlaps with the blue sub-cells blends. In most of the cases, the EQE_{PV} of the PTB7-Th:$PC_{70}BM$ is higher than the EQE_{PV} of the blue sub-cell. The latter is a clear example of overshadowing (see Figure 4.6 (a)), and the IoBC is null since there is no advantage on dividing the spectrum.

5.3.2.2 *3-J RAINBOW solar cells simulations*

Finally, we have run simulations with the same materials in a 3-J configuration. In this scenario we have three sub-cell named red, green and blue by increasing E_{bg}. The simulations are done in a similar way using the model described in Section 4.2.1.1. Nevertheless, in this case, we have to define two dividing wavelengths, $\lambda_{d,red}$ and $\lambda_{d,blue}$, corresponding to the spectral division between the red-green and the green-blue sub-cells pairs, respectively. Notice that, by definition, the dividing wavelengths have to satisfy: $\lambda_{d,red} \geq \lambda_{d,blue}$. The spectral fractions that each sub-cell receives are defined by the following $H(\lambda, \lambda_d)$:

$$H_{\text{red}}(\lambda,\ \lambda_{\text{d,red}}) = \begin{cases} 0 & \text{if } \lambda < \lambda_{\text{d,red}} \\ 1 & \text{if } \lambda \geq \lambda_{\text{d,red}} \end{cases} \tag{5.9}$$

$$H_{\text{green}}(\lambda,\ \lambda_{\text{d,red}},\ \lambda_{\text{d,blue}}) = \begin{cases} 0 & \text{if } \lambda < \lambda_{\text{d,blue}} \\ 1 & \text{if } \lambda_{\text{d,blue}} \leq \lambda < \lambda_{\text{d,red}} \\ 0 & \text{if } \lambda > \lambda_{\text{d,red}} \end{cases} \tag{5.10}$$

$$H_{\text{blue}}(\lambda,\ \lambda_{\text{d,blue}}) = \begin{cases} 1 & \text{if } \lambda < \lambda_{\text{d,blue}} \\ 0 & \text{if } \lambda \geq \lambda_{\text{d,blue}} \end{cases} \tag{5.11}$$

As the number of junctions increases the computational time, the storage space (bits), and the complexity of representing the results increases. In this case, we run various simulations only with the best materials, and with a λ_d step of 5 nm to reduce computing time and storage space. By analyzing the simulations we have derived a new rule for design and material selection of 3-J RAINBOW solar cells. The latter states that, for a 3-J RAINBOW solar cell to work it is mandatory that all 2-J RAINBOW combinations show a positive IoBC.

We only show the results for the 3-J RAINBOW solar cell with the highest PCE_R (see Figure 5.26). The latter is composed of the blends PTQ10:O-IDFBR in CB, PTB7-Th:IEICO-4F and PTB7-Th:COTIC-4F as the blue, green and red sub-cells, respectively. Figure 5.26 (a) and (b) shows the simulated PCE_R and $J_{sc,R}$, respectively, as a function of $\lambda_{d,red}$ and $\lambda_{d,blue}$. The EQE_{PV} of all three sub-cells is shown in Figure 5.26 (c). The 3-J RAINBOW plots of the FoM are essentially triangles because $\lambda_{d,red} \geq \lambda_{d,blue}$. The sides of the triangle corresponds to the three possible 2-J combinations between sub-cells, which are shown in Figure 5.26 (d), (e) and (f). For example, the diagonal side in Figure 5.26 (a) and (b) corresponds to all situations where $\lambda_{d,red} = \lambda_{d,blue}$, i.e., the 2-J RAINBOW between the red and the blue sub-cells (Figure 5.26 (d)), since the green sub-cell does not recieve any photon. In Figure 5.26 (c)-(f), colors are maitained according to the red, green and blue sub-cells, while PCE_R and $J_{sc,R}$ are ploted in brown. The simulation shows that the 3-J RAINBOW reaches a $PCE_{R,max}$ of 14.50% with an IoBC of 40.48%. The 3-J results improve the highest $PCE_{R,max}$ of the composing 2-J which has a $PCE_{R,max}$ = 13.18% and an IoBC = 27.74%.

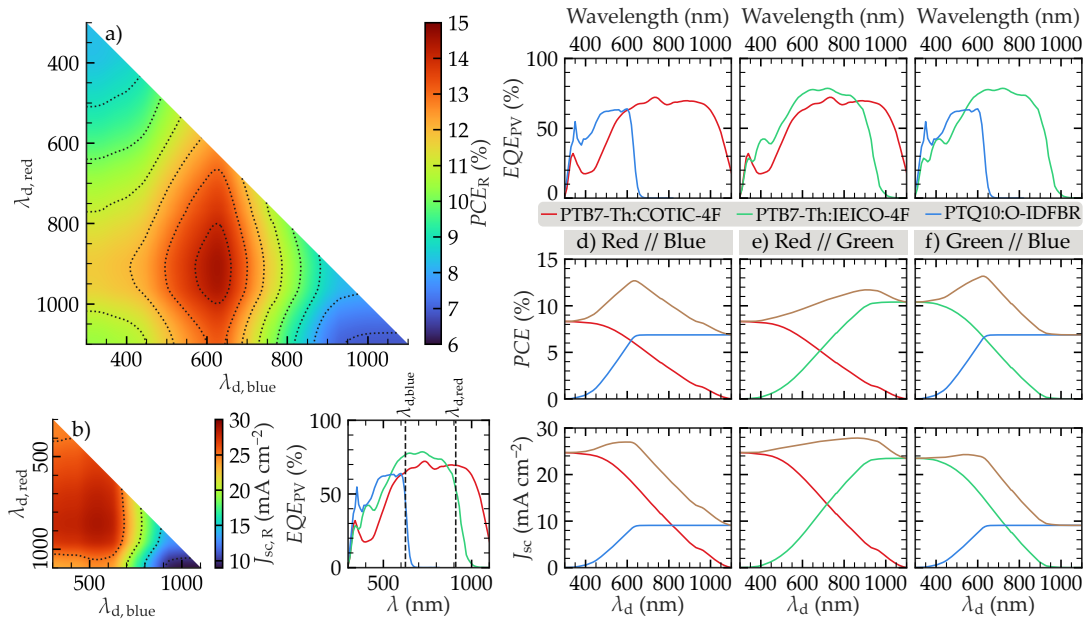

Figure 5.26: 3-J RAINBOW simulation results for PTQ10:O-IDFBR in CB, PTB7-Th:IEICO-4F and PTB7-Th:COTIC-4F as the blue, green and red sub-cells, respectively. PCE_R (a) and $J_{sc,R}$ (b) are plotted as a funciton of $\lambda_{d,red}$ and $\lambda_{d,blue}$. The dividing wavelengths are sweeped between 300 and 1100 nm with a step of 5 nm. (c) shows the EQE_{PV} for the three sub-cells, with the colors representing their sub-cell type. (d), (e), and (f) are the 2-J RAINBOW simulations of the red-blue, red-green and green-blue, respectively. They are represented in (a) and (b) as the diagonal, vertical and horizontal sidex of the triangular plots.

5.4 UPSCALING OF PTQ10:O-IDFBR OPV

During the last stages of my PhD thesis, I had the opportunity to visit EURECAT's labs in Mataró. EURECAT is one of the most important technological centers in Catalunya. There I joined Dr. Ignasi Burgués Ceballos and Ms. Paula Pinyol. They are working on up-scaling organic photovoltaics: transitioning from lab-scale cells to industrial production of modules. My stay at EURECAT mainly aimed to investigate the up-scaling of PTQ10:O-IDFBR blend as the active layer for organic PV modules. The latter can be interesting for the industrial application of OPV as indoor light harvesters. For this reason, part of the challenge was to use techniques compatible with industrialization (i.e., preferably roll-to-roll (R2R) compatible). We did not change the methodology for preparing the electron transport layer (ETL) and the active layer, which were prepared by blade coating. Nevertheless, active layer (AL) deposition was done outside the glovebox, aiming for a more industry-compatible solution for the already R2R-compatible technique. On the other hand, the hole transport layer (HTL) and the top electrode were deposited by physical vapor deposition, as we do

in our labs. The compatibility with solution-processable HTL and top electrodes for the PTQ10:O-IDFBR blend was not studied to avoid more unknown variables and sources of errors. Nevertheless, it is important to highlight that the physical vapor deposition technique is undesirable for industrialization, and using R2R-compatible inks like PEDOT:PSS or Ag nanowires is a better choice.[74, 75, 139] The latter is a topic under study at EURECAT, and at this point, they are trying to find suitable candidates for other systems.

5.4.1 *Depositing the active layer at ambient air*

A typical difference when moving from lab-scale processing to R2R schemes is the processing atmosphere. At the lab scale, the use of inert atmospheres achieved by working inside a glovebox is common, at least for steps like the deposition and thermal annealing of the active layer. Conversely, up-scale production aims to operate in the air, thus reducing the process cost.[143, 255, 256, 257, 258] This may induce some degree of degradation in the corresponding layers, mainly those composed of organic molecules, like the active layer. The latter can affect their electrical properties. Therefore, when depositing the active layer outside the glovebox, one may expect a decrease in the efficiency of the solar cell. The latter can be more or less critical depending on different factors like the materials composing the active layer, the deposition temperature, or the time exposed to air.[78, 259]

In this case, we want to see the effect of depositing the active layer outside the glovebox, i.e., in a different atmosphere. With this scope, we have fabricated two samples with the standard NANOPTO procedure described in Chapter 2, and two samples with identical conditions except that the AL was deposited outside the glovebox. Since the solvent used in both cases was chlorobenzene (CB), the deposition temperature was 80°C. The efficiency of all devices under 1 sun light was measured to assess the effect of the atmosphere on device performance. Ideally, we would compare the *PCE* of pixels between the different substrates. Nevertheless, reproducing the thickness profile is challenging, and every substrate may have a slightly different thickness profile. For this reason, we selected the eight highest-performing pixels of the two samples deposited inside and the two samples deposited outside as the datasets to compare.

Figure 5.27 shows the boxplot of the FoM of those datasets to compare the effect of the atmospheric conditions during blade coating of the active layer. First, we must notice that the *PCE* mean of the samples prepared inside the glovebox is below the previous efficiency

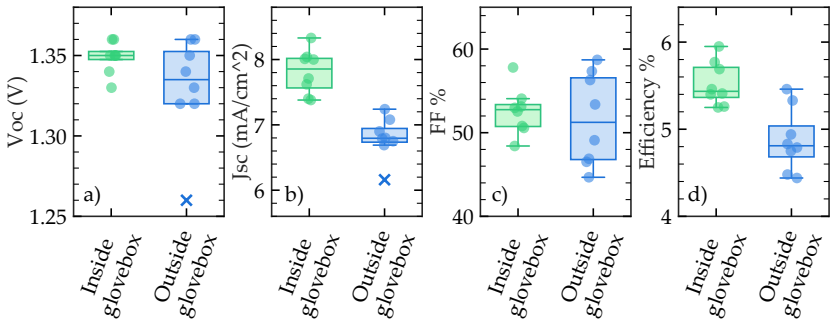

Figure 5.27: Comparison between solar cells of PTQ10:O-IDFBR prepared inside and outside the glovebox. Two samples for each atmospheric condition (inside the glovebox (green) and outside the glovebox (blue)) were prepared and the 8 best-performing cells were selected as datasets. Their different FoM are plotted as boxplots with data points shown as dots for points inside the boxplot limits and crosses for outliers.

with the same system (PTQ10:O-IDFBR in CB). Explaining the latter is not in the scope of this experiment. Nevertheless, one possible explanation could be that the batch of PTQ10 used was different from that of the previous cells. As shown by Riera-Galindo et al., PTQ10-based cells have a strong dependence on molecular weight.[260] On average, samples prepared outside the glovebox have lower *PCE* than those prepared inside, as expected by a possible degradation due to oxygen and moisture present only outside the glovebox. The decrease in the mean performance is 0.65% in absolute value. To find statistical evidence that the sample sets are different, we performed the t-test analysis.[261] Our alternative hypothesis is that devices prepared outside the glovebox have lower efficiency than devices prepared inside. Therefore, we consider a one-tail t-test with a typical confidence interval of 0.05%. In our case, the threshold value for $t_{0.95}$ is 1.782, and the calculated t value is 4.131. Thus, the samples prepared outside the glovebox statistically have lower performance than those prepared inside. Therefore, we confirm the expected detrimental effect of depositing the active layer in the air. Nevertheless, this effect does not dramatically decrease device performance and only affects the efficiency by 11%.

The comparison of the FoM between the two data sets (Figure 5.27) shows that the difference in *PCE* between devices fabricated in different atmospheres is mainly due to J_{sc}. The latter is the parameter that has a higher decrease due to blade coating outside the glovebox. V_{oc} and *FF* means are similar regardless of the atmospheric conditions but they exhibit higher standard deviation outside the glovebox. The latter might be an indication of poorer stability. Nevertheless, no more experiments were carried out in that direction.

5.4.2 *Effect of cell width on modules performance*

In lab-scale, we typically study solar cells, i.e., a single photovoltaic device. Nevertheless, single solar cells are not suitable for the commercial application of PV, and the connection of multiple solar cells is needed. The devices resulting from connecting multiple solar cells are known as modules. Within OPV modules, solar cells are typically connected in series. It is important to make this difference because different challenges appear when fabricating modules besides the efficiency of each single cell itself, with the interconnection between cells being one of the most critical aspects. This is mainly due to the fact that solution-processing methodologies (R2R) produce thin films that need to be patterned in order to construct a geometry with multiple cells placed along the thin film plane. There are different ways to achieve this lateral patterning. For example, slot die coating can produce stripes of material, thus defining the different cells. Nevertheless, the need for patterning multiple layers (ETL, HTL, and electrical contacts) introduces the challenge of aligning the patterns. Additionally, border effects can introduce thickness gradients along each strip, reducing homogeneity between cells. A more promising approach is using laser pattering to define the individual cells in an initially fully coated substrate. Investigators from EURECAT are developing this method in their labs. In this case, one of the most critical aspects is the interconnections between cells. One must have a reliable interconnection with low series resistance and avoid short-circuiting the cell, for which patterning must be very specific to certain layers.

5.4.2.1 *Laser patterning of modules*

Figure 5.28 shows a scheme of the laser patterning used for the fabrication of modules. The process comprises four laser patterning steps named P1, P2, P3, and P1 final. The first patterning step (P1) aims

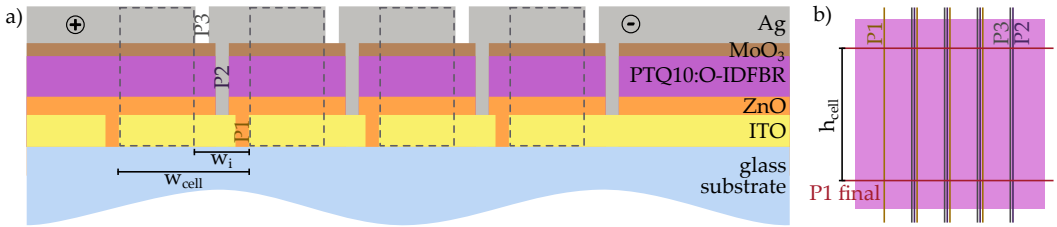

Figure 5.28: Schematics of laser patterning used to fabricate PTQ10:O-IDFBR modules. (a) Cross-section view of the laser patterning. P1, P2, and P3 refer to the different laser patterning steps to define the four cells connected in series. Each cell has a width (w_{cell}) composed by an active area (highlighted with a dashed line) and the interconnection with the next cell with a width of w_i. (b) Top-view of the laser patterning. P1 final is done after P3 and defines a cell height of h_{cell}=2 cm.

to define the bottom electrode of the cells, defining its width (W_{cell}). In our case, we are using ITO-covered glass substrates. Therefore, P1 has to blaze the ITO film. The latter is achieved because the laser emits at a wavelength of 1064 nm, the ITO absorbs that radiation and heats up quickly, and gets ablated in that region. After P1, substrates are cleaned with the standard procedure described in Chapter 2. Then, ETL (ZnO) and the active layer are prepared as described in Chapter 2, with the only difference being that the active layer is deposited outside the glovebox. After the active layer deposition, samples are entered inside the glovebox, and a 10 nm thin film of MoO_3 is physically evaporated. Afterward, the second laser patterning step (P2) is performed. The investigators at EURECAT found in previous studies that performing P2 (which is done in air atmosphere) after deposition of MoO_3 gave better results than performing it before the deposition of the HTL. They attribute it to the fact that the thin HTL can protect from oxygen and moisture degradation of the active layer interface with the HTL. In this P2 step, we want to create a vertical trench so that the top electrode deposited afterward creates the electrical interconnection between the top electrode of one cell and the next cell's bottom electrode (ITO). Therefore, we need to set conditions for the laser patterning that ablaze the ETL/AL/HTL stack with the minimum possible impact on ITO conductivity.

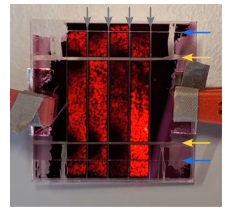

Figure 5.29: Electroluminescence of a module where P1 final laser patterning is not done correctly. The gray arrows are the P1, P2, and P3 lines and the blue arrows are the P1 final. The yellow arrows correspond to scratching the module with a toothpick.

Subsequently, substrates are entered again inside the glovebox to evaporate 100 nm of silver as the top electrode. Due to the formed trenches, the evaporation will create the interconnections between cells. Nevertheless, a final patterning step (P3) needs to be done in order to isolate the top electrodes of the different cells. The latter has to be done by adapting the laser conditions to affect only the silver top electrode and minimizing the ablation of all other layers. The vertical trench created by the P2 and the silver evaporation must also remain intact. Last but not least, a final patterning step is done in the direction perpendicular to P1, P2, and P3. This final patterning aims to define a known module height (h_{cell}=2 cm) and isolate the central part of the substrate (where the module is built) from its edges (where some unwanted edge effects could introduce extra shunt resistance to the device due to unwanted contacts between non-adjacent layers). For this reason, this last step (P1 final) has to be done with laser parameters that are more extreme than P1 to ensure that the trench created by the laser ablates all layers.

As a curiosity, in the first modules fabricated, the P1 final laser patterning was not done correctly because the laser conditions were too soft. The resulting modules had no rectifying behavior and did not work as PV modules. I discovered that the problem was the P1

final because, during a $J-V$ measurement of a module, I observed electroluminescence inside and outside the module area defined by the laser patterning.

5.4.3 *Studying cell width dependence*

One of the most important parameters to optimize in the fabrication of modules is the cell width (w_{cell}). From the perspective of a single cell, cells with larger areas tend to suffer from low *FF* due to parasitic losses and a higher effect of the series resistance. The first is due to more pinholes and active layer defects in larger areas while the second is related to a higher photocurrent (not photocurrent density) due to increased area. Notice that, as discussed before, for indoor applications the parasitic resistance has a more important role because of the low light intensity. Therefore, different active layer and selective transport layer materials would have different properties that may result in a different optimal w_{cell}. Nevertheless, there is an opposite trend when cells are incorporated into modules. Consider the total area of each cell in a device as the active area of the cell plus the interconnection area (like that depicted in Figure 5.28 (a)). The interconnection area is a constant that depends on the laser patterning but not on the cell width. The resolution of the laser and the separation between P1 and P3 (w_i in Figure 5.28 (a)) define this area. The ratio between the module's active area (the sum of individual cells active areas) and the module's total area is known as the geometrical fill factor (*GFF*). The *GFF* represents which percentage of the total area of the module is active area, therefore high *GFF* values are desired. Considering a constant interconnection area, the wider the cell width, the higher the *GFF*. Nevertheless, *GFF* can never be equal to 100% because interconnections are always needed in a module. Thus, *GFF* dependence on cell width is the opposite of the *FF*. In this case, *GFF* is mainly dependent on the equipment used for laser patterning but can also be influenced by the materials composing the device since different materials may behave differently to laser patterning and produce, for example, wider or narrower P2 trenches. Figure 5.30 shows the *GFF* dependence on cell width for our devices. The interconnection distance (w_i in Figure 5.28) was obtained by measuring the distance between P1 and P3 with an optical microscope of a few samples and considering the average value. Figure 5.31 shows two examples of this measurement. The average w_i obtained is 180 µm.

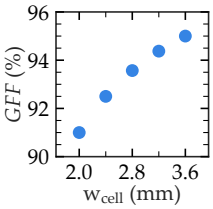

Figure 5.30: *GFF* vs. w_{cell} for the modules fabricated. The measured w_i of 180 μm was considered for the calculation of *GFF*.

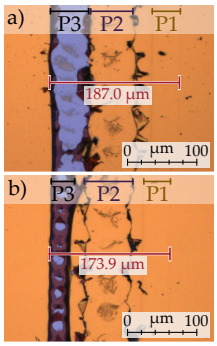

Figure 5.31: Optical microscopy images of the interconnection between cells. P1, P2, and P3 laser patterning lines are marked in the top part as a reference.

We fabricated modules of four cells with cell widths varying from 2 to 3.6 mm in 0.4 mm steps. The height of the cells defined by the P1 final patterning was maintained constant with a value of 2 cm. The modules were fabricated for three different active layer thicknesses achieved by

depositing at 40, 60 and 80 mm s^{-1}. Figure 5.32 shows the FoM of all modules measured under 1 sun conditions. We can see a strong V_{oc} dependence on cell width (Figure 5.32 (a)). Considering that all modules were made of four cells, one may expect a V_{oc} similar for all modules. The value should approach the V_{oc} of a single cell (V_{oc}^{cell}) multiplied by four because cells are connected in series. Nevertheless, the module achieving the highest V_{oc} shows a $V_{oc}^{cell} = V_{oc}/4$ of 5.16 V/4=1.29 V. The latter is close to the V_{oc}^{cell} =1.33 V expected from the devices fabricated outside the glovebox shown in Figure 5.27 (a). Nevertheless, the V_{oc} still shows room for improvement since some of the cells showed $V_{oc}^{cell} \geq$1.35 V. On the opposite, the modules with $V_{oc} \leq 2$ V exhibit a $V_{oc}^{cell} \leq 0.5$ V which is clearly below the expected value. The decrease in V_{oc} as cell width increases, observed from 2.8 to 3.6 mm cell width, can be explained as an increase in the series resistance of the electrodes in a single cell. The latter also affects the *FF*, which also decreases with cell width. Nevertheless, we did not find any explanation for the opposite trend of V_{oc} for lower cell widths, and further studying this behavior may be needed to understand its nature. On the other hand, a decrease in *FF* as cell width decreases can be explained by the reduction of the geometrical fill factor (*GFF*) as the fraction of area used as interconnection increases when decreasing cell width.

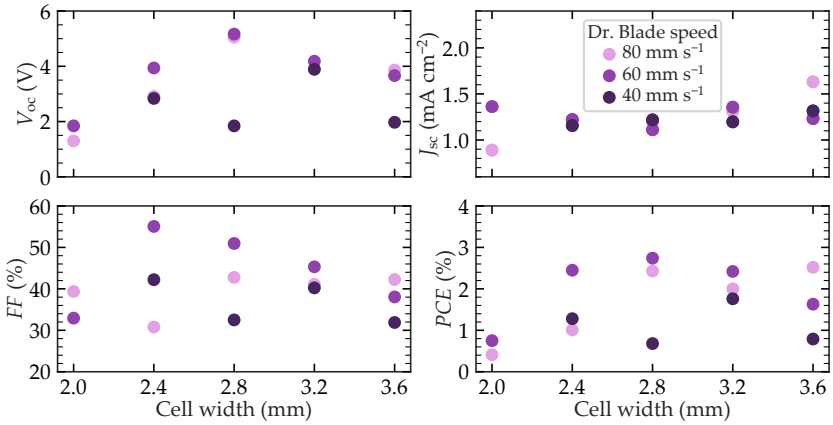

Figure 5.32: Cell width study of PTQ10:O-IDFBR modules. FoM of PTQ10:O-IDFBR modules fabricated with different w_{cell} measured under 1 sun illumination.

J_{sc} shown in Figure 5.32 (c) is calculated considering only the active area of the device (i.e., without considering the interconnection between cells). In this case, since cells are connected in series, the J_{sc} value of the single cell device (J_{sc}^{cell}) has to be compared with the J_{sc} of the module multiplied by four. The values of Figure 5.32 (c) lay between 1.1 and 1.4 mA cm^{-2} which corresponds to a J_{sc}^{cell} in between 4.4 and 5.6 mA cm^{-2}. The latter is lower than expected considering that

the J_{sc}^{cell} of the reference devices fabricated outside is 6.8 mA cm^{-2} (see Figure 5.27). This represents a loss of approximately 25% of the J_{sc} achieved in the reference devices. The latter suggests that the interconnections do not offer a good connection and may decrease the shunt resistance of the device.

It seems clear that for the modules deposited at 60 mm s^{-1}, the optimum cell width is 2.8 mm since in these conditions we have measured the maximum *PCE* of 2.74% of a module in this study. The latter could be also the case for thinner modules (deposited at 40 mm s^{-1}), because the low efficiency of the module with w_{cell}=2.8 mm could be an outlier. Nevertheless, for the thicker modules (deposited at 80 mm s^{-1}), the tendency seems to be that higher cell widths could give better performance. Therefore, the optimum cell width for this active layer system may lay around 2.8 mm although higher cell widths may also achieve good performance for thick active layers.

The best modules were also tested under indoor illumination with a professional photograph LED setup at 6500K with an intensity of 500 and 1000 Lux. We do not show any results because the modules showed almost no rectifying behavior, with efficiency values below 0.2%. We attribute the latter to the low shunt resistance (R_{sh}) of the modules compared with the devices prepared in the first instance. One possible origin of the decrease in R_{sh} may be the module fabrication itself. The latter could be improved by further optimizing the laser patterning conditions and the fabrication of the modules. Additionally, one can also think on strategies to improve the R_{sh} of each cell. For example, by introducing a vertical stratification in the active layer one should be able to avoid the percloration of charges to unwanted contacts as well as direct percolation paths from one contact to the other. One way to achieve this vertical stratification is by depositing an active layer with a bilayer morphology. The latter is achieved by sequentially depositing solutions of pure donor and acceptor materials. The need for thin layers for proper exciton dissociation and charge extraction is generally a problem for cells aiming to harvest 1 sun spectra due to a low J_{sc}. Nevertheless, for harvesting indoor light this problem may be less important and the theoretically improved R_{sh} may play a crucial role.

5.5 CONCLUSIONS AND OUTLOOK

This chapter is motivated by the need for novel wide band-gap materials to use as blue sub-cells for RAINBOW geometries. We performed a combinatorial study between three donors (D18, PTQ10, and PM6), three acceptors (O-IDFBR, PMI-FF-PMI, IO-4Cl), and two solvents

(chloroform and chlorobenzene). Owing to the variation in the blade coating velocity used during active layer deposition, 12 different thicknesses (with duplicates for each layer thickness) were tested for each combination, thus giving a total of 432 devices. From this combinatorial screening study, we found that IO-4Cl cells have the highest efficiency under AM1.5G illumination, mainly because IO-4Cl is the material with the lowest E_{bg}, which is closer to the optimal Shockley-Queiser limit. PMI-FF-PMI-based devices showed the lowest efficiencies, mainly due to low J_{sc}, attributed not only to the lower absorption due to the higher E_{bg} of the blends, but also to a worse exciton dissociation and/or charge carrier extraction. The O-IDFBR-based devices are in-between both cases, similar to PMI-FF-PMI for the case where D18 was used as the donor and similar to IO-4Cl when PTQ10 was used as the donor.

We also studied the V_{oc} losses for selected blends. The analysis showed a ΔV_{oc}^{total} between 0.6 and 0.7 V, with cells containing PTQ10 always exhibiting the lowest ΔV_{oc}^{total} compared to their counterparts. The latter, together with PTQ10 being the donor with the deepest HOMO level, leads PTQ10-based devices to exhibit a higher V_{oc} compared to the other donors used. Based on these results, we suggest PTQ10 as a suitable donor for wide band-gap organic solar cells. This was tested, as a preliminary result, in a blend with FCC-Cl (a wide band-gap NFA), reaching an efficiency of 10.98% with a V_{oc} of 1.07 V. Specially interesting was the PTQ10:O-IDFBR blend due to its low ΔV_{oc}^{nr}, relatively high efficiency (6.87%) and remarkably high V_{oc} (1.35 V). These cells were also tested under indoor light conditions, showing an efficiency of 22.6% with a V_{oc} of 1.21 V. This blend efficiency under indoor lighting is among the best in the OPV, and the achieved V_{oc} is, as far as we know, the highest reported value of indoor OPV.

These interesting results were crossed with narrow band-gap materials developed in the group by Dr. Alfonsina Abat Amelenan Torimtubun. The 2-J RAINBOW geometries simulated reached a $PCE_{R,max}$ of 13.12% with an IoBC of 26.58% for the PTQ10:O-IDFBR deposited from CB as blue sub-cell, combined with PTB7-Th:IEICO-4F as red sub-cell. The same blend combination also gave the highest 3-J RAINBOW efficiency when a narrower blend (PTB7-Th:COTIC-4F) was used as the red sub-cell and PTB7-Th:IEICO-4F was used as the middle green sub-cell. This combination gave the highest $PCE_{R,max}$ in all the PhD Thesis with a value of 14.50% and an IoBC of 40.48%.

Additionally, I carried out a stay at EURECAT Mataró in order to investigate on the up-scaling of PTQ10:O-IDFBR cells for applications in indoor light harvesting. The study on cell width led to the first

indication of the optimal cell width being at 2.8 mm. Nevertheless, the modules' efficiencies were not as good as those of single cells. The latter is attributed to the geometry of the modules and the poor performance of the contacts between cells. The latter affects all FoM measured in the $J - V$ curve. Especially critical is the decrease of the shunt resistance, R_{sh}, which led to useless modules under 6500 K and 1000 lux indoor light. Thus, more optimization is needed in this area in order to achieve useful modules, especially focusing on increasing the R_{sh} and improving the interconnections.

6 THESIS CONCLUSIONS AND OUTLOOK

During this thesis, we achieved a significant breakthrough in the field of solar cell technology. We developed and investigated RAINBOW solar cells, a novel multi-junction geometry that holds the promise of surpassing the single-junction Shockley-Queisser limit. Our contribution to the scientific community extends beyond this innovative design. We have also developed tools for RAINBOW characterization, modeling, and optimization, including the SOLS (spectrum on-demand light source). This equipment, initially designed to illuminate solar cells in a RAINBOW configuration in a tunable way, has opened up new possibilities in solar cell research, resulting in interesting applications beyond RAINBOW characterization due to its highly tunable output spectrum. The actual SOLS equipment has a spectral range of approximately 350 nm up to 1100 nm, which is facilitated by the use of refractive dispersive optical elements instead of diffractive. Additionally, the SOLS has a wide dynamic range of at least 2 orders of magnitude and highly tunable spectral features. With these properties, the equipment can be used for the standard $J - V$ measurement under the solar AM1.5G spectrum achieving an ABA class solar simulator. More interestingly, it can also serve as a new and versatile characterization tool to study the efficiency of solar cells (not restricted to organic devices) under a large variety of spectral conditions such as indoor photovoltaics, underwater, tandem devices, spacial irradiation, or building integrated photovoltaics among others. We have demonstrated that the same piece of equipment can be used to measure solar cells' photovoltaic external quantum efficiency. Nevertheless, it is essential to remark that the spectral resolution of the latter is lower than that of the specialized equipment. The SOLS can also help elucidate the processes inside organic photovoltaics thanks to the possibility of measuring intensity-dependent studies.

The unique capabilities of the SOLS and its novel design are supported by a patent of the technology and various grants to develop it further. Nevertheless, there is room for improvement to transfer the SOLS technology to the market. We have to improve the automatization of the setup, which right now is half manual with 3D-printed cards that are time-consuming to produce. We have considered different solutions, and the most feasible one seems to be the use of a digital micromirror device. Nevertheless, the small dimensions of the latter and its low reflectance are problems that still need to be solved. Another challenge

for the SOLS setup is its spectral resolution, which is acceptable in the UV and visible regions but is too poor in the red and IR spectral ranges. We have demonstrated that the latter depends to a great extent on the characteristics of the input beam: a collimated and small light spot increases wavelength resolution, which is difficult to achieve and always comes at the expense of light intensity.

We have proved the feasibility of the RAINBOW solar cell multi-junction architecture. Using simulations, we defined design rules for selecting materials and devices, helping the community to search for materials to achieve these specific rules. The RAINBOW device is optimized when choosing materials with maximum EQE_{PV} value matching (rather than current matching) and low thermal losses, mainly in the blue sub-cells. We used these criteria to select three active layer blends, namely, PM6:IO-4Cl, PM6:Y6, and PTB7-Th:COTIC-4F, with energy band gaps that cover a wide range of the solar spectrum. The simulated efficiency increase-over-best-cell that we could obtain for two-junction cells with the selected materials span up to 46%. We then used the SOLS to validate the simulations, thus providing a theoretical tool for material and device screening. With the SOLS setup, we achieved an IoBC of close to 46% for the wide–narrow bandgap RAINBOW combination, which has PM6:IO-4Cl as blue sub-cell and PTB7-Th:COTIC-4F as red sub-cell.

We also manufactured two proofs-of-concept monolithic RAINBOW devices using the partial coverage deposition technique. The combination between PM6:IO-4Cl and PTB7-Th:COTIC-4F yielded an IoBC of 39.50% arising from reduced thermalization losses, while RAINBOW combinations based on PM6:Y6 and PTB7-Th:COTIC-4F, resulted in an 11.47% IoBC, in good agreement with simulations that explain this improvement in terms of enhanced photocurrent arising from a significant reduction in absorption losses. We have also quantified the thermalization and absorption losses for each RAINBOW system, understanding the nature of the improvement in the lateral multi-junction geometry. Our results demonstrate the feasibility and significant potential of the RAINBOW concept. Nevertheless, the fabricated proof-of-concept devices are one step behind a RAINBOW device with all its components (the dispersive optical element and a RAINBOW cell with sub-cells connected to a DC-DC converter). Thus, we find that the fabrication and study of an actual RAINBOW device with all its components is a necessary step in the future. Future efforts for RAINBOW solar cells also include exploring novel combinations, demonstrating multi-junctions with more than two sub-cells, and designing efficient dispersive elements.

We find the design and exploration of new wide bandgap materials especially important since they are responsible for lowering thermalization losses in the multi-junction approach. We performed a combinatorial study between 3 donors (D18, PTQ10, and PM6), 3 acceptors (O-IDFBR, PMI-FF-PMI, IO-4Cl), and 2 solvents (chloroform and chlorobenzene). From this combinatorial screening study, we found that IO-4Cl cells have the highest efficiency under AM1.5G illumination, mainly because IO-4Cl is the material with the lowest E_{bg}, which is closer to the optimal Shockley-Queiser limit. PMI-FF-PMI-based devices showed the lowest efficiencies, mainly due to low J_{sc}, attributed not only to the lower absorption due to the higher E_{bg} of the blends but also to a worse exciton dissociation and/or charge carrier extraction. The O-IDFBR-based devices are in-between both cases, similar to PMI-FF-PMI for the case where D18 was used as the donor and similar to IO-4Cl when PTQ10 was used as the donor.

We also studied the V_{oc} losses for selected blends. The analysis showed a ΔV_{oc}^{total} between 0.6 and 0.7 V, with cells containing PTQ10 always exhibiting the lowest ΔV_{oc}^{total} compared to their counterparts. The latter, together with PTQ10 being the donor with the deepest HOMO level, leads PTQ10-based devices to exhibit a higher V_{oc} compared to the other donors used. Based on these results, we suggest PTQ10 as a suitable donor for wide band-gap organic solar cells. As a preliminary result, this was tested in a blend with FCC-Cl (a wide band-gap NFA), reaching an efficiency of 10.98% with a V_{oc} of 1.07 V. Specially interesting was the PTQ10:O-IDFBR blend due to its low ΔV_{oc}^{nr}, relatively high efficiency (6.87%) and remarkably high V_{oc} (1.35 V). These cells were also tested under indoor light conditions, showing an efficiency of 22.6% with a V_{oc} of 1.21 V. This blend efficiency under indoor lighting is among the best in the OPV, and the achieved V_{oc} is, as far as we know, the highest reported value of indoor OPV. Further developments in the area of wide-bandgap active layer materials will result in an increase in RAINBOW performance. Additionally, this will also benefit the tandem multi-junction the approach, especially if the J_{sc} of wide-bandgap materials is increased.

These interesting results were crossed with narrow band-gap materials, simulating 2-J and 3-J RAINBOW devices. The 2-J RAINBOW geometries simulated reached a $PCE_{R,max}$ of 13.12% with an IoBC of 26.58% for the PTQ10:O-IDFBR deposited from CB as blue sub-cell, combined with PTB7-Th:IEICO-4F as red sub-cell. The same blend combination also gave the highest 3-J RAINBOW efficiency when a narrower blend (PTB7-Th:COTIC-4F) was used as the red sub-cell and PTB7-Th:IEICO-4F was used as the middle green sub-cell. This combination gave the highest theoretical $PCE_{R,max}$ in all the PhD Thesis

with a value of 14.50% and an IoBC of 40.48%.

Additionally, I carried out a stay at EURECAT Mataró to investigate the up-scaling of PTQ10:O-IDFBR cells for applications in indoor light harvesting. The study on cell width led to the first indication of the optimal cell width at 2.8 mm. Nevertheless, the modules' efficiencies were not as good as those of single cells. The latter is attributed to the geometry of the modules and the poor performance of the contacts between cells. It affects all FoM measured in the $J-V$ curve. Specially critical is the decrease of the shunt resistance, R_{sh}, which led to useless modules under 6500 K indoor light. Thus, more optimization is needed in this area to achieve functional modules, especially focusing on increasing the R_{sh}.

BIBLIOGRAPHY

1. I. I. E. Agency. *World Energy Outlook 2023* https://www.iea.org/reports/world-energy-outlook-2023. Accessed on 2024-09-07.
2. I. E. Agency. *Net Zero Roadmap: A Global Pathway to Keep the 1.5 °C Goal in Reach - 2023 Update* https://www.iea.org/reports/net-zero-roadmap-a-global-pathway-to-keep-the-15-0c-goal-in-reach. Accessed on 2024-09-07.
3. *Renewables 2023 – Analysis - IEA* https://www.iea.org/reports/renewables-2023. Accessed on 2024-09-07.
4. I. E. Agency. *Solar PV Global Supply Chains* https://www.iea.org/reports/solar-pv-global-supply-chains. Accessed on 2024-09-07.
5. A. Al-Fuqaha, M. Guizani, M. Mohammadi, M. Aledhari and M. Ayyash. Internet of Things: A Survey on Enabling Technologies, Protocols, and Applications. *IEEE Communications Surveys & Tutorials* **17,** 2347–2376 (2015). DOI: 10.1109/COMST.2015.2444095.
6. H. Michaels, M. Rinderle, R. Freitag, I. Benesperi, T. Edvinsson, R. Socher, A. Gagliardi and M. Freitag. Dye-sensitized solar cells under ambient light powering machine learning: towards autonomous smart sensors for the internet of things. *Chemical Science* **11,** 2895–2906 (2020). DOI: 10.1039/C9SC06145B.
7. O. Almora, C. I. Cabrera, S. Erten-Ela, K. Forberich, K. Fukuda, F. Guo, J. Hauch, A. W. Y. Ho-Baillie, T. J. Jacobsson, R. A. J. Janssen, T. Kirchartz, M. A. Loi, X. Mathew, D. B. Mitzi, M. K. Nazeeruddin, U. W. Paetzold, B. P. Rand, U. Rau, T. Someya, E. Unger, L. Vaillant-Roca and C. J. Brabec. Device Performance of Emerging Photovoltaic Materials (Version 4). *Advanced Energy Materials* **14,** 2303173 (2024). DOI: 10.1002/aenm.202303173.
8. M. A. Alkhalayfeh, A. A. Aziz, M. Z. Pakhuruddin, K. M. M. Katubi and N. Ahmadi. Recent Development of Indoor Organic Photovoltaics. *physica status solidi (a)* **219,** 2100639 (2022). DOI: 10.1002/pssa.202100639.
9. T. H. Kim, N. W. Park, M. A. Saeed, S. Y. Jeong, H. Y. Woo, J. Park and J. W. Shim. Record indoor performance of organic photovoltaics with long-term stability enabled by self-assembled monolayer-based interface management. *Nano Energy* **112,** 108429 (2023). DOI: 10.1016/j.nanoen.2023.108429.

10. E. Han, M. Lyu, E. Choi, Y. Zhao, Y. Zhang, J. Lee, S. Lee, Y. Jiao, S. H. A. Ahmad, J. Seidel, J. S. Yun, J. Yun and L. Wang. High-Performance Indoor Perovskite Solar Cells by Self-Suppression of Intrinsic Defects via a Facile Solvent-Engineering Strategy. *Small* **20,** 2305192 (2024). DOI: 10.1002/smll.202305192.

11. P. Pollack. *Fine chemicals : the industry and the business* 2nd ed (John Wiley & Sons, 2011).

12. M. A. Benvenuto. *Industrial Organic Chemistry* DOI: 10.1515/9783110494471 (De Gruyter, Oct. 2017).

13. C. Schneider, T. Leischner, P. Ryabchuk, R. Jackstell, K. Junge and M. Beller. Development of Bulk Organic Chemical Processes—History, Status, and Opportunities for Academic Research. *CCS Chemistry* **3,** 512–530 (2021). DOI: 10.31635/ccschem.021.202000680.

14. B. van der Wiel, H.-J. Egelhaaf, H. Issa, M. Roos and N. Henze. Market Readiness of Organic Photovoltaics for Building Integration. *MRS Proceedings* **1639,** mrsf13–1639–y10–03 (2014). DOI: 10.1557/opl.2014.88.

15. D. J. Lipomi, B. C. Tee, M. Vosgueritchian and Z. Bao. Stretchable Organic Solar Cells. *Advanced Materials* **23,** 1771–1775 (2011). DOI: 10.1002/adma.201004426.

16. D. J. Lipomi and Z. Bao. Stretchable, elastic materials and devices for solar energy conversion. *Energy & Environmental Science* **4,** 3314 (2011). DOI: 10.1039/c1ee01881g.

17. T. Sekitani, H. Nakajima, H. Maeda, T. Fukushima, T. Aida, K. Hata and T. Someya. Stretchable active-matrix organic light-emitting diode display using printable elastic conductors. *Nature Materials* **8,** 494–499 (2009). DOI: 10.1038/nmat2459.

18. F. C. Krebs, M. Biancardo, B. Winther-Jensen, H. Spanggard and J. Alstrup. Strategies for incorporation of polymer photovoltaics into garments and textiles. *Solar Energy Materials and Solar Cells* **90,** 1058–1067 (2006). DOI: 10.1016/j.solmat.2005.06.003.

19. M. C. Scharber and N. S. Sariciftci. Low Band Gap Conjugated Semiconducting Polymers. *Advanced Materials Technologies* **6,** 2000857 (2021). DOI: 10.1002/admt.202000857.

20. A. M. Schneider, L. Lu, E. F. Manley, T. Zheng, V. Sharapov, T. Xu, T. J. Marks, L. X. Chen and L. Yu. Wide bandgap OPV polymers based on pyridinonedithiophene unit with efficiency >5%. *Chemical Science* **6,** 4860–4866 (2015). DOI: 10.1039/C5SC01427A.

21. J. Yan, X. Rodríguez-Martínez, D. Pearce, H. Douglas, D. Bili, M. Azzouzi, F. Eisner, A. Virbule, E. Rezasoltani, V. Belova, B. Dörling, S. Few, A. A. Szumska, X. Hou, G. Zhang, H.-L. Yip, M. Campoy-Quiles and J. Nelson. Identifying structure–absorption relationships and predicting absorption strength of non-fullerene acceptors for organic photovoltaics. *Energy & Environmental Science* **15,** 2958–2973 (2022). DOI: 10.1039/D2EE00887D.

22. W. Shockley and H. J. Queisser. Detailed Balance Limit of Efficiency of p-n Junction Solar Cells. *Journal of Applied Physics* **32,** 510–519 (1961). DOI: 10.1063/1.1736034.

23. M. Välimäki, P. Apilo, R. Po, E. Jansson, A. Bernardi, M. Ylikunnari, M. Vilkman, G. Corso, J. Puustinen, J. Tuominen and J. Hast. R2R-printed inverted OPV modules – towards arbitrary patterned designs. *Nanoscale* **7,** 9570–9580 (2015). DOI: 10.1039/C5NR00204D.

24. F. C. Krebs, J. Fyenbo, D. M. Tanenbaum, S. A. Gevorgyan, R. Andriessen, B. van Remoortere, Y. Galagan and M. Jørgensen. The OE-A OPV demonstrator anno domini 2011. *Energy & Environmental Science* **4,** 4116 (2011). DOI: 10.1039/c1ee01891d.

25. G. D. Spyropoulos, P. Kubis, N. Li, D. Baran, L. Lucera, M. Salvador, T. Ameri, M. M. Voigt, F. C. Krebs and C. J. Brabec. Flexible organic tandem solar modules with 6% efficiency: combining roll-to-roll compatible processing with high geometric fill factors. *Energy Environ. Sci.* **7,** 3284–3290 (2014). DOI: 10.1039/C4EE02003K.

26. F. C. Krebs, N. Espinosa, M. Hösel, R. R. Søndergaard and M. Jørgensen. 25th Anniversary Article: Rise to Power – OPV-Based Solar Parks. *Advanced Materials* **26,** 29–39 (2014). DOI: 10.1002/adma.201302031.

27. N. Espinosa, M. Hösel, D. Angmo and F. C. Krebs. Solar cells with one-day energy payback for the factories of the future. *Energy Environ. Sci.* **5,** 5117–5132 (2012). DOI: 10.1039/C1EE02728J.

28. S. Lizin, S. V. Passel, E. D. Schepper, W. Maes, L. Lutsen, J. Manca and D. Vanderzande. Life cycle analyses of organic photovoltaics: a review. *Energy & Environmental Science* **6,** 3136 (2013). DOI: 10.1039/c3ee42653j.

29. S. B. Darling and F. You. The case for organic photovoltaics. *RSC Advances* **3,** 17633 (2013). DOI: 10.1039/c3ra42989j.

30. A. Gambhir, P. Sandwell and J. Nelson. The future costs of OPV – A bottom-up model of material and manufacturing costs with uncertainty analysis. *Solar Energy Materials and Solar Cells* **156,** 49–58 (2016). DOI: 10.1016/j.solmat.2016.05.056.

31. K. A. Mazzio and C. K. Luscombe. The future of organic photovoltaics. *Chemical Society Reviews* **44,** 78–90 (2015). DOI: 10.1039/C4CS00227J.

32. N. Li and C. J. Brabec. Washing away barriers. *Nature Energy* **2,** 772–773 (2017). DOI: 10.1038/s41560-017-0011-1.

33. C. J. Brabec, S. E. Shaheen, C. Winder, N. S. Sariciftci and P. Denk. Effect of LiF/metal electrodes on the performance of plastic solar cells. *Applied Physics Letters* **80,** 1288–1290 (2002). DOI: 10.1063/1.1446988.

34. C. Chen, L. Wang, W. Xia, K. Qiu, C. Guo, Z. Gan, J. Zhou, Y. Sun, D. Liu, W. Li and T. Wang. Molecular interaction induced dual fibrils towards organic solar cells with certified efficiency over 20%. *Nature Communications* **15,** 6865 (2024). DOI: 10.1038/s41467-024-51359-w.

35. J. Zhao, Y. Li, G. Yang, K. Jiang, H. Lin, H. Ade, W. Ma and H. Yan. Efficient organic solar cells processed from hydrocarbon solvents. *Nature Energy* **1,** 15027 (2016). DOI: 10.1038/nenergy.2015.27.

36. H. Bin, Z.-G. Zhang, L. Gao, S. Chen, L. Zhong, L. Xue, C. Yang and Y. Li. Non-Fullerene Polymer Solar Cells Based on Alkylthio and Fluorine Substituted 2D-Conjugated Polymers Reach 9.5% Efficiency. *Journal of the American Chemical Society* **138,** 4657–4664 (2016). DOI: 10.1021/jacs.6b01744.

37. W. Zhao, D. Qian, S. Zhang, S. Li, O. Inganäs, F. Gao and J. Hou. Fullerene-Free Polymer Solar Cells with over 11% Efficiency and Excellent Thermal Stability. *Advanced Materials* **28,** 4734–4739 (2016). DOI: 10.1002/adma.201600281.

38. Y. Lin, J. Wang, Z. Zhang, H. Bai, Y. Li, D. Zhu and X. Zhan. An Electron Acceptor Challenging Fullerenes for Efficient Polymer Solar Cells. *Advanced Materials* **27,** 1170–1174 (2015). DOI: 10.1002/adma.201404317.

39. Q. Guo, Q. Guo, Y. Geng, A. Tang, M. Zhang, M. Du, X. Sun and E. Zhou. Recent advances in PM6:Y6-based organic solar cells. *Materials Chemistry Frontiers* **5,** 3257–3280 (2021). DOI: 10.1039/D1QM00060H.

40. M. Ren, G. Zhang, Z. Chen, J. Xiao, X. Jiao, Y. Zou, H.-L. Yip and Y. Cao. High-Performance Ternary Organic Solar Cells with Controllable Morphology via Sequential Layer-by-Layer Deposition. *ACS Applied Materials & Interfaces* **12.** Good introduction to BHJ and OSC history and concepts., 13077–13086 (2020). DOI: 10.1021/acsami.9b23011.

41. M. Campoy-Quiles, T. Ferenczi, T. Agostinelli, P. G. Etchegoin, Y. Kim, T. D. Anthopoulos, P. N. Stavrinou, D. D. C. Bradley and J. Nelson. Morphology evolution via self-organization and lateral and vertical diffusion in polymer:fullerene solar cell blends. *Nature Materials* **7,** 158–164 (2008). DOI: 10.1038/nmat2102.

42. Z. Peng, N. Stingelin, H. Ade and J. J. Michels. A materials physics perspective on structure–processing–function relations in blends of organic semiconductors. *Nature Reviews Materials* **8,** 439–455 (2023). DOI: 10.1038/s41578-023-00541-5.

43. A. Colsmann, H. Röhm and C. Sprau. Shining Light on Organic Solar Cells. *Solar RRL* **4** (2020). DOI: 10.1002/solr.202000015.

44. *Best Research-Cell Efficiency Chart | Photovoltaic Research | NREL* https://www.nrel.gov/pv/cell-efficiency.html. Accessed on 2024-09-07.

45. X. R. Martínez. *Development of organic solar cells by combinatorial methods* (2020).

46. E. Becquerel. Mémoire sur les effets électriques produits sous l'influence des rayons solaires. *Comptes Rendus* **9,** 561–567 (1839).

47. R. Corkish, D. S.-P. Chan and M. A. Green. Excitons in silicon diodes and solar cells: A three-particle theory. *Journal of Applied Physics* **79,** 195–203 (1996). DOI: 10.1063/1.360931.

48. I. Campillo, J. M. Pitarke, A. Rubio, E. Zarate and P. M. Echenique. Inelastic Lifetimes of Hot Electrons in Real Metals. *Physical Review Letters* **83,** 2230–2233 (1999). DOI: 10.1103/PhysRevLett.83.2230.

49. T. J. Ahrenst and F. Wooten. Electrical Conductivity Induced in Insulators by Pulsed Radiation. *IEEE Transactions on Nuclear Science* **23,** 1268–1272 (1976). DOI: 10.1109/TNS.1976.4328451.

50. W. Brütting. in, 1–14 (Wiley, May 2005). DOI: 10.1002/3527606637.ch.

51. J. Yan, E. Rezasoltani, M. Azzouzi, F. Eisner and J. Nelson. Influence of static disorder of charge transfer state on voltage loss in organic photovoltaics. *Nature Communications* **12,** 3642 (2021). DOI: 10.1038/s41467-021-23975-3.

52. X.-K. Chen, D. Qian, Y. Wang, T. Kirchartz, W. Tress, H. Yao, J. Yuan, M. Hülsbeck, M. Zhang, Y. Zou, Y. Sun, Y. Li, J. Hou, O. Inganäs, V. Coropceanu, J.-L. Bredas and F. Gao. A unified description of non-radiative voltage losses in organic solar cells. *Nature Energy* **6,** 799–806 (2021). DOI: 10.1038/s41560-021-00843-4.

53. Y. Tamai. Delocalization boosts charge separation in organic solar cells. *Polymer Journal* **52,** 691–700 (2020). DOI: 10.1038/s41428-020-0339-4.

54. M. A. Faist, T. Kirchartz, W. Gong, R. S. Ashraf, I. McCulloch, J. C. de Mello, N. J. Ekins-Daukes, D. D. C. Bradley and J. Nelson. Competition between the Charge Transfer State and the Singlet States of Donor or Acceptor Limiting the Efficiency in Polymer:Fullerene Solar Cells. *Journal of the American Chemical Society* **134,** 685–692 (2012). DOI: 10.1021/ja210029w.

55. Y. Cui, Y. Xu, H. Yao, P. Bi, L. Hong, J. Zhang, Y. Zu, T. Zhang, J. Qin, J. Ren, Z. Chen, C. He, X. Hao, Z. Wei and J. Hou. Single-Junction Organic Photovoltaic Cell with 19% Efficiency. *Advanced Materials* **33,** 2102420 (2021). DOI: 10.1002/adma.202102420.

56. Q. Liu, J. Fang, J. Wu, L. Zhu, X. Guo, F. Liu and M. Zhang. Tuning Aggregation Behavior of Polymer Donor via Molecular-Weight Control for Achieving 17.1% Efficiency Inverted Polymer Solar Cells. *Chinese Journal of Chemistry* **39,** 1941–1947 (2021). DOI: 10.1002/cjoc.202100112.

57. D. Qian, Z. Zheng, H. Yao, W. Tress, T. R. Hopper, S. Chen, S. Li, J. Liu, S. Chen, J. Zhang, X.-K. Liu, B. Gao, L. Ouyang, Y. Jin, G. Pozina, I. A. Buyanova, W. M. Chen, O. Inganäs, V. Coropceanu, J.-L. Bredas, H. Yan, J. Hou, F. Zhang, A. A. Bakulin and F. Gao. Design rules for minimizing voltage losses in high-efficiency organic solar cells. *Nature Materials* **17,** 703–709 (2018). DOI: 10.1038/s41563-018-0128-z.

58. M. Pranav, A. Shukla, D. Moser, J. Rumeney, W. Liu, R. Wang, B. Sun, S. Smeets, N. Tokmoldin, F. Jaiser, T. Hultzsch, S. Shoaee, W. Maes, L. Lüer, C. Brabec, K. Vandewal, D. Andrienko, S. Ludwigs and D. Neher. On the critical competition between singlet exciton decay and free charge generation in non-fullerene-based organic solar cells with low energetic offsets (2024). DOI: 10.48550/arXiv.2404.03960.

59. M. Azzouzi, J. Yan, T. Kirchartz, K. Liu, J. Wang, H. Wu and J. Nelson. Nonradiative Energy Losses in Bulk-Heterojunction Organic Photovoltaics. *Physical Review X* **8,** 031055 (2018). DOI: 10.1103/PhysRevX.8.031055.

60. A. A. Bakulin, A. Rao, V. G. Pavelyev, P. H. M. van Loosdrecht, M. S. Pshenichnikov, D. Niedzialek, J. Cornil, D. Beljonne and R. H. Friend. The Role of Driving Energy and Delocalized States for Charge Separation in Organic Semiconductors. *Science* **335,** 1340–1344 (2012). DOI: 10.1126/science.1217745.

61. S. ichiro Natsuda, T. Saito, R. Shirouchi, K. Imakita and Y. Tamai. Delocalization suppresses nonradiative charge recombination in polymer solar cells. *Polymer Journal* **54,** 1345–1353 (2022). DOI: 10.1038/s41428-022-00685-1.

62. V. Belova, A. Perevedentsev, J. Gorenflot, C. S. P. D. Castro, M. Casademont-Viñas, S. H. K. Paleti, S. Karuthedath, D. Baran, F. Laquai and M. Campoy-Quiles. Effect of Quencher, Geometry, and Light Outcoupling on the Determination of Exciton Diffusion Length in Nonfullerene Acceptors. *Solar RRL* **6,** 2100822 (2022). DOI: 10.1002/solr.202100822.

63. Y. Firdaus, V. M. L. Corre, S. Karuthedath, W. Liu, A. Markina, W. Huang, S. Chattopadhyay, M. M. Nahid, M. I. Nugraha, Y. Lin, A. Seitkhan, A. Basu, W. Zhang, I. McCulloch, H. Ade, J. Labram, F. Laquai, D. Andrienko, L. J. A. Koster and T. D. Anthopoulos. Long-range exciton diffusion in molecular non-fullerene acceptors. *Nature Communications* **11,** 5220 (2020). DOI: 10.1038/s41467-020-19029-9.

64. M. T. Sajjad, A. Ruseckas, L. K. Jagadamma, Y. Zhang and I. D. W. Samuel. Long-range exciton diffusion in non-fullerene acceptors and coarse bulk heterojunctions enable highly efficient organic photovoltaics. *Journal of Materials Chemistry A* **8,** 15687–15694 (2020). DOI: 10.1039/D0TA06017H.

65. S. Chandrabose, K. Chen, A. J. Barker, J. J. Sutton, S. K. K. Prasad, J. Zhu, J. Zhou, K. C. Gordon, Z. Xie, X. Zhan and J. M. Hodgkiss. High Exciton Diffusion Coefficients in Fused Ring Electron Acceptor Films. *Journal of the American Chemical Society* **141,** 6922–6929 (2019). DOI: 10.1021/jacs.8b12982.

66. M. T. Sajjad, A. Ruseckas and I. D. Samuel. Enhancing Exciton Diffusion Length Provides New Opportunities for Organic Photovoltaics. *Matter* **3,** 341–354 (2020). DOI: 10.1016/j.matt.2020.06.028.

67. G. Yu, J. Gao, J. C. Hummelen, F. Wudl and A. J. Heeger. Polymer Photovoltaic Cells: Enhanced Efficiencies via a Network of Internal Donor-Acceptor Heterojunctions. *Science* **270,** 1789–1791 (1995). DOI: 10.1126/science.270.5243.1789.

68. M. Scharber and N. Sariciftci. Efficiency of bulk-heterojunction organic solar cells. *Progress in Polymer Science* **38,** 1929–1940 (2013). DOI: 10.1016/j.progpolymsci.2013.05.001.

69. H. Youn, H. J. Park and L. J. Guo. Organic Photovoltaic Cells: From Performance Improvement to Manufacturing Processes. *Small* **11,** 2228–2246 (2015). DOI: 10.1002/smll.201402883.

70. A. K. K. Kyaw, D. H. Wang, C. Luo, Y. Cao, T. Nguyen, G. C. Bazan and A. J. Heeger. Effects of Solvent Additives on Morphology, Charge Generation, Transport, and Recombination in Solution-Processed Small-Molecule Solar Cells. *Advanced Energy Materials* **4,** 1301469 (2014). DOI: 10.1002/aenm.201301469.

71. R. Liang, M. Babics, A. Seitkhan, K. Wang, P. B. Geraghty, S. Lopatin, F. Cruciani, Y. Firdaus, M. Caporuscio, D. J. Jones and P. M. Beaujuge. Additive-Morphology Interplay and Loss Channels in "All-Small-Molecule" Bulk-heterojunction (BHJ) Solar Cells with the Nonfullerene Acceptor IDTTBM. *Advanced Functional Materials* **28,** 1705464 (2018). DOI: 10.1002/adfm.201705464.

72. C. McDowell, M. Abdelsamie, M. F. Toney and G. C. Bazan. Solvent Additives: Key Morphology-Directing Agents for Solution-Processed Organic Solar Cells. *Advanced Materials* **30,** 1707114 (2018). DOI: 10.1002/adma.201707114.

73. M. Reyes-Reyes, K. Kim and D. L. Carroll. High-efficiency photovoltaic devices based on annealed poly(3-hexylthiophene) and 1-(3-methoxycarbonyl)-propyl-1- phenyl- (6,6) C61 blends. *Applied Physics Letters* **87** (2005). DOI: 10.1063/1.2006986/117573.

74. H. Huang and J. Huang. *Organic and Hybrid Solar Cells* (eds H. Huang and J. Huang) 1–337. DOI: 10.1007/978-3-319-10855-1 (Springer International Publishing, July 2014).

75. G. Burwell, N. Burridge, E. Bond, W. Li, P. Meredith and A. Armin. Parameterization of Metallic Grids on Transparent Conductive Electrodes for the Scaling of Organic Solar Cells. *Advanced Electronic Materials* **7,** 2100192 (2021). DOI: 10.1002/aelm.202100192.

76. K. Wang, C. Liu, T. Meng, C. Yi and X. Gong. Inverted organic photovoltaic cells. *Chemical Society Reviews* **45,** 2937–2975 (2016). DOI: 10.1039/C5CS00831J.

77. C. E. Petoukhoff, D. K. Vijapurapu and D. M. O'Carroll. Computational comparison of conventional and inverted organic photovoltaic performance parameters with varying metal electrode surface workfunction. *Solar Energy Materials and Solar Cells* **120,** 572–583 (2014). DOI: 10.1016/j.solmat.2013.09.041.

78. M. Jørgensen, K. Norrman and F. C. Krebs. Stability/degradation of polymer solar cells. *Solar Energy Materials and Solar Cells* **92,** 686–714 (2008). DOI: 10.1016/j.solmat.2008.01.005.

79. *Reference Air Mass 1.5 Spectra | Grid Modernization | NREL* https://www.nrel.gov/grid/solar-resource/spectra-am1.5.html. Accessed on 2024-09-07.

80. *Solar spectrum calculator* https://www2.pvlighthouse.com.au/calculators/solar%20spectrum%20calculator/solar%20spectrum%20calculator.aspx. Accessed on 2024-09-07.

81. T. Markvart. Thermodynamics of losses in photovoltaic conversion. *Applied Physics Letters* **91,** 1–3 (2007). DOI: 10.1063/1.2766857.

82. S. Rühle. Tabulated values of the Shockley–Queisser limit for single junction solar cells. *Solar Energy* **130,** 139–147 (2016). DOI: 10.1016/j.solener.2016.02.015.

83. W. G. van Sark, K. W. Barnham, L. H. Slooff, A. J. Chatten, A. Büchtemann, A. Meyer, S. J. McCormack, R. Koole, D. J. Farrell, R. Bose, E. E. Bende, A. R. Burgers, T. Budel, J. Quilitz, M. Kennedy, T. Meyer, C. D. M. Donegá, A. Meijerink and D. Vanmaekelbergh. Luminescent Solar Concentrators - A review of recent results. *Optics Express* **16,** 21773 (2008). DOI: 10.1364/OE.16.021773.

84. U. Rau, F. Einsele and G. C. Glaeser. Efficiency limits of photovoltaic fluorescent collectors. *Applied Physics Letters* **87,** 1–3 (2005). DOI: 10.1063/1.2112196.

85. T. Trupke, M. A. Green and P. Würfel. Improving solar cell efficiencies by up-conversion of sub-band-gap light. *Journal of Applied Physics* **92,** 4117–4122 (2002). DOI: 10.1063/1.1505677.

86. T. Trupke, M. A. Green and P. Würfel. Improving solar cell efficiencies by down-conversion of high-energy photons. *Journal of Applied Physics* **92,** 1668–1674 (2002). DOI: 10.1063/1.1492021.

87. P. F. Baldasaro, J. E. Raynolds, G. W. Charache, D. M. DePoy, C. T. Ballinger, T. Donovan and J. M. Borrego. Thermodynamic analysis of thermophotovoltaic efficiency and power density tradeoffs. *Journal of Applied Physics* **89,** 3319–3327 (2001). DOI: 10.1063/1.1344580.

88. N.-P. Harder and P. W. rfel. Theoretical limits of thermophotovoltaic solar energy conversion. *Semiconductor Science and Technology* **18,** S151–S157 (2003). DOI: 10.1088/0268-1242/18/5/303.

89. M. Yoshida, N. J. Ekins-Daukes, D. J. Farrell and C. C. Phillips. Photon ratchet intermediate band solar cells. *Applied Physics Letters* **100** (2012). DOI: 10.1063/1.4731277.

90. A. S. Brown and M. A. Green. Intermediate band solar cell with many bands: Ideal performance. *Journal of Applied Physics* **94,** 6150–6158 (2003). DOI: 10.1063/1.1610774.

91. S. Deb and H. Saha. Secondary ionisation and its possible bearing on the performance of a solar cell. *Solid-State Electronics* **15,** 1389–1391 (1972). DOI: 10.1016/0038-1101(72)90135-9.

92. F. J. Wilkinson, A. J. D. Farmer and J. Geist. The near ultraviolet quantum yield of silicon. *Journal of Applied Physics* **54,** 1172–1174 (1983). DOI: 10.1063/1.332095.

93. N. J. L. K. Davis, M. L. Böhm, M. Tabachnyk, F. Wisnivesky-Rocca-Rivarola, T. C. Jellicoe, C. Ducati, B. Ehrler and N. C. Greenham. Multiple-exciton generation in lead selenide nanorod solar cells with external quantum efficiencies exceeding 120%. *Nature Communications* **6,** 8259 (2015). DOI: 10.1038/ncomms9259.

94. A. D. Vos. Detailed balance limit of the efficiency of tandem solar cells. *Journal of Physics D: Applied Physics* **13,** 839–846 (1980). DOI: 10.1088/0022-3727/13/5/018.

95. M. A. Green. Commercial progress and challenges for photovoltaics. *Nature Energy* **1,** 15015 (2016). DOI: 10.1038/nenergy.2015.15.

96. T. Ameri, N. Li and C. J. Brabec. Highly efficient organic tandem solar cells: a follow up review. *Energy & Environmental Science* **6,** 2390 (2013). DOI: 10.1039/c3ee40388b.

97. J. Werner, B. Niesen and C. Ballif. Perovskite/Silicon Tandem Solar Cells: Marriage of Convenience or True Love Story? – An Overview. *Advanced Materials Interfaces* **5** (2018). DOI: 10.1002/admi.201700731.

98. T. Ameri, G. Dennler, C. Lungenschmied and C. J. Brabec. Organic tandem solar cells: A review. *Energy & Environmental Science* **2,** 347 (2009). DOI: 10.1039/b817952b.

99. M. Yamaguchi, K.-H. Lee, K. Araki and N. Kojima. A review of recent progress in heterogeneous silicon tandem solar cells. *Journal of Physics D: Applied Physics* **51,** 133002 (2018). DOI: 10.1088/1361-6463/aaaf08.

100. B. Chen, X. Zheng, Y. Bai, N. P. Padture and J. Huang. Progress in Tandem Solar Cells Based on Hybrid Organic–Inorganic Perovskites. *Advanced Energy Materials* **7** (2017). DOI: 10.1002/aenm.201602400.

101. S. Biswas, Y. You, P. Vincent, J. Bae, J. W. Shim and H. Kim. Organic tandem solar cells under indoor light illumination. *Progress in Photovoltaics: Research and Applications* **28,** 946–955 (2020). DOI: 10.1002/pip.3301.

102. M. I. Hossain, W. Qarony, S. Ma, L. Zeng, D. Knipp and Y. H. Tsang. Perovskite/Silicon Tandem Solar Cells: From Detailed Balance Limit Calculations to Photon Management. *Nano-Micro Letters* **11,** 58 (2019). DOI: 10.1007/s40820-019-0287-8.

103. X. Gu, X. Lai, Y. Zhang, T. Wang, W. L. Tan, C. R. McNeill, Q. Liu, P. Sonar, F. He, W. Li, C. Shan and A. K. K. Kyaw. Organic Solar Cell With Efficiency Over 20% and V OC Exceeding 2.1 V Enabled by Tandem With All-Inorganic Perovskite and Thermal Annealing-Free Process. *Advanced Science* **9** (2022). DOI: 10.1002/advs.202200445.

104. X. Chen, Z. Jia, Z. Chen, T. Jiang, L. Bai, F. Tao, J. Chen, X. Chen, T. Liu, X. Xu, C. Yang, W. Shen, W. E. Sha, H. Zhu and Y. M. Yang. Efficient and Reproducible Monolithic Perovskite/Organic Tandem Solar Cells with Low-Loss Interconnecting Layers. *Joule* **4,** 1594–1606 (2020). DOI: 10.1016/j.joule.2020.06.006.

105. M. Bonnet-Eymard, M. Boccard, G. Bugnon, F. Sculati-Meillaud, M. Despeisse and C. Ballif. Optimized short-circuit current mismatch in multi-junction solar cells. *Solar Energy Materials and Solar Cells* **117,** 120–125 (2013). DOI: 10.1016/j.solmat.2013.05.046.

106. M. Meusel, R. Adelhelm, F. Dimroth, A. Bett and W. Warta. Spectral mismatch correction and spectrometric characterization of monolithic III–V multi-junction solar cells. *Progress in Photovoltaics: Research and Applications* **10,** 243–255 (2002). DOI: 10.1002/pip.407.

107. A. Mojiri, R. Taylor, E. Thomsen and G. Rosengarten. Spectral beam splitting for efficient conversion of solar energy—A review. *Renewable and Sustainable Energy Reviews* **28,** 654–663 (2013). DOI: 10.1016/j.rser.2013.08.026.

108. A. Mokri and M. Emziane. *Beam-splitting versus tandem cell approaches for converting the solar spectrum into electricity: A comparative study.* in *International Renewable Energy Conference (IREC)* (2010).

109. C. Lewis, W. Phillips, V. Shields, P. Stella and I. Bekey. *Multi-bandgap high efficiency converter (RAINBOW)* in *IECEC-97 Proceedings of the Thirty-Second Intersociety Energy Conversion Engineering Conference (Cat. No.97CH6203)* **1** (IEEE, 1997), 401–406. DOI: 10.1109/IECEC.1997.659222.

110. M. Smith, S. Sinharoy, V. Weizer, O. Khan, A. Pal, E. Clark, D. Wilt, D. Scheiman and N. Mardesich. *Solar cells for NASA RAINBOW concentrator* in *Conference Record of the Twenty-Eighth IEEE Photovoltaic Specialists Conference - 2000 (Cat. No.00CH37036)* (IEEE, 2000), 1139–1141. DOI: 10.1109/PVSC.2000.916088.

111. B. Mitchell, G. Peharz, G. Siefer, M. Peters, T. Gandy, J. C. Goldschmidt, J. Benick, S. W. Glunz, A. W. Bett and F. Dimroth. Four-junction spectral beam-splitting photovoltaic receiver with high optical efficiency. *Progress in Photovoltaics: Research and Applications* **19,** 61–72 (2011). DOI: 10.1002/pip.988.

112. H. Uzu, M. Ichikawa, M. Hino, K. Nakano, T. Meguro, J. L. Hernández, H.-S. Kim, N.-G. Park and K. Yamamoto. High efficiency solar cells combining a perovskite and a silicon heterojunction solar cells via an optical splitting system. *Applied Physics Letters* **106** (2015). DOI: 10.1063/1.4905177.

113. H. Ferhati, F. Djeffal, A. Bendjerad, A. Benhaya and A. Saidi. Perovskite/InGaAs tandem cell exceeding 29% efficiency via optimizing spectral splitter based on RF sputtered ITO/Ag/ITO ultra-thin structure. *Physica E: Low-dimensional Systems and Nanostructures* **128,** 114618 (2021). DOI: 10.1016/j.physe.2020.114618.

114. S. Jiang, P. Hu, S. Mo and Z. Chen. Optical modeling for a two-stage parabolic trough concentrating photovoltaic/thermal system using spectral beam splitting technology. *Solar Energy Materials and Solar Cells* **94,** 1686–1696 (2010). DOI: 10.1016/j.solmat.2010.05.029.

115. H. Liang, R. Su, W. Huang, Z. Cheng, F. Wang, G. Huang and D. Yang. A novel spectral beam splitting photovoltaic/thermal hybrid system based on semi-transparent solar cell with serrated groove structure for co-generation of electricity and high-grade thermal energy. *Energy Conversion and Management* **252,** 115049 (2022). DOI: 10.1016/j.enconman.2021.115049.

116. G. Wang, Y. Yao, Z. Chen and P. Hu. Thermodynamic and optical analyses of a hybrid solar CPV/T system with high solar concentrating uniformity based on spectral beam splitting technology. *Energy* **166,** 256–266 (2019). DOI: 10.1016/j.energy.2018.10.089.

117. S. A. Omer and D. G. Infield. Design and thermal analysis of a two stage solar concentrator for combined heat and thermoelectric power generation. *Energy Conversion and Management* **41,** 737–756 (2000). DOI: 10.1016/S0196-8904(99)00134-X.

118. S. Mahmoudinezhad, D. Cotfas, P. Cotfas, E. J. Skjølstrup, K. Pedersen, L. Rosendahl and A. Rezania. Experimental investigation on spectrum beam splitting photovoltaic–thermoelectric generator under moderate solar concentrations. *Energy* **238,** 121988 (2022). DOI: 10.1016/j.energy.2021.121988.

119. G. Rockendorf, R. Sillmann, L. Podlowski and B. Litzenburger. PV-hybrid and thermoelectric collectors. *Solar Energy* **67,** 227–237 (1999). DOI: 10.1016/S0038-092X(00)00075-X.

120. N. Mardesich and V. Shields. Advanced Rainbow Solar Photovoltaic Arrays. *NASA Tech Briefs, June 2003* (2003).

121. A. Ruland, C. Schulz-Drost, V. Sgobba and D. M. Guldi. Enhancing Photocurrent Efficiencies by Resonance Energy Transfer in CdTe Quantum Dot Multilayers: Towards Rainbow Solar Cells. *Advanced Materials* **23,** 4573–4577 (2011). DOI: 10.1002/adma.201101423.

122. S. M. Raupp, M. Schmitt, A.-L. Walz, R. Diehm, H. Hummel, P. Scharfer and W. Schabel. Slot die stripe coating of low viscous fluids. *Journal of Coatings Technology and Research* **15,** 899–911 (2018). DOI: 10.1007/s11998-017-0039-y.

123. D. Shin, J. Lee and J. Park. Effect of Slit Channel Width of a Shim Embedded in Slot-Die Head on High-Density Stripe Coating for OLEDs. *Coatings* **10,** 772 (2020). DOI: 10.3390/coatings10080772.

124. A. W. Parsekian and T. A. L. Harris. Scalable, Alternating Narrow Stripes of Polyvinyl Alcohol Support and Unmodified PEDOT:PSS with Maintained Conductivity Using a Single-Step Slot Die Coating Approach. *ACS Applied Materials & Interfaces* **12,** 3736–3745 (2020). DOI: 10.1021/acsami.9b18936.

125. J. Lee and J. Park. Increased stripe density of slot-coated PEDOT:PSS using a meniscus guide with linearly tapered μ-tips for OLEDs. *Organic Electronics* **83,** 105772 (2020). DOI: 10.1016/j.orgel.2020.105772.

126. F. I. Mime, M. R. Islam, E. Hossain, I. M. Mehedi and M. T. Hasan. Design and Performance Analysis of Tandem Organic Solar Cells: Effect of Cell Parameter. *IEEE Access* **9,** 40665–40680 (2021). DOI: 10.1109/ACCESS.2021.3063810.

127. I. Etxebarria, J. Ajuria and R. Pacios. Solution-processable polymeric solar cells: A review on materials, strategies and cell architectures to overcome 10%. *Organic Electronics* **19,** 34–60 (2015). DOI: 10.1016/j.orgel.2015.01.014.

128. H. Liu, Z. Ren, Z. Liu, A. G. Aberle, T. Buonassisi and I. M. Peters. Predicting the outdoor performance of flat-plate III–V/Si tandem solar cells. *Solar Energy* **149,** 77–84 (2017). DOI: 10.1016/j.solener.2017.04.003.

129. M. T. Hörantner and H. J. Snaith. Predicting and optimising the energy yield of perovskite-on-silicon tandem solar cells under real world conditions. *Energy & Environmental Science* **10,** 1983–1993 (2017). DOI: 10.1039/C7EE01232B.

130. J. M. Ripalda, J. Buencuerpo and I. García. Solar cell designs by maximizing energy production based on machine learning clustering of spectral variations. *Nature Communications* **9,** 5126 (2018). DOI: 10.1038/s41467-018-07431-3.

131. I. M. Peters, C. D. R. Gallegos, L. Lüer, J. A. Hauch and C. J. Brabec. Practical limits of multijunction solar cells. *Progress in Photovoltaics: Research and Applications* **31,** 1006–1015 (2023). DOI: 10.1002/pip.3705.

132. B. Dörling. *Conjugated Materials for Thermoelectrics and Photovoltaics* (Universitat Autònoma de Barcelona, 2017).

133. J. Hofinger, S. Weber, F. Mayr, A. Jodlbauer, M. Reinfelds, T. Rath, G. Trimmel and M. C. Scharber. Wide-bandgap organic solar cells with a novel perylene-based non-fullerene acceptor enabling open-circuit voltages beyond 1.4 V. *Journal of Materials Chemistry A* **10,** 2888–2906 (2022). DOI: 10.1039/D1TA09752K.

134. J. Ahmad, K. Bazaka, L. J. Anderson, R. D. White and M. V. Jacob. Materials and methods for encapsulation of OPV: A review. *Renewable and Sustainable Energy Reviews* **27,** 104–117 (2013). DOI: 10.1016/j.rser.2013.06.027.

135. E. Planes, S. Juillard, M. Matheron, N. Charvin, S. Cros, D. Qian, F. Zhang, S. Berson and L. Flandin. Encapsulation Effect on Performance and Stability of Organic Solar Cells. *Advanced Materials Interfaces* **7,** 2000293 (2020). DOI: 10.1002/admi.202000293.

136. Delo. *DELO ® KATIOBOND ® LP655* https://www.inseto.co.uk/wp-content/uploads/2019/06/KB-LP655-TDS.pdf. Accessed on 2024-09-07.

137. *UV lamps, EL series | VWR* https://es.vwr.com/store/product/8099358/uv-lamps-el-series. Accessed on 2024-09-07.

138. *Glass Substrate Encapsulation Coverslips / Slides | Ossila* https://www.ossila.com/products/encapsulation-coverslips?variant=31488550568032. Accessed on 2024-09-07.

139. P. G. V. Sampaio, M. O. A. González, P. O. Ferreira, P. C. J. Vidal, J. P. P. Pereira, H. R. Ferreira and P. C. Oprime. Overview of printing and coating techniques in the production of organic photovoltaic cells. *International Journal of Energy Research* **44,** 9912–9931 (2020). DOI: 10.1002/er.5664.

140. G. Bernardo, T. Lopes, D. G. Lidzey and A. Mendes. Progress in Upscaling Organic Photovoltaic Devices. *Advanced Energy Materials* **11,** 2100342 (2021). DOI: 10.1002/aenm.202100342.

141. J. Cheng, F. Liu, Z. Tang and Y. Li. Scalable Blade Coating: A Technique Accelerating the Commercialization of Perovskite-Based Photovoltaics. *Energy Technology* **9,** 2100204 (2021). DOI: 10.1002/ente.202100204.

142. M. Riede, D. Spoltore and K. Leo. Organic Solar Cells—The Path to Commercial Success. *Advanced Energy Materials* **11,** 2002653 (2021). DOI: 10.1002/aenm.202002653.

143. R. Adel, G. Morse, F. Silvestri, E. Barrena, E. Martinez-Ferrero, M. Campoy-Quiles, P. Tiwana and M. Stella. Understanding the blade coated to roll-to-roll coated performance gap in organic photovoltaics. *Solar Energy Materials and Solar Cells* **245,** 111852 (2022). DOI: 10.1016/j.solmat.2022.111852.

144. F. C. Krebs. Fabrication and processing of polymer solar cells: A review of printing and coating techniques. *Solar Energy Materials and Solar Cells* **93,** 394–412 (2009). DOI: 10.1016/j.solmat.2008.10.004.

145. L. Landau and B. Levich. in, 141–153 (Elsevier, Jan. 1988). DOI: 10.1016/B978-0-08-092523-3.50016-2.

146. X. Niu, N. Li, Q. Chen and H. Zhou. Insights into Large-Scale Fabrication Methods in Perovskite Photovoltaics. *Advanced Energy and Sustainability Research* **2,** 2000046 (2021). DOI: 10.1002/aesr.202000046.

147. Y. Deng, X. Zheng, Y. Bai, Q. Wang, J. Zhao and J. Huang. Surfactant-controlled ink drying enables high-speed deposition of perovskite films for efficient photovoltaic modules. *Nature Energy* **3,** 560–566 (2018). DOI: 10.1038/s41560-018-0153-9.

148. B. G. Higgins. Film flow on a rotating disk. *The Physics of Fluids* **29,** 3522–3529 (1986). DOI: 10.1063/1.865829.

149. K. Norrman, A. Ghanbari-Siahkali and N. B. Larsen. 6 Studies of spin-coated polymer films. *Annual Reports Section "C" (Physical Chemistry)* **101,** 174 (2005). DOI: 10.1039/b408857n.

150. C.-C. Chang, C.-L. Pai, W.-C. Chen and S. A. Jenekhe. Spin coating of conjugated polymers for electronic and optoelectronic applications. *Thin Solid Films* **479,** 254–260 (2005). DOI: 10.1016/j.tsf.2004.12.013.

151. F. L. Givens and W. J. Daughton. On the Uniformity of Thin Films: A New Technique Applied to Polyimides. *Journal of The Electrochemical Society* **126,** 269–272 (1979). DOI: 10.1149/1.2129019.

152. B. T. Chen. Investigation of the solvent-evaporation effect on spin coating of thin films. *Polymer Engineering & Science* **23,** 399–403 (1983). DOI: 10.1002/pen.760230706.

153. D. Meyerhofer. Characteristics of resist films produced by spinning. *Journal of Applied Physics* **49,** 3993–3997 (1978). DOI: 10.1063/1.325357.

154. S. M. Sze and M. K. Lee. Semiconductor devices : physics and technology (2012).

155. *Kurt J. Lesker Company | Silver Ag Evaporation Process Notes | Enabling Technology for a Better World* https://www.lesker.com/newweb/deposition_materials/deposition-materials-notes.cfm?pgid=ag1. Accessed on 2024-09-07.

156. S. K. Deb and J. A. Chopoorian. Optical Properties and Color-Center Formation in Thin Films of Molybdenum Trioxide. *Journal of Applied Physics* **37,** 4818–4825 (1966). DOI: 10.1063/1.1708145.

157. P. Carcia and E. McCarron. Synthesis and properties of thin film polymorphs of molybdenum trioxide. *Thin Solid Films* **155,** 53–63 (1987). DOI: 10.1016/0040-6090(87)90452-4.

158. *Kurt J. Lesker Company | Molybdenum Oxide MoO3 Evaporation Process Notes | Enabling Technology for a Better World* https://www.lesker.com/newweb/deposition_materials/deposition-materials-notes.cfm?pgid=moo3. Accessed on 2024-09-07.

159. M. Gibert-Roca. *On Improving the Efficiency of Organic Photovoltaic Devices : Novel Strategies* (2022).

160. J. Loskot, D. Jezbera, R. Loskot, D. Bušovský, A. Barylski, K. Glowka, P. Duda, K. Aniołek, K. Voglová and M. Zubko. Influence of print speed on the microstructure, morphology, and mechanical properties of 3D-printed PETG products. *Polymer Testing* **123,** 108055 (2023). DOI: 10.1016/j.polymertesting.2023.108055.

161. A. L. Silva, G. M. da Silva Salvador, S. V. F. Castro, N. M. F. Carvalho and R. A. A. Munoz. A 3D Printer Guide for the Development and Application of Electrochemical Cells and Devices. *Frontiers in Chemistry* **9,** 684256 (2021). DOI: 10.3389/fchem.2021.684256.

162. J. Humlíček. in, 3–91 (Elsevier, 2005). DOI: 10.1016/B978-081551499-2.50003-4.

163. H. Fujiwara. in, 1–11 (Wiley, Jan. 2007). DOI: 10.1002/9780470060193.ch1.

164. M. Campoy-Quiles, M. I. Alonso, D. D. C. Bradley and L. J. Richter. Advanced Ellipsometric Characterization of Conjugated Polymer Films. *Advanced Functional Materials* **24,** 2116–2134 (2014). DOI: 10.1002/adfm.201303060.

165. M. I. Alonso and M. Campoy-Quiles. in, 439–461 (Springer Verlag, 2018). DOI: 10.1007/978-3-319-75377-5_15.

166. Y.-H. Lin, K. G. Yager, B. Stewart and R. Verduzco. Lamellar and liquid crystal ordering in solvent-annealed all-conjugated block copolymers. *Soft Matter* **10,** 3817–3825 (2014). DOI: 10.1039/C3SM53090F.

167. M. Casademont-Viñas, M. Gibert-Roca, M. Campoy-Quiles and A. R. Goñi. Spectrum on demand light source (SOLS) for advanced photovoltaic characterization. *Review of Scientific Instruments* **94,** 103907 (2023). DOI: 10.1063/5.0156236.

168. M. Gibert-Roca, M. Casademont-Viñas, A. R. Goñi and M. Campoy-Quiles. Dispositivo de iluminación y modulador espectral. *Oficina española de patentes y marcas,* ES2956835 B2 (2023).

169. D. H. Li, N. T. Chau and K. K. Wan. Predicting daylight illuminance and solar irradiance on vertical surfaces based on classified standard skies. *Energy* **53,** 252–258 (2013). DOI: 10.1016/j.energy.2013.02.049.

170. M. Blumthaler, W. Ambach and R. Ellinger. Increase in solar UV radiation with altitude. *Journal of Photochemistry and Photobiology B: Biology* **39,** 130–134 (1997). DOI: 10.1016/S1011-1344(96)00018-8.

171. P. Faine, S. R. Kurtz, C. Riordan and J. Olson. The influence of spectral solar irradiance variations on the performance of selected single-junction and multijunction solar cells. *Solar Cells* **31,** 259–278 (1991). DOI: 10.1016/0379-6787(91)90027-M.

172. J. A. Röhr, J. Lipton, J. Kong, S. A. Maclean and A. D. Taylor. Efficiency Limits of Underwater Solar Cells. *Joule* **4,** 840–849 (2020). DOI: 10.1016/j.joule.2020.02.005.

173. H. S. Ryu, S. Y. Park, T. H. Lee, J. Y. Kim and H. Y. Woo. Recent progress in indoor organic photovoltaics. *Nanoscale* **12,** 5792–5804 (2020). DOI: 10.1039/D0NR00816H.

174. G. Kumar and F.-C. Chen. A review on recent progress in organic photovoltaic devices for indoor applications. *Journal of Physics D: Applied Physics* **56,** 353001 (2023). DOI: 10.1088/1361-6463/acd2e5.

175. B. Minnaert and P. Veelaert. A Proposal for Typical Artificial Light Sources for the Characterization of Indoor Photovoltaic Applications. *Energies* **7,** 1500–1516 (2014). DOI: 10.3390/en7031500.

176. M. Gibert-Roca, M. Casademont-Viñas, Q. Liu, K. Vandewal, A. R. Goñi and M. Campoy-Quiles. RAINBOW Organic Solar Cells: Implementing Spectral Splitting in Lateral Multi-Junction Architectures. *Advanced Materials* **36,** 2212226 (2024). DOI: 10.1002/adma.202212226.

177. L. Lüer, I. M. Peters, V. M. L. Corre, K. Forberich, D. M. Guldi and C. J. Brabec. Bypassing the Single Junction Limit with Advanced Photovoltaic Architectures. *Advanced Materials* **36,** 2308578 (2024). DOI: 10.1002/adma.202308578.

178. C. E. T. Ayuga and J. Zamorano. LICA AstroCalc, a software to analyze the impact of artificial light: Extracting parameters from the spectra of street and indoor lamps. *Journal of Quantitative Spectroscopy and Radiative Transfer* **214,** 33–38 (2018). DOI: 10.1016/j.jqsrt.2018.04.022.

179. *Spectra of Lamps | GUAIX* https://guaix.fis.ucm.es/lamps_spectra. Accessed on.

180. A. Bracher, M. H. Taylor, B. B. Taylor, T. Dinter, R. Röttgers and F. Steinmetz. in. In supplement to: Bracher, A et al. (2015): Using empirical orthogonal functions derived from remote-sensing reflectance for the prediction of phytoplankton pigment concentrations. Ocean Science, 11(1), 139-158, https://doi.org/10.5194/os-11-139-2015 (PANGAEA, 2015). DOI: 10.1594/PANGAEA.821124.

181. A. Bracher, M. H. Taylor, B. Taylor, T. Dinter, R. Röttgers and F. Steinmetz. Using empirical orthogonal functions derived from remote-sensing reflectance for the prediction of phytoplankton pigment concentrations. *Ocean Science* **11,** 139–158 (2015). DOI: 10.5194/os-11-139-2015.

182. V. Esen, Şafak Sağlam and B. Oral. Light sources of solar simulators for photovoltaic devices: A review. *Renewable and Sustainable Energy Reviews* **77,** 1240–1250 (2017). DOI: 10.1016/j.rser.2017.03.062.

183. J. Vollbrecht, V. V. Brus, S. Ko, J. Lee, A. Karki, D. X. Cao, K. Cho, G. C. Bazan and T. Nguyen. Quantifying the Nongeminate Recombination Dynamics in Nonfullerene Bulk Heterojunction Organic Solar Cells. *Advanced Energy Materials* **9,** 1901438 (2019). DOI: 10.1002/aenm.201901438.

184. D. Lübke, P. Hartnagel, M. Hülsbeck and T. Kirchartz. Understanding the Thickness and Light-Intensity Dependent Performance of Green-Solvent Processed Organic Solar Cells. *ACS Materials Au* **3,** 215–230 (2023). DOI: 10.1021/acsmaterialsau.2c00070.

185. P. Hartnagel and T. Kirchartz. Understanding the Light-Intensity Dependence of the Short-Circuit Current of Organic Solar Cells. *Advanced Theory and Simulations* **3** (2020). DOI: 10.1002/adts.202000116.

186. D. Glowienka and Y. Galagan. Light Intensity Analysis of Photovoltaic Parameters for Perovskite Solar Cells. *Advanced Materials* **34,** 2105920 (2022). DOI: 10.1002/adma.202105920.

187. F. C. Krebs, K. O. Sylvester-Hvid and M. Jørgensen. A self-calibrating led-based solar test platform. *Progress in Photovoltaics: Research and Applications* **19,** 97–112 (2011). DOI: 10.1002/pip.963.

188. E. Lopez-Fraguas, J. M. Sanchez-Pena and R. Vergaz. A Low-Cost LED-Based Solar Simulator. *IEEE Transactions on Instrumentation and Measurement* **68,** 4913–4923 (2019). DOI: 10.1109/TIM.2019.2899513.

189. N. Hagen and T. S. Tkaczyk. Compound prism design principles, I. *Applied Optics* **50,** 4998 (2011). DOI: 10.1364/AO.50.004998.

190. N. Hagen and T. S. Tkaczyk. Compound prism design principles, II: triplet and Janssen prisms. *Applied Optics* **50,** 5012 (2011). DOI: 10.1364/AO.50.005012.

191. N. Hagen and T. S. Tkaczyk. Compound prism design principles, III: linear-in-wavenumber and optical coherence tomography prisms. *Applied Optics* **50,** 5023 (2011). DOI: 10.1364/AO.50.005023.

192. G. B. Donati. Intorno alle strie degli spettri stellari. *Il Nuovo Cimento* **15,** 292–304 (1862). DOI: 10.1007/BF02906594.

193. M. Thollon. Nouveau spectroscope. *Journal de Physique Théorique et Appliquée* **7,** 141–148 (1878). DOI: 10.1051/jphystap:018780070014100.

194. A. Riccò. Combinazioni spettroscopiche a visione diretta. *Memorie della Societa Degli Spettroscopisti Italiani, vol. 8, pp. A21-A34* **8,** A21–A34 (1879).

195. *scipy.optimize.minimize — SciPy v1.13.0 Manual* https://docs.scipy.org/doc/scipy/reference/generated/scipy.optimize.minimize.html#scipy.optimize.minimize. Accessed on.

196. P. Virtanen *et al.* SciPy 1.0: fundamental algorithms for scientific computing in Python. *Nature Methods* **17,** 261–272 (2020). DOI: 10.1038/s41592-019-0686-2.

197. D. D. C. Rasi and R. A. J. Janssen. Advances in Solution-Processed Multijunction Organic Solar Cells. *Advanced Materials* **31,** 1806499 (2019). DOI: 10.1002/adma.201806499.

198. S. K. Thio and S.-Y. Park. Dispersive Optical Systems for Highly-Concentrated Solar Spectrum Splitting: Concept, Design, and Performance Analyses. *Energies* **12,** 4719 (2019). DOI: 10.3390/en12244719.

199. S. D. Vorndran, S. Ayala, Y. Wu, J. M. Russo, R. K. Kostuk, J. T. Friedlein, S. E. Shaheen and C. K. Luscombe. *Holographic spectral beamsplitting for increased organic photovoltaic conversion efficiency* in *Organic Photovoltaics XV* (eds Z. H. Kafafi, P. A. Lane and I. D. W. Samuel) **9184** (Oct. 2014), 918423. DOI: 10.1117/12.2061773.

200. D.-F. Lin, B.-G. Quan, Q.-L. Zhang, D.-X. Zhang, X. Xu, J.-S. Ye, Y. Zhang, D.-M. Li, Q.-B. Meng, L. Pan and G.-Z. Yang. Spectrum-Splitting Diffractive Optical Element of High Concentration Factor and High Optical Efficiency for Three-Junction Photovoltaics. *Chinese Physics Letters* **33,** 094207 (2016). DOI: 10.1088/0256-307X/33/9/094207.

201. S. Kiyaee, Y. Saboohi and A. Z. Moshfegh. A new designed linear Fresnel lens solar concentrator based on spectral splitting for passive cooling of solar cells. *Energy Conversion and Management* **230,** 113782 (2021). DOI: 10.1016/j.enconman.2020.113782.

202. X. Ju, C. Xu, X. Han, X. Du, G. Wei and Y. Yang. A review of the concentrated photovoltaic/thermal (CPVT) hybrid solar systems based on the spectral beam splitting technology. *Applied Energy* **187,** 534–563 (2017). DOI: 10.1016/j.apenergy.2016.11.087.

203. S. Ullbrich, J. Benduhn, X. Jia, V. C. Nikolis, K. Tvingstedt, F. Piersimoni, S. Roland, Y. Liu, J. Wu, A. Fischer, D. Neher, S. Reineke, D. Spoltore and K. Vandewal. Emissive and charge-generating donor–acceptor interfaces for organic optoelectronics with low voltage losses. *Nature Materials* **18,** 459–464 (2019). DOI: 10.1038/s41563-019-0324-5.

204. M. S. Vezie, S. Few, I. Meager, G. Pieridou, B. Dörling, R. S. Ashraf, A. R. Goñi, H. Bronstein, I. McCulloch, S. C. Hayes, M. Campoy-Quiles and J. Nelson. Exploring the origin of high optical absorption in conjugated polymers. *Nature Materials* **15,** 746–753 (2016). DOI: 10.1038/nmat4645.

205. Y. Cui, Y. Wang, J. Bergqvist, H. Yao, Y. Xu, B. Gao, C. Yang, S. Zhang, O. Inganäs, F. Gao and J. Hou. Wide-gap non-fullerene acceptor enabling high-performance organic photovoltaic cells for indoor applications. *Nature Energy* **4,** 768–775 (2019). DOI: 10.1038/s41560-019-0448-5.

206. Y. Yang, C. Xue, H. Yin, Z. Chen and X.-T. Hao. Bandgap matching strategy for organic photovoltaic cells in oceanic applications. *Cell Reports Physical Science* **3,** 100861 (2022). DOI: 10.1016/j.xcrp.2022.100861.

207. J. Lee, S. Ko, M. Seifrid, H. Lee, B. R. Luginbuhl, A. Karki, M. Ford, K. Rosenthal, K. Cho, T. Nguyen and G. C. Bazan. Bandgap Narrowing in Non-Fullerene Acceptors: Single Atom Substitution Leads to High Optoelectronic Response Beyond 1000 nm. *Advanced Energy Materials* **8,** 1801212 (2018). DOI: 10.1002/aenm.201801212.

208. N. Schopp, G. Akhtanova, P. Panoy, A. Arbuz, S. Chae, A. Yi, H. J. Kim, V. Promarak, T. Nguyen and V. V. Brus. Unraveling Device Physics of Dilute-Donor Narrow-Bandgap Organic Solar Cells with Highly Transparent Active Layers. *Advanced Materials* **34,** 2203796 (2022). DOI: 10.1002/adma.202203796.

209. A. A. A. Torimtubun, M. J. Alonso-Navarro, A. Quesada-Ramírez, X. Rodríguez-Martínez, J. L. Segura, A. R. Goñi and M. Campoy-Quiles. High-Throughput Screening of Low-Bandgap Organic Semiconductors for Photovoltaic Applications: In the Search of

Correlations. *Solar RRL* **8,** 2400213 (2024). DOI: 10.1002/solr.202400213.

210. J. Lee, S.-J. Ko, H. Lee, J. Huang, Z. Zhu, M. Seifrid, J. Vollbrecht, V. V. Brus, A. Karki, H. Wang, K. Cho, T.-Q. Nguyen and G. C. Bazan. Side-Chain Engineering of Nonfullerene Acceptors for Near-Infrared Organic Photodetectors and Photovoltaics. *ACS Energy Letters* **4,** 1401–1409 (2019). DOI: 10.1021/acsenergylett.9b00721.

211. D. Kiermasch, L. Gil-Escrig, H. J. Bolink and K. Tvingstedt. Effects of Masking on Open-Circuit Voltage and Fill Factor in Solar Cells. *Joule* **3,** 16–26 (2019). DOI: 10.1016/j.joule.2018.10.016.

212. Y. Cui, L. Hong, T. Zhang, H. Meng, H. Yan, F. Gao and J. Hou. Accurate photovoltaic measurement of organic cells for indoor applications. *Joule* **5,** 1016–1023 (2021). DOI: 10.1016/j.joule.2021.03.029.

213. Y. Cui, H. Yao, T. Zhang, L. Hong, B. Gao, K. Xian, J. Qin and J. Hou. 1 cm 2 Organic Photovoltaic Cells for Indoor Application with over 20% Efficiency. *Advanced Materials* **31,** 1904512 (2019). DOI: 10.1002/adma.201904512.

214. R. Steim, T. Ameri, P. Schilinsky, C. Waldauf, G. Dennler, M. Scharber and C. J. Brabec. Organic photovoltaics for low light applications. *Solar Energy Materials and Solar Cells* **95,** 3256–3261 (2011). DOI: 10.1016/j.solmat.2011.07.011.

215. P. Schilinsky, C. Waldauf, J. Hauch and C. J. Brabec. Simulation of light intensity dependent current characteristics of polymer solar cells. *Journal of Applied Physics* **95,** 2816–2819 (2004). DOI: 10.1063/1.1646435.

216. L. J. A. Koster, V. D. Mihailetchi, R. Ramaker and P. W. M. Blom. Light intensity dependence of open-circuit voltage of polymer:fullerene solar cells. *Applied Physics Letters* **86** (2005). DOI: 10.1063/1.1889240.

217. A. Armin, R. D. J. van Vuuren, N. Kopidakis, P. L. Burn and P. Meredith. Narrowband light detection via internal quantum efficiency manipulation of organic photodiodes. *Nature Communications* **6,** 6343 (2015). DOI: 10.1038/ncomms7343.

218. J. Wang, Z. Zheng, P. Bi, Z. Chen, Y. Wang, X. Liu, S. Zhang, X. Hao, M. Zhang, Y. Li and J. Hou. Tandem organic solar cells with 20.6% efficiency enabled by reduced voltage losses. *National Science Review* **10,** nwad085 (2023). DOI: 10.1093/nsr/nwad085.

219. Z. Zheng, J. Wang, P. Bi, J. Ren, Y. Wang, Y. Yang, X. Liu, S. Zhang and J. Hou. Tandem Organic Solar Cell with 20.2% Efficiency. *Joule* **6,** 171–184 (2022). DOI: 10.1016/j.joule.2021.12.017.

220. L. Zhan, S. Li, T.-K. Lau, Y. Cui, X. Lu, M. Shi, C.-Z. Li, H. Li, J. Hou and H. Chen. Over 17% efficiency ternary organic solar cells enabled by two non-fullerene acceptors working in an alloy-like model. *Energy & Environmental Science* **13,** 635–645 (2020). DOI: 10.1039/C9EE03710A.

221. Y. Cui, H. Yao, J. Zhang, T. Zhang, Y. Wang, L. Hong, K. Xian, B. Xu, S. Zhang, J. Peng, Z. Wei, F. Gao and J. Hou. Over 16% efficiency organic photovoltaic cells enabled by a chlorinated acceptor with increased open-circuit voltages. *Nature Communications* **10,** 2515 (2019). DOI: 10.1038/s41467-019-10351-5.

222. C. B. Nielsen, S. Holliday, H.-Y. Chen, S. J. Cryer and I. McCulloch. Non-Fullerene Electron Acceptors for Use in Organic Solar Cells. *Accounts of Chemical Research* **48,** 2803–2812 (2015). DOI: 10.1021/acs.accounts.5b00199.

223. Y. Cui, L. Hong and J. Hou. Organic Photovoltaic Cells for Indoor Applications: Opportunities and Challenges. *ACS Applied Materials & Interfaces* **12,** 38815–38828 (2020). DOI: 10.1021/acsami.0c10444.

224. M. R. Busireddy, S.-C. Huang, Y.-J. Su, Z.-Y. Lee, C.-H. Wang, M. C. Scharber, J.-T. Chen and C.-S. Hsu. Eco-Friendly Solvent-Processed Dithienosilicon-Bridged Carbazole-Based Small-Molecule Acceptors Achieved over 25.7% PCE in Ternary Devices under Indoor Conditions. *ACS Applied Materials & Interfaces* **15,** 24658–24669 (2023). DOI: 10.1021/acsami.3c02966.

225. C. Lee, J. Lee, H. H. Lee, M. Nam and D. Ko. Over 30% Efficient Indoor Organic Photovoltaics Enabled by Morphological Modification Using Two Compatible Non-Fullerene Acceptors. *Advanced Energy Materials* **12** (2022). DOI: 10.1002/aenm.202200275.

226. L.-K. Ma, Y. Chen, P. C. Chow, G. Zhang, J. Huang, C. Ma, J. Zhang, H. Yin, A. M. H. Cheung, K. S. Wong, S. K. So and H. Yan. High-Efficiency Indoor Organic Photovoltaics with a Band-Aligned Interlayer. *Joule* **4,** 1486–1500 (2020). DOI: 10.1016/j.joule.2020.05.010.

227. D. Lübke, P. Hartnagel, J. Angona and T. Kirchartz. Comparing and Quantifying Indoor Performance of Organic Solar Cells. *Advanced Energy Materials* **11,** 2101474 (2021). DOI: 10.1002/aenm.202101474.

228. A. Hadipour, B. de Boer and P. Blom. Organic Tandem and Multi-Junction Solar Cells. *Advanced Functional Materials* **18,** 169–181 (2008). DOI: 10.1002/adfm.200700517.

229. J. Wang, Z. Zheng, Y. Zu, Y. Wang, X. Liu, S. Zhang, M. Zhang and J. Hou. A Tandem Organic Photovoltaic Cell with 19.6% Efficiency Enabled by Light Distribution Control. *Advanced Materials* **33,** 2102787 (2021). DOI: 10.1002/adma.202102787.

230. M. A. Green. Radiative efficiency of state-of-the-art photovoltaic cells. *Progress in Photovoltaics: Research and Applications* **20,** 472–476 (2012). DOI: 10.1002/pip.1147.

231. U. Rau, B. Blank, T. C. Müller and T. Kirchartz. Efficiency Potential of Photovoltaic Materials and Devices Unveiled by Detailed-Balance Analysis. *Physical Review Applied* **7,** 044016 (2017). DOI: 10.1103/PhysRevApplied.7.044016.

232. J. Benduhn, K. Tvingstedt, F. Piersimoni, S. Ullbrich, Y. Fan, M. Tropiano, K. A. McGarry, O. Zeika, M. K. Riede, C. J. Douglas, S. Barlow, S. R. Marder, D. Neher, D. Spoltore and K. Vandewal. Intrinsic non-radiative voltage losses in fullerene-based organic solar cells. *Nature Energy* **2,** 17053 (2017). DOI: 10.1038/nenergy.2017.53.

233. K. Vandewal, J. Benduhn and V. C. Nikolis. How to determine optical gaps and voltage losses in organic photovoltaic materials. *Sustainable Energy & Fuels* **2,** 538–544 (2018). DOI: 10.1039/C7SE00601B.

234. L. Liu, H. Xiao, K. Jin, Z. Xiao, X. Du, K. Yan, F. Hao, Q. Bao, C. Yi, F. Liu, W. Wang, C. Zuo and L. Ding. 4-Terminal Inorganic Perovskite/Organic Tandem Solar Cells Offer 22% Efficiency. *Nano-Micro Letters* **15,** 23 (2023). DOI: 10.1007/s40820-022-00995-2.

235. X. Rodríguez-Martínez, E. Pascual-San-José and M. Campoy-Quiles. Accelerating organic solar cell material's discovery: high-throughput screening and big data. *Energy & Environmental Science* **14,** 3301–3322 (2021). DOI: 10.1039/D1EE00559F.

236. S. Kim, J. A. Márquez, T. Unold and A. Walsh. Upper limit to the photovoltaic efficiency of imperfect crystals from first principles. *Energy & Environmental Science* **13,** 1481–1491 (2020). DOI: 10.1039/D0EE00291G.

237. J. Hofinger, C. Putz, F. Mayr, K. Gugujonovic, D. Wielend and M. C. Scharber. Understanding the low voltage losses in high-performance non-fullerene acceptor-based organic solar cells. *Materials Advances* **2,** 4291–4302 (2021). DOI: 10.1039/D1MA00293G.

238. Q. Liu, Y. Jiang, K. Jin, J. Qin, J. Xu, W. Li, J. Xiong, J. Liu, Z. Xiao, K. Sun, S. Yang, X. Zhang and L. Ding. 18% Efficiency organic solar cells. *Science Bulletin* **65,** 272–275 (2020). DOI: 10.1016/j.scib.2020.01.001.

239. C. Sun, F. Pan, H. Bin, J. Zhang, L. Xue, B. Qiu, Z. Wei, Z.-G. Zhang and Y. Li. A low cost and high performance polymer donor material for polymer solar cells. *Nature Communications* **9,** 743 (2018). DOI: 10.1038/s41467-018-03207-x.

240. Z. Xu, F. Pan, C. Sun, S. Hong, S. Chen, C. Yang, Z. Zhang, Y. Liu, T. P. Russell, Y. Li and D. Wang. Understanding the Morphology of High-Performance Solar Cells Based on a Low-Cost Polymer Donor. *ACS Applied Materials & Interfaces* **12,** 9537–9544 (2020). DOI: 10.1021/acsami.9b22666.

241. E. Pascual-San-José, X. Rodríguez-Martínez, R. Adel-Abdelaleim, M. Stella, E. Martínez-Ferrero and M. Campoy-Quiles. Blade coated P3HT:non-fullerene acceptor solar cells: a high-throughput parameter study with a focus on up-scalability. *Journal of Materials Chemistry A* **7,** 20369–20382 (2019). DOI: 10.1039/C9TA07361B.

242. D. Baran, R. S. Ashraf, D. A. Hanifi, M. Abdelsamie, N. Gasparini, J. A. Röhr, S. Holliday, A. Wadsworth, S. Lockett, M. Neophytou, C. J. M. Emmott, J. Nelson, C. J. Brabec, A. Amassian, A. Salleo, T. Kirchartz, J. R. Durrant and I. McCulloch. Reducing the efficiency–stability–cost gap of organic photovoltaics with highly efficient and stable small molecule acceptor ternary solar cells. *Nature Materials* **16.** Paper of the O-IDFBR synthesis, 363–369 (2017). DOI: 10.1038/nmat4797.

243. S. Liu, Y. Zhou, Z. Liang, B. Zhao, W. Wang, Z. Xue, K. Ding, Z. Cong, H. Wu, G. Lu and C. Gao. High-Performance Pseudo-Bilayer Organic Solar Cells Enabled by Sequential Deposition of D18/Y6 Chloroform Solution. *ACS Applied Energy Materials* **6,** 5047–5057 (2023). DOI: 10.1021/acsaem.3c00694.

244. Y. Wu, Y. Zheng, H. Yang, C. Sun, Y. Dong, C. Cui, H. Yan and Y. Li. Rationally pairing photoactive materials for high-performance polymer solar cells with efficiency of 16.53%. *Science China Chemistry* **63,** 265–271 (2020). DOI: 10.1007/s11426-019-9599-1.

245. A. Harillo-Baños, X. Rodríguez-Martínez and M. Campoy-Quiles. Efficient Exploration of the Composition Space in Ternary Organic Solar Cells by Combining High-Throughput Material Libraries and Hyperspectral Imaging. *Advanced Energy Materials* **10,** 1902417 (2020). DOI: 10.1002/aenm.201902417.

246. R. Hunt. *The Reproduction of Colour* DOI: 10.1002/0470024275 (Wiley, Sept. 2004).

247. H. Bristow, K. J. Thorley, A. J. P. White, A. Wadsworth, M. Babics, Z. Hamid, W. Zhang, A. F. Paterson, J. Kosco, J. Panidi, T. D. Anthopoulos and I. McCulloch. Impact of Nonfullerene Acceptor Side Chain Variation on Transistor Mobility. *Advanced Electronic Materials* **5,** 1900344 (2019). DOI: 10.1002/aelm.201900344.

248. S. Halaby, M. W. Martynowycz, Z. Zhu, S. Tretiak, A. Zhugayevych, T. Gonen and M. Seifrid. Microcrystal Electron Diffraction for Molecular Design of Functional Non-Fullerene Acceptor Structures. *Chemistry of Materials* **33,** 966–977 (2021). DOI: 10.1021/acs.chemmater.0c04111.

249. S. Marina, A. D. Scaccabarozzi, E. Gutierrez-Fernandez, E. Solano, A. Khirbat, L. Ciammaruchi, A. Iturrospe, A. Balzer, L. Yu, E. Gabirondo, X. Monnier, H. Sardon, T. D. Anthopoulos, M. Caironi, M. Campoy-Quiles, C. Müller, D. Cangialosi, N. Stingelin and J. Martin. Polymorphism in Non-Fullerene Acceptors Based on Indacenodithienothiophene. *Advanced Functional Materials* **31,** 2103784 (2021). DOI: 10.1002/adfm.202103784.

250. P. A. Troshin, H. Hoppe, J. Renz, M. Egginger, J. Y. Mayorova, A. E. Goryachev, A. S. Peregudov, R. N. Lyubovskaya, G. Gobsch, N. S. Sariciftci and V. F. Razumov. Material Solubility-Photovoltaic Performance Relationship in the Design of Novel Fullerene Derivatives for Bulk Heterojunction Solar Cells. *Advanced Functional Materials* **19,** 779–788 (2009). DOI: 10.1002/adfm.200801189.

251. D. Corzo, D. Rosas-Villalva, A. C, G. Tostado-Blázquez, E. B. Alexandre, L. H. Hernandez, J. Han, H. Xu, M. Babics, S. D. Wolf and D. Baran. High-performing organic electronics using terpene green solvents from renewable feedstocks. *Nature Energy* **8,** 62–73 (2022). DOI: 10.1038/s41560-022-01167-7.

252. U. Rau. Reciprocity relation between photovoltaic quantum efficiency and electroluminescent emission of solar cells. *Physical Review B* **76,** 085303 (2007). DOI: 10.1103/PhysRevB.76.085303.

253. F. Bai, J. Zhang, A. Zeng, H. Zhao, K. Duan, H. Yu, K. Cheng, G. Chai, Y. Chen, J. Liang, W. Ma and H. Yan. A highly crystalline non-fullerene acceptor enabling efficient indoor organic photovoltaics with high EQE and fill factor. *Joule* **5,** 1231–1245 (2021). DOI: 10.1016/j.joule.2021.03.020.

254. J. Schanda. *Colorimetry: Understanding the CIE system* (ed J. Schanda) 282. DOI: 10.1002/9780470175637 (Wiley, July 2007).

255. J. E. Carlé, M. Helgesen, O. Hagemann, M. Hösel, I. M. Heckler, E. Bundgaard, S. A. Gevorgyan, R. R. Søndergaard, M. Jørgensen, R. García-Valverde, S. Chaouki-Almagro, J. A. Villarejo and F. C. Krebs. Overcoming the Scaling Lag for Polymer Solar Cells. *Joule* **1,** 274–289 (2017). DOI: 10.1016/j.joule.2017.08.002.

256. M. Hösel, D. Angmo, R. R. Søndergaard, G. A. dos Reis Benatto, J. E. Carlé, M. Jørgensen and F. C. Krebs. High-Volume Processed, ITO-Free Superstrates and Substrates for Roll-to-Roll Development of Organic Electronics. *Advanced Science* **1** (2014). DOI: 10.1002/advs.201400002.

257. T. R. Andersen, H. F. Dam, M. Hösel, M. Helgesen, J. E. Carlé, T. T. Larsen-Olsen, S. A. Gevorgyan, J. W. Andreasen, J. Adams, N. Li, F. Machui, G. D. Spyropoulos, T. Ameri, N. Lemaître, M. Legros, A. Scheel, D. Gaiser, K. Kreul, S. Berny, O. R. Lozman, S. Nordman, M. Välimäki, M. Vilkman, R. R. Søndergaard, M. Jørgensen, C. J. Brabec and F. C. Krebs. Scalable, ambient atmosphere roll-to-roll manufacture of encapsulated large area, flexible organic tandem solar cell modules. *Energy & Environmental Science* **7,** 2925 (2014). DOI: 10.1039/C4EE01223B.

258. F. C. Krebs, T. Tromholt and M. Jørgensen. Upscaling of polymer solar cell fabrication using full roll-to-roll processing. *Nanoscale* **2,** 873 (2010). DOI: 10.1039/b9nr00430k.

259. K. Kawano, R. Pacios, D. Poplavskyy, J. Nelson, D. D. Bradley and J. R. Durrant. Degradation of organic solar cells due to air exposure. *Solar Energy Materials and Solar Cells* **90,** 3520–3530 (2006). DOI: 10.1016/j.solmat.2006.06.041.

260. S. Riera-Galindo, M. Sanz-Lleó, E. Gutiérrez-Fernández, N. Ramos, M. Mas-Torrent, J. Martín, L. López-Mir and M. Campoy-Quiles. High Polymer Molecular Weight Yields Solar Cells with Simultaneously Improved Performance and Thermal Stability. *Small* **20,** 2311735 (2024). DOI: 10.1002/smll.202311735.

261. Student. The Probable Error of a Mean. *Biometrika* **6,** 1 (1908). DOI: 10.2307/2331554.